UHASSELT

KNOWLEDGE IN ACTION

U M **Maastricht University**

Hochschule Kaiserslautern
University of Applied Sciences

Doctoral dissertation submitted to obtain the degree of
Doctoral of Biomedical Sciences, to be defended by

Miriam Schwartz

DOCTORAL DISSERTATION
Detection of biomolecules using multivariant data analysis from silicon nanowire field-effect transistor arrays

IMO-IMOMEC
▶▶ UHASSELT · imec

Abstract

The aim of this thesis was to establish different medically relevant bioassays on silicon nanowire field-effect transistor sensors (SiNW FET). In parallel to this doctoral thesis with biomedical and biosensing focus, another thesis work was done by a colleague, where new readout instruments and a circuit model description of the SiNW FETs and the amplifiers were elaborated. The SiNW FETs used in both thesis works were fabricated in the framework of a previous project. The nanoelectronic SiNW FET platform has unique features, like a label-free detection of biomolecules, an ultra-sensitive and highly specific response as well as a fast detection of the biomolecular binding reaction within some minutes. These beneficial attributes make this platform a promising technology for future healthcare monitoring and, in particular, for the usage in diagnostic applications, where a fast, sensitive, portable and early detection is very important and can save lives.

In initial experiments, the working principle and the functionality of the SiNW FETs were verified by pH and conductivity measurements as well as by detecting the layer-by-layer deposition of polyelectrolyte multilayers. Afterwards, two types of medically relevant bioassays were established on the nanowire platform and on microsized, ion-sensitive field-effect transistors (ISFETs) as control sensors to compare micro- to nanoscale devices. In the first bioassay, DNA hybridization of short oligonucleotides on the sensor surfaces was detected. In initial tests, a synthetic 20 base pair (bp) DNA sequence was used to establish a robust assay. Afterwards, a 20 bp DNA sequence specific to Human Leukocyte Antigen-B27 (HLA-B27) was used towards biomedically relevant experiments. Carriers of the HLA-B27 allele have a higher risk to suffer from auto immune diseases, such as Morbus Bechterew, Morbus Reiter and other inflammatory disorders. In contrast to standard DNA-microarrays, which typically utilize fluorescence of previously labeled target analytes, the detection with the SiNW FET biosensors is direct and label-free. Therefore, electronic or electrochemical assays reduce costs and time. Secondly, protein bioassays were performed, in which the target protein binding to its specific antibody was measured. With electrochemical biosensors such as SiNW FETs, the detection of larger, globular

biomolecules is more difficult than the detection of short DNA sequences. In the bioassay, the brain-derived neurotrophic factor (BDNF), which is reduced in Alzheimer, Parkinson's and Huntington's disease, was detected. In the human body, BDNF is present in serum, tears, saliva and liquor. The detection of BDNF was done in differently concentrated phosphate buffers and in Hank's balanced salt solution. It was possible to measure clinically relevant concentrations with the SiNW FET biosensor. Moreover, the detected BDNF concentrations were lower than the limit-of-detection of a commercially available ELISA kit. Besides its higher sensitivity, the SiNW FET method presented in this thesis has further advantages compared to an ELISA assay: It is label-free so that no secondary antibody is necessary, fully-electronic, which means it could be miniaturized and integrated into a battery powered handheld device, and the results are available within some minutes depending on the affinity of the binding partners. The results obtained in this thesis indicate that the SiNW FET platform has a tremendous potential as a future point-of-care platform technology for biomedical applications. In a biomedical company, further research was done in highly concentrated buffer, synthetic and human serum on the nanowire-based platform. The obtained results were promising and some of them were published in a patent.

For the practical experiments presented in this work, the SiNW FETs were fabricated and encapsulated such that they can electronically record the biomolecule binding at the solid-liquid interface in different liquid matrices. For the establishment of a bioassay on the sensors, the sensor surface had to be functionalized with a siloxane layer and modified with specific capture molecules as a bioreceptor layer. To avoid false-positive signals, free areas of the sensor surface were blocked with a suitable blocking agent. To verify that the experimental procedures of the assays were stable and reliable, optical controls were firstly established on bare glass or silicon surfaces and on non-functionalized nanowire chips. The electronic recordings were done in two different modes: Firstly, potentiometric DC detection was used by measuring the transfer characteristic of the SiNW FETs before and after the target binding. This detection scheme is used by most of the research groups in the silicon nanowire field. Upon binding of biomolecules to the SiNW FET surface, the typical shift of the transfer characteristic was observed, which was already reported before for

ISFET and other silicon nanowire devices. The results obtained in this thesis work indicated that the SiNW FETs function similarly to long-channel field-effect transistor devices. Furthermore, the dimensions of the nanowires have a strong influence on the shape of the transfer characteristic curves and, with this, also on their sensitivity. This was not reported before in the research field. In DNA experiments, it was shown that in thinner wires the curve was steeper than in wider wires. The second detection method was an impedimetric AC mode, where the transistor transfer function, *i.e.* the frequency bandwidth, of the SiNW FETs was measured. The theory of the AC recording is still under discussion and latest experimental findings are presented. The transistor transfer function in general is the mathematical representation of the relation between the input and the output signals of a frequency-dependent system. Biomolecular interactions at the sensor surface lead to a change in their input impedance and, hence, to a change in the transistor transfer function spectrum. However, the experimental results demonstrate that various parameters have an influence on this recording mode. In case of the microscale ISFET devices, the transistor transfer function decreases after each biomolecule layer. This is in agreement with previously published observations. For the SiNW FET sensors, the results were not fully reliable, wherefore it was concluded that, besides the attachment of the biomolecules, also the charge type, the charge density and the conformation of the biomolecules might influence this readout mode. To derive further information and conclusions from the results of the protein bioassay, a multivariant data analysis was developed with the help of a custom-made MATLAB program. In doing so, the two previously mentioned readout principles were combined, since they can be measured simultaneously. Seven different parameters of the DC and AC readouts were evaluated and plotted against each other in a radar plot to allow a comparison of all variants. A classification model consisting of various decision trees was implemented. The purpose was to differentiate between the different experimental steps as well as between the different concentrations. Finally, the accuracy of the classification model was evaluated. So far, it is only feasible to verify an analyte by functionalizing the sensor surface with specific capture molecules. However, no further information of the target molecules, such as size, surface activity or conformation can be derived. Therefore, the ultimate goal of this multivariant data analysis is to

create a library of various parameters in order to identify an unknown analyte and the corresponding characteristics by means of its structure, concentration, total charge, and charge distribution in future works.

In conclusion, this thesis work demonstrates that it is possible to detect ultra-low concentrations of biomolecules (down to the fM regime) with the SiNW FET platform, which make it an interesting tool in different applications areas, in which the detection of very tiny concentrations is crucial. Because it was possible to detect BDNF as a target molecule, which is involved in different diseases, the SiNW FETs are a promising technology for the detection of other analytes related to medical disorders. This could be realized by changing the surface modification protocol of the sensors and by applying other, specific capture molecules. In future, more experimental studies need to be performed in human samples, such as serum, saliva or tears. It is assumed that the sensitivity of the SiNW FETs might be reduced in body fluids due to the various components of these liquids. However, by optimizing the surface modification and functionalization, it is expected that the SiNW FET platform can compete with commercially available ELISA tests or fluorescence microarrays. The differential readout of SiNW FETs in an array format offers the possibility to identify different target molecules, simultaneously. This property would be beneficial to detect multiple biomarkers at the same time for panel assays using multivariant recording with different parameters. It is well known in the biosensor field that many novel bioassays on electronic platforms are highly prone to false recordings caused by side influences from parameters such as temperature, pH and ionic strength variations in the detection matrix. The here developed method for multivariant data analysis of multiple, partly independent transducer principles might also be expanded to include these parameters on future multisensoric SiNW FET platforms. By this, the multivariant method offers many promising features for future point-of-care instruments.

Nederlandse samenvatting

De doelstelling van deze thesis is de ontwikkeling van nieuwe biosensorische analysemethoden waarbij veldeffect-transistoren op de basis van silicium-nanodraden (SiNW-FETs) een centrale rol spelen. De fabricage van deze nanodraden was al eerder op punt gesteld (Research Institute Jülich, Peter Grünberg Institute) en deze thesis richt zich dan ook volledig op biomedische applicaties, met het beschikbaar sensor-platform als vertrekpunt. Het nanodraad-platform combineert unieke en wenselijke sensor-eigenschappen zoals de label-vrije detectie van bio-moleculaire interacties met ultra-lage detectielimieten en hoge specificiteit dankzij een gunstige oppervlak-volume verhouding. Ook de responsietijden zijn betrekkelijk kort op een schaal van slechts enkel minuten. Hierdoor zijn nanodraad-biosensoren geknipte kandidaten voor biomedische- en diagnostische analyses die snel en nauwkeurig moeten gebeuren, bij voorkeur zelfs in een zo vroeg mogelijk stadium van een medische aandoening.

In pilotexperimenten werden de functie en het werkingsprincipe van de nanodraad-transistoren gekarakteriseerd, meer bepaald met pH- en geleidbaarheidsmetingen en studies op de zelfassemblage van polyelektrolyt multilagen. Vervolgens werden twee assaytypes op zowel het nanodraad-platform als op ionengevoelige veldeffect-transistoren (ISFETs) op microschaal ontwikkeld om rechtstreeks de invloed van de grootte van de sensorelementen te kunnen vergelijken. Het eerste assay was de elektronische uitlezing van DNA-hybridisatie en het tweede assay richtte zich tot de detectie van proteïnen met behulp van specifieke antilichamen. In de DNA experimenten werd het sensorprincipe eerst uitgetest met synthetische DNA- fragmenten bestaande uit 20 basenparen (bp). De ervaringen met dit modelsysteem werden nadien toegepast op 20-bp sequenties van het humane leukocyten antigen B27 (HLA-B27): Dragers van het HLA-B27 allel vertonen een verhoogt risico op auto-immuunaandoeningen zoals morbus Bechterew, morbus Reiter en andere chronische ontstekingsreacties. In tegenstelling tot de gebruikelijke DNA-microarrays, die een beroep doen op fluorescerend gelabelde target-moleculen, zijn SiNM-FETs een rechtstreekse detectiemethode voor die geen labels

benodigd worden. Eens op punt gesteld zullen de elektronische en elektrochemische analysemethoden inherente voordelen bieden, in het bijzonder wat de tijd en kosten per analyse betreft. Bij het proteïne-assay op basis van antilichaam-antigen herkenning moet duidelijk worden gesteld dat de opsporing van de relatief grote, sferische doelmoleculen met de SiNM-FET techniek veel uitdagender is dan in geval van korte DNA sequenties. In onderhavig geval ging de aandacht uit naar het neurotrofine BDNF (brain-derived neurotrophic factor) waarvan de concentratie verlaagd is bij, onder andere, de ziektes van Alzheimer, Parkinson en Huntington. In het lichaam is BDNF aanwezig in bloedserum, hersen- en ruggenmergsvocht, speeksel en traanvocht. Om deze media zover mogelijk na te bootsen werden waterige oplossingen onderzocht zoals fosfaatbuffers met verschillende zoutconcentraties en Hanks' gebufferde zoutoplossing. Het is inderdaad gelukt om met het SiNM-FET platform klinisch relevante BDNF concentraties kwantitatief te bepalen en de detectielimiet was zelfs lager dan bij een commercieel beschikbare ELISA-test voor BDNF. Los van de hogere gevoeligheid van de SiNM-FETs vergeleken met ELISA springen nog bijkomende voordelen in het oog: De nieuwe methode is labelvrij, er worden geen secundaire antilichamen gebruikt en de meting gebeurt volledig elektronisch. Het laatste betekent dat alle componenten miniaturiseerbaar zijn zodat ze zich gemakkelijk in een compact meetinstrument laten integreren dat het resultaat binnen enkele minuten levert, dit in functie van de affiniteit tussen de bindende moleculen. Hiermee is de basis voor toekomstige point-of-care toepassingen gelegd en het principe is generisch wat betekend dat zich ook andere merker-proteïnen met dezelfde basismethode laten detecteren. In beide assays werden de sensoroppervlakken eerst van een linker-laag van silanen voorzien en vervolgens met selectieve receptormoleculen (ofwel enkelstreng DNA ofwel immunoglobulines) gefunctionaliseerd. Om vals-positieve signalen door aspecifieke adsorptie te vermijden werden de blootliggende delen van de sensoren bovendien met een adsorptie-werende coating bedekt. Ook aan de incapsulatie van de sensorchips met betrekking tot de vloeistofstalen en de connectie van de chips met de meetelektronica werd uitvoerig de aandacht besteed. Tevens werden optische referentiemetingen uitgevoerd om alle experimentele stappen van de assays met een onaf-hankelijke methode te verifiëren, los van de eigenlijke, elektronische sensoruitlezing.

De opname van de elektronische signalen gebeurde in twee verschillende meetmodes: De eerste meetmode, die in de context van nanodraadsensoren door de meeste onderzoeksgroepen wordt gebruikt, was de potentiometrische gelijkspanningsmeting (D.C.) op basis van de transistor-transferfunctie. Door de binding van biomoleculen aan het sensoroppervlak gebeurt een karakteristieke verschuiving van deze transferfunctie die de stroom in functie van de gate-spanning weergeeft en dit is zowel bij nanodraden als bij ISFETs een bekend fenomeen. De metingen tonen nu echter ook aan dat de dimensies van de nanodraden een sterke invloed op de vorm van deze transferfunctie hebben. Kortere nanodraden resulteren in een hogere stijging van de transferfunctie (hogere nauwkeurigheid) dan langere draden en dat wijst op een verhoudings-gewijs hogere concentratie van ladingsdragers in de kortere transistor-draden. Deze waarneming is nieuw en het effect was dan ook tot op heden nog niet bekend. Voor analytische applicaties waarin biomoleculen geïdentificeerd en gekwantificeerd worden blijkt dit echter heel nuttig te zijn: Niet enkel de verschuiving van de transferfunctie is een analytisch waardevolle, uitleesbare parameter maar ook de richtingscoëfficiënt aan het buigpunt van deze transferkromme. De tweede meetmode was de impedimetrische detectie waarin de transferfunctie van de transistoren met een wisselspanningssignaal (A.C.) opgemeten werd. De theorie achter de A.C.-uitlezing van transistoren is op dit ogenblik nog onderwerp van wetenschappelijke discussies en kort samengevat is de transferfunctie een wiskundige voorstelling van het verband tussen de ingangs- en uitgangssignalen van een frequentieafhankelijk systeem. Bio-moleculaire interacties die aan het gate-oxide van de transistor plaatsvinden leiden tot veranderingen in de membraan-impedantie wat zich neerslaat in een frequentieafhankelijkheid van de transferfunctie zelf. De resultaten van ons onderzoek wijzen duidelijk in de richting dat verschillende parameters de gedetecteerde signalen beïnvloeden: Bij de microschaal-ISFETs werd een systematische afname van de transferfunctie met een toenemend aantal lagen van biomoleculen vastgesteld en dit stemt overeen met de bevindingen van gerelateerd onderzoek. In het geval van het nanodraad-platform is de situatie echter meer complex en parameters die daarin een rol spelen zijn niet alleen de binding van biomoleculen aan het sensoroppervlak maar ook het ladingstype, de ladingsverdeling en de conformatie van deze moleculen. Met de bedoeling om

nog diepgaandere informatie uit de ontwikkelde proteïne-assay te winnen werd met behulp van een Matlab programma een multivariate gegevensanalyse ontwikkeld en toegepast. Hierbij werden de gegevens van beide meetmodes gecombineerd omdat, per bio-assay, toch beide informaties simultaan ter beschikking staan. In totaal werd met zeven verschillende parameters uit de D.C.- en A.C. transistor-metingen rekening gehouden en ze werden in functie van elkaar als radar-plots voorgesteld om hun relatief belang in te schatten. Tenslotte werd ook de nauwkeurigheid van het assay zelf geëvalueerd door middel van een classificatiemodel met ingebouwde beslissingsstructuren. Zodoende is het mogelijk vals positieve of vals negatieve resultaten te identificeren wat de betrouwbaarheid van de metingen uiteraard ten goede komt. De multivariate gegevensanalyse biedt ook bijkomende perspectieven: De gevoeligheid van huidige assays berust op de selectiviteit van de gebruikte receptormoleculen terwijl geen of slechts beperkte informatie wordt verkregen over de grootte, oppervlakactiviteit en conformatie van de targetmoleculen. Op termijn zal de multivariate analyse naar een bibliotheek van parameters leiden waarmee zich ook onbekende targetmoleculen laten identificeren op basis van hun structuur, concentratie, conformatie, lading en ladingsverdeling.

In conclusie toont dit werk aan dat de silicium-nanodraad veldeffect-transistoren een krachtig platform bieden om ultra-lage concentraties van biomoleculen te detecteren, dit zelfs tot in het femto-molaire concentratiegebied. Bijgevolg zijn nanodraad-sensoren beloftevol voor tal van point-of-care applicaties waarin zeer lage molecuulconcentraties gedetecteerd moeten worden zonder gebruik te hoeven maken van fluorescerende, radioactieve of enzymatisch gelabelde hulpstoffen. Hiervoor is echter nog bijkomende optimalisatie vereist, vooral om de relevante bio-merkers niet enkel in buffer-oplossingen te kunnen opsporen maar ook in patiëntenstalen met een complexe samenstelling en het risico voor aspecifieke effecten: In toekomstig onderzoek zal langs twee routes aan deze uitdaging gewerkt worden, namelijk ter hoogte van de biochemische architectuur van de sensoroppervlakken en ook aan de parallelle uitlezing van verschillende sensorkanalen. Zodoende laten zich aspecifieke signalen door differentiële metingen compenseren en bovendien kunnen de nanodraad-assays uitgebreid worden tot de gelijktijdige detectie van hele panels van moleculaire bio-merkers. Hiervoor werd in deze thesis de basis gelegd.

Table of Contents

Chapter 1 - Introduction

In recent years, a lot of effort was invested into the diagnosis of diseases in an early stage so that a further progress and development can be prevented. Moreover, numerous research groups have focused on the identification of defects in the DNA sequence or in the protein structure. In this field, the ultimate aim is the detection of a patient's potential risk to suffer from a minor or severe disease in future by the identification of the defect, which might cause the outbreak of this disorder [1–3]. This means, a detection principle and platform is needed with which it would be feasible to verify the mutation or defect of interest so that any precaution can be performed to contain and eliminate the disease or to start the medical treatment as early as possible. For fulfilling this goal, the identification of the exact structure, assembly and working principle in protein and DNA sequences attracted an increasing interest over the last decades. Furthermore, considerable research effort was invested in developing platforms for early-stage detection [4–6]. The preferred platforms to be used for this purpose are biosensors because of their portability, specificity and low-cost fabrication [7].

A biosensor consists of a receptor or (bio-) chemical recognition element, which can be antibodies, antigens, cells, DNA, enzymes or even a molecular imprinted polymer. The biorecognition reaction takes place, when an analyte binds to its specific receptor. The transducer converts this recognition reaction into a measurable signal. This signal can be *e.g.* optical, electrochemical, gravimetric, thermal or acoustical. Afterwards, the signal reaches an amplifier which amplifies the signal and leads it to a computer, where a direct readout can be performed [8]. An optimized biosensor needs to fulfill several requirements: The detection should be fast so that the user has the results within some minutes or, in best case, some seconds. It should be specific so that only the target molecules are measured in a solution composed of different components to prevent false-positive results created by binding of competitive analytes. The ideal sensor should possess a high sensitivity so that even a very low concentration of the analyte of interest is generating a signal and, hence, can be identified. This is important for the detection of, for example, explosives or toxic

substances, but also for single nucleotide polymorphisms in the DNA sequence. Moreover, the assay should be reliable so that false-positive or false-negative results are avoided, as described before. Besides this, the biosensor should also be stable over a long period by preventing any degradation effects [9]. Nowadays, much progress was achieved in developing label-free readout platforms [10–14]. With these devices, the target analyte can be directly monitored without the need to add a labeling step, which might be time consuming or which could influence the reaction by the label itself [15]. The readout of the detection principle is fully electronic [16,17]. This means it is fast and automated and the result is directly shown on a display.

Since 1970, when Piet Bergveld and coworkers introduced the ion-sensitive field-effect transistor (ISFET) for the first time [18], this detection platform has gained plenty of attention in terms of its application possibility as biosensor. In the following years, they were focusing on the further development of ISFETs [19–21]. Other groups started to use ISFET devices as well and showed that, besides the detection of DNA [16,17,22–25], they are also usable in other biological fields, *e.g.* for the detection of cellular signals [26–28], enzymes [29–31] and proteins [32–34]. The devices offer the feasibility for a label-free, fully-electronic readout of the molecules of interest. Moreover, the target analytes can be detected in real-time measurements, which make this readout fast. These features save time and money compared to conventional assays, like for example, an ELISA assay, where time- and material-consuming labeling steps are required.

In recent years, silicon nanowire field-effect transistors attracted considerable attention since they possess many profitable properties compared to the generally larger ISFET devices. Thanks to the development of nanostructured field-effect transistors, it was possible to detect ultra-low concentrations of the target analytes, which were reported to be in the femtomolar range. The ultrahigh sensitivity can be explained by a high surface to volume ratio and the size of the nanowire, which is in the range of the biomolecules which need to be detected [35,36]. It was shown that the nanowire sensors can be used as DNA sensors [37–40], as immunosensors [41], and as sensor arrays for extracellular recordings [42–44]. In terms of DNA detection, SiNW FETs offer the possibility to distinguish single nucleotide polymorphisms in short oligonucleotide

sequences [37,38,40,45]. Furthermore, it was shown that, besides their ultrasensitivity, the field-effect devices are specific as well. This specificity can be obtained by modifying the biosensors' surface in such a way that only the analyte binds to a specific capture molecule. The typically-used detection principle is based on field-effect sensing, where the binding of the negatively or positively charged molecules to the solid-liquid interface is influencing the surface potential of the transistor devices. As a result, the number of charge carriers inside of the semiconductor devices is influenced and quite often the conductance changes of the nanowires are displayed [46–48]. In some cases, the subthreshold region of the wires is displayed most of the time by using high-precision semiconductor devices and wafer probe stations. In the linear operation regime, where the drift carrier conduction is dominating over the diffusion-based conductance the typically-used readout can be regarded as a potentiometric mode (DC readout) in which the FET's transfer characteristic [49–53] and the shift in threshold-voltage of the FET devices are measured.

This thesis focuses on the biomolecular detection with silicon nanowire field-effect transistors. The goal of this work was to establish a protein and DNA assay on basis of the top-down fabricated silicon nanowire field-effect platform. The obtained results are represented and discussed in this thesis. The silicon nanowire sensors used in this work were fabricated during a previous doctoral thesis [54]. Except of the fabrication process, all experiments and further developments as well as the corresponding results shown in Chapter 4, 5 and 6 were done in framework of the present thesis. The nanoscaled transistors were developed further as a biomedical platform towards clinical relevance in this world.

Before summarizing the achieved data, a general description and overview of the structure, assembly, working principle, function and defects of proteins and DNA will be given in the fundamentals chapter. Besides this, some assays and sensor platforms for the evaluation of defects or mutations in the protein and DNA sequence will be described. Moreover, the progress in the field of field-effect transistors, especially silicon nanowire field-effect transistors, is focused and application possibilities are shown. The theory of the detection principle is described in Chapter 2 as well. Finally, it is explained which advancements we did with our silicon nanowire devices.

In Chapter 3, the applied materials and methods are summarized, and the fabrication of the used chips is described. The surface modification process is explained in Chapter 3, as well as the performed DNA and protein assay. The last part of this section is about the readout methods that were performed.

The proof-of-principle experiments as well as the results of the DNA and of the protein experiments are demonstrated and discussed in Chapter 4, 5 and 6. For DNA and proteins assays, the achieved data is highlighted for the potentiometric as well as for the impedimetric readout mode.

To start with, some proof-of-principle experiments, in which pH changes, conductivity differences and the assembly of polyelectrolyte multilayers are measured on the nanowire platform, are presented in Chapter 4.

The results of the detection of an artificial DNA sequence are presented in Chapter 5. For this purpose, the DNA immobilization and hybridization processes were monitored. Furthermore, conclusions of the influence of the nanowire size on the behavior of the transistor's transfer characteristic are drawn. The subchapter 5.4 is about the results of the detection of a real DNA assay, where the immobilization and hybridization of one human leucocyte antigen gene sequence, HLA-B 27, was measured on the microscaled ISFETs available in our research group.

In Chapter 6, the measurements and evaluation of the protein experiments are presented. The binding of the cytokine growth factor brain-derived neurotrophic factor (BDNF) to its specific antibody is depicted by evaluation of the DC and AC readout methods in this section. Furthermore, the influence of the buffer concentration on the signal strength is discussed.

In Chapter 7, a summary of the results of all experiments is briefly given. This includes the proof-of-principle experiments performed by measuring the change in pH and in conductance as well as by the layer-by-layer assembly of polyelectrolyte multilayers. However, the focus is based on the bioassays, in which specific DNA molecules were detected and a sensitive readout of the growth factor BDNF was developed.

To finalize this thesis, a conclusion and a short outlook will be given as last chapter, in which all achieved progresses but also drawbacks of the sensor platform are summarized. Moreover, future perspectives concerning improvements and application possibilities of the system are depicted.

Chapter 2 - Fundamentals

2.1 Proteins

2.1.1 Structure and assembly

Proteins are small or big macromolecules with either mainly hydrophilic, or mainly lipophilic characteristics. They can exist as single unit or as part of a bigger compound. Depending on their function and composition, their shape can be either rigid or flexible [55]. Proteins consist of more than hundred L-amino acids, whereas polypeptides are composed of up to 100 amino acids. The sequence of the amino acids determines the structure, folding and the function of a protein. In general, each amino acid has the same main structure: A hydrogen atom, an amino group, a carboxyl group and a side chain, which are bound to a central carbon atom. There are 20 different amino acids in nature, which are used by living cells and organisms. Among them, there are eight essential amino acids, which cannot be built by the human body itself and which have to be applied by nourishments. These essential amino acids are isoleucine, leucine, lysine, methionine, phenylalanine, threonine, tryptophan and valine. In *Figure 1*, *a*n overview of the essential amino acids is displayed. Moreover, twelve unessential amino acids exist which can be synthesized by the human body itself. The unessential amino acids are alanine, arginine, aspartate, cysteine, glutamate, glutamine, glycine, histidine, proline, serine, tyrosine and asparagine. A schematic of the unessential amino acids is shown in *Figure 2*. Depending on their side chain, the 20 amino acids can be classified into different groups with characteristic physicochemical properties:

1. Nonpolar, hydrophobic (alanine, glycine, isoleucine, leucine, proline, valine)
2. polar, neutral (asparagine, cysteine, glutamine, methionine, serine, threonine)
3. aromatic (phenylalanine, tryptophan, tyrosine)
4. basic (arginine, histidine, lysine)
5. acidic (aspartic acid/aspartate, glutamic acid/glutamate) [56].

These amino acids are assembled to polypeptides by forming peptide bonds. The sequence of the amino acids is unique for every protein and specified by the genetic code [56].
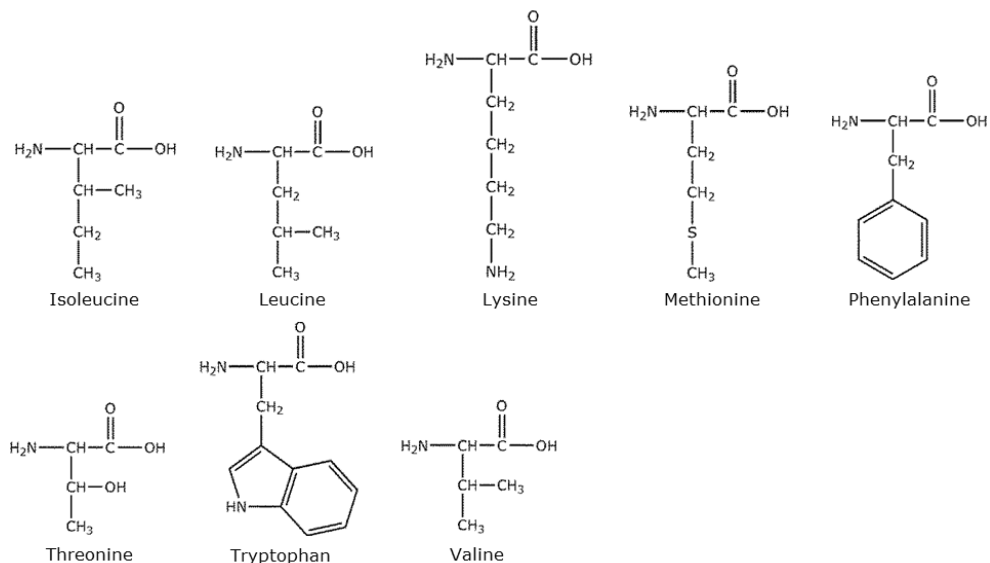
Figure 1: The eight essential amino acids.

In this figure, an overview of the eight essential amino acids is given. The figure was adapted from [57]*.*

According to their sequence, the amino acid compounds are folded inside the cell to a specific three-dimensional structure. The structure of all amino acids can be divided in primary, secondary and tertiary structure. The primary structure is the lowest structure in a protein where a peptide bond is created between the amino group of the α-carbon atom of one amino acid and the carboxyl group of the neighboring amino acid so that polypeptide chains are built up. The amino end of the sequence is considered as the starting point of the primary structure whereas the carboxyl group represents the end of the chain. In proteins, several peptide bonds of different amino acids can assemble to one complex in a specific spatial arrangement which is called quaternary structure. The secondary structure is the folding of the amino acid sequence, *i.e.* peptide chains, to a defined structure. Besides the amino acid sequence, hydrogen bonds are responsible for the secondary structure as well [57]. The secondary structure has different forms of appearance. There are the α-helix, β-sheet, loops and

hairpin bend secondary structures. Mostly, α-helix and β-sheet can be observed. The α-helix has a spiral shape and can be right- or left-handed.

Alanine | Arginine | Asparagine | Aspartate | Cysteine

Glutamate | Glutamine | Glycine | Histidine | Proline

Serine | Tyrosine
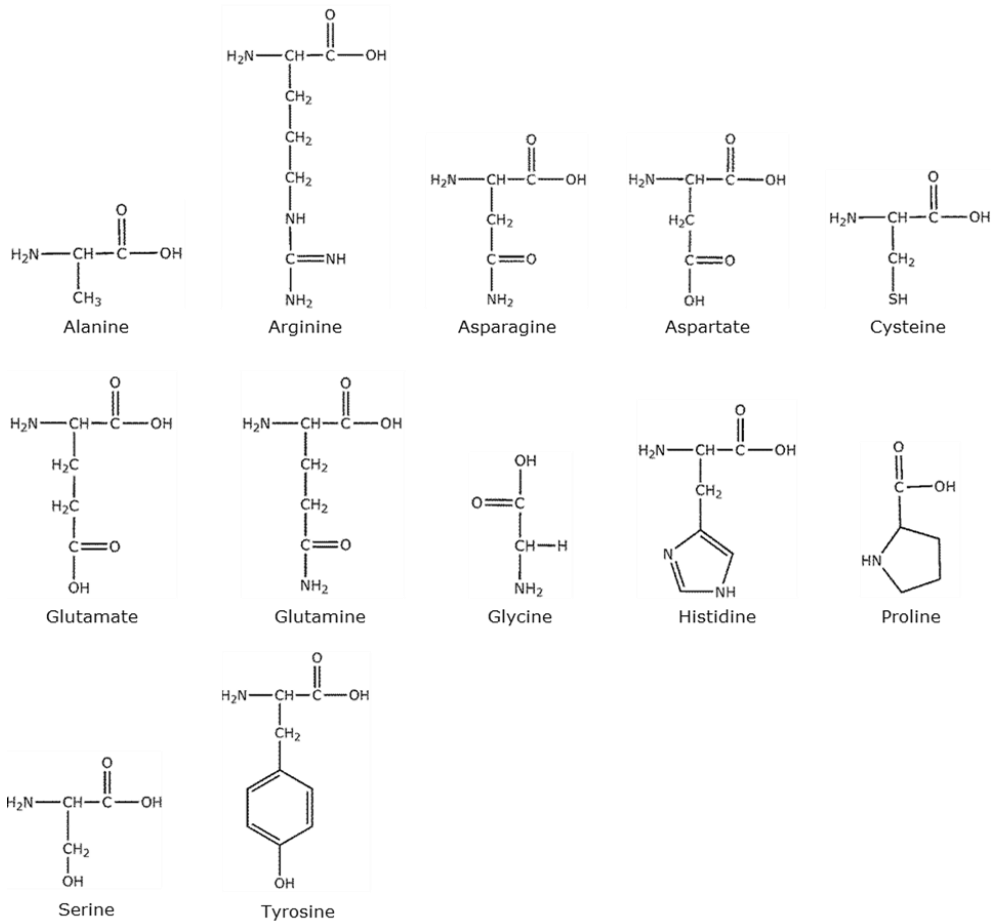
Figure 2: Overview of the twelve unessential amino acids.
In this figure, the twelve unessential amino acids are displayed. This figure was adapted from [57].

In most cases, the helix is right-handed because this is the energetic more advantageous condition. Inside an α-helix, the carboxyl group of every first amino acid forms a hydrogen bond with the amino group of every fifth amino acid (*Figure 3 a*). The shape of a β-sheet can be compared with an accordion (*Figure 3 b*) [57]: Due to hydrogen bonds of at least two amino acid strands, a parallel or anti-parallel β-sheet is formed. If more than 2 strands are building a β-sheet, the parallel and anti-parallel formation can be mixed. Loops show a

non-regular, but well-defined, rigid structure. Hairpin bends are more periodic and are characterized by multiple changes of direction. Once more, this structure is caused by hydrogen bonds between amino and carboxyl groups. Loops and hairpin bends are influencing the possible interactions at the surface of a protein. The tertiary structure is caused by three-dimensional folding of the secondary structure (*Figure 3 c*) [57].
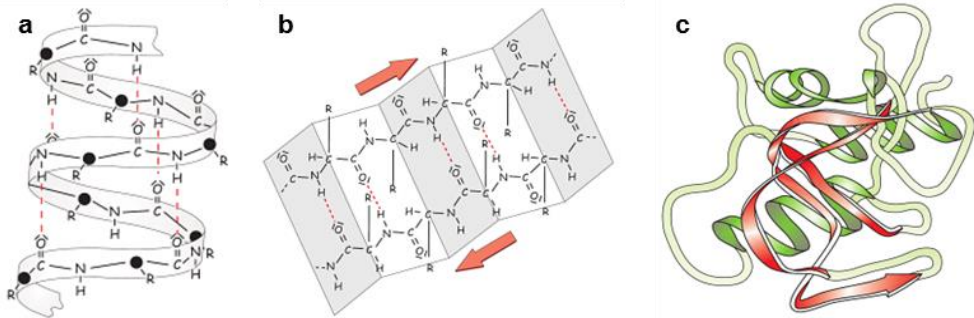
Figure 3: Secondary and tertiary protein structure.
In (a) and (b), the α -helix and β-sheet are represented, respectively. Both belong to the secondary structure of the protein assembly. In (c), the tertiary structure is depicted. The picture was taken from [57]*.*

In aqueous solutions, the polar (charged) parts of the strands are building the outer part of the tertiary structure whereas the uncharged parts are located in the inside of the structure [58]. Covalent and non-covalent bounds are shaping the tertiary structure. This includes the covalent disulfide bonds as well as the non-covalent hydrogen, ionic, van-der-Waals and hydrophobic bonds. The quaternary structure is formed due to the aggregation of several tertiary structures [57]. The simplest version is the assembly of two polypeptide chains to a dimer. Depending on their surface composition, different molecules can interact with the folded proteins. Due to binding of specific molecules, the protein conformation is changed [55]. The composition and a correct folding are assumed to contribute to the proper function of a protein. In the next subsection, some protein functions are briefly described.

2.1.2 Functions of proteins

Due to different amino acid sequence and different folding, there are many

proteins in the human body with varying structures and, hence, various functions. All proteins play a crucial role in the human body. The function of a protein is activated by phosphorylation by the enzyme kinase and inactivated by the enzyme phosphatase due to dephosphorylation [55]. A transferase enzyme causes a change in protein confirmation right after translation. The dephosphorylation is performed in a post-translational process to obtain the original confirmation of the protein [55]. Except for some RNA-molecules, all enzymes are proteins and involved in biochemical reactions. As catalysts, they speed up biochemical reactions by decreasing the activation energy. Furthermore, they can promote non-spontaneous reaction by coupling a reaction that releases energy with a reaction that needs energy [59]. Enzymes always bind specifically to their substrate according to the so-called key-lock principle [60]. This binding is non-covalent *via* hydrogen bonds, van-der-Waals bonds and hydrophobic interactions and leads to a change in conformation of the protein [60]. They control and influence the transport of different metabolites, act as catalysts, have functions in the neuronal system, such as the transfer of impulses, control of differentiation and growth, and, as antibodies, they are responsible for the immune response [58]. Structural proteins, like collagen, are another protein group. Collagen is part of the bones, skin and connective tissue. Actin and myosin contribute to cell movement (muscle contraction, locomotion, division) [55,60]. Intermediate filaments are strong fibers which are architectural elements inside the cell. Microtubules influence the cytoplasm structure and the distribution of organelles. Furthermore, they can also be involved in the cell division process in which they create the mitotic spindle [55]. Cell membrane proteins are involved in transport and signal distribution. Moreover, they also act as enzymes and receptors. Metabolites are transported *via* channel proteins from the inside to the outside of the cell or from the cell outside to the inside. Other proteins are responsible for the transport of their specific analyte through the blood to the target organ or target cell [55,60]. The signal distribution is done by receptors which reversibly bind specific ligands [59]. This leads to conformation change of the protein which causes the development of a signal [59]. Regulatory proteins bind to the specific metabolite and change their function [60]. As part of the immune system, proteins also have a protective function. This is just a brief overview of the protein functions.

Of course, there are other tasks, the proteins need to fulfill. All of these functions can be affected by a change in the amino acid sequence, which can cause severe defects. Some defects in the protein structure and the accompanying symptoms are presented in the next chapter.

2.1.3 Defects in proteins

A defect in the amino acid sequence or in the folding of a protein may lead to serious consequences. One disease related to a defect in the amino acid sequence is the cystic fibrosis (mucoviscidosis) [61]. Cystic fibrosis is triggered by different mutations in the cystic fibrosis transmembrane conductance regulator (CFTR), an epithelial transport protein [61]. The overall function of CFTR is still under discussion but it is assumed to be a chloride channel. Cystic fibrosis can be caused by two defects: It is reasoned by either a loss of one amino acid or by an exchange of an amino acid for another one. The disease induces an increase in secretion of the intestine, lungs, liver, genital tract, pancreas, nasal mucosa and the perspiratory glands. The mucus is thickened because of a higher resorption of sodium ions and water. The breathing is complicated due to the thickened mucus and the possibility for infections is much higher [61]. The Lyme borreliosis is an example for a disease in which the immune system, represented by antibodies, is involved. The *borrelia burgdorferi* bacteria are responsible for borreliosis [62], which is also known as Lyme disease. Ticks are the carrier of *borrelia burgdorferi* bacteria and, hence, of Lyme borreliosis [62]. If the tick has chosen a host, which can be animals or humans, it penetrates with its mandibles the skin of the victim and starts to suck the host´s blood. During blood sucking, borrelia bacteria can be transferred from the gut of the tick to the host. As soon as the tick is full of blood, it drops off. After two to four weeks or even a longer latency period, the immune system begins to produce antibodies against the borrelia. A typical clinical manifestation of the disease is the *Erythema migrans*, a migrant redness of the skin [63]. The redness of the skin is not the only clinical manifestation of the disease which is associated with a wide spectrum of symptoms. In general, three stages with certain guiding symptoms can be distinguished. This can be fever, headache and other flu symptoms in stage one, neurological disorders and intense pain in stage two [62] and arthritis or even mental degeneration in the third stage

[63,64]. If the infection with borreliosis is recognized in an early stage, it can be treated with antibiotics. Otherwise it can become chronic and the probability of neurodegeneration increases [65]. The disease can be verified, for example, by the detection of IgG antibodies against *borrelia burgdorferi* [62] or by PCR (polymerase chain reaction), in which the bacteria DNA has to be amplified and detected. For PCR detection, blood, cerebrospinal fluid, urine, skin and synovial fluid can be used as sample material [64,66].

In the framework of this thesis, the cytokine BDNF (brain-derived neurotrophic factor) was used for the antibody-antigen experiments. BDNF is an endogenous protein [67] which belongs to the family of nerve growth factors (NGF) [68]. It has a molecular weight of 27.818 kDa and can be detected in very small amounts in the adult central nervous system. Moreover, it was verified in serum, tears [69], liquor [70] and saliva [71,72]. The specific receptors for the BDNF protein are the tropomyosin related kinase B (TrkB) [73] and the low affinity nerve growth factor receptor (LNGFR) [74,75]. In contrast to the Trk receptors, the function of LNGFR is not completely examined yet. Among other factors, BDNF is responsible for the neuronal function and the plasticity of synapses [67]. As shown before, the factor also influences the survival of neural, crest-derived sensory neurons, of sensory neurons of the nodose ganglion, of cultured retinal ganglion cells, of septal cholinergic neurons in vitro and the survival of dopaminergic neurons as well as neuronal cells which degenerate in Parkinson's disease [68]. Parkinson's disease is a combination of different symptoms. They range from movement dysfunction, like tremor and rigidity, cognitive impairments, *e.g.* dementia and psychosis, to mood disorders, which are, for example, depression and anxiety. Further manifestations might be insomnia and other sleep disorders, autonomic disorders, pain as well as sensory dysfunctions [76,77]. Besides Parkinson's disease, there are several diseases related to a decreased concentration of BDNF in the nervous system [78]. A modified BDNF level is related to Huntington's disease. Huntington is a neurodegenerative disorder where the neurons in the striatum and cerebral cortex are degenerated. The Huntington disease gene, huntingtin, which normally stimulates the production of BDNF, is mutated in Huntington's diseases. It was demonstrated that the wild-type huntingtin enhances the production of BDNF. Furthermore, Zuccato et al. showed in a mouse model that a lower level of BDNF messenger

in the cortex is in correlation with the progression of Huntington's disease [79,80]. The symptoms of this disease can be divided in three different main types. Mental and behavioral disorders, mostly manifested in depressions, belong to the first group. The second type is related to cognitive impairments with reduced intellectual abilities, like decreased learning and thinking aptitudes. The last kind can be summarized as neurological disorders with unintentional movements and restrictions in voluntary movements [81,82].

In Alzheimer disease, the concentration of BDNF mRNA is decreased [83,84] due to a structural change of either the BDNF itself or of the BDNF receptor [85]. The diseases can be divided into 3 stages:

1. In the early phase, the patients are powerless. This results in a reduced learning and reaction ability as well as slowed down thinking and speaking processes. These symptoms are often not noticed by other people and the patient himself.

2. The middle stage, in which known people are hardly recognized, is accompanied by the loss of independence leading to the incapability to solve complicated situations.

3. In the late-stage, the long-term memory is affected. Known people are not recognized at all and the patients need to be under care for the whole day. Due to a reduced immune system, the patients die of pneumonia or other inflammations [86].

In their study, Laske et al. compared how the BDNF concentration is changed in different stages of Alzheimer's diseases [67]. They were able to show that the BDNF level was increased for patients suffering from early-state Alzheimer's disease compared to patients in a more progressed clinical picture. They claimed this to be a compensatory repair effect. In a more advanced and severe stadium of Alzheimer's disease, the BDNF was reduced. Moreover, they suggest that the BDNF serum level could be used as indicator for the progressing of the neurodegenerative disease [67].

2.1.4 Antibodies and antigens

Antibodies are glycoproteins and an important part of the immune system. They are also known as immunoglobulins. All antibodies possess an IgG Y-shape

appearance and consist of oligomers with two identical heavy (50 kDa) and two identical light (24 kDa) polypeptide chains. The light chains can be divided in κ- and λ-chains, which have both the same function [57]. Heavy as well as light chains are connected *via* disulfide bonds and non-covalent bonds. They possess a variable region with identical length and a constant region which is three times longer for heavy chains in comparison to the light ones [87]. The constant region of the heavy chains is also known as Fc region which is the effector site. F stands for fragment, whereas there are different meanings for the c in literature, either for complement binding [87] or for crystallizable since it crystallizes in vitro according to [57]. The Fab fragment (Fab = antigen binding fragment) is a specific part of the variable chains to which the antigens bind. There are two Fab fragments, to which the antigens can bind. In *Figure 4*, a schematic of the structure of an antibody can be seen.
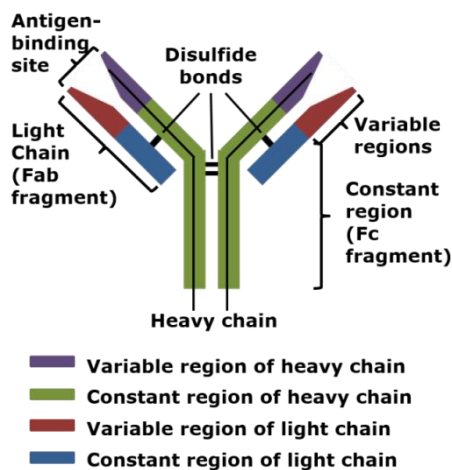
Figure 4: Schematic of the antibody structure.
In this figure, the components of an antibody can be seen. The general structure of all antibodies is the same. There are slight differences in the heavy chains, which make it possible to differentiate between the various antibodies. The figure was adapted from [57].

Besides the conventional antibodies, which consist of two light and two heavy chains, so-called heavy–chain antibodies, composed of only two heavy chains, exist. Since their discovery in 1993 by Hamers et al. [88], they have only been found in camelids (*e.g.* camel, llama) and cartilaginous fish (*e.g.* shark, ray) [89]. In contrast to the conventional antibody, in which the light and heavy

chains are part of the antigen-antibody binding site, this site is formed by solely one domain of the heavy chains [90]. One group of heavy-chain antibody is the single-domain antibody or nanobody. Nanobodies are antibody fragments and the smallest naturally appearing antibody [91]. With a molecular weight of about 15 kDa, they are about ten times lighter than a normal antibody. Nevertheless, they can still bind antibody *via* a specific binding site [92]. The single-domain antibodies own a similar structure as the variable domain of the human heavy chain, show a low toxicity and a high stability [93]. These characteristics make them a promising candidate for biomedical applications [91,93]. There are five different immunoglobulin classes in total. They are almost similar in structure and can be distinguished by their heavy chains which are presented in different isoforms and, hence, own different functions. The constant region of the light chains can be distinguished in either λ- or κ-type [87]. The differentiation of the immunoglobulins is done according to their heavy chains. The isoform and the corresponding heavy chains are: IgA (α-chain), IgD (δ-chain), IgE (ε-chain), IgG (γ-chain) and IgM (μ-chain) [94]. IgG and IgA can further be divided in the subclasses $IgG_1 - IgG_4$ and $IgA_1 - IgA_2$, respectively [57]. There are monomeric immunoglobulins, which only consist of one antibody structure, dimeric immunoglobulins, assembled of two antibody structures and pentameric immunoglobulins, made of five antibodies. A schematic overview is given in *Figure 5*.
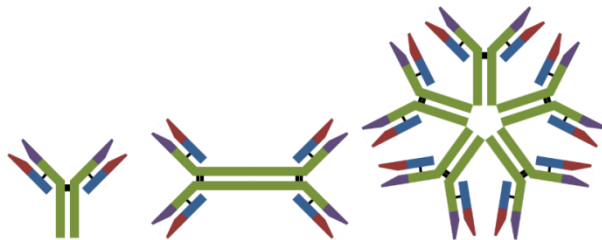
Figure 5: Schematic overview of a monomeric (left), dimeric (middle) and pentamer antibody (right).
IgD, IgE and IgG are monomers, which are varying in the structure of their heavy chains. IgA is mostly represented in the dimeric form, whereas IgM can be found as pentamer The figure was adapted from [57]*.*

In the following part, the most important characteristics and functions of the immune-globulins will be summarized briefly: IgG is the smallest antibody

(150 kDa) and displays a monomeric structure. Since it possesses an active transport mechanism, it is the only antibody which can pass the placental barrier and, hence, it is the first antibody available in the fetus. Regarding the total amount of antibodies in the human blood, the concentration of IgG is the highest [57]. It is produced in the late-stage of the primary immune reaction and typically presented during the secondary immune reaction. If IgG can be detected in a patient's blood, this indicates that either a vaccination has been done or an infection has taken placed [94]. IgM indicates an acute infection since it is the first immunoglobulin produced in the primary immune reaction. A single IgM molecule is able to start the whole cascade of the complement system, whereas the binding of two IgG molecules is needed to activate the same process. The IgM class represents the antibodies of the blood group system. This is caused by the early-stage production of IgM. The IgM isoform has a pentamer structure composed by the assembly of five individual IgM molecules. The pentamer structure is stabilized *via* polypeptide bonds, the so-called J-chains (J = joining). All IgM molecules of a pentamer are directed against the same epitope of an antigen but possess a low binding affinity. Since the bound antigen is only removed from the IgM when all five antibodies detach from their antigen, the pentamer possesses a high binding strength [94]. The serum concentration of IgE is increased due to an allergic reaction. IgE bind to receptors of mast cells, eosinophil and basophil granulocytes [94]. IgE belongs to the monomeric antibodies. IgA exists as mono- and dimer [94]. Even though, IgG is the quantitative predominating immunoglobulin in serum, IgA represents the mostly produced antibody. However in contrast to IgG and IgM, only a low amount of IgA is present in serum since most of it is ingested *via* endocytosis by epithelial cell [57]. The function of the monomer IgD is still not verified. Similar to IgM, it is located at the surface of native B-cells [94]. Besides the subdivision into five immunoglobulin classes, a distinction between regular and irregular antibodies can be done. Regular antibodies, also known as neutral antibodies, belong to the IgM type. They are part of the AB0 blood group system and presented in the blood even without ever having any antigen contact. This type of antibodies needs to be identified before a blood transfusion to avoid incompatibilities. Irregular antibodies are built by plasma cells when exogenous substances, the antigens, are recognized inside the human body by the receptor

domains of B-lymphocytes [57], whereby a B-lymphocyte and its progenies always produce the same kind of antibody [87]. Antibodies bind specifically to an antigen *via* the key-lock principle. In doing so, the paratope of the antibody connects to the adhesion site of the antigen, which is also called epitope [87]. The antibody-antigen complex is detected and disassembled by proteases and enzymes after endocytosis into lymphocytes [95], which are the immunological memory of the immunosystem. The lymphocytes possess the ability to produce antibodies against the specific antigens even years after the first infection. Antibodies which are naturally developed during the immune response are called polyclonal antibodies. They are produced by different types of plasma cells and have a slightly different structural sequence. Therefore, they recognize different epitopes of one antigen. In contrast to this, monoclonal antibodies are artificial and synthesized in the laboratory. They are produced by identical cells and only specific to one epitope [87]. The advantage of monoclonal antibodies is that their reaction is more specific and, in consequence, more selective. Therefore, they are often and preferably used in Enzyme-linked Immunosorbent Assays (ELISA) and other immunoassays.

2.2 DNA

2.2.1 Structure and assembly

The DNA (deoxyribonucleic acid) molecule is made of 2 antiparallel strands. Each strand consists of a random order of different nucleotides. There are four different nucleotides in total which are built up of:

1. A pentose sugar (2'-desoxyribose)
2. Either one of the purine bases, adenine or guanine, or one of the pyrimidine bases, cytosine and thymine. Both purine and pyrimidine bases are aromatic bases.
3. A phosphate group [96].

One of the bases bind with the pentose sugar to a complex called nucleoside. Since there are four bases, four different nucleosides can be built up. They are named adenosine, cytidine, guanosine and thymidine. Apart from the DNA, the ribonucleic acid (RNA) exists, which is responsible for the translation of the

genetic information in proteins. In principal, the DNA and RNA have the same structural assembly. There are only a few differences: In the RNA, thymidine is replaced by uracil. Moreover, it consists of a single strand and is made of the pentose sugar ribose [97]. In *Figure 6*, the assembly of a DNA strand is presented [97].
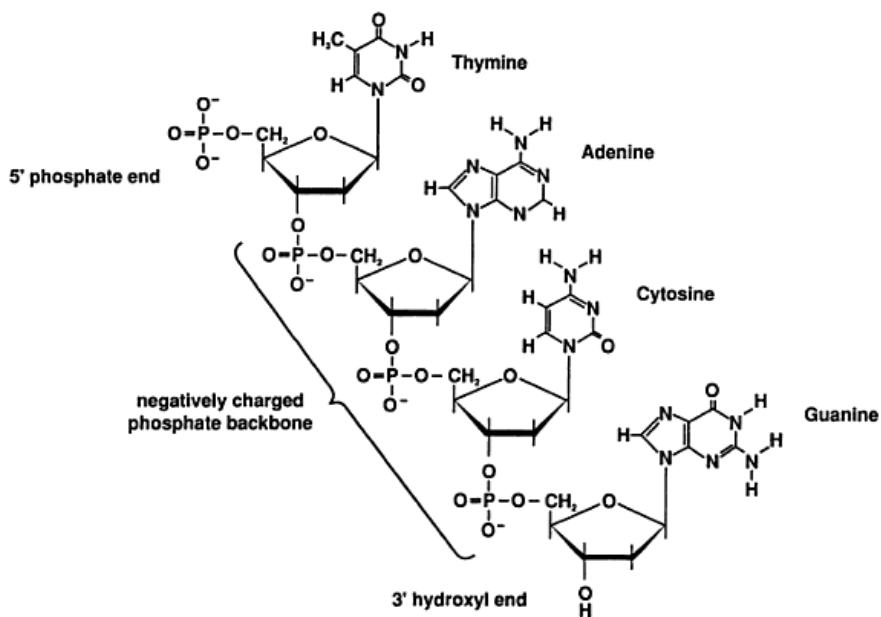
Figure 6: Composition and binding of the four nucleotides.

This figure shows the four different nucleotides, thymine, adenine, cytosine and guanine, of which a DNA strand is composed. The 5'-phosphate end as well as the 3'-hydroxyl end can be seen. The nucleotides are composed of a phosphate group, a pentose sugar and a purine or pyrimidine base. The figure was taken from [98].

The phosphate groups are pointing towards the outside of the DNA molecule and are building up the negatively charged backbone of the DNA strand. The pyrimidine and purine bases are located at the inside and, hence, shielded from any modifications or changes [98]. The β-N-glycosidic bonds can be rotated so that a change in conformation is achieved. The phosphate group is bound to the 5'-carbon atom of the pentose and connects the carbon atom of one nucleotide with the 3'-carbon atom of the proximate sugar due to a 3'-5'-phosphodiester bond. A polynucleotide results in consequence. The DNA single-strand is polar [98] due to a negatively charged single phosphate at the 5'-end of the

polynucleotide and a hydroxyl group at the 3'-end [96]. The exact order of the nucleotides within the DNA can be identified with help of DNA sequencing. The goal of the Human Genome Project is to determine the precise sequence of every human chromosome [99]. One platform for doing the DNA sequencing is the DNA microarray which is described in Chapter 2.3.3.

2.2.2 Hybridization and denaturation

The aggregation of two single-stranded DNA sequences to a double-strand is called hybridization. The hybridization is performed antiparallel, which means that the first strand proceeds in 5'→3' direction and the second strand in 3'→5' direction [96]. The double-stranded DNA is curled to a helix, which is comparable to the α-helix of the secondary structure of proteins. Inside the double strand, adenine and thymine as well as guanine and cytosine are complementary bound *via* hydrogen bonds and form base pairs [96]. These hydrogen bonds are formed between the hydrogen atom of the amino groups and the nitrogen atom of the carboxyl groups. Two hydrogen bonds are formed between adenine and thymine and three hydrogen bonds between cytosine and guanine. Furthermore, the DNA is stabilized by $\pi - \pi$ interactions between neighboring bases (base stacking). Mainly, the DNA helix is right-handed and, then, termed B-DNA. Approximately, 10.5 base pairs are forming one right-handed helical turn with a length of about 3.4 nm (= 34 Å) and a width of about 2 nm (= 20 Å) [98]. The helix surface of the B-DNA possesses a major and a minor groove. Besides the B-DNA, another right-handed DNA, the A-DNA, exists. The difference between these two right-handed DNA versions is that the bases are more tilted in the A-DNA than in the B-DNA and that the grooves are not that deep. In *Figure 7*, a schematic of the DNA double helix is shown. In addition to the natural right-handed B-DNA, there is also a left-handed DNA, the Z-DNA. C-, D- and T-DNA are other DNA structures which can be distinguished because of specific numbers in base pairs which build one helical turn [98]. The disassembly process of the DNA double-strand into two single-strands is called denaturation where the hydrogen bonds between two complementary bases are cut. It can be initiated by heating, in highly basic or acidic solutions and in distilled water. Acids and bases prevent the building of hydrogen bonds by protonation or deprotonation, respectively. The adequate temperature for

denaturation is the melting temperature (T_m). Per definition, 50 % of the DNA molecules are separated into single strands at that temperature, which depends on the structure and length of the DNA and is influenced by the salt concentration of the surrounding electrolyte as well. In general, it can be said that the melting temperature is depending on the number of guanine-cytosine pairs in the DNA.
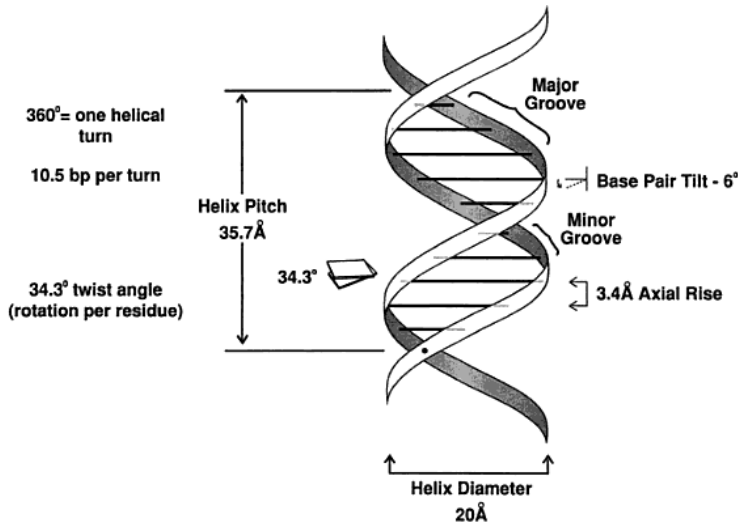
Figure 7: The B-DNA double-strand.

This picture shows a B-DNA double-strand. The minor and the major grooves of the DNA double helix are depicted, too. The picture was taken from [98].

Solutions with high ionic concentrations stabilize the DNA since counterions inside the electrolyte solution shield the electrostatic repulsion between the negatively charged phosphate groups. Two single-stranded DNA strands can be assembled again by stepwise decreasing of the temperature below T_m. This process is called renaturation, reannealing or hybridization [98]. In the next subchapter, the misassembly of base pairs between two hybridized single-strands and its consequences are highlighted.

2.2.3 DNA mutation

A lot of diseases are caused by the assembly of wrong base pairs when guanine is inserted instead of adenine or cytosine instead of thymine. Several types of

mutation exist which will be briefly described in the following part.

Point mutations change the reading frame of the DNA sequence. They can cause either a deletion of a base or insertion of an additional base into the DNA strand. However, there are also mutations were the reading frame stays constant. In case of transversion, a purine is inserted instead of a pyrimidine or a pyrimidine instead of a purine. The process of replacing a purine by a purine or a pyrimidine by a pyrimidine is known as transition or substitution. If transition or transversion results in the exchange of one amino acid against another, this is called a missense mutation. Nonsense mutations are mutations, in which the base changes the reading frame such that a stop codon is created. In silent or neutral mutations, the amino acid stays constant even though a base is modified. In case that a stop codon is encoded as an amino acid, this is called readthrough mutation [100].

The sickle-cell anaemia is an example for a point mutation. Due to transversion, an adenine is exchanged against a thymine at a certain point in the gene sequence. In consequence, the insertion of the amino acid valine results instead of glutamic acid [101]. The sickle-cell anaemia is transmitted autosomal recessive which means that both healthy parents are carrier of one sickle-cell allele and pass this defect allele to their common child who finally suffers from the disease [102]. The affected gene controls the synthesis of normal hemoglobin. If the gene sequence is changed, the structure of hemoglobin is mutated, too. This leads to the building of an abnormal hemoglobin S (S for sickle-cell) and crystallization inside the red blood cells (erythrocytes) [101]. The crystallization induces a growing of the polymer nucleus which leads to a deformation (sickle-shaping) of the erythrocytes and which initiates dehydration of cells. This is accompanied by oxidative and physical cellular stress. Moreover, the deformed shape of the blood cells may cause obstruction of capillaries and, therefore, ischaemia [103]. The sickle-cell anaemia is widely-spread in countries where malaria occurs, *e.g.* Africa. This can be explained by the fact that patients with one sickle-cell anaemia gene (heterozygote carriers) possess some resistance to malaria in contrast to homozygote carriers who mostly decease because of malaria [104].

2.2.4 HLA-B27

The Human Leukocyte Antigen-B 27 (HLA-B27; B = isotype, 27 =variant) is a membrane-associated glycoprotein of the major histocompatibility complex class 1 and is encoded by the HLA-B27 gene. In total, more than 100 subtypes of this gene are classified [105]. The glycoprotein is located on every nucleated cell and controls the T-cell mediated immune reaction: It possesses a special affinity to viral antigens and, hence, affects an effective immune reaction against the presented viruses [105]. It was shown that the progression to AIDS of HIV infected patients carrying the hereditary characteristic of the HLA-B27 allele is significantly delayed [105–107]. In contrast to that, people with the HLA-B27 allele have a higher risk for certain auto immune disease even though the absolute percentage of suffering from one of those diseases is quite low. An example is the spondylarthritis, Morbus Bechterew, a chronic inflammation of the vertebral column where the body's own cells are affected by the immune system [108,109]. In the late-stage, the vertebral column can get stiff and the organs can be influenced as well. Only 6-7 % of the allele carriers are affected by Morbus Bechterew, but 90 % of Morbus Bechterew patients carry the HLA-B27 gene [110]. Morbus Bechterew can be treated with painkillers, physiotherapy, surgery of a stiffening of the vertebral column [109]. Other HLA-B27 related diseases are:

- Morbus Reiter a combination of the triad arthritis, urethritis (inflammation of the urethra) and conjunctivitis (inflammation of the conjunctiva) [111].
- Psoriatic arthritis an inflammation of the joints, especially of hands and feet, and of the vertebral column accompanied with psoriasis of the skin [112].
- Juvenile idiopathic arthritis an inflammation manifested before the age of 16. Symptoms are similar to the symptoms described for the other HLA-B27 related arthritis [113,114].
- Uveitis an inflammation of the uvea [105,115,116].
- Iritis an inflammation of the iris [105].
- Iridocyclitis an inflammation of the eye's vitreous cavity [105].
- Schizophrenia [117].

The typification of HLA needs to be performed before transplantations of bone marrow, stem cells and organs to identify if donor and recipient are matching or not [118–120]. Morishima et al. showed in 2002 that a mismatch in HLA-A and -B leads to a drastically higher amount of transplantation failure [121].

2.3 Overview of protein and DNA detection platforms

In the last decades, the possibility of early-stage detection attracted a lot of attention. If the disease is determined in an early phase, there is the feasibility for an early treatment to prevent proliferation of infections or to avoid the inheritance of mutations to the next generation. A better control of the patient´s condition is possible. Furthermore, an early application of pharmaceuticals may improve the state of health. A couple of diagnostic tools are available on the market for the detection of immune effects. There are immunoassays, protein microarrays and immunosensors. These platforms rely on the highly specific binding between antibody and antigen. For the detection DNA molecules, DNA-microarrays and DNA-sensors which monitor the hybridization between two complementary single-stranded DNA sequences are applied. There are some requirements for the systems used for the disease detection. The detection sensitivity should be as high as possible so that even a very low concentration of analyte can be detected. This also requires that the signal-to-noise-ratio is very good. The specificity of the test system has to be high to avoid false positive results and the amount of non-specific bindings has to be reduced to a minimum. The evaluation of the results should be as fast as possible to save time and, therefore, costs. A good diagnostic tool must be stable and reliable under different conditions to avoid variations in results. To allow detection of different diseases, the feasibility to immobilize cells, bacteria and different biomolecules, such as DNA or antibodies, on the surface of the biomedical platform should be given. A cheap fabrication and easy handling of the sensor are other aims. A label-free measurement with a fully electronic read-out is aspired to save costs and to make the system much easier to use. As described by G. A. Urban and coworkers [122], the detection of proteins by microarrays or immunoassays/-sensors is not as easy as with DNA. One reason is that the proteins can interact with other molecules not only with the immobilized capture molecule. Another reason is the different levels of structure within a protein.

Since there is a primary, secondary, tertiary and quaternary structure, the amino acid sequence does not provide enough information to determine a highly specific capture molecule [122]. Furthermore, the immobilization of antibodies to the device surface is not simple because it is possible that the antibody does not immobilize with its Fc-region to the surface, but with its Fab region at which usually the antigens are bound. There are many approaches to solve and overcome this problem and these concepts are reviewed by Lu et al. [123]. In this work, just a brief overview of detection platforms for antibodies and DNA sequence will be given.

2.3.1 Immunoassays

As mentioned before, immunoassays are based on the reaction between antibodies and antigens. They are widely spread and are applied for numerous different bioanalytical tests. Immunoassays with sensitivities up to zeptomole regimes were reported in [124]. In general, four kinds of immunoassays can be distinguished due to different labeling [122]:

1. Enzyme immunoassay
2. Enzyme-linked immunosorbent assay (ELISA)
3. Fluorescence immunoassay
4. Radioimmunoassay

To perform enzyme immunoassays, enzymes have to be bound covalently to an antibody or antigen. Such enzymes can be *e.g.* horseradish peroxidase or alkaline phosphatase. The enzyme-labeled capture molecule binds to a specific target molecule. The binding between capture and target molecules leads to a signal which can be measured in three different ways: The first way is colorimetry where the signal is represented *via* a color reaction. This color reaction is proportional to the amount of bound target molecule and can be determined with a spectrophotometer. Sensitivities comparable with radioimmunoassay are only achieved in very few experiments. The second type is the fluorometry. The capture molecule can be directly marked with a fluorescent dye or an applied substrate is transformed into a fluorescent end-product. The fluorescent signal is measured by a fluorometer. The sensitivity of fluorometry is several times higher than for colorimetry. The third way to

measure the signal of an enzyme immunoassay is the chemiluminescence where luminescent molecules are applied which emit electromagnetic radiation in form of visible light. The chemiluminescence is triggered by a chemical reaction and detected by a luminometer. With luminescence, a sensitivity even better than with radioactive or fluorometric immunoassays can be obtained [124]. Enzyme immunoassays are used in endocrinology for the detection of hormones like estrogens, for evaluation of IgG, IgM, IgE in immunopathology, in microbiology and parasitology [125]. The enzyme-linked immunosorbent assay or shortly ELISA can be divided in two different methods. The first one is the sandwich ELISA which can be direct or indirect. For the direct ELISA, the capture antibody is immobilized on a microtitre plane. Then the test solution is added. If the solution contains specific antigens, these antigens bind to the antibodies. After having washed away unspecifically bound molecules, an enzyme-labeled antibody (detection antibody) is added and it binds to the antigen, too. In the indirect sandwich ELISA, antigens bind to the antibody immobilized on the microtitre plane. Once more, unspecific bound antibodies are rinsed away. In the next step, a second antibody is added, which is highly specific against the antigen. Afterwards, an enzyme-labeled antibody is pipetted to the solution. This antibody only reacts with the secondary antibody, but not with the immobilized capture biomolecule. The evaluation of either direct or indirect sandwich ELISA is performed with help of a chromogen. The chromogen is converted by the enzyme-label which is visible by a change in color. This color change can be detected by chemiluminescence of fluorescence. The concentration of the colored products is proportional to the concentration of target molecules [126,127]. The second type of ELISA is the competitive ELISA. Like in the sandwich ELISA, the capture antibody is immobilized on a surface. Then a solution is added, which contains the target antigen and an enzyme-labeled antigen. Both antigens compete against each other for a binding site to the antibody. In this case, the color reaction is inversely proportional to the concentration of target antigen. This means, the higher the concentration of target molecules the more intensive is the color reaction. It exist a direct and an indirect competitive ELISA which can be described like it was done for the sandwich ELISA [127]. The ELISA technique is used in home pregnancy tests, in the food industry to determine allergens and in different virus tests (*e.g.* HIV)

[128]. In fluorescence immunoassays, the target antibody or antigen is labeled with a fluorescent dye or molecule. The fluorescent dye is excited at a certain wavelength and the fluorescence is emitted at a wavelength that is a bit higher than the excitation wavelength. If the target antibody (antibody/antigen) is specific for the capture antigen (antigen/antibody), a fluorescence signal can be measured or seen *via* fluorescence microscopy. In case that the target molecules cannot bind to the capture molecule, no fluorescence signal occurs [129]. Fluorescence immunoassays are used *e.g.* for the determination of human IgG [130] or cortisol [131]. In radioimmunoassay, either antibodies or antigens are labeled with a certain, known amount of radioactivity. Radioactive antibodies are used in immunometric assays which allow measuring the number of bound antigens. Radioactive antigens provide information about how many antibody fractions are bound or free in a competitive assay. The radioimmunoassay has some disadvantages: Every isotope possesses a specific half-life period, which describes in which time a half of the isotope is decomposed. This means that the radioactive labeling is unstable. Another great problem of radioimmunoassay is that radioactive material is used. Radioactive experiments can only be performed in special, licensed laboratories and the radioactive waste must be disposed in a special way. These are reasons for the high costs of radioimmunoassay [124]. The radioactivity itself is measured by an expensive scintillation counter. Radioimmunoassays can be used *e.g.* for drug analysis [132].

2.3.2 Immunosensors

Immunosensors belong to the group of biosensors. Antibodies are immobilized on the sensor surface and serve as (bio-) receptor and capture molecules. Those antibodies are building immune complexes with specific antigens (target molecules) [133]. Besides antibodies and antigens, a lot of other target molecules can be evaluated with immunosensors. This includes bacteria, drugs and environmental pollutants [133] as well as pituitary and steroid hormones [134]. The binding of antigen and antibody is converted into a measurable signal by a transducer. The signal is directly measured as a change in current, heat, mass, optical properties, potential or resistance [134]. The capture molecules are usually immobilized on or nearby the transducer [135]. The sensitivity limit

is in the range of 10^{-9} - 10^{-13} M. The great benefit of immunosensors is the possibility of real-time measurements and a direct read-out and representation of the obtained results. Hence, it enables the study of the kinetic of antibody-antigen binding. There are various immunosensors composed of different materials. They rely on different read-out mechanisms depending on the used transducer. In this work, solely the group of electrochemical immunosensors is briefly summarized. It is reported that concentrations of about 10^{-12} M can be detected with electrochemical sensors [133]. Immunosensors can rely on different detection principles, *e.g.* amperometric, conductometric and potentiometric sensors. The first electrochemical readout mechanism is based on the principle of amperometry. This means that a certain current flow is measured at a constant voltage due to a redox reaction of target molecules at the electrode surface. The current is directly proportional to the concentration of measured target molecule. Amperometric sensors show high sensitivity and specificity. A disadvantage is that an enzyme labeling is necessary for molecules, which are not electroactive. Electroactive molecules can be both oxidized and reduced. Labeled and label-free sensors are available on the market. The glucose sensor is a well-known example for an amperometric platform. The immobilized glucose oxidase converts glucose into gluconolactone and hydrogen peroxide. As soon as the glucose binds to the enzyme, electrons are transferred to FAD (flavin adenine dinucleotide), which is bound to the glucose oxidase and reduced to $FADH_2$ (hydrogenated form of FAD). The change in the amount of the electrons, caused by an increase of hydrogen peroxide or a decrease in oxygen, is detected with the glucose sensor [134]. The second electrochemical sensor relies on the measurement of the change in electrical conductivity of an analyte solution by applying an electrical field. The electrical conductivity is caused by the migration, production or consumption of ions. For reliable results, the pH value and buffer capacity should be held constant. Problems can be created by the fact that all ions in the solution influence the conductivity and, therefore, unspecifically influence the conductivity. The electrodes of a conductometric device are fabricated of noble metal such as chromium, gold or silver, on which enzymes are immobilized [134]. Potentiometric sensors measure the change in electrical potential induced by the binding of target molecules to the capture molecules. Since every molecule is charged, the method is applicable for all

kinds of substances. The potential change is proportional to the concentration of capture molecules. The current at a reference electrode is set to zero. The change in potential is given as the logarithmic ratio of potential and analyte concentration. Like in all immunosensors, the capture molecules are immobilized onto the electrode surface. Furthermore, ions can be bound to electrodes to achieve a better sensitivity. Nowadays, field-effect transistors (FETs) are applied as potentiometric platform. Due to the small size of FETs, small volumes of test solutions are sufficient for the measurements. In ISFETs, ion-sensitive membranes are combined with FETs. This leads to a reduction of background interferences. The problem with ISFETs is that the signal-to-noise ratio is low, and the signal can be influenced by the pH and the ionic strength of the liquid under test. Used as immunosensors, the ISFET can reach a detection limit of approximately 10^{-9} M [134].

2.3.3 DNA microarrays and DNA sensors

DNA microarrays are widely used in genome studies and genetic analysis to determine gene expression levels and to do genotyping [136,137]. Another area of application is the DNA sequencing where the exact nucleotide order within a DNA molecule is identified [136]. Due to a lot of effort in this field, great improvements have been achieved, *e.g.* the automatization of the sequencing process and a parallel readout of various DNA molecules with a length of hundred bases [138]. DNA microarrays rely on the base pairing reaction (hybridization) of a single-stranded DNA sequence and a complementary single-stranded DNA sequence [139,140]. A large number of oligonucleotides can be immobilized on one DNA microarray to allow simultaneous measurements and quantifications of a great number of target DNA sequences [139,141]. There are three different methods for the immobilization of capture molecules on a defined area of the microarray: By applying a current, the negatively charged DNA is deposited precisely and site-specifically on positively charged areas of the device. The second technology is the *in situ* synthesis of a DNA array. The first nucleotide is immobilized on a defined area. In a subsequent cycle, a second nucleotide binds with its the phosphate group to the hydroxyl group of the sugar of the first nucleotide, which possesses a protective group at this 5' end to avoid an attachment of more than one nucleotide per cycle [142]. The cycles are

repeated until an oligonucleotide with a certain number of nucleotides is reached. For spotted DNA microarrays, the capture DNA is spotted by contact or non-contact printing onto the device [142]. The readout is mostly done by an optical method, *i.e.* fluorescence.

In the last decades, electronic DNA sensors have become an important platform for the detection of DNA. The detection principle is based on the recognition of hybridization processes between two complementary DNA strands. Those biosensors offer the possibility of rapid measurements in real-time. Moreover, they are portable and can be integrated into microfabrication [143]. It is possible to evaluate specific DNA sequences with DNA sensors. To prevent expensive fluorescence-based assays, DNA sensors are used [139]. The structure of the DNA sensor is similar to the immunosensor. This means the sensor consists of a receptor/capture molecule, *i.e.* a single-stranded DNA strand with a certain number of base pairs. The capture molecule is immobilized directly on the sensor surface and hybridizes specifically with its complementary single-stranded DNA sequence. Usually, the target sequence has the same number of base pairs as the capture molecule [139]. The immobilization can be accomplished by adsorption, (strept-) avidin-biotin complex formation, entrapment and covalent binding [142,143]. The covalent binding is the most stable immobilization technique. Unspecific bindings are avoided by blocking of free sensor areas. The hybridization reaction is detected by a transducer, which amplifies and converts the reaction into a measurable signal. The signal is evaluated electronically. For DNA microarrays, the DNA is immobilized on the whole chip surface, whereas DNA sequences are directly immobilized on the transducer, when a DNA sensor is used. If a complementary target DNA sequence is added, the hybridization reaction takes place between both DNA strands, which is measured by the sensor [139,143]. In Table 1, the most sensitive detection methods are displayed. As described for the immunosensors, the readout for DNA arrays and sensors is based on electrochemical, enzymatic, microgravimetric and optical readout mechanisms. Microgravimetric sensors can be either microcantilever or quartz crystal microbalance (QCM) DNA sensors. The optical methods include fluorescence, chemiluminescence, calorimetry, surface-enhanced Raman scattering spectroscopy, dual polarization interferometry and surface-plasmon based techniques [142].

Method - main group	Method - subgroup	Detection limit in M
Microgravimetry	QCM	3×10^{-16}
Optics	Fluorescence	10^{-17}
Electrochemistry	Voltammetry	6×10^{-16}

Table 1: Sensitive detection methods.

This table shows the three detection methods with the best detection limits and, hence, the highest sensitivity. Table adapted from [142]*.*

Since fluorescence imaging and an electrochemical readout are used in framework of this thesis, the focus is set onto these two methods which are briefly described in the following part. Fluorescence-based methods rely on the determination of the fluorescence intensity which depends on the efficacy of the base pairing. The hybridization between two perfectly matching DNA strands is the strongest and is reduced with increasing number of mismatching base pairs [142]. In case that the both DNA strands are fully-mismatching, no hybridization and no fluorescence will be seen. This means that even point mutations can be detected by fluorescence-based assays [139,142]. One problem of all fluorescence-based assays is the possibility of the bleaching of the fluorescence [139,144]. In a fluorescence-based DNA-microarray, up to a hundred thousand DNA sequences can be evaluated simultaneously and in parallel. A disadvantage of a fluorescence-based DNA-microarray is that a large number of data is produced that needs to be analyzed. This needs trained employees and expensive equipment. Besides those sensors, which require a label, there are also label-free platforms available, *e.g.* electrochemical biosensors, which do not need any marker and which are cheaper and faster than the labeled sensors [139,142]. The design of the electrochemical sensors is not as complex as for other platforms and, due to microfabrication, small sensor dimensions are possible [142]. One type of electrochemical DNA biosensors relies on the impedimetric readout method. Hybridization processes can be measured with help of impedance spectroscopy. The impedance is defined as the quotient of frequency-dependent voltage and current functions. In impedimetric measurements, the change in impedance is determined. The change in impedance is triggered by redox reactions. The impedance is increased by the

hybridization of two negatively charged DNA sequences, which leads to an accumulation of charge carriers at the sensor surface. Like with voltammetric measurements, mismatching base pairs can be detected and the amount on DNA can be quantified. The detection of other electrochemical characteristics can also be measured. In addition, the electrochemical DNA sensor can be combined with other methods for a further increase in sensitivity. For this purpose, it can be coupled with either enzymes or PCR (polymerase chain reaction). PCR is used to amplify a low volume of DNA. As described in [143], PCR and DNA sensor can be incorporated in a lab-on-a-chip device. In the last few years, nanoparticles and other nanostructures, like nanowires and nanotubes, have attracted more and more attention for the detection of DNA sequences. In a later section, only nanowires will be discussed in more detail [143]. DNA sensors can be applied for a wide range of implementations. They are feasible to determine changes in the DNA sequence, *e.g.* point mutations, and to investigate if there are genetic modifications in plants and microorganisms. This is therefore especially interesting for the food industry. They can also be used for paternity tests or to study further family relationships [139]. Besides the impedimetric readout of DNA [145], it can also be detected by measuring the heat-transfer resistance. The method relies on the recording of a heat flow instead of electrical currents. In several publication, it was shown that the heat-transfer resistance is changed when a DNA double strand is thermally denaturized and that even single-nucleotide polymorphisms in DNA can be identified with this method [146–148]. Using this detection principle, it was possible to identify phenylketonuria [147].

2.4 Field-effect transistor-based biosensors

DNA and immunosensors have in common that there is the aim to increase further the sensitivity and the specificity of the platforms. It is also a goal to decrease the costs of the fabrication and to facilitate the usage by integration of microfluidics, which would allow automated washing of the probes and addition of capture molecules and other chemicals. The platform has to be fast and measurements should be displayed in real-time. Miniaturized diagnostic platforms can be produced by using electrochemical techniques. Due to microfabrication, simultaneous measurements should be possible in parallel. In ideal case, the sensors are reusable. The reusability of DNA sensors and

microarrays has already been achieved by thermal or chemical treatments which cause a denaturation of the double strand to single-strands [142]. In a subsequent washing step, the target DNA is rinsed away. Only the immobilized capture DNA stays on the sensor surface. In the last years, field-effect transistors (FETs) were used as biosensors for the label-free detection of DNA, enzymes, proteins and cells. Changes in surface charge and impedance can be directly measured with FETs [143]. The change in charge is caused by binding of charged target molecules to charged capture molecules, which were immobilized on the sensor gate before. In consequence, a change in threshold voltage results during the hybridization reaction [24]. The field-effect device transfers this change into an electrical signal [149]. The working principle is described more precisely in the following chapters. It was shown in literature that even single base mismatches can be detected with field-effect transistors. The microfabricated FETs have several advantages compared to other assays [16]. Multianalyte detection is possible with the device. They are suitable for the detection of very small analyte volumes and concentrations. In addition, it was shown that even single nucleotide polymorphisms of DNA sequences consisting of 12 base pairs can be measured [16]. These properties make them a good tool for biomedical applications. As described before, FETs can be combined with ion-sensitive membranes (ISFET). This combination leads to less background noise [134]. However, there are also disadvantages: Due to degradation and contaminations on the sensor surface, the device shows a poor reliability. The sensitivity is not as good as with fluorescent assays. Another disadvantage is that the FETs must be produced in clean room processes, which leads to higher costs compared to other assays [134]. In the next two subchapters, the structure and working principle of ion-sensitive field-effect transistor and silicon nanowire field-effect transistors are introduced. The characterization methods will be described in the material and methods chapter (Chapter 3).

2.4.1 Ion-sensitive field-effect transistors

In principle, the structure of ion-sensitive field-effect transistors (ISFETs) is comparable to that of metal-oxide semiconductor FETs (MOSFETs). The difference between the two kinds of FETs is that the ISFET possesses an electrolyte solution instead of a metal gate contact. Hence, measurements of

biological and chemical compounds are feasible [150]. The ISFET was firstly described by Bergveld et al. in 1970 [18]. An ISFET is built up by three terminals, which are source, drain and gate electrode. The transistor array is insulated from the electrolyte solution by an insulator layer to avoid leakage currents. The gate to source voltage (V_{GS}) is applied *via* the gate electrode which is composed of a reference electrode inserted into an electrolyte solution to fix the potential of the solution [151]. By applying a voltage between the drain and source electrodes (V_{DS}), an electric current can flow between source and drain, which is controlled by the gate voltage that creates an electric field [152]. The drain-source current (I_{DS}) is given by following equations [151,153–155]:

$$I_{DS} = \frac{W}{L} \mu C_{Ox} ((V_{GS} - V_{TH})V_{DS} - \frac{1}{2}V_{DS}^2) \quad \text{for } V_{DS} < V_{GS} - V_{TH} \text{ (non-saturation mode) (2.1)}$$

$$I_{DS} = \frac{W}{2L} \mu C_{Ox} (V_{GS} - V_{TH})^2 \quad \text{for } V_{DS} \geq V_{GS} - V_{TH} \text{ (saturation mode)} \quad (2.2)$$

with W and L as the width and length of the channel, respectively, μ the carrier mobility, C_{Ox} the capacitance of the insulting oxide layer, V_G the gate voltage, V_{TH} the threshold voltage, and V_{DS} the drain to source voltage. I_{DS} depends, for example, on the pH and the ionic strength of the electrolyte solution or the charge of the biomolecules attached to the surface. The current is caused by either electrons (n-type transistor) or holes (p-type transistor). Since only p-doped field-effect based devices were used in the framework of this thesis, the theory is solely described for p-type semiconductors: Regarding a p-type transistor, drain and source contacts are highly p-doped, which means that positively charged holes are acting as majority carriers. If no voltage is applied between source and drain contacts, a movement of the charge carriers through the channels is not possible. Upon applying a negative voltage at the gate, an accumulation of carriers and, hence, an increase of conductance is obtained [152]. As soon as the threshold voltage is achieved, a thin conducting channel between source and drain is built up. Then, a current flow can be achieved by applying a drain voltage Due to the variation of electric charges, the modification of the gate surface of a p-or n-type FET with negatively charged single-stranded DNA molecules leads to depletion or an accumulation of carriers, respectively. This effect is subject to the same principle as if a voltage is applied [152].

ISFETs are used for the label-free detection of biomolecular processes. In 2006, Ingebrandt and Offenhäuser reported about a FET and an amplifier system that they build up for the label-free and fully electronic detection of DNA [24]. The immobilized single-stranded DNA consisting of 20 base pairs was precisely spotted on the sensors of the chips with help of a microspotter. Then target DNA (perfect match, one, two and three mismatches, fully mismatched) was added and the hybridization of both single strands was measured. They were able to increase the signal amplitude to higher values and to accelerate the reaction time. However, the hybridization signal was very low. They assumed that this was because of steric hindrance of the capture molecules which hampered the binding of the target DNA. The detection of DNA with two mismatching base pairs was possible, but single nucleotide polymorphisms could not be measured. These FETs offer the possibility to measure *ex situ* by comparison the signal before and after the hybridization and *in situ* right when the hybridization reaction takes place [156]. Both, the new FET and the new amplifier have been the basis for a further development towards nanowire-based field-effect devices with a high sensitivity and specificity and were used in framework of this thesis.

2.4.2 Silicon nanowire field-effect transistors

In 2009, an article about silicon nanowire field-effect transistors (SiNW FETs) was published by Vu et al. [53]. Since they show a good biocompatibility, SiNW FETs can be used for a wide range of applications, like the detection of DNA [37,38,40,157], proteins such as antibodies [41,158], cells [159] and other biological substances [160]. They possess a high surface to volume ratio, and, therefore, the sensitivity of the SiNW FETS is ultrahigh. This is also caused by the fact that their size is in the range of the biomolecules that need to be detected. It was shown that label-free and fast real-time measurements can be performed with a fully-electronic readout system [11]. Label-free tools do not need fluorescence or any other labeling. This saves time and costs. Moreover, this avoids that the labeling influences the evaluated signal in a wrong way.

Concerning its structure and its working principle, the SiNW FET can be regarded as nanosized ISFET. The working principle is described more in detail in Chapters 3.7.1 and 3.7.2. The SiNW FET consists of four terminals, which are the source and the drain electrode, the back-gate and the front-gate electrode.

The source and drain electrode are connected with the nanowire. The back-gate electrode is coupled to the silicon substrate. To ensure the reliability of the system by avoiding any leakage current, nanowire, source and drain electrode are isolated from the silicon substrate by a silicon dioxide layer (*Figure 8*). For this reason, the SiNW FET can be separately or in common controlled by the back– or the front-gate mode. In conclusion, the drain-source current (I_{DS}) can be controlled by simultaneously or separately applying a voltage at the front-gate (V_{FG}) or at the back-gate (V_{BG}) [54,161]. The experiments, presented in this thesis were performed in the front-gate mode since it was shown before that these SiNW chips are more stable in this configuration since the back-gate mode was not consistent [54]. This was caused by the disturbance of the electrolyte solution during the exchange of the solution. Furthermore, higher voltages had to be applied [54]. The front-gate electrode consisted of a reference electrode immersed into an electrolyte solution. The silicon nanowire serves as gate on which the capture molecules are immobilized. The problem with SiNW FETs as biomedical platform is that there are certain parameters that have to be kept constant during the experiments because those parameters can influence the field-effect and, therefore, the measured results and the sensitivity [36]. To avoid such negative influences, pH [53,162], the Debye length [163], the size [35], the surface modification of the nanowire [164] as well as the distance and the position of the reference electrode to the surface has to be stable. In *Figure 8*, a schematic of a SiNW FET is represented. In several articles, it was shown that SiNW FETs offer the feasibility to differentiate between perfect-match, mismatch as well as fully-mismatch DNA sequences [37,38,40]. Due to all the beneficial characteristics of silicon nanowires, SiNW FETs may serve as future tool for biomedical purposes. To do a further step in this direction, we implemented DNA- and immunoassays on our SiNW FETs. Our SiNW platform showed a high sensitivity in general [53]. In initial experiments, it was shown that pH changes, cell sealing, DNA and proteins can be detected with this kind of sensors [39,53,157,165]. For the work represented here, the goal was to establish a stable and reliable immobilization protocol for capture DNA or antibodies and a stable and reliable binding/hybridization protocol for target DNA sequences and antigens on our SiNW FETs.
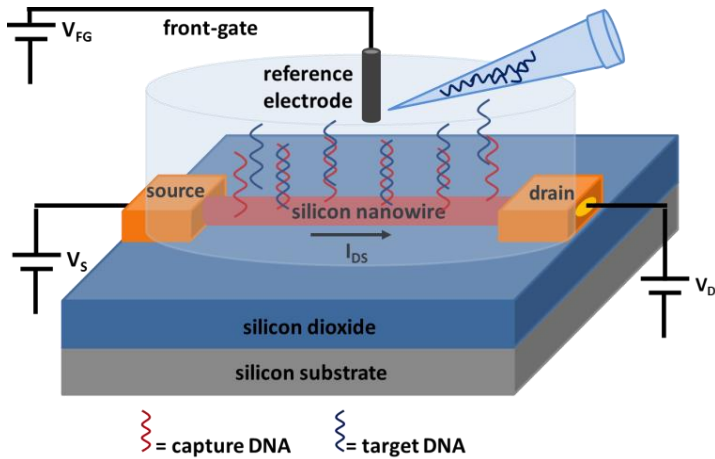
Figure 8: Schematic of a silicon nanowire field-effect transistor.

The single-stranded capture DNA (red) is directly immobilized on the nanowire with help of a microspotter. The target DNA (blue) is slowly added. The pipette tip should not get in contact with the sensor surface or the reference electrode because this would affect the detected signal. At the front-gate, represented by the reference electrode, a certain current is applied (V_{FG}). To provide a current flow between source and drain, a voltage is applied at source and drain (V_S and V_D).

Another aim was to transfer the established immuno- and DNA assays of the company Euroimmun Medizinische Labordiagnostika AG, Lübeck, Germany, onto our devices. For this purpose, the transistors were silanized with 3-(glycidoxypropyl)trimethoxysilane (GPTMS) as a primer layer for further attachment of bioreceptors. For the use of the devices in biodetection experiments, a microspotter was used to site-specifically immobilize different capture sequences on different sensors. This enables differential readout of the sensor array. The results were evaluated by comparing the transfer characteristic and the transfer function before and after each experimental step, *i.e.* silanization, immobilization, blocking, addition of target DNA. The concentration of target molecules was increased stepwise during the experiments to see if differences in the concentrations can be measured, too. The detection of hybridization/binding reactions was done in two different manners:

1. DC readout: The DC readout is also called potentiometric readout, in which the transfer characteristic of the transistor is measured [156]. The

working principle is described more in detail in the 'Material & Method' chapter.

2. AC readout: this method is called impedimetric readout, which is not completely correct, since, besides the impedance, also other effects seem to influence this method. By performing the AC measurement the transistor transfer function is recorded, as already reported in [156]. The theory of this readout method is described further in the next chapter.

The sensitivity of the FET is limited by the diffusion of the target molecules to the capture molecules, which can take several hours. This is mainly valid for low capture molecules concentrations [24]. To enhance the sensitivity, an integration of the SiNW FETs into a microfluidic cartridge can be done. By using microfluidics, the required volume can be reduced. Furthermore, there is the possibility of a complete automatization of the chip systems since washing steps and addition of target molecules can be done in distinguished compartments of the microfluidics on the chip. The different compartments are separated so that the reactions can take place in isolated parts. Due to the miniaturization and the low volumes, the whole experimental procedure can be speeded up and material can be saved, which reduces the costs [148,150,151]. In one publication, microfluidic channel modifications as one of three strategies to increase the performance of SiNW sensors were proposed [152]. Other problems like the distance between reference electrode or avoiding contact between pipette and sensor are solved. The chance to damage the nanowires, which are very fragile, is reduced, too [152]. The article of Choi et al. can be recommended for a further reading about different microfluidic configurations and their application possibilities. They reviewed papers dealing with microfluidic-based sensors published from 2006-2011 [150]. The summarized sensor platforms served for the detection of DNA or proteins and detection limits in the picomolar range were described. Those microfluidic sensor combinations will probably be the future tools for point-of-care usage in biomedical analysis because of their easy implementation and their small size which makes them portable [150].

2.4.3 The electrical double layer

The working principle of field-effect transistors is mainly based on charges at the interface between the solid silicon dioxide surface and the molecules in the liquid buffer solution. van Hal et al. described in 1996, how the pH value of the solution and the surface potential are related [166]. In aqueous solution, hydroxyl groups are built up at the silicon oxide surface which can be either protonated or deprotonated depending on the pH value of the electrolyte solution. Since the isoelectric point (IP) of silicon oxide is in the range of 2.2 – 2.5, the surface is negatively charged at a pH higher than its IP. The isoelectric point, also known as point of zero charge (pzc), corresponds to a pH where the molecule or surface does not have an electrical charge. In consequence, the silicon surface becomes negative at neutral pH values due to the deprotonation of its hydroxyl groups (SiOH → SiO⁻ + H⁺) [54]. Hence, a surface potential Ψ_S is created at the oxide surface, leading to a charge difference between bulk and surface which is in compliance with the Boltzmann theory [166]:

$$a_{H_S^+} = a_{H_B^+} \exp \frac{-q\psi_S}{kT} \qquad (2.3)$$

$$pH_S = pH_B + \frac{q\psi_S}{2.3kT} \qquad (2.4)$$

Here, $a_{H_i^+}$ is the activity of H⁺, pH$_S$ and pH$_B$ are the pH value at the surface and in the electrolyte bulk, respectively, q is the elementary charge, k is the Boltzmann constant and T is the temperature in Kelvin. By rearranging formula (2.4), the Nernst equation, with which the surface potential can be calculated, can be derived:

$$\psi_S = 2.3 \frac{kT}{q} (pH_S - pH_B) \qquad (2.5)$$

The intrinsic buffer capacity ß$_{int}$ defines the capability to neutralize small pH changes at the surface. In doing so, charges are stored at the surface whereas the bulk pH is not affected. ß$_{int}$ is given by:

$$\beta_{int} = -\frac{1}{q}\frac{\delta\sigma_0}{\delta pH_S} \qquad (2.6)$$

where σ_0 is the surface charge. In the electrolyte solution side at the oxide-liquid interface, an opposite but equal charge is created due to the charge neutrality. The double-layer capacitance C_{DL} describes the capability of the bulk solution to deliver charges to neutralize charge differences at the oxide surface which are caused by changes in the surface potential.

$$C_{DL} = \frac{\delta\sigma_0}{\delta\psi_S} \qquad (2.7)$$

The sensitivity of the surface potential to changes in the surface pH can be described by combining equation (2.6) and (2.7)

$$\frac{\delta\psi_S}{\delta pH_S} = \frac{-q\beta_{int}}{C_{DL}} \qquad (2.8)$$

The sensitivity of the surface potential towards changes in the bulk pH is given by the combination of equation (2.5) and (2.8):

$$\frac{\delta\psi_S}{\delta pH_B} = -2.3\alpha\frac{kT}{q} \qquad (2.9)$$

with

$$\alpha = \frac{1}{\dfrac{2.3kTC_{DL}}{q^2\beta_{int}}+1} \qquad (2.10)$$

α is a sensitivity parameter. It is dimensionless and ranges between 0 and 1: α reaches almost 1 if the sensitivity is close to its theoretical maximum. According to formula (2.8), the intrinsic buffer capacity is high whereas the double-layer capacitance is low. With the site-dissociation model of Yates at al. [167] and the multisite complexation model (MUSIC) of Hiemstra et al. [168], the charging mechanism of oxides of the electrical double layer can be explained. According to the site-dissociation model, the charging of an oxide

surface relies on the equilibrium of the hydroxyl groups and the protons in the bulk solution. In case of ISFETs, the top layer consists of silicon dioxide, where hydroxyl groups are available on the surface. This hydroxyl groups act as amphoteric groups and can donate as well as accept a hydrogen ion from the bulk solution. This means, there is an equilibrium between the SiOH groups and the hydrogen ions of the bulk solution, which dissociate as follows [54,166,167]:
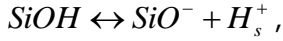
$$SiOH \leftrightarrow SiO^- + H_s^+ \, ,$$

with the dimensionless dissociation constant for acids $K_a = \dfrac{SiO^- + H_S^+}{SiOH}$ (2.11)
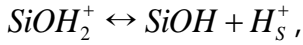
$$SiOH_2^+ \leftrightarrow SiOH + H_S^+ \, ,$$

with the dimensionless dissociation constant for bases $K_b = \dfrac{SiOH \;\; + H_S^+}{SiOH_2^+}$ (2.12)

The dimensionless dissociation constants are not influenced by the ionization state of the oxide surface. From the Boltzmann equation, the relation between the surface activity and the bulk activity of the hydrogen ions can be derived. The surface charge density relies on the dissociation of the surface groups and can be calculated by:

$$\sigma_0 = qN_S \left(\frac{a_{H_S^+}^2 - K_a K_b}{K_a K_b + K_b a_{H_S^+} + a_{H_S^+}^2} \right) \qquad (2.13)$$

with N_S is the density of the available sites on the surface. As published in [166], the intrinsic buffer capacity of an oxide, which depends on the pH of the solution, can be derived by combining equations (2.6) and (2.13):

$$\beta_{\text{int}} = N_S \frac{K_b a_{H_S^+}^2 - 4K_a K_b a_{H_S^+} - K_a K_b^2}{K_a K_b + K_b a_{H_S^+} + a_{H_S^+}^2} 2.3 a_{H_S^+} \qquad (2.14)$$

with N_S, K_a and K_b are oxide dependent [166]. The MUSIC (Multisite Complexation) theory of Hiemstra et al. considers crystallographic facts [168].

According to this model, a silicon dioxide surface consists of siloxane and silanol groups. This theory states that the SiO_2 has a very high dissociation constant (pK_D = -16.9). Moreover, Hiemstra et al. say that the pK_D of the silanol groups is about -1.9 so that their protonation is negligible. Therefore, the surface charge density is only depending on the dissociation of individually coordinated, neutral groups:

$$\sigma_0 = qN_S \frac{-K_a}{K_a + a_{H_S^+}}$$

(2.15)

In the MUSIC model, the intrinsic buffer capacity is given by:

$$\beta_{\text{int}} = N_S \frac{K_a}{(K_a + a_{H_S^+})^2} 2.3 a_{H_S^+}$$

(2.16)

Originally, the term "electrical double layer" was introduced by Georg Quincke to describe two layers of oppositely charged ions, *i.e.* anions and cations in 1861 [169,170]. However nowadays, it is well known that this was just a simplified theory [169]. By having a closer look to the history of theories about the electrical double layer, it was Hermann Ludwig Ferdinand Helmholtz who first developed a model for an electrical double layer in 1853. In this Helmholtz theory, the electrical double layer is created by the charges inside the solid surface and counterions on the surface. This is called the Helmholtz layer and represents the simplest explanation of the electrical double layer. The counterions are attracted by the electric field which is built up by the charge of the solid surface [171]. In this theory, the double layer is regarded to be stiff with a linear potential [172]. However, the capacitance of the double layer cannot be described with this model since the bulk solution is influencing the surface charge and, hence, the double layer capacitance. In the Gouy-Chapman theory [173,174], the motion of the counterions due to thermal fluctuations in a liquid and the development of a diffuse layer are included [171]. The ions in the solution are attracted by counterions on the oxide surface as well as by counterions in the solution itself. Based on the Gouy-Chapman model, the Grahame equation was developed to calculate the charge density in the diffuse layer [166]:

$$\sigma_{DL} = -\sqrt{(8kT\varepsilon_0 n_0)} \sinh \frac{zq\psi_S}{2kT} \tag{2.17}$$

with ε is the dielectric constant of the bulk solution, ε_0 is the dielectric constant of vacuum, n_0 is the concentration of each individual ion in the bulk solution and z is the valance of the ions. The capacity of the electrical double layer is given as:

$$C_{DL} = \sqrt{\frac{2z^2 q^2 \varepsilon_0 n_0}{kT}} \cosh \frac{zq\psi_S}{2kT} \tag{2.18}$$

where z is the charge of the ion. The main problem of this model was that the charges were considered to be point charges which can reach close to the surface [166]. Therefore, the Gouy-Chapman model was further expanded by Otto Stern who combined the Helmholtz and the Gouy-Chapman theory [175]. He considers the solid-liquid interface to be composed of an immobile layer and a diffuse layer. The immobile layer, also called Stern layer, consists of the ions inside the solid surface and the attracted counterions. The outer layer of ions is in further distance to the Stern layer. The diffuse layer begins at the distance x_d from the surface. The Helmholtz plane is the distance of the center of the counterions from the surface. This distance is caused by the hydration shell of the ions, wherefore they cannot completely reach the surface. At the passage from the immobile to the diffuse layer, the zeta potential (ζ) can be observed [171]. In this theory, the capacitance of the double layer can be derived by:

$$C_{DL} = \frac{x_2}{\varepsilon_0} + \left(\sqrt{\frac{2\varepsilon_0 z^2 q^2 n_0}{kT}} \cosh \frac{zq\psi_S}{2kT} \right)^{-1} \tag{2.19}$$

with x is the distance of the center of the charge from the surface [166]. In *Figure 9*, an overview of the three different models of the electrical double layer is given [176]. Depending on the concentration of the buffer solution, different Debye lengths λ_D can be observed: In high buffer concentration, where the ionic strength is high, the Debye length is lower compared to low concentrated buffer solutions. At a low Debye length, ion charges are shielded by their counterions. At the Debye length, the number of positive charges is equal to the negative charges, therefore the charge is neutralized. This screening effect is also known

as Debye screening [163]. The Debye screening is a function of the electrolyte concentration.
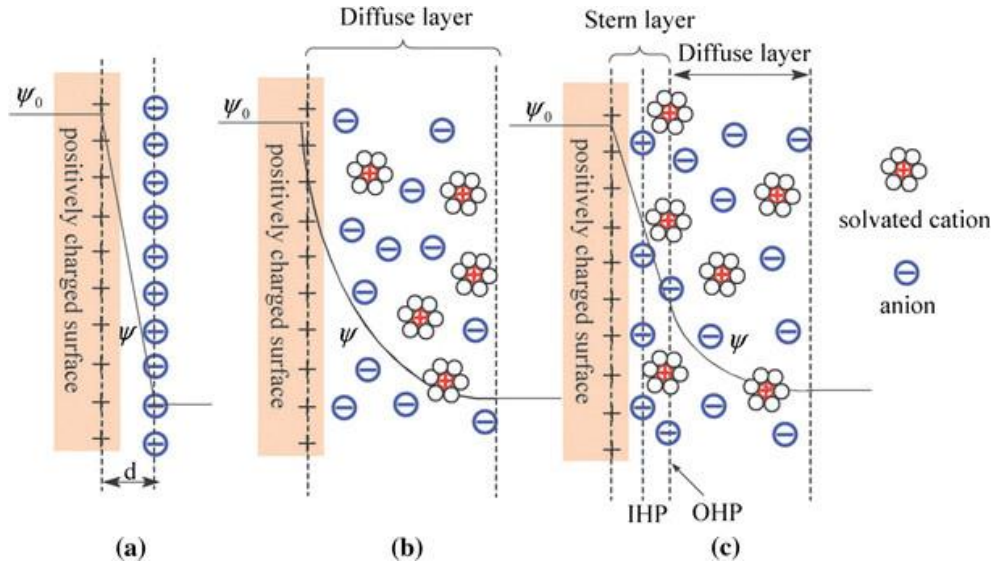
Figure 9: Overview of the three different theories of the electrical double layer.
The simplest model is the Helmholtz in which the double layer is stiff with a linear potential and built up by charges inside the solid surface and counterions on the surface model. The double-layer distance is marked with 'd' (a). In the Gouy-Chapman explanation, the ions are attracted by counterions in the solution and on the oxide surface. The charges are considered as point charges. A diffuse layer is created (b). In the Gouy-Chapman-Stern model, an immobile Stern layer and a diffuse outer layer are described. The Stern layer consists of the ions inside the solid surface and their counterions with the inner Helmholtz plane (IHP), which marks the closest specifically adsorbed ions. The diffuse layer is in further distance to the immobile layer. At the outer Helmholtz plane (OHP), the diffuse layer begins (c). ψ is the potential at the electrode-electrolyte interface and ψ₀ stands for the potential of the electrode. The picture is taken from [176].

In a physiological environment, the Debye length amounts 1 nm [164] and in distilled water it can be at maximum 680 nm [171]. It can be calculated by:

$$\lambda_D = \sqrt{\frac{\varepsilon_0 kT}{2N_A e^2 l}} \tag{2.20}$$

where N_A is the Avogadro constant, I represents the ionic strength and e stands for the elementary charge [171]. The ionic strength is given as follows

$$I = \frac{1}{2} \sum_{i=1}^{n} c_i z_i^2$$

(2.21)

with c_i being the molar concentration of the ion I in M (mol/l), z_i meaning the charge number of this ion. Since cations and anions are represented in this equation the sum is multiplied with one half. Since the Debye length in physiological solutions is about 1 nm [164] whereas the size of a DNA strand with 20 base pairs amounts around 6 nm [97] and that of an antibody approximately 10 nm [177], the biomolecules are bigger than the Debye length and not detectable in full size with the reported sensors. This fact makes the direct charge detection methods with potentiometric transducers (such as ISFETs and SiNW FETs) a real challenge, since large molecules with distributed charges are very difficult to detect in these methods.

Chapter 3 - Materials and Methods

3.1 Chip fabrication

In framework of this thesis, two different kinds of field-effect transistors were used. The first type was the microscaled ion-sensitive field-effect transistors (ISFETs) and the other transistors were the nanosized silicon nanowire field-effect transistors (SiNW FETs). The fabrication process is only briefly described, in the following two subchapters, since the transistor productions was not part of this thesis.

3.1.1 ISFETs

The ISFETs used in this work were fabricated at the Max-Planck-Institute for Polymer Research in Mainz, Germany. The initial fabrication procedure was described previously [28]. To achieve smaller gate sizes and a lower resistance, Krause et al. modified this procedure in 2000 [178,179]. The ISFET fabrication process is shortly summarized as follows: An n-doped silicon wafer was covered with a 1000 nm thick oxide layer with help of thermal oxidation under wet atmosphere. The drain and source regions were etched with buffered HF by photolithography followed by ion implantation to perform boron doping to achieve a p-channel transistor. Drain and source were covered with an oxide layer of 400 nm thickness due to oxidation and diffusion. The gates were photolithographically defined with buffered HF, where after an oxide layer of 250 nm was thermally deposited on this area under wet atmosphere. Afterwards, low-pressure chemical vapor deposition (LPCVD) was applied to cover the wafer with silicon nitride (130 nm thickness) followed by a plasma enhanced chemical vapor deposition (PECVD) step to grow a 100 nm thick silicon oxide layer. This oxide-nitride-oxide (ONO) stack minimized the risk for leakage currents and the possibility of damages caused by an electrolyte solution and, therefore, served as isolation layer. At the gate area, the PECVD oxide and the LPCVD nitride were removed with buffered HF and isotropic chemical plasma etching, respectively. Afterwards, the remaining wet oxide, which served as an etch stop layer before,

was eliminated with ammonium-fluoride buffered HF. A 10 nm thick gate oxide layer was deposited in dry oxygen atmosphere. In a final step, a 200 nm thick aluminum film was evaporated to create the bond pads by lift-off. All ISFET chips, used in this thesis, were p-channel transistors. The sensors had a 4 × 4 layout with a gate distance of 200 μm (*Figure 10*).
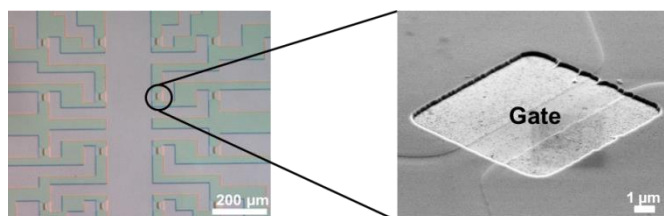
Figure 10: Microscopic picture of an ISFET.

On the left, an optical microscopy image of the 4 × 4 array of an ISFET can be seen. Picture taken from [209]*. The right picture shows a magnification of the transistor gate area taken by SEM*.

For this thesis, ISFETs with gate dimensions of 25 × 5 μm², 24 × 7 μm², 24 × 4 μm², 16 × 7 μm², 12 × 5 μm², 12 × 4 μm², 8 × 7 μm² and 8 × 6 μm² (length × width) were utilized.

3.1.2 SiNW FETs

The silicon nanowire field-effects transistors used for the experiments, represented in this thesis, were all fabricated in the framework of another PhD project performed by Dr. Xuan Thang Vu at the Peter Grünberg Institute-8 (PGI-8) of the Research Center Jülich, Germany. For further information and processing details, please refer to the PhD thesis [54]. The SiNW FETs used in this study were p-type transistors with a layout of 2 × 28 nanowires per chip (*Figure 11*). The complete size of the chip was 7 mm × 7 mm. All nanowires possessed individual drain contacts and were connected with one common source [39,53,157]. The dimensions of the nanowires varied from chip to chip. For the performed measurements, FETs consisting of single nanowires with sizes of 200 nm × 10 μm, 200 nm × 20 μm, 200 nm × 40 μm, 400 nm × 10 μm, 400 nm × 20 μm and 400 nm × 40 μm (width × length of mask measures, respectively) were applied. The actual size of the fabricated chips was thinner than these measures due to the anisotropic wet etching procedure used during

the process. Furthermore, chips with different number of nanowires per channel were used in some experiments. The number varied from one to five nanowires per channel. The dimensions for those chips were 200 nm × 10 µm and 400 nm × 10 µm (width × length, respectively). Within a row of 28 nanowires, the distance from nanowire to nanowire was 50 µm and the distance between the two nanowire rows was 500 µm.
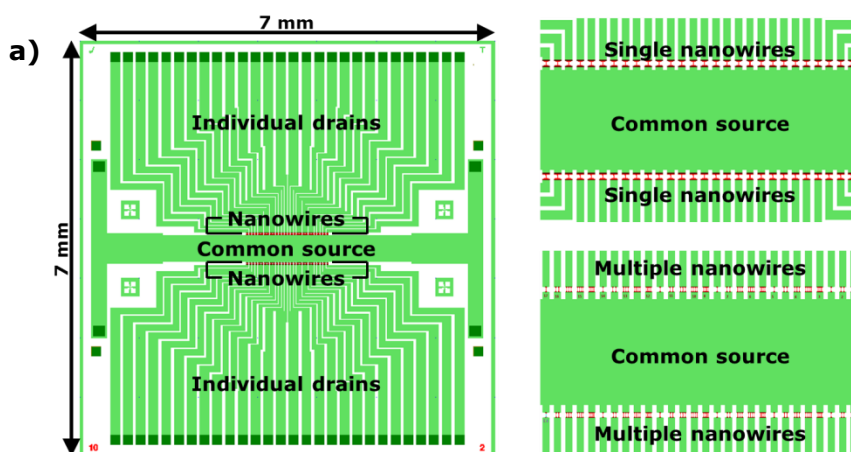
Figure 11: Schematic of a SiNW array.

Figure a) shows a schematic of a 2 × 28 nanowire array chip. In b) and c) a magnification of the nanowire area of two different types of chips can be seen. Figure b) shows an overview of a FET consisting of single nanowires. In c), the magnification of a chip with different numbers of nanowires per channel is displayed. The red structure in a) - c) are the nanowires whereas the individual drains and the source are colored in light green. The dark green square areas are the electrical contacts to the back gate, source and drain.

An optical microscopy image of a nanowire array and a single nanowire can be seen in *Figure 12*. The size of the implantation area equaled the length of the nanowire, whereas the opening of the gate was 2 µm bigger in both directions compared with the nanowire length. The obtained nanowire structures had a trapezoid shape caused by the wet etching and oxidation steps. With the applied design it was possible to integrate the nanosized chips into a microfluidic cartridge [39,53,54,157]. For the nanoimprint mold fabrication, wet oxidation was used to thermally grow a 200 nm thick SiO_2 layer on a 4'' wafer. After having spin-coated a poly(methyl methacrylate) (PMMA) resist (thickness: 230 nm), the wafer was prebaked at 180 °C on a hot plate.
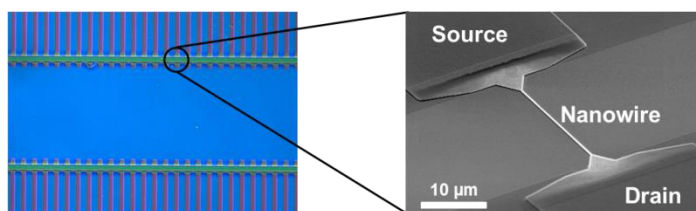
Figure 12: Microscopic picture of a silicon nanowire field-effect transistor.

An optical microscopy image of a 2 × 28 silicon nanowire array can be seen on the left. The right figure displays a scanning electron microscopy (SEM) picture of a single nanowire.

Electron beam lithography (EBL) was performed onto the PMMA resist to define the contact lines and the nanowires followed by the developing of the resist. With help of reactive ion etching (RIE) in CHF_3 plasma, the SiO_2 layer was over-etched to receive a uniform structure. The excess PMMA resist was etched off by using oxygen plasma. The height of the obtained structure was measured to be 170 nm with a roughness at the edges of about 10 nm. To avoid that the imprint resist remained in the mold, the wafer was silanized with a fluorosilane (1H,1H,2H,2H-perfluorooctyl-trichlorosilane (FOTCS)) to create an anti-adhesion layer. The SiNW chips were fabricated in a top-down process on a silicon-on-insulator (SOI) wafer (SOITEC, France), composed of a buried oxide (BOX) layer (400 nm), a Si layer (360 nm, Si<100>, boron-doped) and a Si substrate (boron-doped). The upper Si layer of the SOI wafer was thinned out by thermal oxidation and wet etching, followed by the growth of a thin layer of dry oxide (100 nm). This oxide layer was taken as hard mask for the anisotropic etching with tetramethylammonium hydroxide (TMAH). The structures from the mold were transferred onto the SOI wafer with thermal nanoimprint lithography (NIL). The contact lines and nanowires were defined by NIL in one step. The residual resist layer and the SiO_2 layer between the contact lines and the nanowires were dry-etched by applying RIE. This SiO_2 layer served as a bond mask for the following wet etching. With the TMAH solution, the Si was anisotropically etched to transfer the structures of the mold onto the wafer. Afterwards, the mask oxide was removed by HF etching. Low pressure chemical vapor deposition (LPCVD) was performed to deposit silicon oxide (100 nm) on top of the nanowires, following by an optical lithography step to structure the oxide in such a way that it can be used as protection mask for the feed line implantation.

Afterwards, the contact lines were implanted with boron ions to decrease the serial resistance at source and drain. A very thin, dry thermal SiO_2 layer (8 nm) was deposited before LPCVD to receive a front gate oxide. LPCVD was performed to create a SiO_2 layer (270 nm) onto the wafer, which served as protection against electrolyte solutions. Optical lithography and wet etching was performed to open the bond pads and the gate area of the chip. The LPCVD oxide was wet-etched chemically with 1 % HF. Finally, a stack of metals (Al 150 nm – Ti 10 nm – Au 200 nm) was built up by a lift-off process on the contact pads. The ohmic contacts were built by rapid thermal annealing. Plasma enhanced chemical vapor deposition (PECVD) was applied to create an oxide-nitride-oxide (ONO) stack to ensure a passivation against an electrolyte solution [39,53,54,157].

3.2 Chip encapsulation

For stable measurements in electrolyte solutions, the transistor chips needed to be encapsulated. First, both sensors were carefully and alternately cleaned in acetone and isopropanol, two times for 5 min, respectively. While the ISFETs could be cleaned in an ultrasonic bath, the SiNW FETs were too easy to be loosened and, hence, damaged during the sonication. Therefore, the nanowire chips were only gently swayed. The sensors were afterwards dried with nitrogen. To confirm that the chips were really clean, they were checked under the microscope. In *Figure 13*, the raw material for the chip encapsulation (carrier, glass ring and funnel) and an encapsulated SiNW FET are displayed.

Figure 13: From individual components to the encapsulated nanowire chip.
In this figure, the chip carrier, the outer glass ring, the custom-made funnel and a finished encapsulated SiNW chip can be seen (from left to right).

The chips were then glued onto a 68-pin LCC carrier (LCC 0850, Spectrum, USA) with epoxy glue (377 1LB kit, Epoxy Technology Inc., USA). The epoxy glue was cured at 150 °C in an oven for 1 h. The devices were then bonded with 25 µm

aluminum wires to the bond pads of the LCC carrier to create an electrical contact between chip and carrier and, thus, be able to do electronic measurements. A wedge-wedge bonder (West Bond Inc., USA) was used for this purpose. In the following step, a custom-made funnel (Sylgard® 184 silicone elastomer kit, Dow Corning, Germany) was carefully glued in the center of the transistors without harming the nanowires by applying a silicone adhesive (96-083 silicon adhesive kit, Dow Corning, Germany) and baked for 30 min at 120 °C. To be able to do measurements in a liquid, a glass ring was glued onto the LCC carrier with help of the silicone adhesive. The gap between the glass ring and the funnel was completely filled with the silicone adhesive to prevent any short cuts or leakage from the solution to the electronics. The silicone adhesive was finally hardened in the oven at 130 °C for 1 h.

3.3 Characterization experiments

The basic experiments served as proof-of-principle experiments to clarify that the sensors were working properly. Furthermore, those measurements were done to gain more information about the used field-effect transistors and the applied readout methods. For verifying that the DC readout was correct, stable and reliable, pH solutions with different values and the layer-by-layer assembly of polyelectrolyte multilayers were measured. The reliability of the AC readout was examined by measuring buffer solutions with different conductivities. In the following three subchapters, the experimental procedure is described.

3.3.1 pH measurements

pH measurements were done with the SiNW FET sensors. These experiments were performed to clarify if the transistors were working properly. For this purpose, the sensors surface was cleaned with Piranha solution, consisting of hydrogen peroxide (H_2O_2) and sulfuric acid (H_2SO_4) in a ratio of 1:2, for 10 min at 60 – 80 °C. Due to the Piranha solution, the surface was activated with hydroxyl groups. No further modification of the sensor surface was done after the cleaning. 100 mM phosphate buffer solutions, consisting of NaH_2PO_4 and Na_2HPO_4, with six different pH values were prepared: pH 4.5, pH 5, pH 6.0, pH 7.0, pH 8.0 and pH 9.0. Measurements were started with the lowest pH solution.

Then the pH value was stepwise increased up to the highest value. In between each measurement, the sensor was thoroughly cleaned with the respective buffer solution that was measured in the following step. Depending on whether the pH solution was acidic or alkaline, the oxide surface of the transistor was either protonated or deprotonated due to its amphoteric groups. This caused a change in the surface potential, as described in Chapter 2.4.3. The corresponding results are shown in Chapter 4.1. According to the change in threshold voltage, the sensitivity of the SiNW FET upon changing the pH was calculated. It was reported to be 30 – 40 mV/pH on bare SiO_2 surfaces [180]. Besides the material, of which the surface was made, the degree of purity was affecting the sensitivity to pH changes. Since only chips, which were already used for other experiments, were available for the pH measurements, a lower sensitivity was expected.

3.3.2 Conductivity measurements

Another set of basic experiments was done for the conductivity measurements. For these experiments, four differently concentrated phosphate buffer solutions with different conductivities were used. The experimental procedure was started with the lowest buffer concentration, *i.e.* 0.15 mM, and then increased by three orders of magnitude to 150 mM. Each buffer was measured with the transistor devices by means of the transistor transfer function. Before reading-out the buffer concentration, the chip was carefully rinsed with the respective buffer solution so that the surface could adapt to the phosphate buffer conductivity.

3.3.3 Assembly of polyelectrolyte multilayers

The polyelectrolyte experiments were done as proof-of-principle experiments on both platforms, the nanoscaled and the microscaled devices and served as model system for the charged biomolecules. Polyelectrolytes are polymer chains which possess ionizable groups and which are soluble in polar solvents such as water. By diluting them in a polar liquid, the ionizable groups like amines or sulfonates dissociate into positive and negative ions (amines: $R - NH_3Cl \rightarrow R - NH_3^+ + Cl^-$; sulfonates: $R - SO_3M \rightarrow R - SO_3^- + M^+$) [171,181]. Depending on the dissociation of the groups there are more or less charges in the solution [171].

Polyelectrolytes can be composed of cations (polybases/polycations), anions (polyacids/polyanions) or a mixture of anions and cations (polyampholytes). The polyelectrolyte can be classified into natural, chemically modified and synthetic compounds. There are homopolymers that consist of only one type of monomer and copolymers, consisting of different types of monomers. Polyelectrolytes have either a linear, branched or cross linked structure [182]. The best-known example for a negatively charged polyelectrolyte is the deoxyribonucleic acid (DNA). For the experiments shown in this thesis, poly(sodium 4-styrenesulfonate) (PSS) and poly(allylamine hydrochloride) (PAH) were used. PSS belongs to the negatively charged polyelectrolytes whereas PAH is a positively charged one. In *Figure 14*, both compounds can be seen.

PSS   PAH
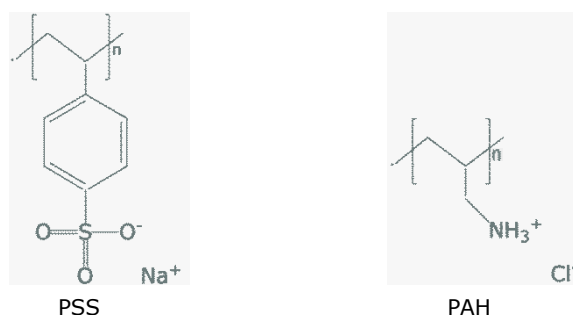
Figure 14: Structural formula of PSS and PAH.
In this figure, the chemical structures of the positively and negatively charged polyelectrolytes PAH and PSS are displayed. Picture adapted from [171]*.*

In the first experimental step, the SiNW chip area was cleaned with a Piranha solution, consisting of hydrogen peroxide (H_2O_2) and sulfuric acid (H_2SO_4) in a ratio of 1:2, for 10 min at 60 – 80 °C. The Piranha solution also activated the surface with hydroxyl groups. Two solutions composed of 50 µM PAH and PSS, respectively, were prepared in 10 mM phosphate buffer pH 5.5. To assemble polyelectrolyte multilayers, the activated nanowire array was firstly incubated with PAH for 20 min., followed by the addition of PSS for 20 min. In between the incubation with the two different polyelectrolytes, the chip was thoroughly rinsed with 150 mM phosphate buffer pH 7, deionized water and 0.15 mM phosphate buffer pH 7. This experimental procedure was repeated for seven times so that 14 monolayers of alternately PAH and PSS were obtained (*Figure 15*). The formation of the polyelectrolyte multilayers is based on a layer-by-layer

adsorption where the positively charged PAH to the negatively charged nanowire surface and the subsequent adsorption of the negatively charged PSS to the positive PAH [54,171,183,184].

Figure 15: Schematic diagram of the assembly of polyelectrolyte multilayers.

The green coiled structures are the positively charged PAH and the purple structures represent the negatively charged PSS. The construction of the multilayers is caused by the attraction of opposite charges. The numbers of measurable layers with an electronic readout system depends on the applied buffer since the ionic strength and the Debye length influence the screening effect of the ions in the solution.

The transfer characteristic and the transistor transfer function were measured after cleaning and activating the chip as well as after each addition of polyelectrolyte. Furthermore, to study the influence of the ionic strength of the buffer solution, the electronic readout was performed in 150 mM, 15 mM, 1.5 mM and 0.15 mM phosphate buffer pH 7. At high salt concentrations, the charges of the polyelectrolytes are shielded by counterions due to a small Debye length. In consequence, the polyelectrolytes form coil-like structures and, hence, are denser. In comparison to that approach, the polyelectrolytes are more stretched out in buffers with low ionic strength since the charges of either the anions or cations within a polyelectrolyte are repelling each other [171]. Due to the shielding effect in high salt concentrations, the multilayer assembly should be more likely observed in low buffer concentrations. Moreover, a higher number of multilayers should be possible to detect electronically in solutions with low ionic strength caused by a larger Debye length and, hence, a lower Debye screening.

3.4 Surface functionalization

For the DNA and antibody-antigen experiments, the transistor surface needed to be functionalized to implement the assays. To clean the chip surface, the FET was carefully cleaned with Piranha solution (H_2O_2:H_2SO_4 = 1:2) for 10 min at 60 °C to maximum 80 °C. Besides cleaning the device, the acid also activated the

surface, which became more hydrophilic due to an increased amount of hydroxyl groups. To remove the cleaning acid, the transistor was properly rinsed with deionized water followed by drying with nitrogen. Subsequently, silanization was performed. For this purpose, 3-(glycidoxypropyl)trimethoxysilane (GPTMS, Sigma-Aldrich, Germany) was used. GPTMS possesses an epoxy ring and enables the deposition of homogeneous layers [185]. Furthermore, the amino groups of a molecule can be directly bound to the epoxy ring. Therefore, the epoxy ring needs to be opened, which can be done either by UV light or by incubation with a solution owning a pH of 8.5 – 9. For the experiments reported in this thesis, the capture molecules were diluted in 150 mM phosphate buffer pH 8.6, consisting of NaH_2PO_4 and Na_2HPO_4, to allow a binding between their amino groups and the opened epoxy ring of the silane. The silanization process was done under gas-phase conditions to avoid damaging of the encapsulated material and to assemble a homogeneous layer. In doing so, a custom-made vacuum chamber was used. This chamber consisted of a tightly sealed desiccator connected to a plasma oven (PICO, diener electronic Plasma-Surface-Technology, Germany) and a vacuum pump (*Figure 16*). The GPTMS itself was injected in a special tube which could be connected to the desiccator. The injection of the silane was done in a glove box with inert nitrogen atmosphere to avoid that the silane groups of the silane were transformed to siloxane groups. The silanization was performed for 2.5 to 3 h at 80 °C to 85 °C at a pressure of 130 mbar. After the silane modification of the chip surface, the transistor was cleaned with water and the quality of the silanization was characterized by determination of the contact angle. The contact angle was measured with an optical contact angle measurement setup (OCA 15 plus, DataPhysics Instruments GmbH, Germany) and the corresponding evaluation software (SCA 20, DataPhysics Instruments GmbH, Germany). In *Figure 17*, the OCA contact angle measurement setup is displayed. With this surface characterization method, it was possible to evaluate whether a homogeneous siloxane layer was obtained. A benefit of this user-friendly method is that the determination of the contact angle can be performed within some minutes. The contact angle was characterized by pipetting one drop of a certain liquid with help of a syringe onto the silanized device. Then the drop was recorded with a camera and the angle was evaluated by the SCA software. The sessile drop method was chosen to

measure the contact angle. For this purpose, the water drop was deposited onto the silanized device and illuminated with a diffuse light source.
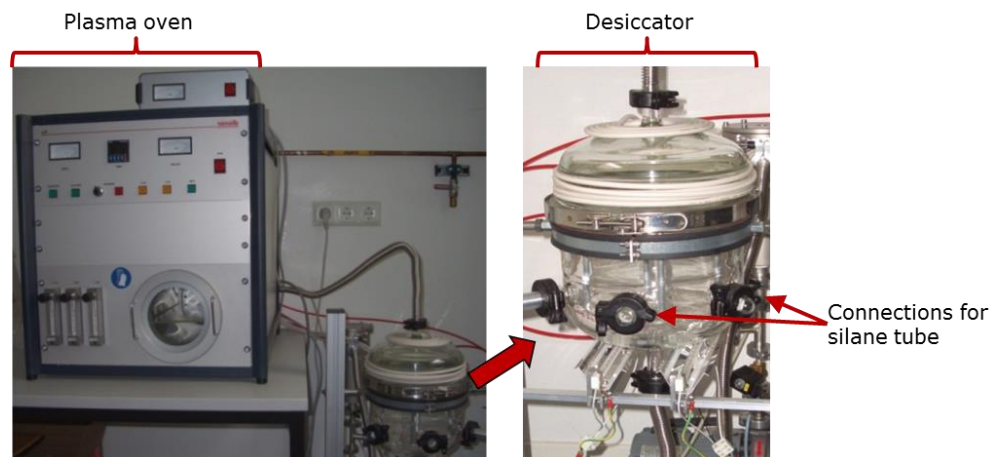
Figure 16: The silanization device.

The silanization was performed in a desiccator connected to a plasma oven and to a pump, which was responsible for the application of a vacuum inside of the desiccator.

The recording of the drop was caught from the other side. With help of the recorded picture, the basis line of the drop was set. The contour of the drop was determined by the brightness difference of the drop and its surrounding area [186,187].
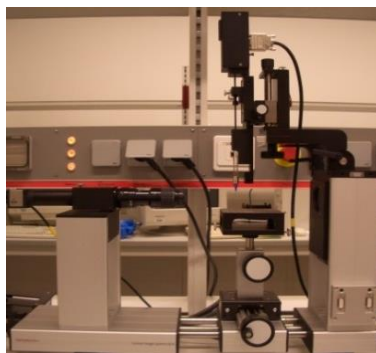
Figure 17: Picture of the OCA 15 plus contact angle measurement setup.

The setup allows a precise determination of the contact angle of a surface by use of the Young-Laplace fitting.

In 1805, Thomas Young established the equation for calculating the contact angle or wettability of a liquid drop on an ideal solid surface:

$$\gamma_{LG} \cos \theta_{CA} = \gamma_{SG} - \gamma_{SL} \tag{3.1}$$

with γ_{LG}, γ_{SG} and γ_{SL} as the liquid-gas, solid-gas and solid liquid interfacial energy, respectively, and with θ_{CA} as the contact angle [188,189]. To obtain more accurate contact angle results, it was analyzed by applying the Young-Laplace fitting, where the interface of the drop is modeled. The Young-Laplace equation is given by

$$\Delta P = \gamma \left(\frac{1}{R_1} + \frac{1}{R_2} \right) \tag{3.2}$$

With ΔP being the pressure across a curved liquid surface (Laplace pressure), γ being the interfacial energy, R_1 and R_2 being the primary radii of the drop curvature [171,189]. By implementing several conversion of the Young-Laplace equation, the contact angel θ_{CA} is given by the following equations [189]:

$$\frac{dX}{dS} = \cos \theta \quad \text{or} \quad \frac{dZ}{dS} = \sin \theta \tag{3.3}$$

The meaning of the parameters X, S and Z can be identified by the right schematics in *Figure 18*.
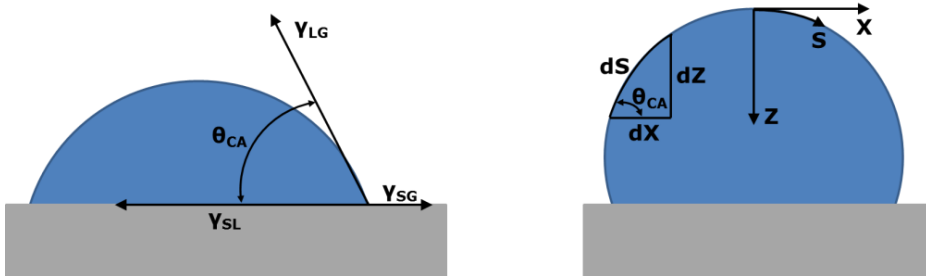
Figure 18: Calculation of the contact angle.
On the left, all parameters that are included in the Young equation are shown. On the right, the same is shown for the Young-Laplace calculation of the contact angle is displayed.

All parameters were calculated automatically by the SCA software.

3.5 Immobilization of capture molecules and binding of target molecules

After a successful silanization with GPTMS, the immobilization of the capture molecules needed to be performed. For this purpose, a microspotting system was used (sciFLEXARRAYER S3, Scienion AG, Germany). A picture of the microspotter and its components can be seen in *Figure 19*.
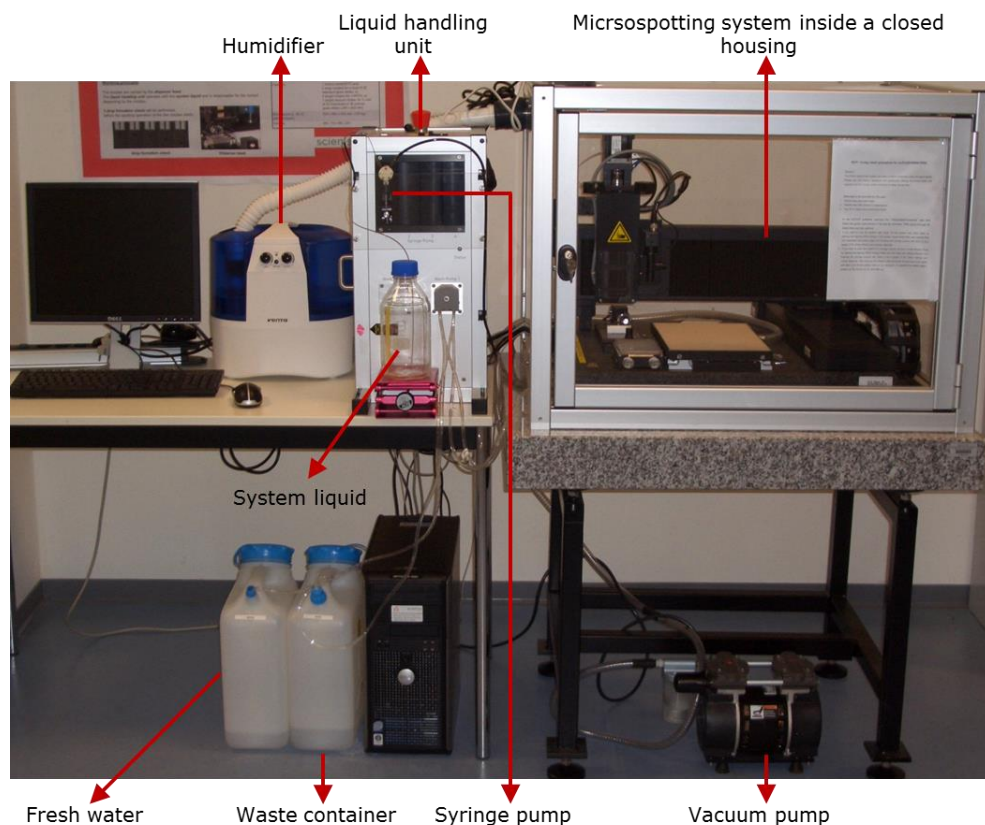
Figure 19: Basic components of the microspotting system.
The microspotting setup is consisting of different components, including a humidifier to produce a defined humidity inside a closed housing to prevent the evaporation of the spotted probe molecules.

This microspotter is a piezo dispenser, with which the probes can be spotted automatically. A big benefit of this system was that the spotting is performed in a non-contact mode so that the surface of the chip was not affected. This was

particularly important for the SiNW FETs since even a light contact might break the tiny nanowire and, hence, destroy one of the transistor channels. It was possible to immobilize the capture molecules on defined areas of the chip surface, *i.e.* the transistor gates and nanowires. Furthermore, a site-specific binding of the immobilized probe was feasible. In principle, the microspotter could have also been used for the immobilization of different capture molecules onto the same device since the probes could have been spotted with defined distances to avoid cross-contaminations. However, this was not done in framework of this thesis due to the lack of good SiNW FET devices. To prevent the evaporation of the biomolecule solution, a humidifier was connected to the inside of the microspotter housing. The humidity was adjusted to 65-70 % for all experiments. Before the microspotting procedure could be started, the areas, on which the molecules should been immobilized, had to be defined. Thereafter, two to three drops were spotted, each with a volume of 250 to 300 pl. The probe solution was only immobilized on certain sensor spots of the chip. The blank sensor spots served as reference channels. Immediately after the microspotting process, a microscopic image of the drops was taken to confirm that the molecules were immobilized onto the desired areas (*Figure 20*). The immobilization process was done overnight at 37 °C in a separate incubation chamber. A humidity of 65 % was adjusted at the inside of this chamber to ensure that the solution was not dried out during the immobilization. Unspecifically bound molecules were eliminated by properly rinsing the chips. Before adding the target molecule solution, the gate surface, to which no capture molecules had bound, had to be blocked for 2 h at 37 °C, 65 % humidity. Non-bound blocking molecules were washed away, followed by the addition of the target solution. The binding of the target molecules was performed for 2 h at 37 °C, 65 % humidity. Then, the chip was rinsed once more to eliminate unspecifically bound molecules. The electronic readout was done after

1. Silanization
2. Immobilization of the capture molecules
3. Blocking
4. Binding of target molecules

The measurements were done in 0.15 mM, 1.5 mM, 15 mM and 150 mM

phosphate buffer pH 7.4, whereby the lowest concentration was used first, continuing by increasing the concentration by a factor of 10.
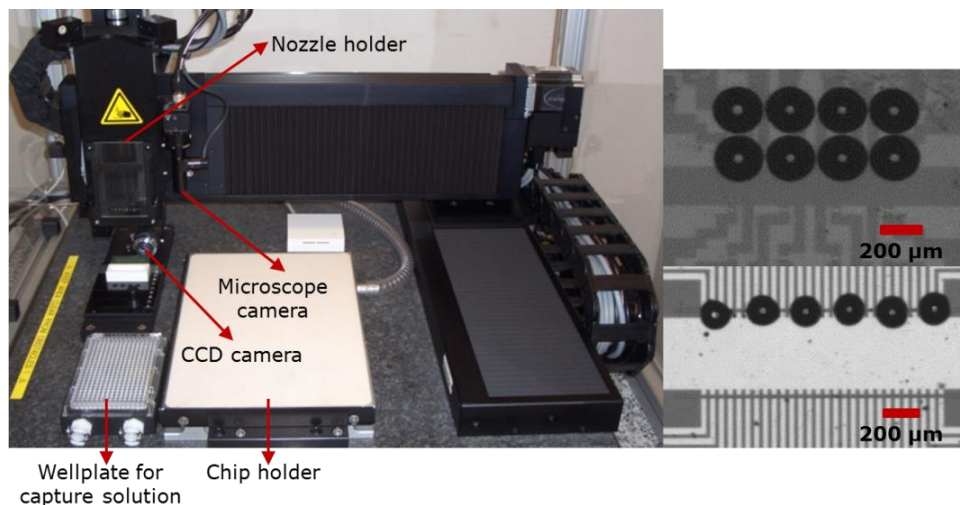
Figure 20: Main microspotter unit and microspotted probe solution.

On the left, the microspotting unit can be seen. In the right upper image, an ISFET surface is displayed. The capture molecules were only spotted onto the upper eight transistor gates. In the lower picture on the right side, the nanowire area of a SINW FET is shown. The capture solution was spotted on the upper nanowire row. For both, the ISFET and the nanowire FET, the lower gates served as reference channels.

In the chapters 3.6.1 and 3.6.2, the DNA assay and the antibody-antigen assay are described in more detail. All applied capture and target molecules, the used washing and blocking solutions as well as all appropriated concentrations are summarized in the two following subchapters.

3.6 Biomolecular assays

After performing the basic experiments, biomolecular assays were established on the platforms. For one assay the devices were used as DNA sensors, with which the hybridization of single-stranded target DNA to the immobilized, complementary capture DNA strand was detected. Moreover, the sensors also served as immunosensors. Therefore, a monoclonal antibody was bound to the gate area so that the binding and the detection of its specific antigen protein was feasible. In the next subchapters, the experimental procedures for the

assays are described in detail.

3.6.1 DNA assay

To establish a stable DNA assay, customized DNA sequences were used in first experiments. The experiments with artificial DNA were performed on ISFETs and SiNW FETs. The DNA sequences were purchased from Eurofins Genomics, Germany and had a length of 20 base pairs. All applied, customized DNA sequences, which were used for immobilization and hybridization, are summarized in *Table 2*.

	Name	Sequence
Capture DNA	ssDNA	5'AC6-ATGAACACTGCATGTAGTCA-3'
	Cy3 ssDNA	5'Cy3-ATGAACACTGCATGTAGTCA-3'-AC6
Target DNA	cDNA	5'-TGACTACATGCAGTGTTCAT-3'
	Cy3 cDNA	5'Cy3-TGACTACATGCAGTGTTCAT-3'

Table 2: Capture and target DNA sequences.
In Table 2, the customized DNA sequences used for immobilization and hybridization are displayed.

The AC6 label represents the amino-modifier, which is needed for the binding of the capture molecules to the silanized chip surface. For the immobilization, single-stranded capture DNA (ssDNA) was attached to the transistor gates *via* microspotting as described before. In doing so, 1 µM ssDNA was diluted in 150 mM phosphate buffer pH 8.5. The binding proceeded overnight at 37 °C at a humidity of around 65 % in an incubator. Unspecifically bound molecules were eliminated by rinsing the chips with 4× saline sodium citrate buffer (SSC), 1× SCC, and deionized water. Afterwards, the surface was blocked to avoid unspecific binding of the complementary target DNA (cDNA). For this purpose, two different blocking agents were tested. First, 1 µM fully-mismatching DNA, diluted in 1× PBS, was deposited to avoid unspecific binding of the target molecules. However, this did not lead to desired results. Therefore, the blocking step was also performed with bovine serum albumin (BSA, Sigma-Aldrich,

Germany), which was diluted to a percentage of 1 % in 1× phosphate buffered saline (PBS, Sigma-Aldrich, Germany, composition: 137 mM NaCL, 2.7 mM KCl, 8.1 mM Na_2HPO_4 and 1.47 mM KH_2PO_4). Blocking was done for 2 h at 37 °C, 65 % humidity. Exceeding blocking molecules were washed away by using 1× PBS. Single-stranded complementary target DNA was added in a concentration of 0.5 µM and 1 mM to hybridize with the ssDNA. In low buffer concentrations, where the ionic strength is low as well, the electrostatic repulsion between two complementary DNA strands is high wherefore the probability and the speed of the hybridization process are reduced. This means that the annealing of two single strands to one double strand requires more time [16,156]. Therefore, the target molecules were diluted in 1× PBS, which corresponds to a concentration of around 150 mM. Hybridization was first measured after the hybridization with 0.5 µM, followed by incubation with 1 µM cDNA. Each hybridization process was performed for 2 h at 37 °C and a humidity of 65 %. In between the hybridization steps, the chip was rinsed with 4× saline sodium citrate buffer (SSC), 1× SCC, and deionized water. After each experimental step, the measurements were done in 0.15 mM, 1.5 mM, 15 mM and 150 mM phosphate buffer pH 7.4 starting with the lowest concentration. To evaluate the recorded results of the different experimental steps, all obtained transfer characteristic and transistor transfer function curves for each channel were compared, respectively. An overview of the whole DNA assay is shown in *Figure 21*. To confirm that the electronic results were really based on the immobilization and hybridization process, fluorescence microscopy was performed. The experimental procedure and applied molecule concentrations were the same as described before. To verify the immobilization of capture DNA, cyanine 3 (Cy3)-labeled capture molecules were microspotted onto silanized glass slides and FETs. Cy3 is a fluorophore which belongs to the cyanine group. It is widely used for fluorescence experiments in microarray technology [190]. The fluorescent dye has an absorbance maximum of 550 nm and an emission maximum of 570 nm [191]. Fluorescence microscopy was performed with an inverted fluorescence microscope (Olympus IX50, Olympus Optical CO. (Europe), GmbH, Germany). Concerning the hybridization, non-fluorescent capture DNA was immobilized, and Cy3-labeled cDNA was added. A fluorescence signal was only measured if the immobilization or hybridization were successful. Besides experiments with

customized DNA sequences, initial trials with real DNA sequences were performed. The measurements were only performed on ISFETs since no SiNW FETs were available anymore. For this experiment, the HLA-B 27 assay, provided by Euroimmun Medizinische Labordiagnostika AG, was utilized.
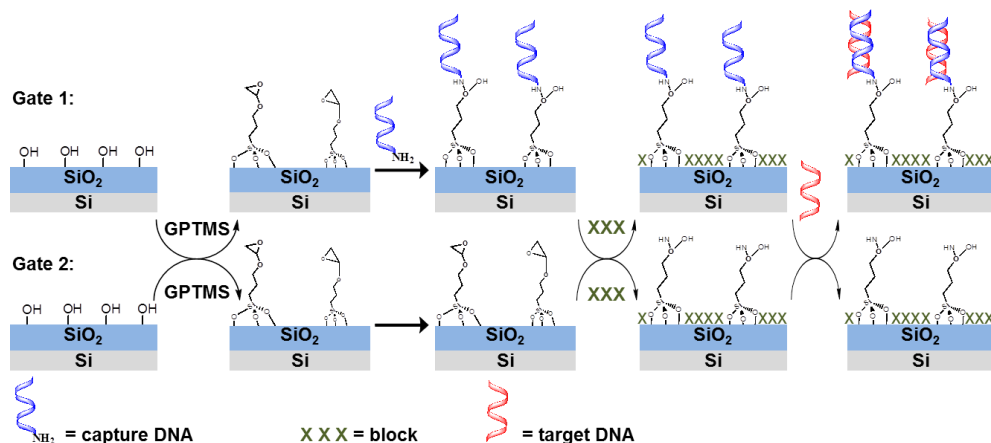
Figure 21: Schematic of the experimental procedure of the DNA assay.

The ssDNA was immobilized onto gate 1, whereas no capture molecules were bound to gate 2, which served as reference channel for the readout. Except for the precisely microspotting of the capture DNA, both gates were treated under the same conditions.

As already described in Chapter 2.2.4, the membrane-associated glycoprotein Human Leukocyte Antigen-B 27 (HLA-B27; B = isotype, 27 =variant) belongs to the major histocompatibility complex class 1 [105]. Since HLA-B27 triggers an immune reaction if a virus is resent, it plays an important role in the T-cell mediated immune reaction [105]. There are several auto immune diseases which are more likely to break out if people are carrier of the HLA-B27 allele: Morbus Bechterew [108,109], Morbus Reiter [111], psoriatic arthritis [112], juvenile idiopathic arthritis [113], uveitis [105], iritis [105], iridocyclitis [105] and schizophrenia [117]. Furthermore, it is important to perform a HLA typification before transplantations of bone marrow, organs and stem cells to avoid a transplant rejection [118–121]. The experimental procedure and the applied concentrations for the HLA-B 27 assay was the same as for the customized DNA assay in this thesis. HLA-B27 detection was done to prove a possible application of the SiNW FET platform for real patient monitoring.

3.6.2 Protein assay

The protein brain-derived neurotrophic factor (BDNF) was applied for the antibody-antigen experiments. This cytokine is important for various functions in the central nervous system. It was shown that BDNF is involved in the development of Parkinson's disease [68], Huntington's disease [78] and Alzheimer disease [83]. BDNF and the related clinical pictures are described in more detail in Chapter 2.1.3. The experimental procedure for the immune sensing experiments was very similar to the DNA assay. Mouse anti-human BDNF antibody (R&D Systems, Inc., USA) was immobilized onto the GPTMS modified gate surface with help of the microspotter. For this procedure, 1 µg/mL antibody was diluted in 150 mM phosphate buffer pH 8.5. The binding process was done overnight at 4 °C. To eliminate excess capture antibodies, the chip was carefully rinsed with 150 mM phosphate buffer pH 7.4, deionized water and 0.15 mM phosphate buffer pH 7.4. Free regions of the transistor gate were blocked by using either 5 % skimmed milk (Sigma Aldrich, Germany) or 1 % BSA, both diluted in 1× PBS. Blocking was done for 2 h, at room temperature. Afterwards, the chip was washed with 150 mM phosphate buffer pH 7.4, deionized water and 0.15 mM phosphate buffer pH 7.4. Four different concentrations of the target antigen BDNF (R&D Systems, Inc., USA) were added successively. In the beginning, the lowest concentration of 1 pg/mL (~ 35.7 fM) was applied, followed by 5 pg/mL (~ 178.5 fM), 10 pg/mL (~ 357 fM) and 50 pg/mL (~ 1785 fM). The binding proceeded for 2 h at room temperature. Finally, the chip was rinsed once more with the buffer mentioned above. Like before, the electronic readout was performed after each experimental step in the four differently concentrated phosphate buffers (0.15 mM, 1.5 mM, 15 mM and 150 mM; pH 7.4) and the received results of each channel were compared. An overview of all steps of the protein assay is shown in *Figure 22*. Fluorescence imaging was used to verify the successful antibody immobilization and antibody-antigen binding. To confirm the binding of the capture molecule, the Alexa Fluor® dye 488 goat anti-mouse (GAM 488) IgG antibody was used as a secondary antibody. The absorbance maximum of Alexa488 is reported to be 485 ± 11 nm. It emits green light with a wavelength of 530 ± 15 nm [192]. The incubation with the secondary antibody was performed after the blocking step in

the dark for 1 h, at room temperature. Unbound fluorescent molecules were rinsed away with 150 mM phosphate buffer pH 7.4 and deionized water.
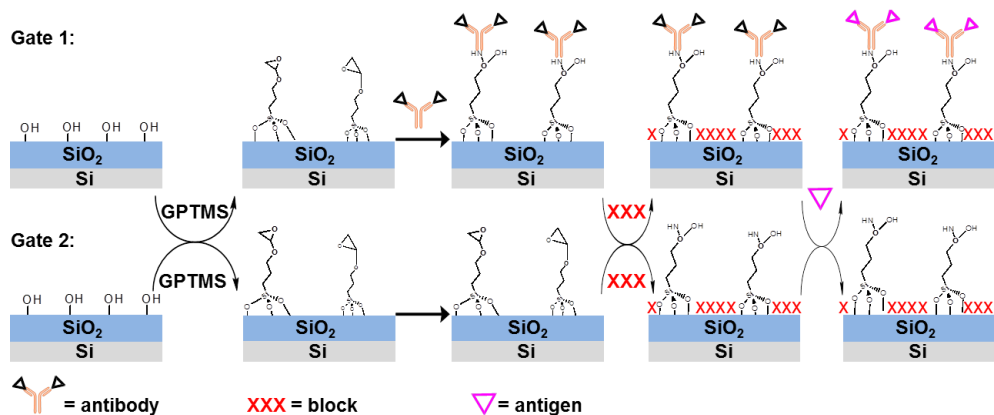
Figure 22: Schematic of the experimental procedure of the BDNF assay.

Here, the experimental steps of the antibody-antigen assay are shown in a schematic. Like for the DNA experiments, only on the upper sensor area capture antibody was immobilized whereas the lower sensor area served as reference sensors. Except for the immobilization, both areas were treated equally.

Fluorescence microscopy was performed with an inverted fluorescence microscope (Olympus IX50, Olympus Optical CO. (Europe), GmbH, Germany). To verify the BDNF binding to its capture antibody, 2 ng/mL BDNF (~ 71.8 pM) was bound to 2 µg/mL (~ 71.8 nM) BDNF antibody after having blocked the surface. The binding was performed for 2 h at room temperature. Then, 25 ng/mL biotinylated mouse anti-human BDNF detection antibody was attached for 2 h at room temperature. To be able to perform fluorescence microscopy, streptavidin-ALEXA 488 was bound for 30 min at room temperature.

3.7 Electronic readout system

As mentioned in the previous chapters, electronic measurements were done after each experimental step. Therefore, an FET amplifier system was used, which was already described more in details in previous reports [39,156,193,194]. The working principle of both, the ISFET and the SiNW FET readout system, was similar, whereas the resistance of the resistor in the transimpedance amplifier defining the amplification factor was different. In the

ISFET setup, a 10 kΩ resistor was built in. In contrast to that, a bigger resistor (500 kΩ) was integrated in the feedback loop of the transimpedance amplifier to measure the much smaller currents (µA range) of the SiNW FETs. Simultaneous measurements of up to 16 channels could be done with this amplifier setup. Furthermore, a differential readout with reference channels could be performed. The temperature of the FETs was precisely controlled to be 25 °C by a heating plate, which was incorporated in the system. This was important for stable and reproducible measurements since the temperature has an influence to the results since ISFETs and SiNW FETs are known to be temperature sensitive [20,29,195–197]. At high temperature, there is also the risk that proteins and DNA denaturize caused by the thermal effects on the secondary and tertiary structure of the proteins and the DNA double strand [198–201]. Measurements were done by using the front-gate mode, which can be established by applying a gate voltage *via* a liquid-junction Ag/AgCl reference electrode (DRIREF-2SH, World Precision Instruments, Inc., Germany) immersed into the buffer solution [157]. The reference electrode had to be kept in a stable position during the measurements to avoid an undesirable influence of the movement of the reference electrode on the measured data. Especially in diluted buffer solutions, even a slight movement could have caused a change in signal since the distance between reference electrode and gate influences the impedance signal and, hence, can also be applied for conductivity examinations of an electrolyte solution [54,202]. The front-gate readout was implemented with a fixed back-gate bias as described in [39,53,54,157]. As mentioned before, the transfer characteristic curves were measured after each experimental step in four different phosphate buffer concentrations (0.15 mM, 1.5 mM, 15 mM, 150 mM; pH7.4, respectively), starting from the lowest concentration. The pH value of all solutions was kept stable since the pH of the solution affects the obtained results [46,53,203–205]. Besides the pH, the Debye length and its corresponding screening effect inside the electrolyte solution also influences the received data [163,206].

3.7.1 DC readout: Transfer characteristic

The transfer characteristic (TC), also known as DC readout, is given by the drain-source current (I_{DS}) as a function of the front-gate voltage (V_{FG}) at a constant drain-source voltage (V_{DS}). By measuring the TC, the change of threshold voltage (V_{TH}) upon binding of charged molecules can be evaluated. Per definition, the threshold voltage is the minimum gate voltage, which needs to be applied to create a conducting channel between source and drain electrode [152]. For the ISFETs and the SiNW FETs, which can be treated as a long-channel version of an ISFET, the V_{TH} can be calculated by following equation [20]:

$$V_{TH} = E_{ref} - \psi_S + \chi_{sol} - \frac{\psi_{Si}}{q} - \frac{Q_{Ox} - Q_{SS}}{C_{Ox}} - \frac{Q_B}{C_{Ox}} + 2\phi_F \qquad (3.4)$$

with E_{ref} is the potential of the reference electrode, Ψ_S stands for the surface potential, χ_{sol} denotes the surface dipole potential of the solution at the gate oxide-electrolyte interface, Ψ_{Si} describes the silicon work function, q means the elementary charge, Q_{Ox} marks the fixed oxide charge, Q_{SS} represents the surface state density at the silicon surface, Q_B implies the depletion charge in silicon, C_{Ox} entails the capacitance of the gate oxide and Φ_F is the potential difference between the Fermi level in silicon between source and drain and Fermi level of the intrinsic silicon. Except the surface potential Ψ_S, all other terms of this equation are constant during an electrochemical measurement. Ψ_S is the only variable and is changed upon binding of charged molecules to the sensor surface, like DNA or proteins. In conclusion, the change in V_{TH} is proportional to the change in Ψ_S. Either an accumulation or depletion of hole carriers on the gate surface is obtained depending on the charge of the binding molecules. Negatively charged molecules lead to an accumulation whereas positive charges result in depletion of the hole carriers in a channel of a p-type FET. If positively charged molecules bind to a gate, Ψ_S is changed and, therefore, V_{TH} is shifted to lower values. The surface potential can be determined by changes in conductivity or capacity [16]. In 2009, it was shown in proof-of-principal experiments that this theory can be verified experimentally [53]. For this purpose, they used positively and negatively charged polyelectrolytes to assembly polyelectrolyte multilayers.
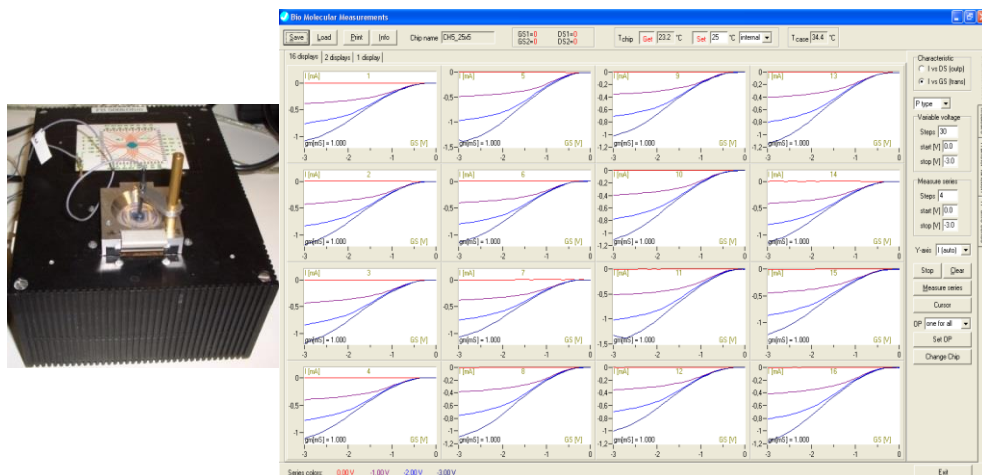
Figure 23: Measurement setup and exemplary TC readout.

In the left image, the amplifier system for SiNW FET can be seen. The measuring box for the ISFETs differs only in the feedback resistance of the integrated resistor. On the right, a characteristic measurement of an ISFET is displayed. The readout of 16 channels can be done simultaneously.

These experiments were repeated in the framework of this thesis to obtain a better understanding of the working principle. The corresponding results are shown in section 4.1.2.

3.7.2 AC readout: Transistor transfer function

The detection of the transistor transfer function (TTF) is another possibility to do the readout with the field-effect arrays. In doing so, the TC needs to be measured first to be able to set the working point at maximum transconductance (*Figure 24*) [207]. A stable voltage, v_{stim}, with a sinusoidal shape of 10 mV is applied at the reference electrode. After the application of a stimulus, the change in current response, ΔI_{DS}, can be recorded as TTF. The frequency recording was done from 1 Hz to 1 MHz. Molecule detection based on the TTF sensing was described in several publications even though the theory, on which the TTF relies, is still under discussion [32,33,208–213]. Per definition, the transfer function $H(\omega)$ is the mathematical representation between the input (v_{stim}) and the output signal (v_{out}) of a frequency-dependent system:

$$H(\omega) = \frac{v_{out}(\omega)}{v_{stim}(\omega)} \qquad\qquad (3.5)$$

The silicon nanowires are contacted and operated as long-channel ISFET devices.
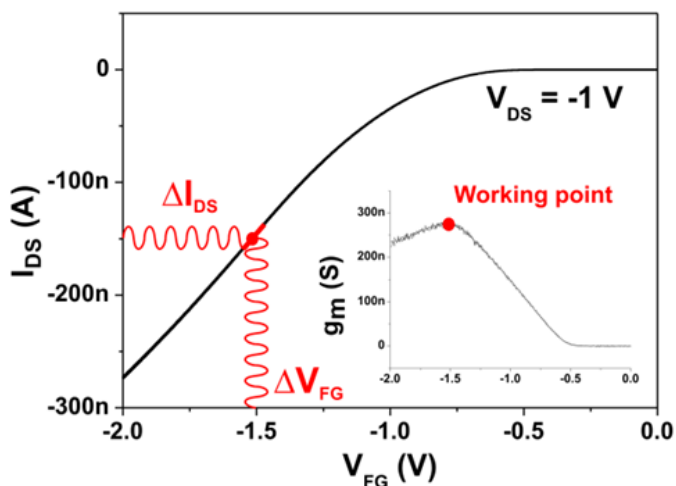
Figure 24: Determination of the working point.

In order to perform TTF measurements, the transfer characteristic needs to be recorded first to choose the working point at the highest transconductance g_m. The 16 channels of a SiNW FET are set to the same working point because of the common source of the channels. Picture published before in [207].

As reported previously, the impedance of the system is changed upon the attachment of molecules onto the gate surface. The impedance can be described in a first approximation by the capacitance C_{Bio} and the resistance R_{Bio}. In *Figure 25*, a simplified schematic of the equivalent circuit, with which the TTF of a SiNW FET can be described, can be seen. The capacitance and resistance are in parallel to each other [32,156,210,211,214]. Furthermore, in our more complicated model, the capacitance of the common source contact lines C_{CLCS} is in parallel to the capacitance of the drain contact line C_{CLD}. The capacitance of the oxide layer C_{Ox}, the resistance of the reference electrode R_{RE} and the resistance of the electrolyte solution R_{Sol} are in series to C_{Bio} and R_{Bio}. In general, the transconductance g_m of a field-effect transistor is defined as [215]:

$$g_m = \frac{\partial I_{DS}}{\partial V_{GS}} = \frac{i_{DS}}{v_{GS}}$$

(3.6)

with i_{DS} the small-signal drain-source current and v_{GS} the small-signal gate-source voltage. To define the TTF spectra, it is necessary to take the parasitic parameters C_{CLCS} and C_{CLD} into account [216,217]. This can be done by following equation, in which the contact line capacitance C is evaluated from the size of the non-encapsulated chip area and the chip design

$$C = \frac{\varepsilon_0 \varepsilon_{SiO_2} A}{d}$$

(3.7)

where ε_0 is the electric constant, ε_{SiO2} means the relative permittivity of SiO_2, A stands for the area of the passivation layer and d represents the thickness of the SiO_2 passivation layer. The small-signal output voltage v_{out} can be calculated by:

$$v_{out} = -R i_{DS} = -H(\omega) v_{GS}$$

(3.8)

Due to binding of biomolecules, like *e.g.* DNA, on the transistor gate, *i.e.* the nanowire, the impedance of the sensor is changed and the transconductance becomes frequency-dependent [156,215]. The TTF for the simplified circuit is given by:

$$H(j\omega) = \frac{1 + j\omega R_{Mem} C_{Mem}}{1 + j\omega R_{Mem}(C_{Mem} + C_{Ox})}$$

(3.9)

with j standing for the imaginary unit, ω being the angular frequency and R_{Mem} and C_{Mem} the resistance and the capacitance of the molecule membrane, respectively. As previously shown by Bergveld et al. [215], the two time constants τ_1 and τ_2 can be evaluated from the idealized theoretical transfer function H(jω):

$$\tau_1 = R_{Bio}(C_{Bio} + C_{Ox}) = \tau_2 + R_{Bio} C_{Ox}$$

(3.10)

$$\tau_2 = R_{BIO} C_{Bio}$$

(3.11)

with T_2 representing the relaxation time of the biomolecule.
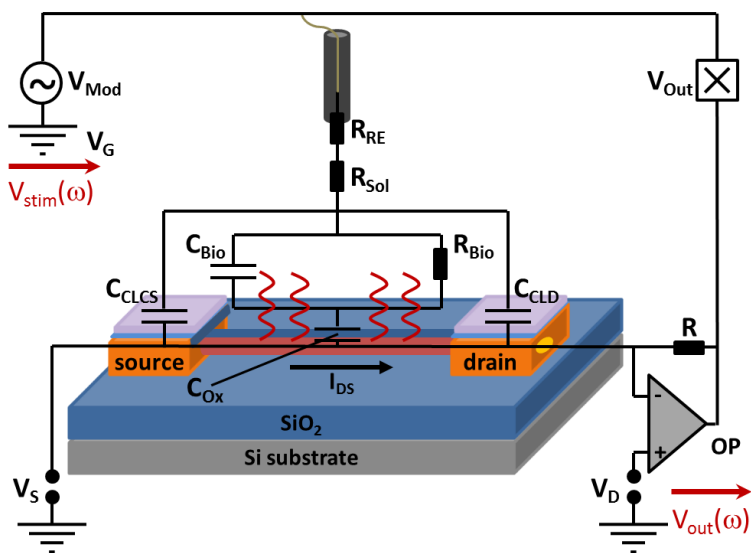
Figure 25: Electronic circuit to explain the TTF.

Here, a simplified schematic of the SiNW FET is shown. With the corresponding electronic circuit, the TTF method can be explained. A constant voltage (V_G) is applied at the front-gate. The capture molecules, described as capacitance (C_{Bio}) and resistance (R_{Bio}), are directly attached to the nanowire surface. When the target molecules bind to the capture molecules, the impedance of the system changes which leads to a change in the TTF curve. Picture taken from [207]*.*

In *Figure 26 a*, it is shown how the very simplified TTF looks in theory. The left curve shows the TF for a bare device and the right curve after having attached biomolecules. The shift between these two curves can be described by the cut-off frequency, which depends on the solution and the density of the biomolecules. From the cut-off frequency, it is possible to estimate the concentration of the biomolecules [33][210]. The shape of the real TTF curve, recorded by our system, depends on additional parameters like the reference electrode resistance R_{RE}, the solution resistance R_{Sol}, the capacitances of the contact lines (C_{CLCS}, C_{CLD}) and of the gate oxide C_{Ox} (*Figure 26 b*). PSPICE modeling of ISFETs was done for TTF measurements of cells [218]. In previous publication, a PSPICE model was used to describe the TTF spectra of the applied SiNW FETs [217]. The parasitic parameters and the operational amplifier influence the TTF spectra. Since the g_m value of a SiNW FET is smaller than that of an ISFET, the TTF spectra of the nanowire devices are different compared to

the microscale FETs [216,219]. In *Figure 26 b*, it is visible that a peak-like increase or decrease at elevated frequencies is recorded in the TTF measurements of the utilized SiNW devices.
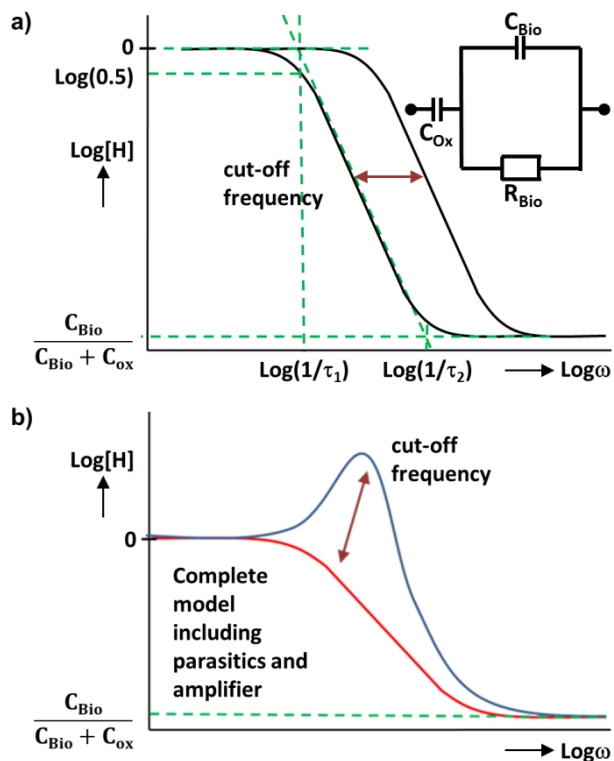
Figure 26: The theoretical and the real TTF curve.

In (a), a simplified electronic circuit to explain the TTF method is shown. It is further displayed how the TTF of this simplified circuit not including the contact lines would look in theory. The left and right curves are without and with attached biomolecules, respectively. The picture is adapted from [211]. In (b), a real TTF recording is shown in which reference electrode resistance R_{RE}, solution resistance R_{Sol}, capacitances of the contact lines (C_{CSCL}, C_{CLD}) and the frequency bandwidth of the transimpedance amplifier influence the result. In contrast to the theoretical TTF spectra, a peak-like decrease or increase of the TTF amplitude at elevated frequencies can be recognized. This decrease or increase is affected by the impedance of the biomolecule layer. Figures published in [207].

In the frequency range of 50 – 800 kHz, variations of the TTF spectra are noticeable, which are caused by the amplifier design and its bandpass characteristics as well as by the large parasitic values of the contact lines of the

nanowire platform [207]. In order to be able to derive conclusions about the TTF behavior, the TTF amplitudes of the different experimental steps were compared at a frequency of 100 kHz.

Chapter 4 – Proof-of-principle experiments

Before establishing assays on the SiNW platform, initial measurements were done to study how the sensors behave under different conditions. This should also help for a better understanding of the working principle of the biosensors. For this purpose, pH measurements were performed on the silicon nanowire field-effect transistors. The aim was to display the change in V_{TH} upon increasing the pH value of the buffer solution by detecting the transfer characteristic (TC) of the sensor. In a second set of experiments, conductivity recordings were done in different concentrated buffer solution. This was done to identify how the ionic strength of the applied test liquid is affecting the obtained results. In doing so, the impedimetric readout method by measuring the transistor transfer function (TTF) was evaluated for micro- and nanoscaled transistors. Moreover, polyelectrolyte multilayers were built up on our readout platform. The objective of these experiments was to work out how the TC and the TTF evolve after successive binding of positively charged and negatively charged biomolecules and to investigate if the charge influences the TTF as well.

4.1 pH sensing

The sensing of variations in pH attracted a lot of attention in the last decades, since it can be used in biomedical applications to monitor biochemical reactions. There are assays with which bacteria [220] or viruses [46] can be determined by measuring variations in pH. The detection of pH changes is also used in agriculture and for environmental purposes [221]. In framework of this thesis, pH measurements were performed as proof-of-principle experiments to gain an in-depth understanding of the behavior and working principle of the applied SiNW FETs. The main advantage of using SiNW FET in contrast to the larger ISFETs is their small size enabling measurements even underneath single cells and their low µW power range.

In initial tests, pH sensing was done on cleaned SiNW FETs to analyze how the transfer characteristics behave upon the addition of buffer solutions with increasing pH value. For this purpose, six phosphate buffer solutions with

different pH values were used on p-type SiNW FETs. The surface of the nanowire devices was firstly cleaned like described in Chapter 3.4. After that, the measurements were started by adding a solution with a pH value of 4.5. The pH was successively increased to 5.0, 6.0, 7.0, 8.0 and 9.0. The chip was cleaned with the subsequent pH solution in between each experimental step. The TC was measured after the addition of each pH solution. In our measurement setup, a stable liquid-junction Ag/AgCl reference electrode was used to bias the SiNW FET. The change in proton concentration, contained in the electrolyte solution, changes the protonation level of the surface groups. This results in a charge accumulation in the transistor channel, which changes the threshold voltage of the sensor [222]. One exemplary measurement at V_{DS} = -3 V in linear scale is displayed in *Figure 27*.
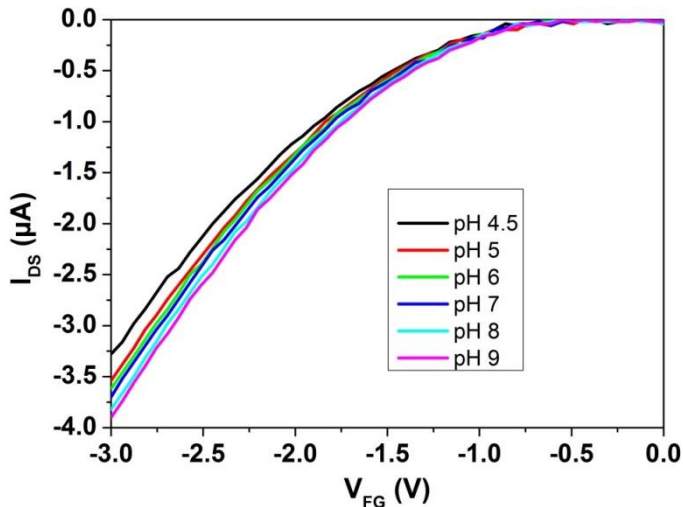
Figure 27: pH dependent TC measurements.
Change of the TC caused by different pH values at V_{DS} = −3 V. The transfer characteristic is shifted to more positive values (from left to the right) due to an increase in negative charge on the sensor surface. This is caused by the release of protons from the hydroxyl groups on top of the device into the bulk solution.

An increasing pH value leads to a shift of the voltage to more positive values. The reason for this is a change of the charges on the sensor's surface at the oxide-electrolyte interface, which leads to a shift of the flatband voltage within the transistor [54]. As described in paragraph 2.4.3, the surface of the field-effect sensor is made of silicon dioxide. If the SiO_2 surface gets into contact with

aqueous solutions, like the phosphate buffer solution, silanol groups (Si-OH) are built up [223] and, hence, hydroxyl groups are formed on top of the silicon dioxide layer. The hydroxyl groups at the oxide surface are amphoteric groups, which means that can be protonated and deprotonated, which leads to pH dependent changes of the surface potential [224]. In consequence, an equilibrium between hydroxyl groups on the device and the hydrogen ions of the bulk solution exists [54,166,167]. As already mentioned, the SiNW FETs can be considered as nanoscale ISFETs [154] and, hence, the same equation as for the microscale devices can be taken into account [225]. With the site-binding model, the principle of the pH sensitivity of oxide-terminated surface can be described [167]. This model was later on transferred onto ISFETs [226,227]. The threshold voltage V_{TH} of both devices is given by

$$V_{TH} = V_0 - \psi_S \tag{4.1}$$

with ψ as the surface potential of the transistor and V_0 as constant voltage. The change in surface potential can be calculated as follows

$$\Delta\psi_S = 2.3\alpha\frac{k_bT}{q}\Delta pH_{Bulk} \tag{4.2}$$

Here, α is the sensitivity factor and q the ionic charge, T the temperature in Kelvin and k_b the Boltzmann constant. The change in surface potential of a SiO_2 substrate as a function of the pH change is depending on its surface groups, the ionic strength and the composition of the applied buffer [161]. For an ideal oxide surface with a sensitivity factor $\alpha = 1$, a maximum sensitivity at room temperature can be assumed

$$\frac{\Delta\psi_S}{\Delta pH_{Bulk}} = -2.3\alpha\frac{k_bT}{q} \approx 60mV \tag{4.3}$$

with Nernstian behavior. However, as shown in previous examination, silicon dioxide is not an ideal pH sensing surface in comparison to Ta_2O_5, which possesses almost Nernstian characteristics [53]. Furthermore, silicon dioxide displays a large hysteresis compared to other gate oxides like Si_3N_4, Al_2O_3 or the already mentioned Ta_2O_5 [227,228]. For silicon dioxide surfaces, it is well known

that point of zero charge (PZC), at which the net surface charge is zero, is at pH_{PZC} 2.2 [205]. PZC can be calculated with the following equation

$$pH_{PZC} = \frac{pK_a + pK_b}{2} \quad \text{with} \quad pK_a = -\log K_a \text{ and } pK_b = -\log K_b \quad (4.4)$$

where K_a and K_b are dimensionless dissociation constants for acids or bases. At pH values higher than the pH_{PZC}, the silicon dioxide surface becomes negative. This means that upon increasing the pH value in the solution, the hydroxyl groups start to release hydrogen ions, *i.e.* protons, to the solution [205]. Therefore, the surface of the nanowire platform gets more negatively charged. The higher the pH value of the introduced solution, the more protons are released from the hydroxyl surface and the more negative charges are available at the FET surface. This induces a change in the surface potential and a shift in threshold voltage [54]. The change in surface charge at the oxide-electrolyte interface influences the change of the surface potential, which can be calculated by the Grahame equation (2.17). This leads to a change in flatband voltage of the device, which results in a shift of the transistor's transfer characteristic upon pH variation [54]. In *Figure 27*, the shift of the transfer characteristic and the corresponding shift of the threshold voltage of a p-type nanowire transistor caused by pH changes are displayed. By increasing the pH value of the solution, the flatband voltage of the device is shifted to higher voltages. In case of p-channel FETs, the V_{FG} is negative which induces a depletion of charge carriers in the nanowire channel upon increasing the pH [54]. By calculating the change in mV/pH, the sensitivity of a sensor can be determined which describes the signal change caused by a variation of the pH value. The sensitivity of the devices used in this thesis, was calculated to be only 34 mV/pH, which corresponds to an α-value of 0.57. This value is slightly lower than usually reported for surfaces made of SiO_2 [166]. As reported by Bousse already in 1982, impurities, like dust or dirt particles, influence the sensitivity towards pH changes [229]. Due to the fact that no fresh sensors were used for these basic experiments, this result is in good agreement with the sensitivity of 30 – 40 mV/pH reported earlier [229]. Due to the lack of new fabricated sensors, the pH measurements were performed on SiNW FETs, which were already applied in previous biomolecular experiments. Furthermore, the pH measurements were performed on the bare

SiO_2 surface without any modification. In a previous publication, in which the same type of chips was used, a sensitivity of new SiNW FETs of 41 mV/pH with an α value of 0.69 was reported [53]. Like mentioned there, the sensor, nevertheless, showed the typical p-type behavior upon changing the pH value of a buffer solution.

To increase the sensor's sensitivity to pH changes, it is possible to modify the surface by performing silanization before measuring the pH. In several publications, it was shown that the surface modification with the amino siloxane (3-aminopropyl)triethoxysilane (APTES) leads to a higher sensitivity to pH changes in the electrolyte solution [230–232]. This can be explained by the possibility to undergo protonation and deprotonation of the amino group in dependence of the pH at the sensor surface. Furthermore, amino ($-NH_2$) and silanol ($-SiOH$) groups are available on the surface after APTES silanization. Both groups possess different dissociation constants [231]. As described by Cui et al., the $-SiOH$ groups are deprotonated to SiO^- at high pH values. This leads to an accumulation of hole carriers in the p-type transistor and to a shift of V_{TH} to lower values. The amino group is protonated to $-NH_3^+$ at low pH values, which is accompanied by a depletion of hole carriers [231].

4.2 Conductivity measurements

Conductivity measurements were performed to test the influence of the ionic strength of an applied buffer solution on the shape of the TTF. The same experiments were done on ISFETs and on SiNW FETs (*Figure 28*). The influence of the ionic strength onto the TTF measurements is described in a subsequent chapter. For this kind of experiments, four differently concentrated phosphate buffer solutions were prepared. The TTF measurements were started with 0.15 mM phosphate buffer. The buffer concentration was increased by a magnitude of 10 till a maximum concentration of 150 mM was reached. In between the measurements, the chip was carefully rinsed with the buffer, in which it was measured in the following step. In *Figure 28*, two exemplary TTF readouts of the four buffer solutions can be seen. The measurements in *Figure 28 a* were done on an ISFET and in *Figure 28 b* on a SiNW FET. The shift in TTF is in good agreement with what was published in literature before [54,179,202]. By evaluating the cut-off frequency, it was clearly visible that it is shifted to higher

frequencies with increasing buffer concentration. This is caused by a change in resistance which is lower in solutions with high ionic strength [202]. The shift of the cut-off frequency can be observed for the nano- and the microscaled devices.
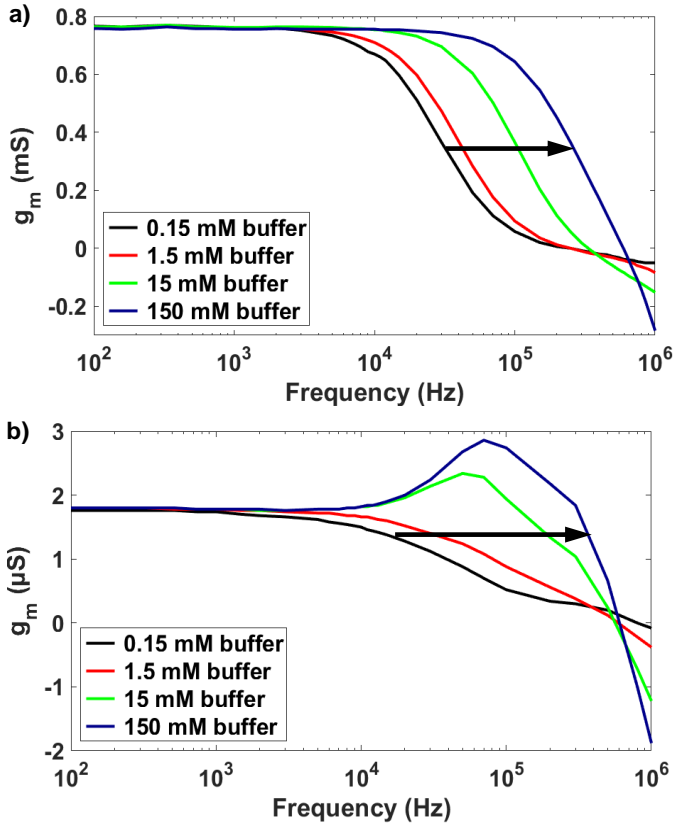
Figure 28: Exemplary transistor transfer function of conductivity measurements. *The TTF was measured in four different buffer concentrations on an ISFET and a SiNW FET. The buffer has different conductivity values, which varied by a factor of 10, respectively. The arrows in (a) and (b) indicate the direction of increasing ionic strength. In (a), the conductivity measurements performed on an ISFET are shown, in (b), the results for the nanowire device is displayed.*

However, it is more pronounced for the ISFETs, since the TTF curves measured on the SiNW FETs mostly had this bump characteristic at a frequency of around 10 kHz. This bump is most likely caused by the operational amplifier of the readout system in combination with parasitic parts of the chip such as contact line capacitance and resistance [217].

4.3 Assembly of polyelectrolyte multilayers

Another set of initial experiments was performed to gain further information and understanding about the working principle of the nanowire transistors. Besides pH measurements, the assembly of polyelectrolyte multilayers was performed to investigate the behavior of the field-effect transistor upon binding of positively and negatively charged molecules. Per definition, polyelectrolytes are polymers which possess chargeable groups [181]. These polymers release counterions due to dissociation which is caused by solving them in *e.g.* water and which results in a charged chain inside the polyelectrolyte [181]. These experiments were performed on ISFETs and on SiNW FETs for comparison.

4.3.1 DC readout of polyelectrolyte multilayers on ISFETs

The sensors were cleaned with Piranha solution as described in Chapter 3.4 prior the incubation with the first polyelectrolyte solutions. By doing layer-to-layer adsorption, the sensor was alternately incubated with positively and negatively charged polyelectrolytes. The silicon dioxide surface is negatively charged at a pH higher than 3.5. In consequence, it is feasible to first electrostatically bind positively charged molecules on top of the surface to which a polyelectrolyte with negative charged can be adsorbed [233]. For this purpose, the cationic poly(allylamine hydrochloride) (PAH) and the anionic poly(sodium 4-styrene sulfonate) (PSS) were applied. When dissolved in water, the negatively charged PSS is completely charged over a wide range of pH [234,235] whereas PAH is only charged at neutral and acidic pH values. At a pH above 10, it becomes neutral [234,235]. The assembly of the polyelectrolyte multilayers was performed in 10 mM phosphate buffer pH 5.5, while the measurements were done in four differently concentrated phosphate buffer solutions (0.15 mM, 1.5 mM, 15 mM, 150 mM). In between the different experimental steps, the transistors were cleaned thoroughly with deionized water to eliminate excess polyelectrolytes, unspecifically bound to the sensor surface.

It is known that the conformation and the adsorption strength of the polyelectrolyte are depending on the salt concentration in the buffer solution [171]. As reported in previous publications, the polyelectrolytes exhibit a linear, stretched conformation when dissolved in buffers with low ionic strength [17]. In

higher salt concentrations, where the Debye length is relatively small, the polyelectrolytes are coiling up because their charges are screened by the counterions from the buffer solution [171]. This means that the thickness of the polyelectrolyte layer depends strongly on the ionic strength of the applied buffer solution [233,236]. At low buffer concentrations of around 6 mM, the thickness of either a single PAH or PSS layer is assumed to be around 0.5 nm according to literature [17,237]. Because of the Debye screening effect, a decrease in signal strength is expected upon assembly of polyelectrolyte multilayers. The signal strength is depending on the distance to the sensor surface. This relies on the shielding effect of the biomolecule charges by counterions in the buffer solution. The Debye screening length is given by

$$\lambda_D = \sqrt{\frac{\varepsilon \varepsilon_0 k_b T}{2 N_A e^2 l}} \tag{4.5}$$

where ε is the dielectric constant of the bulk solution, ε_0 is the dielectric constant in vacuum, k_b and N_A are the Boltzmann and Avogadro constant, respectively, e is the elementary charge and l is the ionic strength [171]. Since the measurements were conducted in phosphate buffer solutions with ionic strengths of 0.15 mM, 1.5 mM, 15 mM and 150 mM, Debye lengths of approximately 17 nm, 7.5 nm, 2.5 nm and 0.75 nm resulted according to equation 4.5, respectively. The assembly of the polyelectrolyte multilayers was monitored by measuring the TC and the change in threshold voltage after each polyelectrolyte deposition. Besides that, the transistor transfer function was recorded as well to analyze whether charges also have an influence on this readout mode. An exemplary DC readout of the assembly of the polyelectrolyte multilayer on ISFETs can be seen in *Figure 29*. It is one exemplary result for the measurement performed in 0.15 mM buffer at V_{DS} = -3 V. Eight polyelectrolyte layers were assembled in total onto the cleaned chip and the positively charged PAH and the negatively charged PSS were alternately adsorbed. The following TC curves are displayed in *Figure 29*: cleaned chip (black curve), first polyelectrolyte layer (PAH; red curve), second layer (PSS; light green curve), third layer (PAH; dark blue curve), fourth layer (PSS; light blue curve), fifth layer (PAH; pink curve), sixth layer (PSS; purple curve), seventh layer (PAH; dark green curve) and eighth layer (PSS; grey curve).
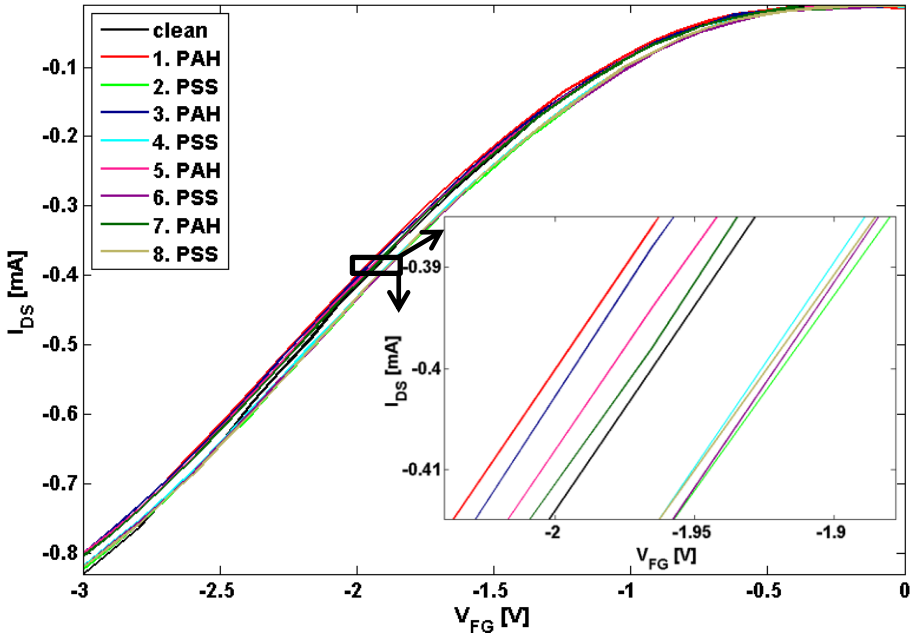
Figure 29: Exemplary TC measurements of polyelectrolyte multilayers on ISFETs.
These exemplary results were measured in 0.15 mM phosphate buffer at V_{DS} = -3 V. After having cleaned the chip (black line), the polyelectrolyte multilayers were assembled as follows: first layer PAH (red), second layer PSS (light green), third layer PAH (dark blue), fourth layer PSS (light blue), fifth layer PAH (pink), sixth layer PSS (purple), seventh layer PAH (dark green) and, finally, eighth layer PSS (grey). The inset, the magnification of the curve is shown.

For all four buffer concentrations, which were used on the microscaled device, the same effects were observed: The adsorption of the positively charged PAH charged lead to a shift of the TC to lower voltages, whereas the incubation with the negatively charged PSS shifted the TC to more positive values. This observation agrees with published data [17]. In *Figure 30*, the evaluated TC results for the change in the front gate voltage, ΔV_{FG}, are shown. The corresponding mean values of each polyelectrolyte layer and the number of experiments (n) can be taken from *Table 3*. As can be seen by the evaluation, there is the tendency that the signal strength decreases with increasing buffer concentration which is in agreement with the already mentioned Debye screening effect.
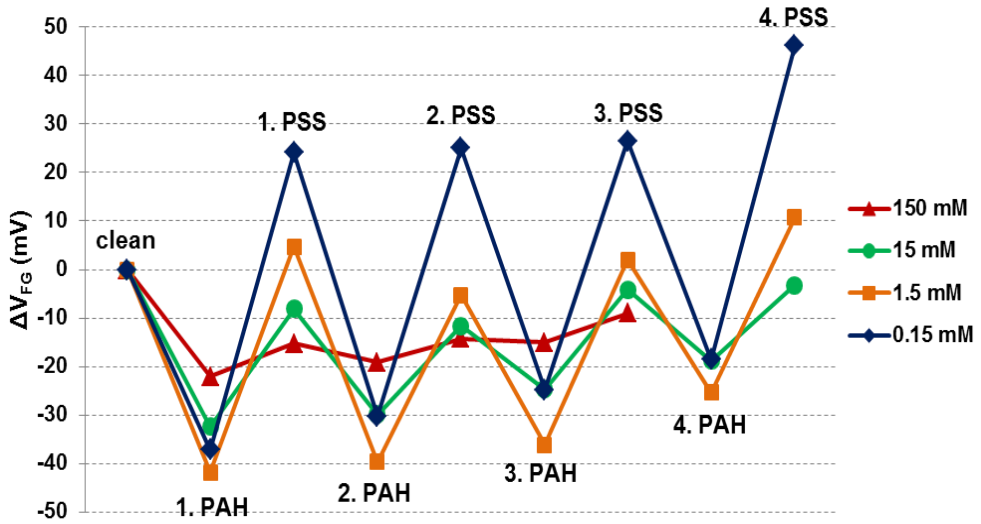
Figure 30: Assembly of polyelectrolyte multilayers on ISFETs - ΔV_{FG} evaluation.
In this figure, the exemplary ΔV_{FG} results of the polyelectrolyte assembly for all four buffer concentrations can be seen. For the calculation of ΔV_{FG}, the results measured for the clean chip are taken as baseline.

In 150 mM buffer, the 4th layer of PAH and PSS, meaning layers seven and eight, were not detectable anymore. For the other buffer concentrations, both layers were still measurable. According to literature, the signal strength should decrease with increasing number of layers. This effect could not be clearly verified within these proof-of-principle experiments. One reason might be that the mean values for several chips are demonstrated in *Figure 30* and *Table 3*. Another explanation could be that only eight layers in total were adsorbed to the chip surface. It was not tested how many layers would have been detectable with our sensors.

	150 mM buffer	15 mM buffer	1.5 mM buffer	0.15 mM buffer
clean	0 mV	0 mV	0 mV	0 mV
1st layer (PAH)	- 22.1 mV (n= 3, 27 chan)	- 32.4 mV (n= 4, 47 chan)	- 41.9 mV (n= 4, 47 chan)	- 37.2 mV (n= 4, 47 chan)
2nd layer (PSS)	6.8 mV (n= 3, 27 chan)	24.3 mV (n= 4, 47 chan)	46.6 mV (n= 4, 47 chan)	61.3 mV (n= 4, 47 chan)
3rd layer (PAH)	- 3.8 mV (n= 3, 27 chan)	- 21.8 mV (n= 4, 47 chan)	- 44.4 mV (n= 4, 47 chan)	- 54.4 mV (n= 4, 47 chan)
4th layer (PSS)	4.8 mV (n= 3, 27 chan)	18.3 mV (n= 4, 47 chan)	34.5 mV (n= 4, 47 chan)	55.3 mV (n= 4, 47 chan)
5th layer (PAH)	- 0.7 mV (n= 3, 27 chan)	- 13 mV (n= 4, 47 chan)	- 30.9 mV (n= 4, 47 chan)	- 49.9 mV (n= 4, 47 chan)
6th layer (PSS)	6.0 mV (n= 3, 27 chan)	20.6 mV (n= 4, 47 chan)	38.2 mV (n= 4, 47 chan)	51.3 mV (n= 4, 47 chan)
7th layer (PAH)	not detectable	- 14.6 mV (n= 3, 34 chan)	- 27.5 mV (n= 3, 34 chan)	- 45.1 mV (n= 3, 34 chan)
8th layer (PSS)	not detectable	15.5 mV (n= 3, 24 chan)	36.2 mV (n= 3, 24 chan)	64.7 mV (n= 3, 24 chan)

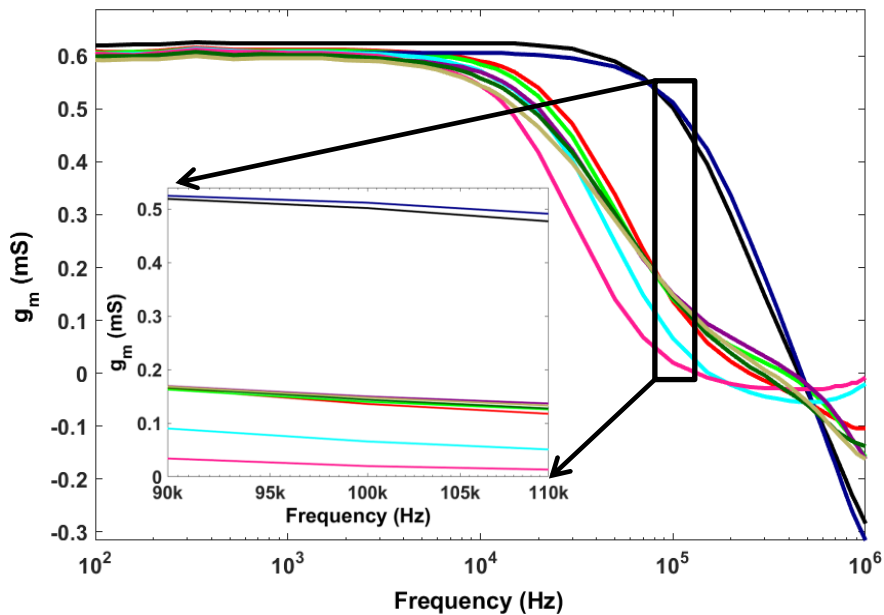**Table 3: Assembly of polyelectrolyte multilayers on ISFETs – mean ΔV_{FG} values.**
The mean values of the change in threshold voltage for the microscaled devices are displayed in this table. Furthermore, the number of experiments and the total number of measured channels (chan) are written in brackets.

These experiments only served for a better understanding of the sensors upon binding of charged molecules. Furthermore, the intention was to examine how the different buffer concentrations influence the signal strength.

4.3.2 DC readout of polyelectrolyte multilayers on SiNW FETs

The same polyelectrolyte experiments were performed on the nanoscaled transistors. SiNW FET devices with different nanowire size and different numbers

of nanowires per channel were used in framework of these experiments. Assembling the polyelectrolyte multilayers was conducted under the same experimental conditions: Eight polyelectrolyte layers were adsorbed onto the cleaned nanowires and the measurements were performed in four different buffer concentrations, *i.e.* 0.15 mM, 1.5 mM, 15 mM and 150 mM phosphate buffer. In *Figure 31*, an exemplary TC result of the assembly of polyelectrolyte multilayers is represented.
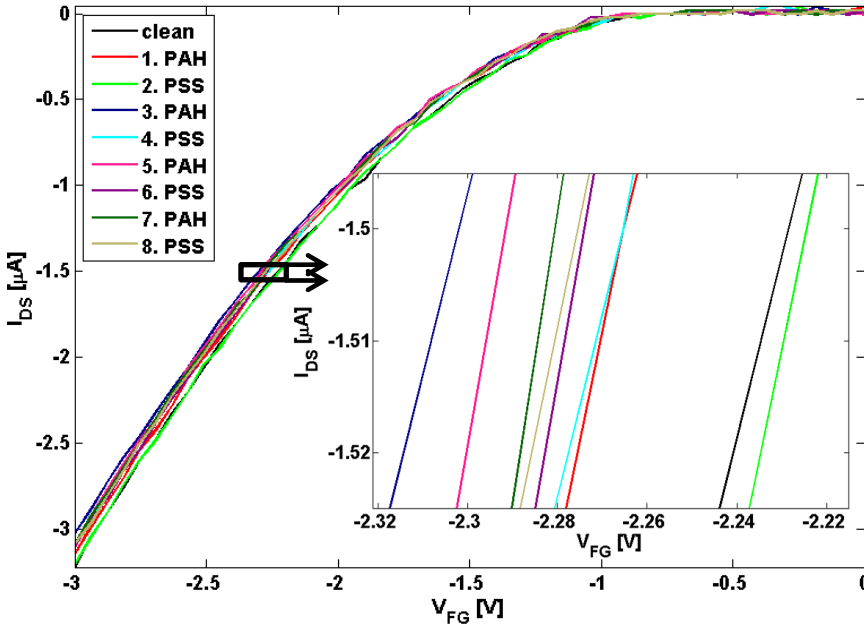
Figure 31: Exemplary TC readout of polyelectrolyte multilayers on SiNW FETs.

The measurement was performed in 0.15 mM phosphate buffer pH 7.0 at V_{DS} =-3 V. The black TC curve was measured after having cleaned the device. The polyelectrolytes were alternatingly adsorbed onto the chip to obtain eight multilayers in total. The adsorption was started with PAH (first layer; red curve) followed by a PSS layer (second layer; light green curve). Layer three (PAH; dark blue), four (PSS; light blue), five (PAH; pink), six (PSS; purple), seven (PAH; dark green) and eight (PSS; grey) were added successively.

The displayed measurements were done in 0.15 mM phosphate buffer pH 7.0 at V_{DS} = -3 V. In the right lower inset, a magnification of this exemplary readout is shown to obtain a better overview of the V_{TH} change after each experimental step. As shown in *Figure 29* for the ISFETs, the black TC curve was measured after cleaning of the chip. Then, the transistor was alternately modified with four

layers of PAH and of PSS, respectively, to obtain eight polyelectrolyte layers (first layer – 1. PAH (red curve), second layer – 1. PSS (light green), third layer – 2. PAH (dark blue), fourth layer – PSS (light blue), fifth layer – 3. PAH (pink), sixth layer – 3. PSS (purple), seventh layer – 4. PAH (dark green) and eighth layer – PSS (grey)). The same observation was made as with the microscaled transistors: The adsorption of the positively charged PAH polyelectrolyte led to a change of the flatband voltage to lower V_{FG} values, whereas the addition of the negative PSS molecules shifted the TC back to higher V_{FG} values. These results are in agreement with previous studies [53,54]. In *Figure 32*, the ΔV_{FG} results for the assembly of polyelectrolyte multilayers on SiNW FETs are represented.
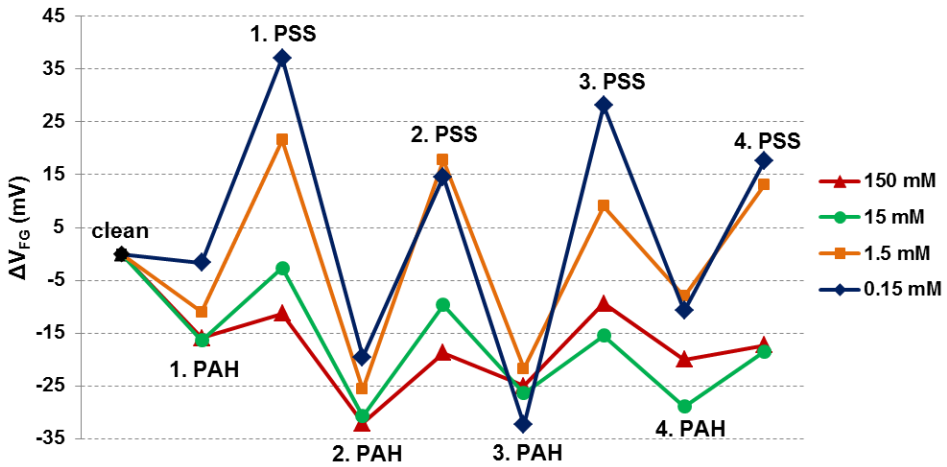
Figure 32: Assembly of polyelectrolyte multilayers on SiNW FETs - ΔV_{FG} evaluation.

To draw conclusions about the assembly of polyelectrolyte multilayers, ΔV_{FG} was evaluated for all four buffer concentrations. Therefore, the results measured for the clean chip served as baseline.

For this evaluation, several experiments were compared and the corresponding mean values, the number of experiments as well as the associated number of channels can be taken from *Table 4*. As mentioned before, nanoscaled devices with different nanowire dimensions and different numbers of nanowires per channel were used and, finally, compared. Since the obtained signal is also depending on the wire dimensions and the amount of wires per channel, there is only the tendency that the signal intensity decreases with increasing number of polyelectrolyte layers and increasing thickness of the biomolecule layer.

However, this tendency is in agreement with previous publications [183,184]. Furthermore, it is preferable to use freshly encapsulated chips, which were not used for any experiments before, to ensure that no remaining biomolecules from previous trials are present on the surface.

	150 mM buffer	15 mM buffer	1.5 mM buffer	0.15 mM buffer
clean	0 mV	0 mV	0 mV	0 mV
1st layer (PAH)	-16.0 mV (n= 6, 34 chan)	-16.4 mV (n= 7, 65 chan)	-11.1 mV (n= 7, 65 chan)	-1.6 mV (n= 7, 71 chan)
2nd layer (PSS)	4.7 mV (n= 6, 34 chan)	13.7 mV (n= 7, 65 chan)	32.7 mV (n= 7, 65 chan)	38.7 mV (n= 7, 71 chan)
3rd layer (PAH)	-20.8 mV (n= 6, 34 chan)	-28.1 mV (n= 7, 65 chan)	-47.3 mV (n= 7, 65 chan)	-56.7 mV (n= 7, 71 chan)
4th layer (PSS)	13.3 mV (n= 6, 34 chan)	21.1 mV (n= 7, 65 chan)	43.5 mV (n= 7, 65 chan)	34.3 mV (n= 7, 71 chan)
5th layer (PAH)	-6.2 mV (n= 2, 9 chan)	-16.7mV (n= 5, 53 chan)	-40.5 mV (n= 5, 53 chan)	-47.0 mV (n= 5, 55 chan)
6th layer (PSS)	15.6 mV (n= 2, 9 chan)	10.9 mV (n= 5, 53 chan)	-30.8 mV (n= 5, 53 chan)	60.5 mV (n= 5, 55 chan)
7th layer (PAH)	-10.6 mV (n= 2, 9 chan)	- 13.5 mV (n= 2, 23 chan)	- 17.1 mV (n= 5, 53 chan)	-38.9 mV (n= 5, 55 chan)
8th layer (PSS)	2.7 mV (n= 2, 9 chan)	10.5 mV (n= 2, 23 chan)	21.2 mV (n= 5, 53 chan)	28.5 mV (n= 5, 55 chan)

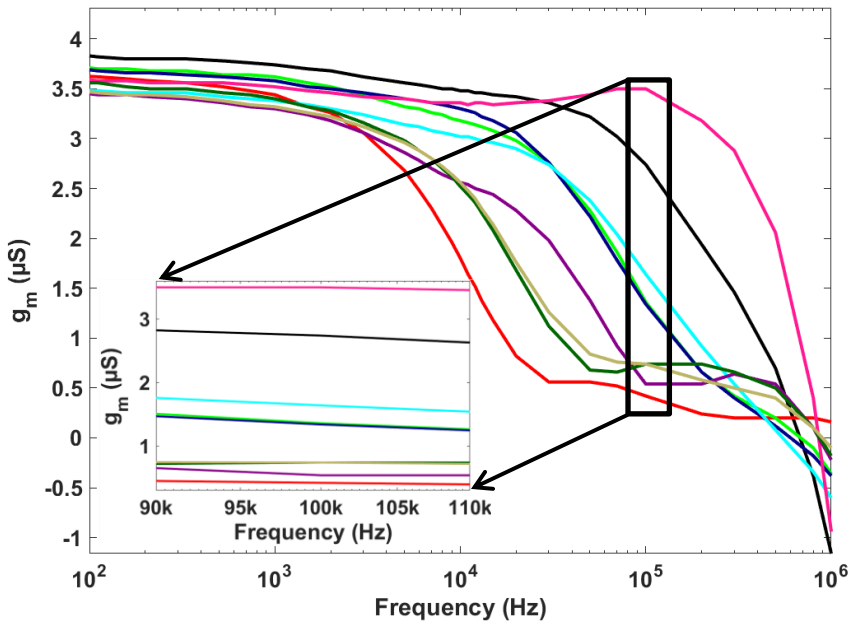**Table 4: Assembly of polyelectrolyte multilayers on SiNW FETs – mean ΔV_{FG} values.**

In this table, an overview of ΔV_{FG} caused by the assembly of polyelectrolyte multilayers in different buffer concentrations is given. The experiments were implemented on SiNW FETs.

To really examine this effect and to derive a final conclusion, more polyelectrolyte layers would have been needed to find out how many layers can be detected in which buffer concentration. As already mentioned these

experiments served as initial trials to gain more information about the difference of the signal strength in the different concentrated buffers. There is a clear tendency that the signal is more pronounced in lower buffer concentrations as in high-concentrated solutions.

4.3.3 AC readout of polyelectrolyte multilayers on ISFETs

Besides measuring the change in threshold voltage upon binding of the charged molecules, the change in transconductance, Δg_m, was also detected. For this purpose, the transistor transfer function (TTF) was recorded by performing the AC readout. This was done for both, the ISFETs and the SiNW FETs, to examine if the charge of the molecules influences the TTF and the Δg_m. In *Figure 33*, an exemplary TTF measurement of the assembly of polyelectrolyte multilayers on an ISFET device is displayed.

Figure 33: Exemplary TTF readout of polyelectrolyte multilayers on ISFETs.
Here, an exemplary ac readout of polyelectrolyte multilayers is represented. The measurement was done right after the TC detection and the determination of the respective working point. The TTF was measured after each experimental step, which means after leaning and after depositing of eight polyelectrolyte layers.

For the evaluation of the TTF curves, no suitable model was available. Therefore,

a certain frequency range was examined and analyzed to derive conclusions about the measurements. This frequency of interest was set around the maximum change of the TTF curves of the different chips, which was observed at 10^5 Hz. The statistics of the assembly of eight polyelectrolyte layers are shown in *Figure 34* and *Table 5*. The g_m measured after cleaning the chip served as baseline. Then, Δg_m of two following steps was calculated and plotted (*Figure 34*).
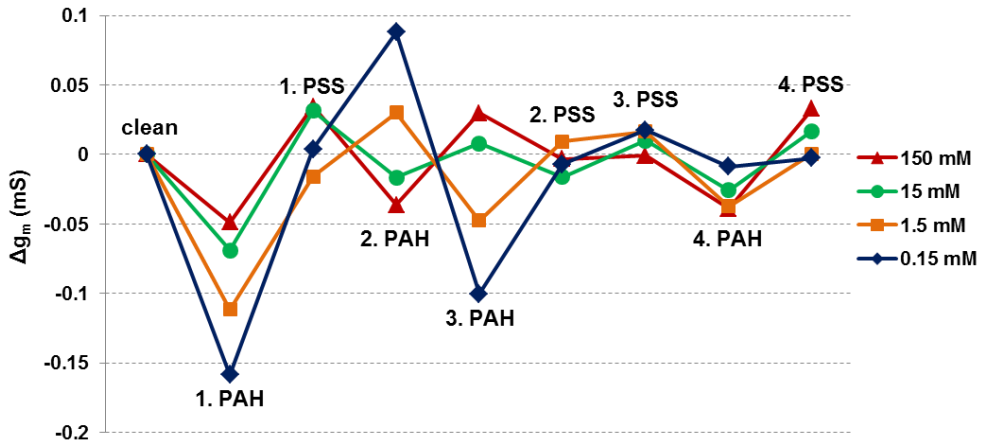
Figure 34: *Assembly of polyelectrolyte multilayers on ISFETs - Δg_m evaluation.*
In this figure, the statistical evaluation of the AC-results of the assembly of in total eight polyelectrolyte layers is represented. The evaluation of Δg_m was done at 100 kHz. The experiments were performed on ISFETs.

The corresponding Δg_m values are shown in *Table 5*. The measurements were done in four different buffer concentrations. Due to the different conductivities within the different buffers, the highest signal strength was obtained in the lowest concentration and, in consequence, the lowest intensity in the highest concentrated solution. The experiments and the corresponding statistics were performed on four different chips with 54 working channels. For the statistical evaluation, Δg_m was calculated at a frequency of 100 kHz. It can be seen that the g_m value is changing upon binding of molecules. However, no meaningful order of the different steps and, hence, the different charged molecules can be observed. Nevertheless, it seems that the change of transconductance is the same for 15 mM and 150 mM phosphate buffer, as well as for 0.15 mM and 1.5 mM buffer.

	150 mM buffer	15 mM buffer	1.5 mM buffer	0.15 mM buffer
clean	0 mS (n= 4, 54 chan)	0 mS (n= 4, 54 chan)	0 mS (n= 4, 54 chan)	0 mS (n= 4, 54 chan)
1st layer (PAH)	-0.049 mS (n= 4, 54 chan)	-0.069 mS (n= 4, 54 chan)	-0.11 mS (n= 4, 54 chan)	-0.16 mS (n= 4, 54 chan)
2nd layer (PSS)	0.035 mS (n= 4, 54 chan)	0.032 mS (n= 4, 54 chan)	0.016 mS (n= 4, 54 chan)	0.0039 mS (n= 4, 54 chan)
3rd layer (PAH)	-0.036 mS (n= 4, 54 chan)	-0.017 mS (n= 4, 54 chan)	0.03 mS (n= 4, 54 chan)	0.088 mS (n= 4, 54 chan)
4th layer (PSS)	0.03 mS (n= 4, 54 chan)	0.008 mS (n= 4, 54 chan)	-0.048 mS (n= 4, 54 chan)	-0.1 mS (n= 4, 54 chan)
5th layer (PAH)	-0.003 mS (n= 4, 54 chan)	-0.016 mS (n= 4, 54 chan)	0.01 mS (n= 4, 54 chan)	0.007 mS (n= 4, 54 chan)
6th layer (PSS)	-0.001 mS (n= 4, 54 chan)	0.01 mS (n= 4, 54 chan)	0.016 mS (n= 4, 54 chan)	0.017 mS (n= 4, 54 chan)
7th layer (PSS)	-0.039 mS (n= 4, 54 chan)	-0.026 mS (n= 4, 54 chan)	-0.037 mS (n= 4, 54 chan)	-0.009 mS (n= 4, 54 chan)
8th layer (PSS)	0.033 mS (n= 4, 54 chan)	0.017 mS (n= 4, 54 chan)	0.0005 mS (n= 4, 54 chan)	-0.003 mS (n= 4, 54 chan)

Table 5: Assembly of polyelectrolyte multilayers on ISFETs – mean Δg_m values.
Here, the calculated Δg_m values of the ac readout of eight polyelectrolyte layers are shown. The total number of evaluated chips was 4 with 54 working nanowire channels.

The results show the same tendency for all four buffers till the second polyelectrolyte layer, *i.e.* PAH. Starting from the third to the fifth multilayer, the results are opposite for the two highest compared to the two lowest concentrations, whereas from the sixth to the eight layers, the same tendency was again observed for all buffers. It might be that the conductivity difference influences these results, but in order to derive meaningful conclusions about the observed phenomena, simulations need to be performed. Nevertheless, it seems

that the charge of molecules also influences the TTF measurements on ISFETs, in particular when the thickness of the layer is in the range of the Debye length.

4.3.4 AC readout of polyelectrolyte multilayers on SiNW FETs

Since the charge seems to affect the transconductance of a microscaled field-effect device, it was assumed that the nanowire platform is influenced by this parameter as well. Therefore, the same measurements were implemented on SiNW FETs, too. In *Figure 35*, an exemplary TTF result derived from a SiNW FET can be seen.

Figure 35: Exemplary TTF readout of polyelectrolyte multilayers on SiNW FETs.
In this figure, the TTF results of the assembly of polyelectrolyte multilayers are shown. The measurements were performed in 0.15 mM phosphate buffer pH 7.0. The conductivity of the buffer was adjusted and kept stable during the measurements to avoid the influence of any conductivity changes.

For the evaluation, the g_m recorded for the cleaned, blank chip was set as baseline and the Δg_m values were calculated like it was done for the ISFET data, before. In *Figure 36*, the statistical evaluation of the change in transconductance is shown.
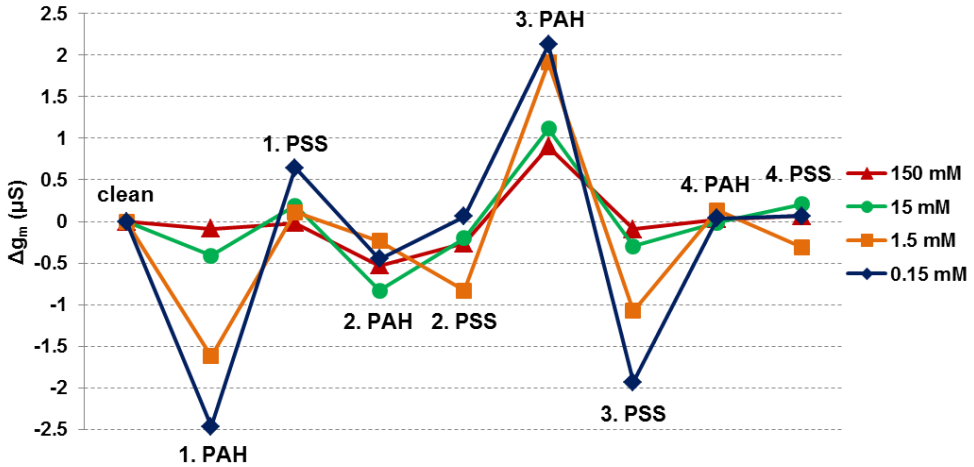
Figure 36: Assembly of polyelectrolyte multilayers on SiNW FETs - Δg$_m$ evaluation.

In this figure, the evaluation of the AC readout of polyelectrolyte multilayers is represented. The measurements were performed in four different concentrated buffers.

The statistics was done for six chips in total. The corresponding mean Δg$_m$ values are displayed in *Table 6*. As mentioned previously, the signal strength was increasing with decreasing buffer concentration. In contrast to the results for the experiments, performed on ISFETs, the change in conductance showed the same tendency for all polyelectrolyte layers and for all buffer concentration, except of the fourth and the eighth PE layer, where the shift in g$_m$ measured in 1.5 mM buffer was opposite to the other buffer concentrations. By comparing the results for both applied platforms, a same tendency was observed until the second layer for all buffer concentrations, and until the fourth layer when comparing the ISEFT results for the two highest concentrated buffers with the nanowire data. In a future project, these examinations for the SiNW FETs are further examined, which include the modeling and simulation of the data. The polyelectrolyte measurements, presented in this subchapter, were performed to confirm the possibility that the applied platforms can be used for the detection of biomolecules like DNA or proteins. They were performed to document how the sensor behaves upon binding of negatively and positively charged molecules and how the transfer characteristics and the transistors transfer function are changed due to different charges. It was shown that the flatband voltage is changing accordingly to the charge of the biomolecules attached to the nanowire

for both, the micro- and the nanoscaled platform. Moreover, the Debye screening effect was observed, which needed to be taken into consideration for the following bioassays that were established on the nanowire chips.

	150 mM buffer	15 mM buffer	1.5 mM buffer	0.15 mM buffer
clean	0 mS (n= 6, 55 chan)	0 mS (n= 6, 61 chan)	0 mS (n= 6, 69 chan)	0 mS (n= 6, 70 chan)
1st layer (PAH)	-0.086 mS (n= 6, 55 chan)	-0.41 mS (n= 6, 61 chan)	-1.6 mS (n= 6, 69 chan)	-2.47 mS (n= 6, 70 chan)
2nd layer (PSS)	-0.019 mS (n= 6, 55 chan)	0.19 mS (n= 6, 61 chan)	0.11 mS (n= 6, 69 chan)	0.64 mS (n= 6, 70 chan)
3rd layer (PAH)	-0.053 mS (n= 6, 55 chan)	-0.83 mS (n= 6, 61 chan)	-0.24 mS (n= 6, 69 chan)	-0.45 mS (n= 6, 70 chan)
4th layer (PSS)	-0.27 mS (n= 6, 55 chan)	-0.2 mS (n= 6, 61 chan)	-0.83 mS (n= 6, 69 chan)	0.06 mS (n= 6, 70 chan)
5th layer (PAH)	0.9 mS (n= 6, 55 chan)	1.12 mS (n= 6, 61 chan)	1.91 mS (n= 6, 69 chan)	2.13 mS (n= 6, 70 chan)
6th layer (PSS)	-0.1 mS (n= 6, 55 chan)	-0.3 mS (n= 6, 61 chan)	-1.1 mS (n= 6, 69 chan)	-1.94 mS (n= 6, 70 chan)
7th layer (PSS)	0.027 mS (n= 6, 55 chan)	-0.016 mS (n= 6, 61 chan)	0.13 mS (n= 6, 69 chan)	0.04 mS (n= 6, 70 chan)
8th layer (PSS)	0.067 mS (n= 6, 55 chan)	0.21 mS (n= 6, 61 chan)	-0.31 mS (n= 6, 69 chan)	0.06 mS (n= 6, 70 chan)

Table 6: Assembly of polyelectrolyte multilayers on SiNW FETs – mean Δg_m values.

The Δg_m values were all evaluated at a frequency of 100 kHz. The TTF curve measured after cleaning the chip served as baseline. In order to determine the shift of the g_m values, two TTF curves at 100 kHz were subtracted.

A change in g_m was observed after each polyelectrolyte deposition. Since the conductivity of the buffer was adjusted before the experiments and kept stable during the measurements, an influence of changes caused by the buffer solution

itself can be excluded. Furthermore, it might be that different effects are influencing the TTF results for the micro- and nanoscaled devices, since the obtained results for both platforms were slightly different. It is assumed that the parasitic parameters for each device type play a role, which can only be followed up by experiments with more devices available in future [238].

Chapter 5 – DNA experiments

After having verified with the proof-of-principle experiments that the sensors are able to detect charged molecules, assays were performed with artificial DNA sequences and two complementary HLA-B27 DNA sequences, provided by Euroimmun Medizinische Labordiagnostika AG. A typification of HLA-B27 is for instance important for organ transplantation to verify that donor and recipient are matching. Carriers of the HLA-B27 allele were shown to possess a higher risk to suffer from several autoimmune diseases. The respective results of the assays are represented and discussed in this chapter[1].

5.1 DNA fluorescence reference experiments

To verify that the immobilization of the capture DNA sequence was successful, fluorescence-labeled DNA was bound to the epoxy-terminated surface. For this kind of experiments, silanized glass slides and SiNW FETs were used. For the surface functionalization and modification, the same protocol was used as for the electronic measurements: Before immobilizing the capture DNA overnight, the chips were cleaned carefully with deionized water after GPTMS silanization. To remove unspecifically bound capture molecules, the devices were thoroughly rinsed with 2× SSC, 1× SSC and deionized water, they were dried with nitrogen and fluorescence microscopic pictures were taken. In basic experiments, different concentrations of the capture molecule were immobilized on glass slides to check if there are differences in the obtained fluorescence intensity. 10 nM, 100 nM, 500 nM and 1 µM of single-stranded capture molecules were bound to the epoxy surface for doing a comparison of the fluorescence signal

---

[1] Parts of this chapter were published in
T.C. Nguyen, M. Schwartz, X.T. Vu, J. Blinn, S. Ingebrandt, "Handheld Readout System For Field-Effect Transistor Biosensor Arrays For Label-Free Detection Of Biomolecules." Physica Status Solidi (A): Applications and Materials Science, 212 (6), 1313–1319 (2015).
M. Schwartz, T.C. Nguyen, X.T. Vu, M. Weil, J. Wilhelm, P. Wagner, R. Thoelen, S. Ingebrandt, "DNA Detection With Top-Down Fabricated Silicon Nanowire Transistor Arrays In The Linear Operation Regime." Physica Status Solidi (A): Applications and Materials Science, 213 (6), 1510–1519 (2016).
M. Schwartz, T.C. Nguyen, X.T. Vu, P. Wagner, R. Thoelen, S. Ingebrandt, "Impedimetric Sensing Of DNA With Silicon Nanowire Transistors As Alternative Transducer Principle." Physica Status Solidi (A): Applications and Materials Science, 1700740 (2018).

afterwards. The capture ssDNA was amino-modified at 3' and Cy3-labeld at 5'. The corresponding sequence and modifications can be taken from *Table 2*. In *Figure 37*, the fluorescence images of the different capture molecule concentrations and the statistical evaluation of the fluorescence signal are depicted.
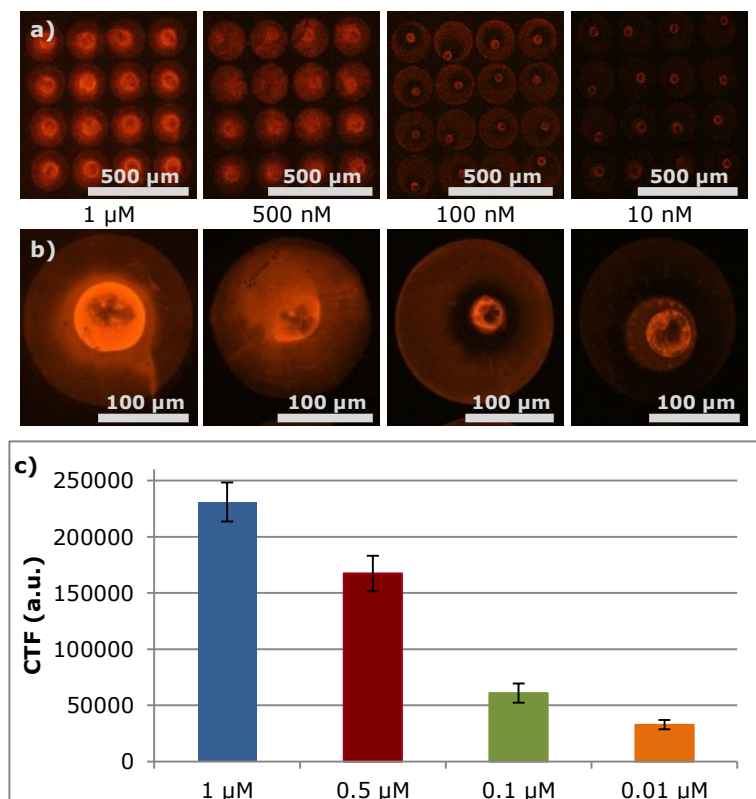
Figure 37: Fluorescence reference control of DNA immobilization on glass slides.
4×4 spots of 1 µM, 0.5 µM, 0.1 µM and 0.01 µM capture ssDNA site-specifically immobilized via microspotting onto a silanized glass slide (a), magnification of one single spot of each concentration (b), statistical evaluation of the fluorescence intensity (c).

For the evaluation and calculation of the fluorescence strength, the program Image J (https://imagej.net) was used. With Image J, it is possible to calculate the corrected total fluorescence (CTF) of a fluorescent area. In doing so, the outer shape of the fluorescent area was marked and the integrated density (IntDen) of this area is calculated by the program by

IntDen = (Area of fluorescent spot) × (mean fluorescence of spot)   (5.1)

It can also be described as the number of pixels of the selected area. To differentiate between real fluorescence and background signal, an area (=background), which is not or only weakly fluorescent, is marked and CTF is also calculated as follows [239–241]

CTF = (IntDen fluorescent spot) - (Area fluorescent spot × mean fluorescence background)   (5.2)

As expected, the fluorescence intensity is decreasing with decreasing DNA concentration because also the number of fluorophores, which means the total amount of fluorescently labeled molecules, is reduced. This is in agreement with literature [242]. The same DNA sequence was also immobilized onto silanized SiNW FETs. The applied concentration was 1 µM. In *Figure 38*, one result of the fluorescence microscopy can be seen.

Figure 38: Fluorescence reference control of DNA immobilization on SiNW FET.
In this picture, a fluorescence image of a successful immobilization is represented. For this purpose, 1 µM of capture ssDNA was site-specifically micro-spotted onto the sensor area of a GPTMS silanized SiNW FET. Fluorescence microscopy was performed with an inverted fluorescence microscope (Olympus IX50, Olympus Optical CO. (Europe), GmbH, Germany).The white circles indicate the nanowire area.

Since the fluorescence signal is clearly visible after thoroughly washing to remove excess capture DNA, it was concluded that the immobilization process was successful. After verifying the immobilization, the hybridization protocol was tested as well. Amino-modified ssDNA was bound to a GPTMS silanized glass slide. Hybridization was performed with 100 nM, 500 nM and 1 µM cDNA_Cy3 as described in Chapter 3.6.1. The whole sequence of the used DNA is shown in *Table 2*. In *Figure 39 a*, the fluorescence images are shown. The result for 1 µM is represented on the left, 500 nM in the middle and 100 nM on the right side. The corresponding CTF results can be taken from *Figure 39 b*.
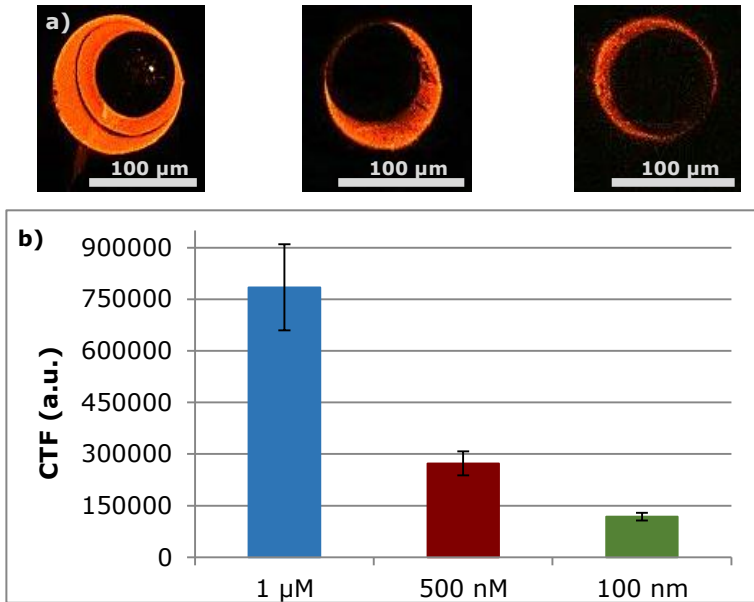
Figure 39: Fluorescence reference control of DNA hybridization on glass slides.
Fluorescence image of a successful hybridization with 1 µM (left), 0.5 µM (middle) and 0.1 µM (right) FM-DNA, which was performed on a silanized glass slide (a), statistical evaluation of the fluorescence intensity of the hybridization with both concentrations (b).

It is clearly visible that the fluorescence intensity is decreasing with decreasing cDNA concentration due to a lower amount of available fluorophores [242]. The hybridization was also confirmed on the nanowire FETs (*Figure 40).*
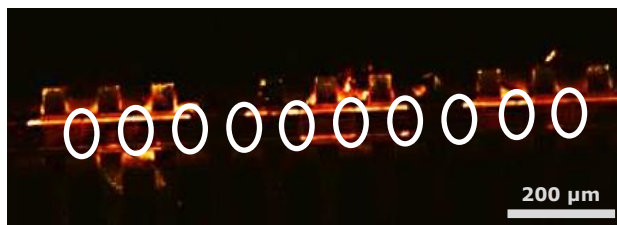
Figure 40: Fluorescence reference control of DNA hybridization on a SiNW FET.
In this fluorescence image, a successful hybridization with 1 µM complementary FM-DNA can be seen. An inverted fluorescence microscope was used (Olympus IX50, Olympus Optical CO. (Europe), GmbH, Germany). The white circles indicate the nanowire area.

1 µM capture DNA was immobilized after silanization on the nanowire chips. Afterwards, hybridization was performed with 1 µM Cy3-labeled cDNA. The

fluorescence images showed that the hybridization on SiNW FETs was successful.

5.2 Detection of artificial DNA with ISFETs

In a few trials, the immobilization of single-stranded capture DNA and the hybridization with complementary fully-matching DNA (cDNA) was performed on microscaled FETs. The corresponding DC and AC results by measuring the transfer characteristic and the transistor transfer function, respectively, are summarized and discussed in the following two subchapters.

5.2.1 DC readout of DNA immobilization and hybridization

Before implementing experiments with artificial DNA sequences on the nanowire platform, initial trials were performed on ISFETs to establish the basic assay principle. The ISFETs, used for these measurements, had gate dimensions 16 × 7 µm² and 12 × 4 µm² (length × width), respectively. The chips were cleaned and silanized with GPTMS as described in the Material & Methods section. Afterwards, a single-stranded, artificial DNA sequence (ssDNA) was site-specifically immobilized on the sensor surfaces by means of microspotting. The remaining sensor surface was blocked with 1 % BSA to avoid unspecific binding. Hybridization was done with the complementary, single-strand DNA (cDNA). The applied DNA sequences and the respective modifications are represented in Table 2. After the hybridization, the DNA double strand was denaturized into the single strands by heating up the sensor to 90 °C. The DC readout by recording the transfer characteristic (TC) was performed after each experimental step in 1.5 mM phosphate buffer pH 7.2. In *Figure 41 a,* an exemplary TC measurement can be seen. In *Figure 41 b*, the statistics for eight channels of one chip is shown. For data evaluation, the TC received after silanization was set as baseline. For calculating the change in threshold voltage, ΔV_{TH}, the working point was determined and, subsequently, the V_{TH} value of one TC curve was subtracted from the V_{TH} value of the following TC curve at the previously determined working point. In doing so, a mean immobilization signal of + 29 mV was measured, while the BSA blocking led to a change in V_{TH} of +13 mV. The hybridization caused another change of +13 mV.
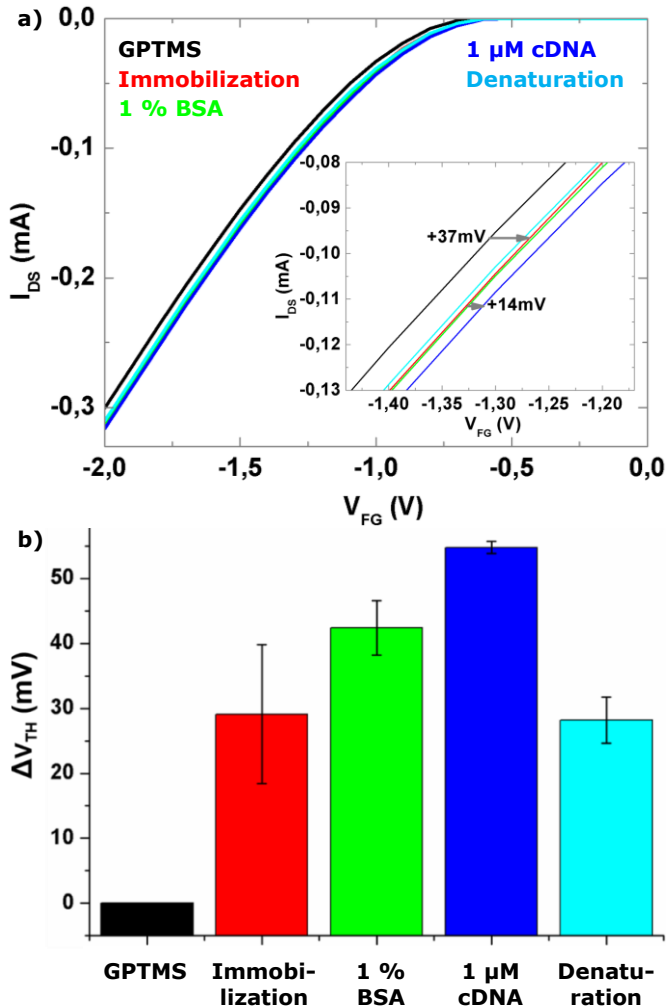
Figure 41: Exemplary DC detection of the immobilization and hybridization of artificial DNA on an ISFET.

In (a), an exemplary TC readout of the DNA assay, performed on one chip, is displayed. The DC measurements were performed after silanization, immobilization, blocking, hybridization and denaturation. The figure shows the TC curve detected at V_{DS} = - 2 V. In (b), the statistical evaluation of the whole chip is shown. In doing so, the change in V_{TH} was calculated at the steepest point of the TC curve (= working point). The results were published in [230].

The TC curve itself shifted to more positive values after immobilization, blocking and hybridization. This is in agreement with previous publications [24,203–205] and the fact that DNA molecules and BSA are both negatively charged at pH 7.2.

After denaturation, the TC curve was almost overlapping with the TC curve, recorded after immobilization. This is the expected effect, since the DNA double strand is denaturized into two single strands. Compared with the GPTMS curve, a shift of + 28 mV was calculated, whereas the ΔV_{TH} after immobilization was previously reported to be + 29 mV. This can be explained by removing the complementary single strand from the immobilized DNA sequence and by also removing the blocking agent BSA. Furthermore, the approximate surface density of the immobilized DNA molecules was calculated. Since the buffer, in which the TC curve was measured, had a concentration of 1.5 mM, a Debye length of 7.5 nm was expected according to equation (2.20). A DNA sequence of 20 base pairs has a length of about 6.5 nm [230]. This means that the utilized DNA sequences are completely within the Debye length and, hence, the 20 negative elementary charges per one single-strand can be measured. With help of the Grahame equation, the change in surface potential upon binding of charged molecules can be calculated according to the Debye-Hückel theory [243]

$$\psi_0 = \sinh^{-1}\left(\frac{\sigma_0}{\sqrt{8kT\varepsilon_W\varepsilon_o n_o}}\right)\frac{2kT}{e} \tag{5.3}$$

with ε_W for the dielectric constant of the measuring solution, ε_0 for the permittivity of free space and n_0 for the ionic strength of the applied measuring buffer. The change in V_{TH}, which is caused by the change in surface charge σ_{DNA} due to the DNA binding, can be estimated with help of the following equation [24]

$$\Delta V_{TH} = \frac{2kT}{e}\left(\sinh^{-1}\left(\frac{\sigma_0}{\sqrt{8kT\varepsilon_W\varepsilon_0 n_0}}\right) - \sinh^{-1}\left(\frac{\sigma_0 - \sigma_{DNA}}{\sqrt{8kT\varepsilon_W\varepsilon_0 n_0}}\right)\right) \tag{5.4}$$

Since the maximum surface charge density σ_0 is reported to be 0.8 C/m² [244], the surface charge density for the immobilized DNA molecules, σ_{DNA}, amounts to 0.346 C/m² with a ΔV_{TH} of - 29 mV. In literature, surface charge densities of 10^9 – 10^{13} DNA strands per cm² can be found for silicon dioxide silicon nitride surfaces [245–247]. Moreover, it was reported that the surface density is influenced by the used surface material and the surface modification. As already mentioned, a DNA single-strand of up to 20 base pairs possesses 20 negative

charges. In consequence, this led to 10^{13} DNA molecules per cm² (= 1 DNA strand per 9.25 nm²) for the experiment, reported here. The reason for the high yield in molecule density might be the epoxy silane that as used since the density of DNA molecules on GPTMS modified surfaces is usually higher than on APTES functionalized surfaces [230,246].

5.2.2 AC readout of DNA immobilization and hybridization

The recording of the transistor's transfer function (TTF) was always done after each step of silanization, immobilization, blocking and hybridization. The used DNA strands were artificial and, hence, the assembly of the base pairs was synthesized according to the customer request. The sequence can be taken from *Table 2*. The experimental procedure was the same as reported before. One exemplary TTF measurement is displayed in *Figure 42*.
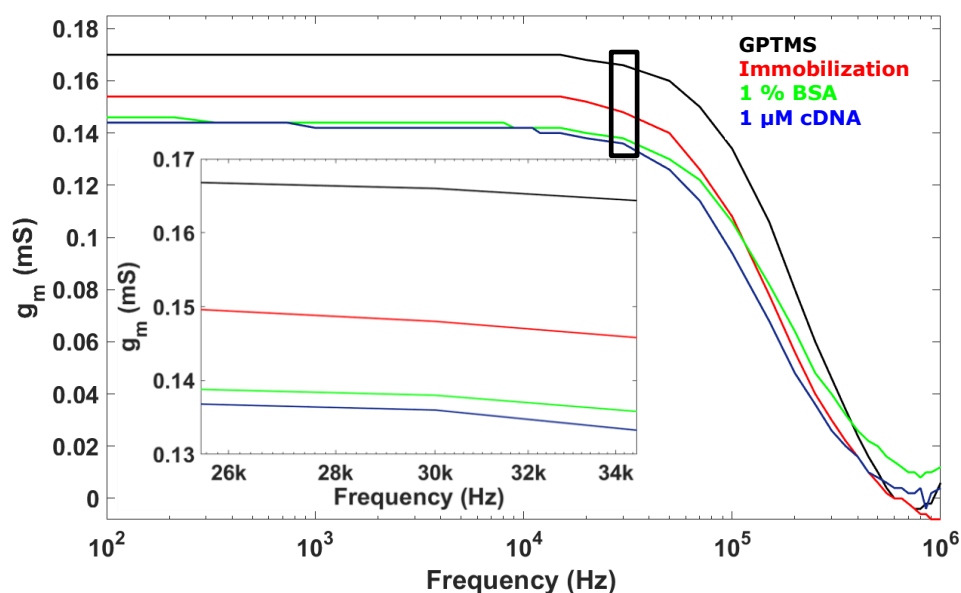
Figure 42: Exemplary AC readout of artificial DNA immobilization and hybridization implemented on an ISFET.

In this figure, the TTF results for the immobilization and hybridization of two complementary DNA sequences are shown. The change in g_m value was calculated at a frequency of 50 kHz. It was evaluated that the transconductance is decreasing after each additional biomolecule binding which is in agreement with previous publications [156]*.*

The change in transconductance, Δg_m, was evaluated at a frequency of 50 kHz. The immobilization of 1 µM single-stranded capture DNA leads to a decrease of the g_m of 20 µS. The blocking caused a Δg_m of 10 µS. The hybridization reduced the transconductance about 4 µS to lower values, in comparison to the blocking step. In conclusion, the transconductance is decreasing after each experimental step and, hence, after every biomolecular attachment. This observation is in agreement with papers published before [156]. Due to the additional biomolecules on the transistor surface, the capacitance of the field-effect device is increased, leading to a change in impedance. This effect is based on the resistance of the biomolecule membrane, R_{Bio}, which becomes higher because of an increase of the resistance to charge transfer. The difference in protonation and deprotonation of single-stranded and double-stranded DNA molecules are reported to be the reason for this change in resistance [156]. Moreover, the two time constants τ_1 and τ_2 are shifted to higher values (see equation (3.10) and (3.11)).

5.3 Detection of artificial DNA with SiNW FETs

After these proof-of-principle experiments, which showed that the readout principle of our transistors was working, first measurements on artificial single-stranded DNA sequences were performed on the nanowire platform. In doing so, the immobilization of a single stranded DNA sequence onto the sensor surface and the hybridization process of a target DNA strand to a complementary capture DNA strand, which was immobilized on the sensors surface before, were detected. Furthermore, the change of V_{TH} and g_m in dependence of different buffer concentrations as well as the influence of the nanowire size on the shape of the transfer characteristic were examined. All measurements were conducted in the DC and the AC readout mode of our setup to gain as much information of the processes on the gate area as possible. The overall aim of these experiments was to establish a stable procedure for the detection of the hybridization process. Afterwards, this experimental protocol was applied for the establishment of a real DNA assay. The assay of choice was the HLA-B27 assay of the company Euroimmun Medizinische Labordiagnostika AG.

5.3.1 DC signal strength in different buffer concentrations

Another aim of this thesis was to examine the influence of the Debye length and its corresponding screening effect on the performed recordings. For this purpose, the measurements were performed in four different buffer concentrations, starting with the lowest concentration of 0.001× PBS. Then, the concentration was stepwise increased by one order of magnitude, respectively. The comparison of exemplary TC results is shown in *Figure 43 a*. The TC data obtained after the silanization with GPTMS (solid lines) was set as baseline and served as reference curves. The results achieved after the immobilization with capture DNA molecules (dashed lines) were compared to the reference data [248]. The smallest change of about 64 mV was obtained for the 1× PBS buffer (black solid and black dashed lines), whereas it was increased to 114 mV and, hence, the highest change in the lowest buffer concentration (red solid and red dashed lines). In 0.01× (light blue solid and light blue dashed) and 0.1× PBS (green solid and green dashed) the signal was almost the same, but lower than for the lowest concentration and higher than for the 1× PBS buffer [248]. The obtained results and observations are in agreement with earlier published data [163]. In low buffer concentrations, the Debye screening is less pronounced due to a relatively high Debye length. Hence, a higher signal can be recorded because less charges are neutralized by their counterions [45,163,249]. It was previously shown that the negative charge of the DNA backbone is screened by counterions in highly concentrated buffer solutions [250,251]. In *Figure 43 b*, the statistical evaluation of the obtained data is displayed. In doing so, a two-tailed pared t-test was performed. The t-test is used to compare the means of one variable between two groups. With a paired t-test, one of the characteristics of the first group can be interconnected with one of the characteristics of the second group. A two-tailed t-test divides the significance in such a way that half of the significance is in one direction (or tail) of the statistical distribution and the other half in the other direction (or tail) [252–254]. The statistics indicate that the signals are not fading as much as expected from the pure Debye screening effect. The reason might be an overlapping of a shift in V_{TH} and an increase in TC curve steepness for some measurements, which might lead to larger signal amplitudes.
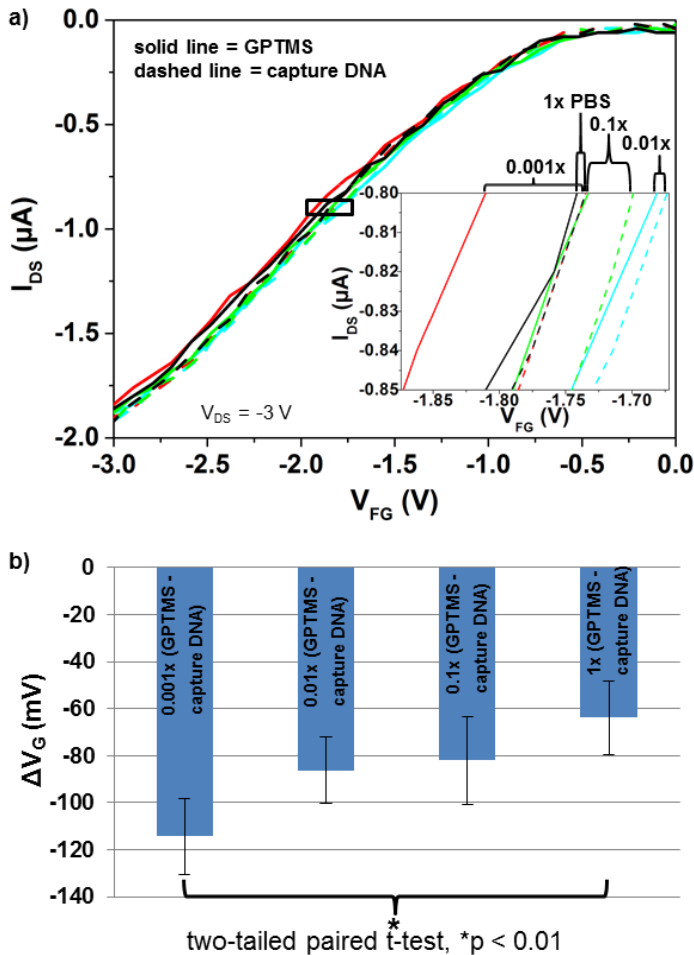
Figure 43: DC measurements in different buffer concentrations.

(a) Exemplary TC measurements in four differently concentrated PBS buffers (0.001 × PBS = red solid and dashed curves; 0.01 × PBS = light blue solid and dashed curves; 0.1 × PBS = light green solid and dashed curves; 1 × PBS = black solid and dashed curves), (b) statistical evaluation of the TC measurements (n = 6). The results were published in [248].

Both parameters were discussed more in detail in Chapter 4.3. Nevertheless, the statistics show that the signal decreases with increasing buffer concentration.

5.3.2 DC readout of immobilization and hybridization signals

In further DNA experiments, a comparison of the performed experimental results was done.

Therefore, the DC readout was done after each surface modification step, *i.e.* silanization, immobilization, blocking and hybridization with 0.5 µM complementary DNA. An exemplary result for the electronic TC recordings is displayed in *Figure 44 a*. The extraction of the data was done at a working point of V_{FG} = -3 V. The experiments were done in 0.001× PBS. Upon binding of the biomolecules, the TC is shifted, which reflects a change in surface potential and, therefore, in V_{TH}. This behavior is well known and can be observed in all kind of solution-gated, field-effect based biosensor devices independent of their size. In more detail, the surface potential Ψ_S and V_{TH} are changing because of the negative charge of the DNA backbone. The immobilization of 1 µM capture DNA (red curve) changed the V_{TH} to the positive side in comparison to the bare nanowire (black curve). By comparing immobilization to the hybridization with 0.5 mM fully matching DNA (FM-DNA) (dark blue curve), the voltage is again shifted to more positive values. Moreover, as already described in the subchapters 4.3 and 5.3.1, a stepwise increasing steepness of the TC characteristics can be observed. The reason might be an additional accumulation of charge carriers inside the nanowire region. In the following subchapter, this steepness changing effect will be described more precisely [248]. The statistical results are displayed in *Figure 44 b*. An average shift of 158 mV was detected for the immobilization process and 209 mV for the hybridization events (n = 6), which are both very high values compared to publications with ISFET devices [17,250]. By evaluating the significance of the two processes, it was seen that only the immobilization seems to be significant (two-tailed, paired t-test), whereas the hybridization is not due to a high standard deviation [248]. From the evaluated results and the shown plots, it can be concluded that the strength of the V_{TH} shift is strongly correlating with the chosen working point, meaning the choice of V_{DS} and V_{GS} to read the record I_{DS}. In earlier publications, the reason for the conductance change in the nanowires was already discussed [46–48,231]. For the approach presented in this thesis, this means that the relative conductance change $\Delta G/G_0$ and the absolute change of the wire's conductance ΔG are functions of both parameters V_{DS} and V_{GS}. It is clearly visible that the

recorded data is strongly depending on an arbitrary choice of the front-gate potential and the bias voltage.
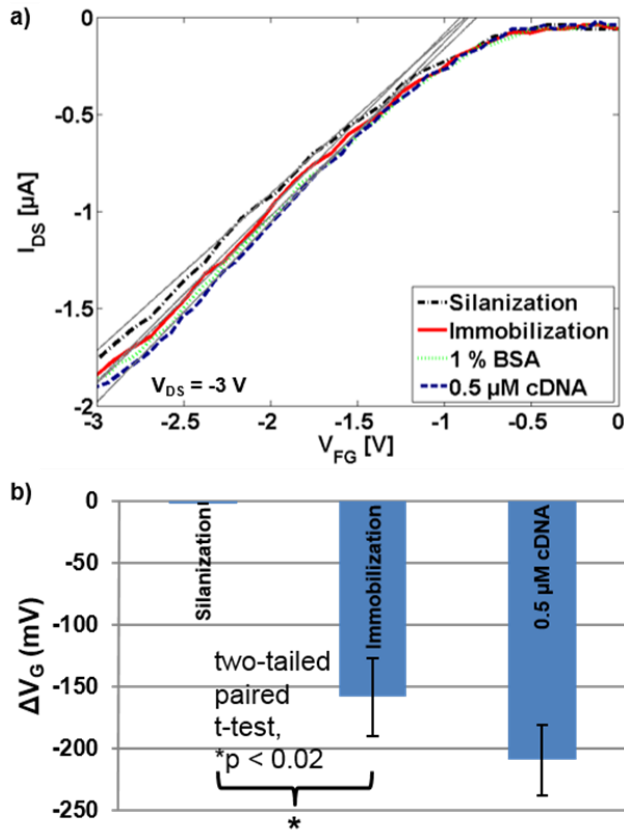
Figure 44: TC measurements of DNA immobilization and hybridization.

(a) In this figure, an exemplary result of the TC curves measured in 0.001× PBS after different experimental steps is represented: GPTMS (black), capture DNA (red), blocking with 1% BSA (green), hybridization with 0.5 mM cDNA (dark blue). It was examined that the binding of DNA is shifting the threshold voltage of the device and causing an increased slope of the characteristic lines (refer to grey lines) simultaneously. (b) The statistical evaluation of the electronic data is shown in the lower figure (n = 6). The value after silanization served as a baseline and was set to zero. The figure was published in [248].

By using uncharged PNA (peptide nucleic acid) molecules as capture molecules instead of the negatively charge DNA single-strand, it would probably be possible to increase the measured V_{TH} shift for a better reproducibility of the hybridization signals [248]. Nevertheless, our results are in full agreement with

data published earlier [165]. The results demonstrate the potential of the silicon nanowire platform towards biomedically relevant DNA bioassays.

5.3.3 Influence of the nanowire size on the transistor's transfer characteristics

In this subchapter, the focus is set on the already mentioned steepness change of the TC curve where I_{DS} versus V_{FG} of different nanowire dimensions is analyzed. To compare the TC steepness behavior depending on the nanowire width, sensors with two different nanowire dimensions were used. The first set of nanowires had widths of 200 nm and lengths of 10 μm, the second type were 400 nm wide and 10 μm long. Concerning the experimental procedure, both devices were treated in the same way. In the performed assays, it was observed that the TC was steeper in thinner than in wider wires. It was assumed that the charger carrier density inside the nanowire depletion area was increased. The results for one exemplary measurement of a chip with a nanowire width of 400 nm can be seen in *Figure 45 a* and an exemplary TC plot for a device with a 200 nm wide nanowire is displayed in *Figure 45 b*. In these graphs, a comparison of the results measured after immobilization and hybridization was done. The difference in steepness of the immobilization curve is clearly visible by comparing both plots [248]. To derive further conclusion about the received data, a statistical evaluation was performed by calculating the change in V_{TH} at two different I_{DS} values. The corresponding statistic is represented in *Figure 45 c*. The statistic was calculated for 28 nanowires with a width of 200 nm and a length of 10 μm and for 13 nanowires with the width of 400 nm and the length of 10 μm in 3 independent experiments. The evaluated result clearly indicated that the shift in V_{TH} is more pronounced at low I_{DS} values than at high I_{DS} values in thinner wires. As mentioned before, this observation possibly relies on an increase of the charger carrier concentration inside the nanowire area due to an additional charge injection from the source and drain contact sides [248]. Many other researchers in the field operate the SiNW FET devices in subthreshold regime, where this effect adding to the classical V_{TH} shift of standard ISFET devices might be more prominent and result in the reported higher sensitivities of these nanoscale devices.
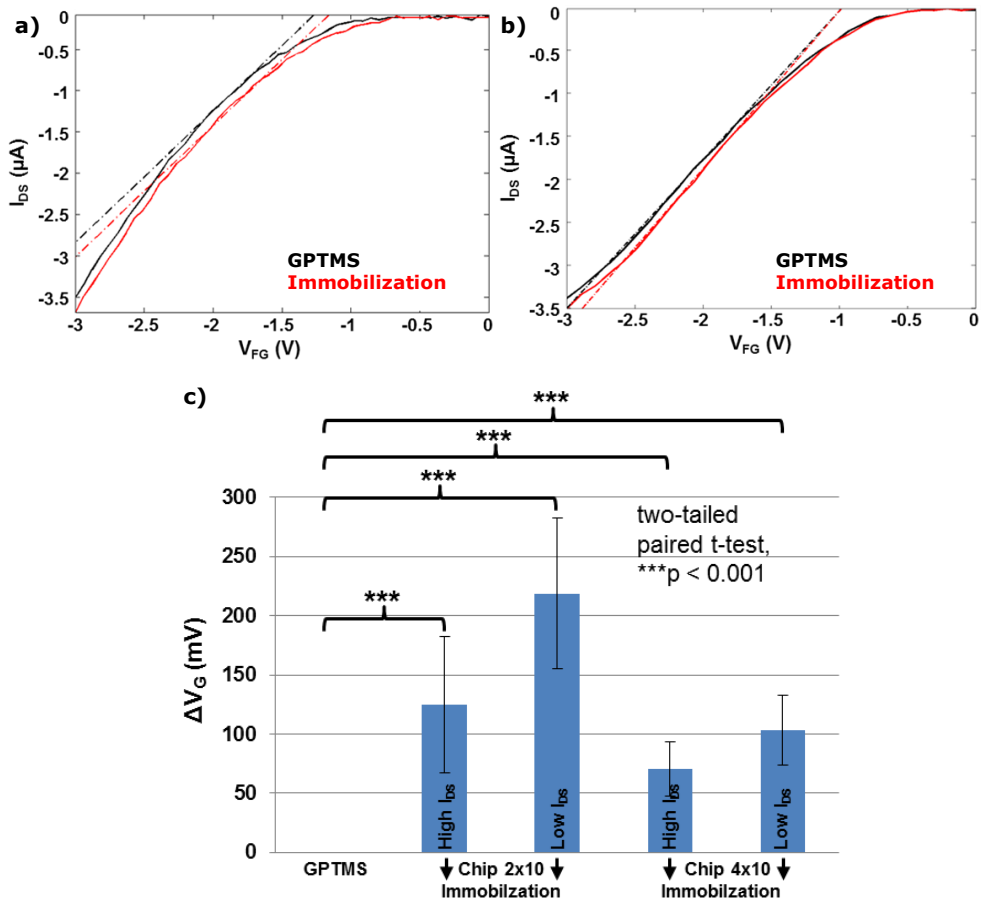
Figure 45: The influence of the I_{DS} onto the TC shape.

The behavior of the TC curves after silanization (black) and immobilization (red) are shown for a chip with a width of 400 nm and a length of 10 μm (a). The same is displayed for a 200 nm wide and 10 μm long chip (b). Furthermore, a fit of the TC curves in (a) and (b) was done to work out the steepness difference more clearly. Due to the fits, it is visible that, in thinner wires, the slope and, hence, the steepness of the dc curve is different to the shift of wider nanowire FETs, where it is parallel. The obtained results were further confirmed by doing statistics (n =28 for chip 2 × 10 and n =13 for chip 4 × 10) (c).The figure was taken from [248].

Further details are discussed in a publication of our group [248]. Simulations were performed by a colleague and are detailed in a related thesis work [255]. Liu and Dutton described in a theoretical work a similar effect of a change in operation regime [256]. In this publication, a theoretical description of an experimental work published earlier was performed [164]. Upon binding of

biomolecules, a change in operation regime from accumulation to flatband and, then, to depletion mode, was described there. The examinations of the authors were done on highly doped wires (10^{18} 1/cm^3). In contrast to this, the wires used for this thesis possess highly doped source and drain contacts (10^{15} 1/cm^3) and, hence, are not directly comparable to the ones used in Ref. [164]. This high intrinsic doping could be the reason for the strong influence on the TC steepness and could also explain why the effects are depending on the nanowire width. To analyze this phenomenon further, a simulation was created (*Figure 46)*.
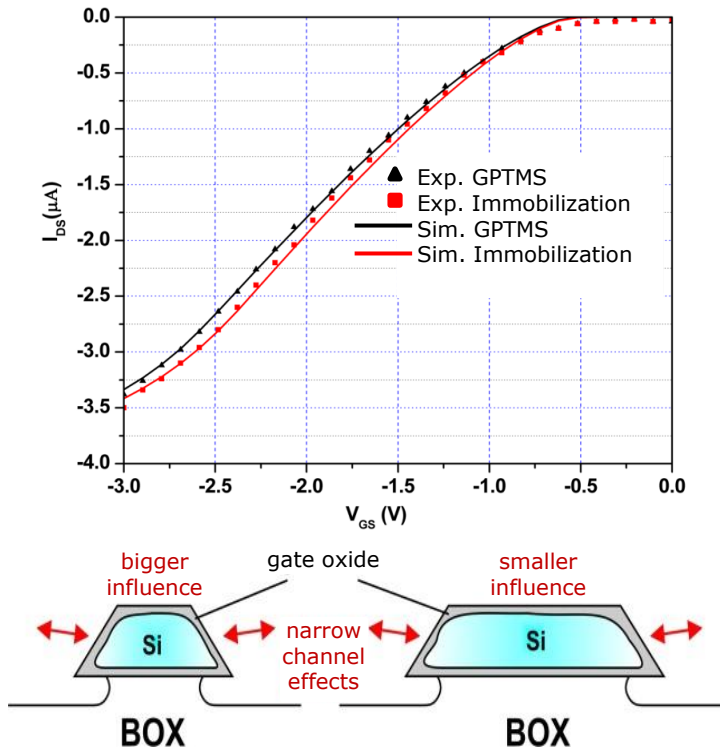
Figure 46: Simulation of the steepness effect in the TC characteristics of thin nanowires.

As discussed before, this effect can be seen more clearly in the thinner nanowires. We assume that in thinner structures the charge injection effect upon biomolecule binding is much more effective than in wider wires. The simulation shown in this figure was done for a 200 nm wide and 10 µm long nanowire. The results were published in [248]*.*

As mentioned previously, the results are discussed more in detail in a publication of our group [248]. Further simulation was done by a colleague in framework of

another related thesis [255]. Like discussed before, the TC steepness change upon biomolecule binding can be fitted by increasing the charge carrier concentrations. In the schematic, the highly doped source and drain contact sides are indicated to which this effect is attributed. If the charge carrier effect scales with smaller nanowire lengths as well, this might be an explanation for the improved sensitivity of silicon nanowire transistors in comparison to ISFETs, which was published earlier [35]. The highly sensitive sensors could then be used for biomedical examinations, where very low analyte concentrations need to be detected. Another conceivable application is the early-stage detection of diseases, such as cancer, where an early treatment might be lifesaving. To proof this assumption and to do more systematical investigations, more measurements need to be performed, in which the nanowire widths and lengths are varied systematically [248].

5.3.4 The impedance of the biological membrane

Several parameters influence the impedance of the biomembrane located on the SiNW chip surface. The dielectric property of the interface layer and the charges of the adhered molecules are only two examples. For ISFETs, a model to describe the change of interface impedance for protein layers was demonstrated. The potential changes upon attaching of the biomolecules were defined by a Donnan potential [257]. The bound proteins were regarded as biological membrane layer at the gate oxide. In this thesis, a similar principle is considered to be valid for the DNA molecules on the nanowire surface. In *Figure 47*, a schematic of a biological membrane on top of a nanowire is shown which is either formed by single-stranded DNA molecules (upper picture) or DNA double strands (lower picture). The DNA membrane is expressed as phase m with a resistance value R_{Bio} and a capacitance value C_{Bio}. Besides that, a phase s is proposed which is referred to the solution [207]. The binding of single-stranded DNA molecules is creating an interface layer of approximately 1 – 2 nm. Due to their negative charges at neutral pH of the solution, a surface charge density is occurring and anions as well as cations are attracted from the solution leading to a compensation of these charges and to a potential drop between phase m and phase s [207]. This is called Donnan potential Ψ_D and, in equilibrium of the electrochemical potential of ions in phase m and s, Ψ_D can be calculated by

$$\Psi_D = \Psi_m - \Psi_S = \frac{kT}{q} \ln \frac{\sqrt{4c_S^2 + c_{Bio}^2} + c_{Bio}}{2c_S} \qquad (5.5)$$

with Ψ_m and Ψ_S being the electrical potentials in phase m and phase s, respectively, c_S representing the salt concentration in the electrolyte solution and c_{Bio} standing for the effective fixed charge concentration inside the biological membrane [207,257]. Due to the formation of the DNA double strand upon hybridization with complementary DNA, the molecules are straightened up, whereas the single-stranded DNA molecules can have a coil-like structure on the sensor surface (upper picture *Figure 47*). This stiffening is increasing the thickness of the layer to 3 – 5 nm and also c_{Bio}. Furthermore, the charge distribution is changing which is resulting in an enhanced ionic diffusion towards the oxide surface and in a change of the Donnan potential. Schasfoort et al. discussed in their publication that the change in threshold voltage ΔV_{TH} of an ISFET upon attachment of proteins is caused by the change of the Donnan potential $\Delta\Psi_D$ at the biomembrane/solution interface and by a change in the surface potential $\Delta\Psi_S$ at the oxide/biomembrane interface [257]. ΔV_{TH} is then give by

$$\Delta V_{TH} = (1-\alpha)\Delta\Psi_D \qquad (5.6)$$

with α representing the dimensionless sensitivity factor with a value of 0-1, which was already introduced in Chapter 4.1. As mentioned there, α would equal 1 for an ideal oxide surface with Nernstian behavior [166]. In contrast to an ideal pH sensor, an α–value below 1 would be profitable for a large Donnan effect, which is achieved for SiNW FETs with SiO_2 as gate oxide. In 2011, it was shown that molecules, which are not present within the Debye length, are influencing ΔV_{TH} due to this effect [258]. In a publication about impedance modeling of FET-based devices, ionic conduction caused by ion diffusion in the electrolyte solution and by electrons and holes in the semiconductor as well as displacement currents for capacitive coupling were defined for diluted buffer solutions and low DNA concentrations [259]. The effect of the salt adsorbed onto the insulator was not included and the electrolyte showed a more complex influence than the shift of V_{TH} as expected from the Donnan theory. They introduced a decrease in capacitance in accumulation mode or an increase in

moderate to strong inversion mode of the device. Das published in 2014 that it is also necessary to identify if the pH value is influencing the charge of the biolayer by protonation or deprotonation [260].
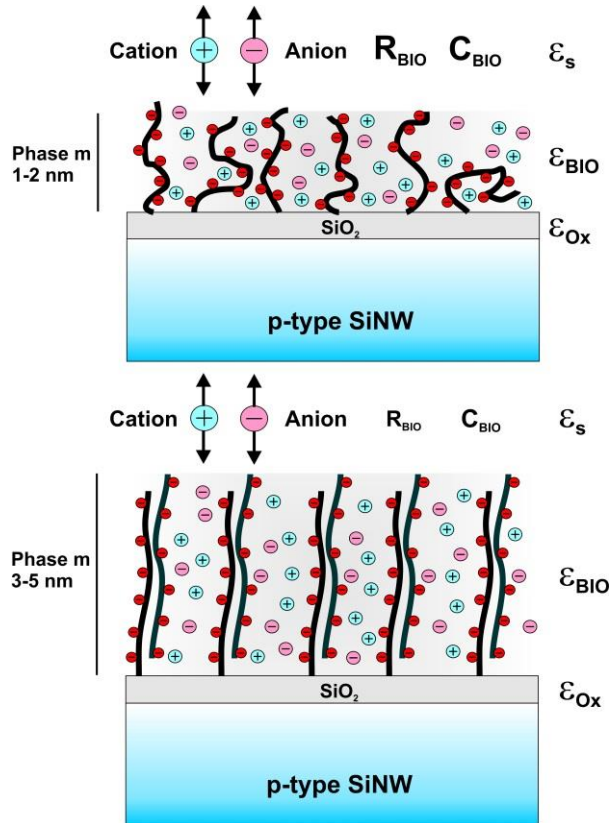
Figure 47: Model of the biological membrane composed of DNA molecules.

In the upper schematic, the biological membrane consists of negatively charged single-stranded capture molecules, which results in a thickness of approximately 1 – 2 nm. The hybridization with complementary DNA increased the layer dimension to 3 – 5 nm (lower picture). Picture taken from [207]*.*

To summarize this briefly, it can be noticed that the impedance of a FET-based DNA biosensor is affected by a wide range of parameters and conditions:

- pH, temperature and ionic strength of the used buffer solution
- DNA length and density on the sensor surface
- DNA layer thickness, which is depending on if the DNA is present as single-strand or double strand

- Charges and pH dependency of the biomolecule
- Surface modification, *i.e.* silanization
- Gate oxide material
- Operation mode and doping level of the sensor
- Local dielectric constants in the biomembrane

In the framework of this thesis, the effect of the ionic strength of the buffer solution on the impedance was evaluated. The corresponding results are shown in the following subchapter.

5.3.5 g_m in different buffer concentrations

For the transfer characteristic measurements, it is known that the buffer concentration influences the signal strength due to a shielding effect of the ions inside the electrolytes solution [163]. To examine whether the Debye length also affects the TTF measurements, silanization and immobilization was measured in four different buffer concentrations (0.001× PBS, 0.01× PBS, 0.1× PBS, 1× PBS). In *Figure 48 a*, the results of ac measurements in the different buffer solutions are represented. It can be seen that the TTF behaves similar to the DC measurements and is affected by the Debye length as well [207]. The highest signal was monitored in the lowest buffer concentration (0.26 µS) whereas the signals were smaller in lower PBS solutions. This is in agreement with the DC results shown in Chapter 5.3.1 and with the transfer characteristic behavior reported in several publications [45,163,249]. The statistical evaluation of the electronic results supports those observations, too. However, the statistical data show that even though the highest signal is obtained in the lowest buffer concentration, the signal is not fading with decreasing buffer concentration [207]. Indeed, there are very high standard deviations which can also be the reason for this observation. The high standard deviation can be caused by the different number of wires per channel, the multiple uses of the sensors and the different characteristic of the channels within a chip. This variation in characteristic can also be accompanied with a difference in channel sensitivity. The two-tailed paired t-test was used to test if the results are significant. A significance change in g_m was examined for each of the four concentrations.
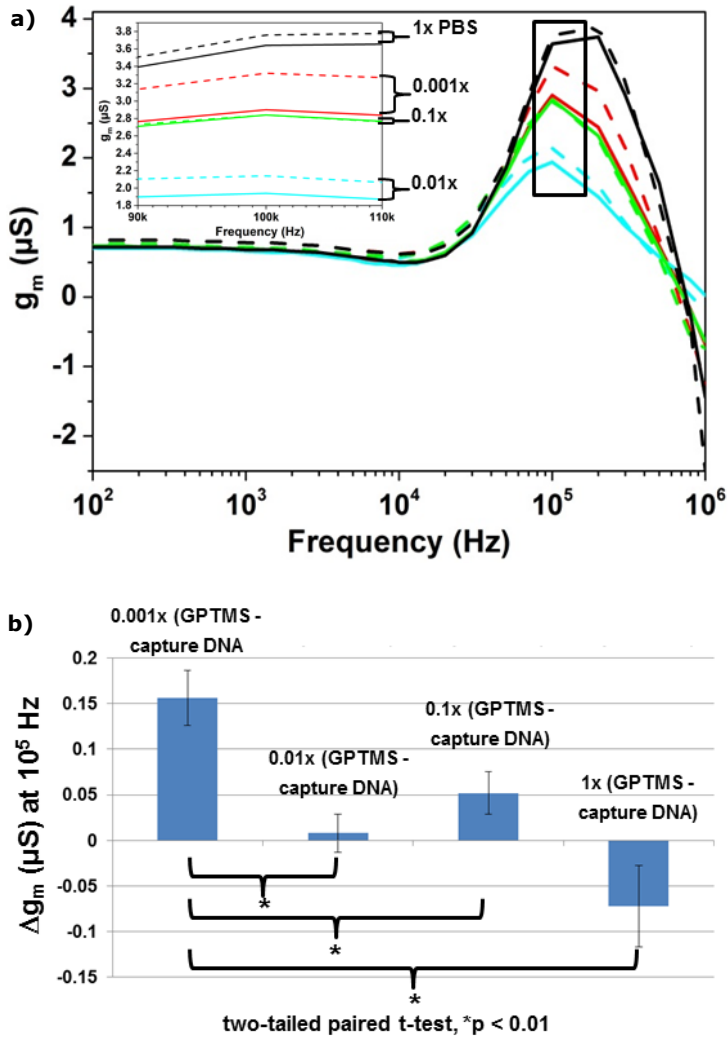
Figure 48: AC measurements in different buffer concentrations.

(a) TTF measurements performed in four different PBS concentrations. The solid line represents the TTF measured after silanization, the dashed lined displays the TTF obtained after immobilization of the capture DNA sequence. The black solid and dashed curves resulted by measuring both experimental steps in $1\times$ PBS, the green solid and dashed line was recorded in $0.1\times$ PBS, the light blue curved represent the measurements done in $0.01\times$ PBS and, finally, the red TTF curves were derived by measuring in $0.001\times$ PBS. (b) Statistical evaluation of the TTF (n = 6). The results were published in [207].

These results indicate that the Debye screening effect influences the AC readout,

too. This means that the shielding of the negative charges at the DNA backbone is also measured by recording the TTF.

So far, it was only assumed that the Debye length influences the DC measurements, where the ions are shielded by counterions in the electrolyte solution. The higher the applied buffer concentration is, the lower is the Debye length. At frequencies higher than 100 kHz, the amplitude variations are even more pronounced. It is known that particularly ionic interactions are affecting the measurements at frequency ranges below 1 MHz [261]. As shown in *Figure 47*, the dielectric property ε_{Bio} of the biomembrane could also play a role due to the surface architecture. Nevertheless, also in physiological buffer regime, the DNA is still detectable in AC mode. It seems, however, that the shift is turning into the opposite direction with higher ionic strength. The exact mechanism needs to be clarified once more sensors will be fabricated in our group. Since it is possible to detect the analytes in physiological buffer solutions by using the AC mode, this readout method is promising towards a direct target molecule detection complex matrix such as tears, saliva, liquor or blood.

5.3.6 AC readout of immobilization and hybridization signals

In the next step, the hybridization was detected by the previous described TTF method. After each experimental step, the TTF was measured in 0.001× PBS so that we were able to compare the shift in g_m. In *Figure 49 a*, the comparison of the electronic results for the TTF spectra are shown. We compared the g_m after silanization, immobilization, blocking, hybridization with concentration 1 (0.5 µM) and hybridization with concentration 2 (1 µM) (n = 6 nanowires). Therefore, the TTF measured after GPTMS silanization was set to zero to serve as baseline. To further compare the results, the change in g_m (Δg_m) between two following experimental steps was calculated. The comparison of the TTF spectra after silanization (GPTMS) and after site-specific immobilization of 1 µM capture DNA resulted in a shift of 0.16 µS to a higher g_m value. An increase of 0.87 µS was evaluated after blocking with 1 % BSA solution. The hybridization with 0.5 µM cDNA led to a shift of about 1.72 µS to lower values whereas Δg_m of about 2.42 µS to higher values was achieved after hybridization with 1 mM cDNA. Since the g_m value is not stable after the second hybridization, it can be

assumed that the nanowire area was not saturated by the lower target molecule concentration. In *Figure 49 b*, the statistical evaluation is shown.
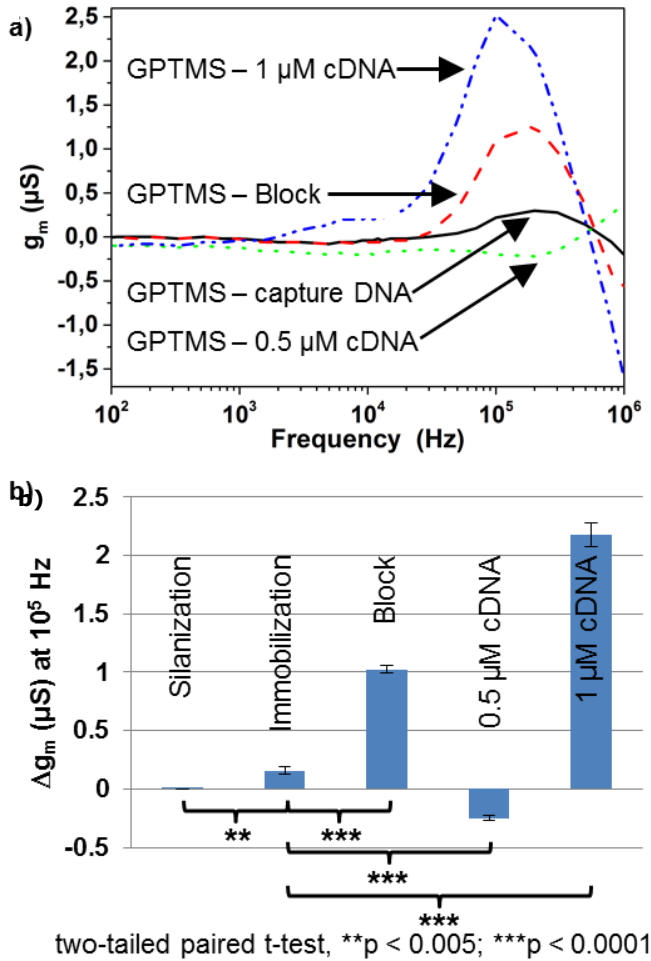
Figure 49: Differential plot of DNA immobilization and hybridization.

Differential plot of the AC readout in 0.001× PBS after different experimental steps: GPTMS (black), capture DNA (red), blocking with 1 % BSA (green), hybridization with 0.5 µM cDNA (dark blue) and 1 µM cDNA (light blue) (a), statistical evaluation of the electronic data (n = 6) (b). The results were published in [207].

The calculated standard deviation is better than the standard deviation achieved for the same measurements achieved with the dc-readout (see Chapter 5.3.2). It might be that the standard deviation can be decreased further by using SiNW FETs with similar characteristics of the different channels. Moreover, SiNW FETs

with different number of wires per channel were applied and the chips were used for several experiments, which is also affecting the standard deviation. In an ideal case, a new sensor with similar characteristics should be used for each experimental trial to obtain a smaller standard deviation. So far, it is assumed that the change of the transistor's transfer function is due to a change in impedance when biomolecules bind to the sensor surface [32,33,156,211,213]. Our results suggest that it is predominantly caused by a capacitance change based on the binding of electrically charged molecules. This results in a change in transconductance. The immobilized charges may influence the TTF spectra as well. This is also supported by the results shown in section 5.3.4, which were performed in different concentration of buffer solution. There, it was shown that the Debye screening is also affecting the TTF. To verify, which parameters and effects influence the TTF, simulation, fittings and further experiments on new transistors need to be performed in future experiments in our group. However, it can be assumed that this readout principle leads to clearer and bigger signals, which makes it a promising method for biomedical applications. In combination with the DC readout, a double verification of the results would be achieved to reduce false-positive or –negative recordings.

5.4 Detection of HLA-B 27 – Preliminary results

As described in Chapter 2.2.4, HLA-B27 is a glycoprotein of the major histocompatibility complex and involved in the T-cell mediated immune reaction [105]. Diseases as Morbus Bechterew, Morbus Reiter and other forms of arthritis are related to the hereditary characteristic of HLA-B27 [108,109]. After having shown that the detection of artificial single-stranded DNA sequences can be performed with our ISFET and silicon nanowire platform, a real assay was tested in a couple of proof-of-principle trials on the microscaled chips. Due to a lack of the SiNW FETs, it was not possible to test this assay also on the nanoscaled device. In doing so, a HLA-B27 assay was transferred onto our sensor. The DNA components of the assay were kindly provided by Euroimmun Medizinische Labordiagnostika AG.

5.4.1 HLA-B27 detection on ISFETs – DC & AC readout

As already mentioned in Chapter 2.2.4 and 3.6.1, the HLA-B27 detection is important for the determination of HLA-B27 related disease and also crucial before implementing bone marrow, organ or stem cell transplantation. For this reason, measurements of a HLA-B27 related DNA sequence were performed on ISFETs. The applied sequence was 20 base pairs long. In brief, the experimental procedure of the assay was done as following: After having silanized the transistors with GPTMS, 1 µM single-stranded capture DNA was site-specifically immobilized onto the gate area by means of microspotting. In the following step, the free binding sites on the sensor surface were blocked with a 1 % BSA solution. Finally, the target sequence was applied to detect the hybridization with the complementary capture DNA. The detection of all experimental steps was done in 0.15 mM phosphate buffer pH 7.4. An exemplary, preliminary result of the experiments at $V_{DS} = -3$ V can be seen in *Figure 50*.
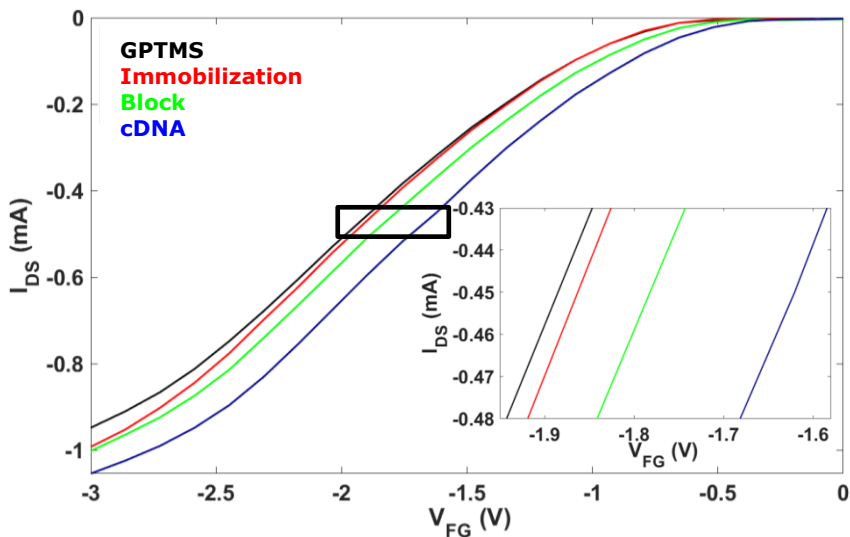
Figure 50: Exemplary DC readout of the HLA-B27 assay performed on an ISFET.
In this figure, the different steps of the HLA-B27 assay, measured by recording the TC curve of an ISFET, are represented. The TC curves were all measured at $V_{DS} = -3$ V. Due to the negative charge of capture, blocking and target molecules, V_{TH} is shifted to more positive values. This is in agreement with previous publications, which dealt with the hybridization of artificial DNA on field-effect based devices [54,165,230].

After immobilization, the ΔV_{TH} is 24 mV to more positive values. The blocking with 1 % BSA causes a shift of 78 mV. The strongest change in V_{TH} was observed after the hybridization. It was calculated to be 156 mV. Since DNA and BSA are both negatively charged at pH 7.4, the V_{TH} shift to more positive values can be explained. These observations are in good agreement with previous publication, which dealt with the immobilization and hybridization of DNA strands [54,165,230]. The experiment was repeated on some other chips, on which the signal change was measured to be in the same direction and about the same magnitude. The only difference between the measurements was the signal intensity and, hence, the ΔV_{TH}. Nevertheless, the preliminary measurements and the corresponding results indicate that the experiment with the HLA-B27 DNA seems to work on our microscaled platform. However, for a profound conclusion more experimental trials need to be performed in further projects, also in order to a significant statistical evaluation. Once the assay is reliably established on the ISFETs, it can be transferred onto the nanowire device. In *Figure 51*, the corresponding TTF can be seen as an exemplary result for the HLA-B 27 measurements on ISFETs. Comparing the TTF curve at a frequency of 30 kHz, it is shifted to lower values after each experimental step. After immobilization of the HLA-B27 capture sequence, $\Delta g_m = 32$ µS, after blocking it is 190 µS and after hybridization with the target DNA, Δg_m was calculated to be 264 µS. It seems that the transconductance is decreased because of an increased capacitance and a change in impedance, caused by the binding of more molecules during the experiment. This effect was already described in a publication of our group before, where a similar experiment was performed [156]. The change of the TTF curve for a fully-mismatched, a one mismatch and a perfect match DNA sequence was detected and, hence, the possibility for point mutation detection was demonstrated [156]. The authors explained that DNA molecules are difficult to be protonated or deprotonated, wherefore the resistance of the charged transfer would be increased, which leads to a higher membrane resistance of the biomolecule, R_{Bio}, in the electrically equivalent circuit. In consequence, the time constants τ_1 and τ_2 (see equation (3.10) and (3.11)) should be shifted to more positive values.
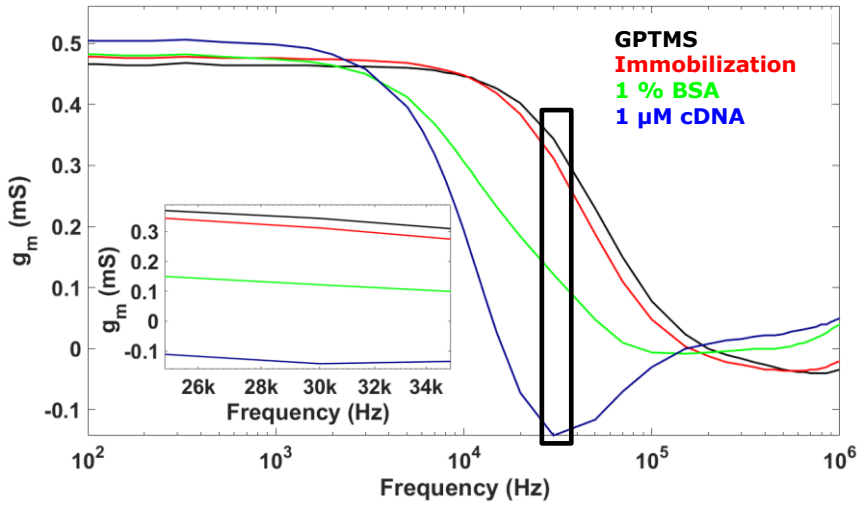
Figure 51: Exemplary AC readout of the HLA-B27 assay performed on an ISFET.

Here, the HLA-B27 assay measured by the AC readout is shown. The biggest change in g_m was evaluated to be at 30 kHz. The experiment was performed on ISFETs and recorded in 0.15 mM phosphate buffer pH 7.4. Similar to an earlier publication by our group, the transconductance decreases after each experimental step [156]*.*

In summary, these preliminary data indicate that the silicon nanowire platform can be used for the detection of medically relevant DNA sequences. By reducing the concentration of the target analytes further, it could be evaluated if the sensors can be used for the measurements of ultralow molecule concentrations. By combining the two readout methods, it would also be possible to obtain more reliable results compared to individual transducer principles.

Chapter 6 - Protein assays: Detection of BDNF

Besides the establishment of a DNA assay, protein experiments were conducted with the sensors. For this purpose, parts of an ELISA assay were transferred onto the nanowire platform as described in Chapter 3.6.2. With this ELISA kit, purchased from R&D systems, Inc., USA, it is possible to detect the brain-derived neurotrophic factor (BDNF), a neurotrophin, which plays an important role in the central and peripheral nervous system. A reduced BDNF level is related to Alzheimer's or Parkinson's disease. Moreover, it is involved in many more severe clinical patterns and, hence, it would be of great benefit to detect a decreased BDNF concentration as soon as possible and as easy as possible. Therefore, a fast and sensitive detection of a pathologic BDNF level could be an important step towards an early-stage determination of different disease. The BDNF concentration is normally determined in human serum.

The BDNF experiments were performed on ISFETs and on SiNW FETs. In doing so, the DC and AC readout were implemented by measuring the TC and the TTF of different experimental steps. Furthermore, different target protein concentrations were applied, and the detection was done in different buffer concentrations. For the nanowire platform, a multivariant data analysis of the obtained results was applied to gain more information and to demonstrate how the two readout methods could be combined for evaluation of the recordings.

6.1 Optical reference experiments with BDNF

To verify that the applied immobilization and protein binding protocol is working, fluorescence-based experiments were performed. The optical result is displayed in *Figure 52 a* and *b*. For the immobilization verification, 2 µg/mL mouse anti-human BDNF (BDNF specific capture antibody) was immobilized overnight at room temperature on epoxy modified SiNW FETs. Blocking was done with 1 % BSA for 30 min at room temperature. To allow fluorescence microscopy, goat anti-mouse (GAM)-ALEXA 488 antibody was bound for 30 min at room temperature. For the initial proof of the BDNF binding, 2 µg/mL BDNF specific

capture antibody was immobilized on GPTMS silanized SiNW FETs as a first step. Afterwards, the surface was blocked with 1 % BSA as described before.
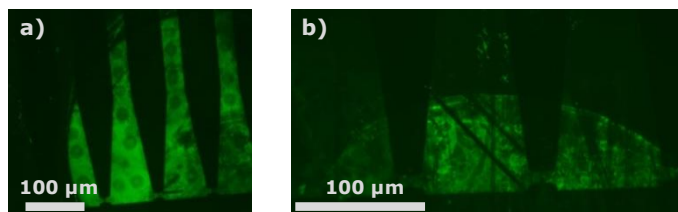
Figure 52: Optical reference experiments of the BDNF assay.

The fluorescence result of the immobilization of the BDNF specific antibody is shown in (a). The antibody was successfully immobilized on some of the nanowires and parts of the surrounding area. In picture (b), a successful binding of BDNF to its capture molecule can be seen.

After the binding of 2 ng/mL BDNF (~ 71.8 pM) for 2 h at room temperature, 25 ng/mL biotinylated mouse anti-human BDNF detection antibody was attached for 2 h at room temperature. Streptavidin-ALEXA 488 was bound as fluorescent dyed molecule for 30 min at room temperature.

6.2 DC and AC readout of BDNF on ISFETs

The BDNF assay kit was chosen because BDNF has various functions in the human body. A malfunction or a limited production of the antigen is described to be involved in different severe diseases like Alzheimer's, Parkinson's or Huntington's disease. More details about the biomolecule are described in Chapters 2.1.3 and 3.6.2 of this thesis.

The intention was to study whether it is feasible to detect concentrations of the target antigen, which are in the range of the detection limit of the commercially available antibody-antigen assay. In the framework of these experiments, concentrations as low as 1 pg/ml (~ 35.9 fM BDNF), 5 pg/ml (~ 179.5 fM), 10 pg/ml (~ 359 fM) and 50 pg/ml (~ 1.8 pM BDNF) of the target molecule BDNF were applied. The BDNF experiments were performed on the microsized FETs by recording the potentiometric and the impedimetric curves. The measurements were performed in 0.15 mM phosphate buffer pH 7.0 with controlled pH and conductivity. At pH 7.0, the neurotrophic factor is reported to be positively charged due to an isoelectric point (IP) of pH 9.99 [262]. The

obtained data of each experimental step, including silanization, immobilization, blocking and the binding of the four target protein concentrations, were plotted in one graph to allow a comparison. For this purpose, one step was also compared with its previous one. In *Figure 53*, an exemplary TC plot can be seen.
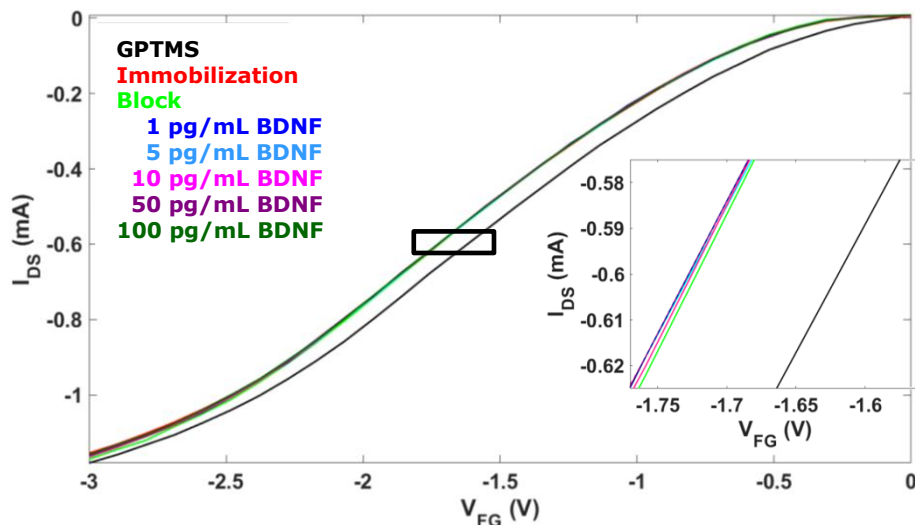
Figure 53: BDNF assay on an ISFET – DC evaluation.
In the inset, it is visible that only the immobilization leads to a shift of V_{TH}. All other steps only lead to tiny changes, which were not significant.

It is visible that only the immobilization can be detected with the used ISFETs. Further experiments on more chips led to the same results. A slightly different observation was obtained after having evaluated and compared the TTF data. The AC readout was done right after each DC measurement. The results of the TTF recordings are displayed in *Figure 54*. In contrast to the DC results, the blocking and the binding of 1 pg/mL and 5 pg/mL BDNF could be detected, whereas the binding of the two higher BDNF concentrations only lead to a tiny change. However, the mentioned shifts are only small and not significant in comparison to the GPTMS baseline. The extracted DC results indicate that it is not possible to detect very low protein concentrations with the microsized platform. Even 50 pg/mL BDNF were not measurable with the devices as well. Furthermore, the change in transconductance was only visible by a magnification of the evaluated plots. The measured changes were not significant. The limit-of-detection of the commercial ELISA kit is reported to be 30 pg/mL (~ 1.08 pM)

BDNF. This means that the used DC mode performed on ISFETs is not as sensitivity as the optical assay.
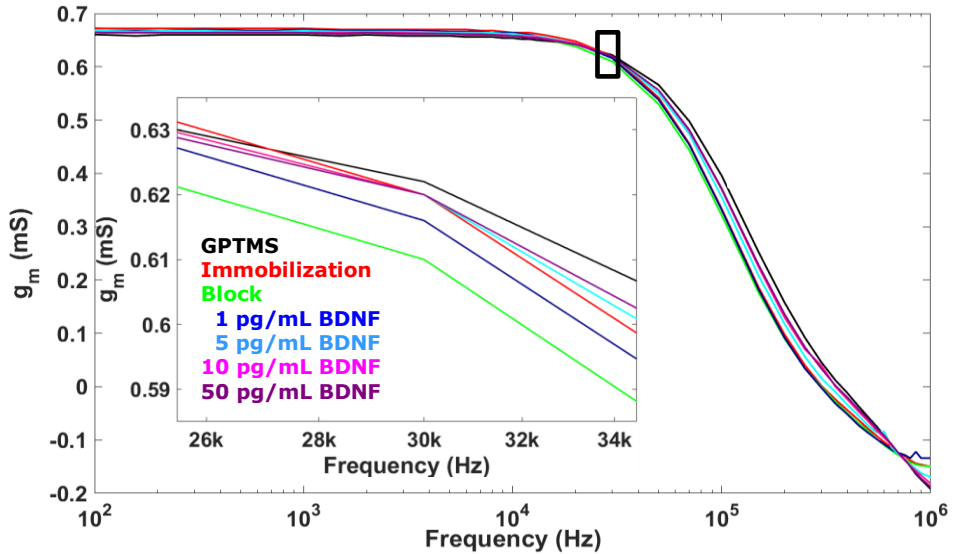
Figure 54: BDNF assay on an ISFET – AC evaluation.

By looking at the inset, it can be seen that the immobilization, blocking and the binding of 1 pg/mL as well as of 5 pg/mL BDNF lead to a shift of V_{TH}. All other steps only lead to a tiny change.

Therefore, further experiments were done on the nanowire FETs, since those biosensors were reported to be capable to detect ultralow molecular concentrations [11,35,36]. Nevertheless, the recordings show the remarkable potential of the SiNW FETs for their application as a biomedical readout tool. Since it was possible to detect concentrations in the fM regime, it can be assumed that the biosensors possess the potential for an early-stage detection of diseases, where very low analyte concentrations need to be detected. This would be helpful for an early treatment of the patient and could at best save lives.

6.3 BDNF readout on SiNW FETs

6.3.1 DC readout of BDNF on SiNW FETs in different buffer concentrations

One aim of the study was to detect the influence of different buffer concentration on the measured signal. In doing so, four different phosphate buffer concentrations were applied. The initial concentration was 0.15 mM which was then stepwise increased by a factor of ten to the final buffer strength of 150 mM. The results for one exemplary DC measurement are shown in *Figure 55*. For all four buffer concentrations, the TC detected after GPTMS served as base lines (solid lines) and were compared with the signal obtained after the binding of 50 pg/ml BDNF (dashed lines). As it can be seen in *Figure 55*, the highest signal was obtained by measuring in the lowest concentrated solution (red solid and red dashed lines). The signal decreased with increasing ionic strength. For 15 mM and 150 mM phosphate buffer, the signal strength was the lowest. These results are agreement with the previous published data [163].
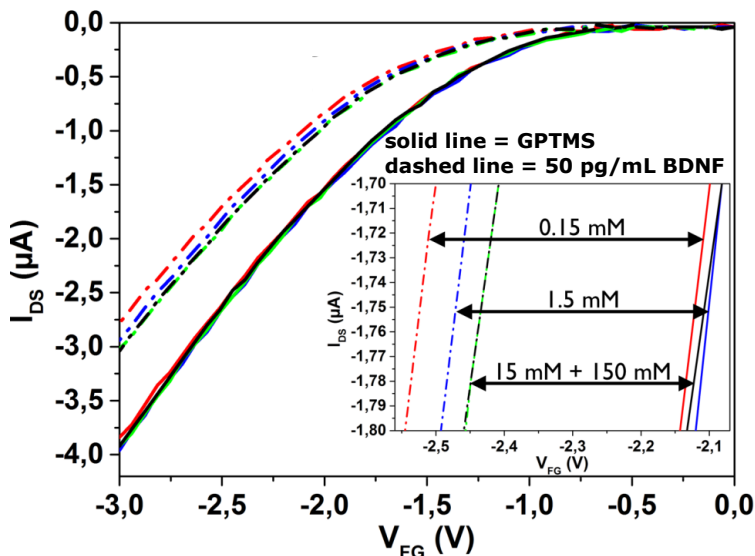
Figure 55: Exemplary result of TC measurements in different buffer concentrations.

The detection was done in 0.15 mM, 1.5 mM, 15 mM and 150 mM phosphate buffer.

As reported for DNA molecules, where the negative charge of the phosphate backbone is shielded by counterions [45], the positive charges of the proteins are screened by counterions as well. However, there was still a measurable shift in the TC, even though the Debye screening effect is relatively large in highly concentrated solutions. As commonly known, the Debye screening has a strong influence on the measured signal gained by the DC readout. In our experiments, we wanted to investigate the effect on the received signal strength to derive conclusions whether a clinically relevant concentration of BDNF could still be measurable in highly concentrated salt solutions. This is of interest since the Debye screening effect of blood is also high and comparable with our highly concentrated buffer solution. The ionic strength of blood is reported to be around 0.16 M in literature [263]. We obtained the typical effect of an increasing signal strength with decreasing buffer concentrations. Nevertheless, our results indicate that 50 pg/ml ($\sim$ 1785 fM) of BDNF can still be measured in solutions with high ionic strength. Lang et al. tested the serum BDNF level of 118 healthy patients with an age of 42.1 $\pm$ 13 years [264]. The serum level of the nerve growth factor was around 16.3 $\pm$ 7.3 ng/mL. They also discovered that this serum concentration is depending on the age and decreases with increasing age. However, there is no gender specificity. Since the clinically relevant concentration of BDNF is reported to be in the range of ng/ml, the limit of detection of our system is much lower than the relevant concentration. In consequence, we assume that our SiNW FETs might be applicable as diagnostic tool for the detection of clinically relevant BDNF levels in highly concentrated buffer solution. By performing several optimization steps, it might even be possible to directly measure the analyte in human liquids. As discussed in a later chapter of this thesis, a differential readout of devices of electronically comparable sensors of a chip and multiparametric detection with precise control of side parameters is advised.

6.3.2 Immobilization of capture molecules and BDNF binding: DC readout

The aim of the experiments was to establish an antibody-antigen assay onto our silicon nanowire platform. Furthermore, the goal of implementing the assay on SiNW FETs was to be able to compare the results with the results obtained on

the microscaled ISFETs later on. A particular point was the sensitivity of both platforms. In this chapter, the focus is set on the DC readout of the experiments, which was performed by measuring the transfer characteristics of the SiNW FETs. The DC readout was done after each experimental step to allow a comparison of the received data. In doing so, we measured the TC after silanization, immobilization of mouse anti-human BDNF antibody, blocking and binding of four different BDNF concentrations. The different target molecule concentrations were successively added. In comparison with the blank device, on which only the surface modification with the silane GPTMS was done (black curve), the TC shifted to more negative values after the immobilization with the capture antibody (red curve). The shift was about 15 mV in average. The blocking step resulted in a shift of 60 mV (green curve). The binding of the four different BDNF concentrations led to a change of around 130 mV (dark blue curve), 133 mV (light blue curve), 144 mV (pink curve) and 155 mV (dark green curve), respectively. In *Figure 56 a*, an exemplary graph for the experiment is shown. Since the isoelectric point of BDNF is reported to be around 9.99 [262], BDNF is positively charged when it is diluted in a buffer solution with pH 7.0. Hence, the observed shifts to more negative values were in agreement with what we expected. To be able to make a more general statement on our measurements, we did also a statistical evaluation of the complete data set. The statistics can be seen in *Figure 56 b*. The values obtained after the GPTMS silanization served as baseline. The immobilization, the blocking step and the binding of 1 pg/ml BDNF showed a significant change in V_{TH}. It was possible to immobilize the mouse anti-human BDNF antibody to our epoxy siloxane modified SiNW FET surface. Furthermore, it was feasible to detect BDNF down to a concentration of 1 pg/ml BDNF, which is equal to ~35.7 fM BDNF. This concentration is lower than the concentration, which can be detected with a commercially available ELISA assay, where the limit of detection is reported to be approximately 30 pg/ml at low optical density. This shows that our SiNW FET sensors are highly sensitive for biomolecular detection. The addition of higher BDNF concentrations, lead to a change of the TC to more negative values as well. However, this shift was evaluated not to be significant. We assume that this can be explained by the fact that the different concentrations were successively added without regeneration of the chip in between the different

molecule concentrations. Moreover, it might be that all binding sites of the capture molecule were already saturated by the target antibody.
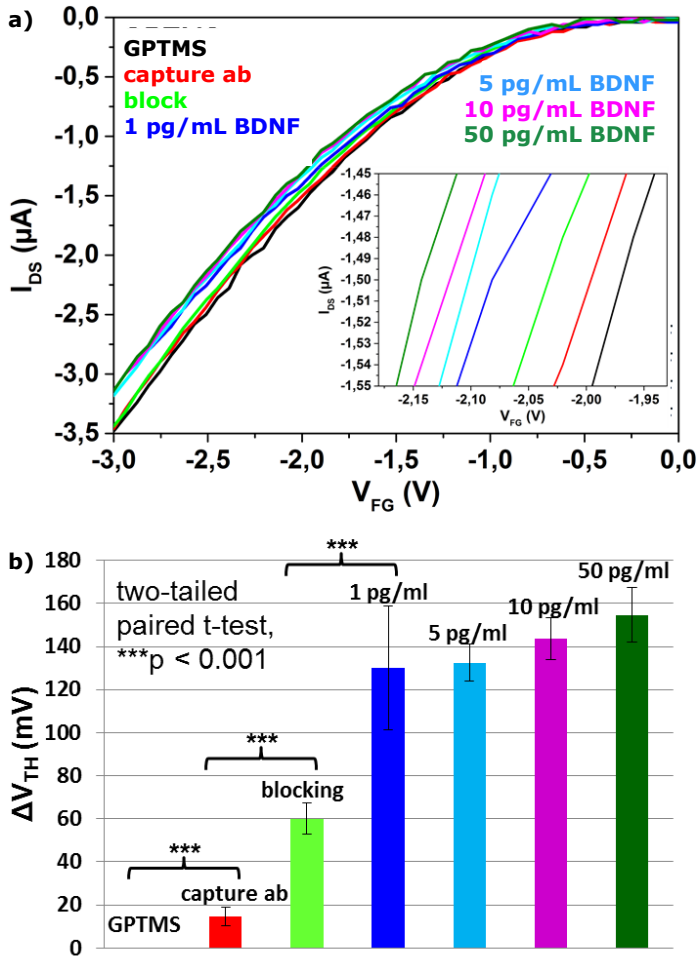
Figure 56: BDNF assay on a SiNW FET – DC evaluation.

Exemplary transfer characteristic of a SiNW FET after different experimental steps: GPTMS (black), capture molecules (red), blocking (green), binding of 1 pg/ml (dark blue), 5 pg/ml (light blue), 10 pg/ml (pink) and 50 pg/ml BDNF (dark green). The transfer characteristics is shifted to more negative values due to a positive charge of capture and target molecules at pH 7.0 (a). Statistical results of the DC measurements. The value after silanization served as baseline. It can be seen that the immobilization, the blocking and the binding of 1 pg/ml BDNF are significant (two-tailed paired t-test) (b).

To verify this, further experiments need to be done, where only one target molecule concentration is applied per chip. To compare the sensitivity of a

commercial BDNF ELISA kit with the SiNW platform used in this thesis, the change in V_{TH} was plotted against the optical density. The result can be seen in *Figure 57*.
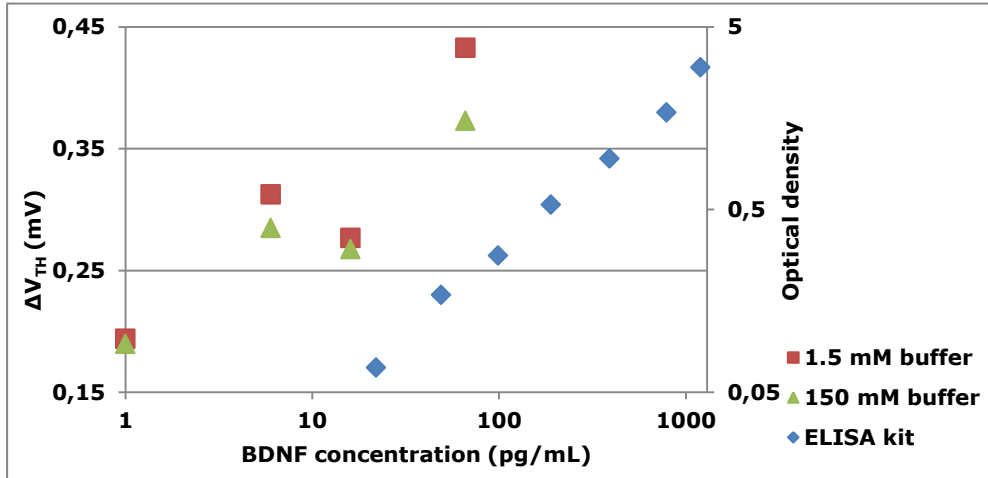
Figure 57: BDNF assay - Commercial ELISA kit versus SiNW FET DC recording.
In this figure, the change in V_{TH} measured in 1.5 mM and 150 mM phosphate buffer on SiNW FETs, was plotted against the optical density derived by a commercial ELISA kit. The BDNF detection seems to be more sensitive with the SiNW FET in comparison to the commercial available optical method.

The plotted values of the optical density were taken from the data sheet of the applied ELISA kit. In doing so, the TC data obtained after measuring in 1.5 mM and 150 mM phosphate buffer were used for comparison. The limit of detection for the ELISA kit is mentioned to be at 30 pg/mL. With the SiNW FET, it was possible to detect BDNF concentrations down to 1 pg/mL by performing the DC readout. This is about 30× lower than the limit of detection of the utilized ELISA kit. Therefore, the nanowire platform seems to be more sensitive than the optical method. Moreover, since the minimum concentration, which could be detected with this device, was not yet determined, it is possible that even lower concentrations than 1 pg/mL are measurable. This is another indication that the silicon nanowire biosensor platform could be used to determine very low target molecule concentrations and, hence, for an early-stage diagnostic at the onset of a disease progression.

6.3.3 Immobilization of capture molecules and BDNF binding: AC readout

To gain further information about the BFND assay, AC measurements were done as well. Like performed for the other biomolecular assays, the TTF was measured subsequently after the DC readout and for each experimental step. After the experiment was finished, the data were evaluated, and all received curves were plotted in one graph to allow a comparison of the different steps. An exemplary graph of one channel for one whole experiment is shown in *Figure 58 a*. For the statistical evaluation, the TTF measured after the silanization was set to zero and served as baseline. By comparing the obtained data at a frequency of 100 kHz, the following examinations were done for this exemplary experiment: After immobilization (red curve), the TTF is shifted about 0.52 µS to a higher g_m value compared to the curve after silanization (black). The g_m value after blocking (green) was heightened to 1.03 µS. Then it was decreased to 0.62 µS after the binding of 1 pg/mL BDNF (dark blue) and even further decreased to 0.34 µS after 5 pg/mL BDNF (light blue). The addition of 10 pg/mL BDNF (pink) led to an increase of the transconductance to 0.42 µS, whereas it was lowered to −0.048 µS after having bound 50 pg/mL target analyte (green). The statistical extraction can be seen in *Figure 58 b*. The statistic showed that it seems that all experimental steps were significant (two-tailed paired t-test). This examination indicated that recording the TTF is as well much more sensitive than the limit-of-detection of the ELISA kit. Furthermore, in comparison to the DC results, there is the tendency that the AC readout is more sensitive to the binding of the target analyte BDNF. Indeed, it was not possible to detect the binding of all four BDNF concentrations with the potentiometric method, but the statistical evaluation showed that the results after 5 pg/mL, 10 pg/mL and 50 pg/mL BDNF were not significant. In contrast to this observation, these results were strongly significant by performing the AC measurements. This is also leads to the conclusion that not all binding sites of the capture molecules, located on the nanowire, were occupied and that the sensor surface was not saturated yet. It can be excluded, too, that a shift of the reference electrode or a change of conductivity of the measuring solution influenced the results, since both parameters were kept stable during the experimental procedure.
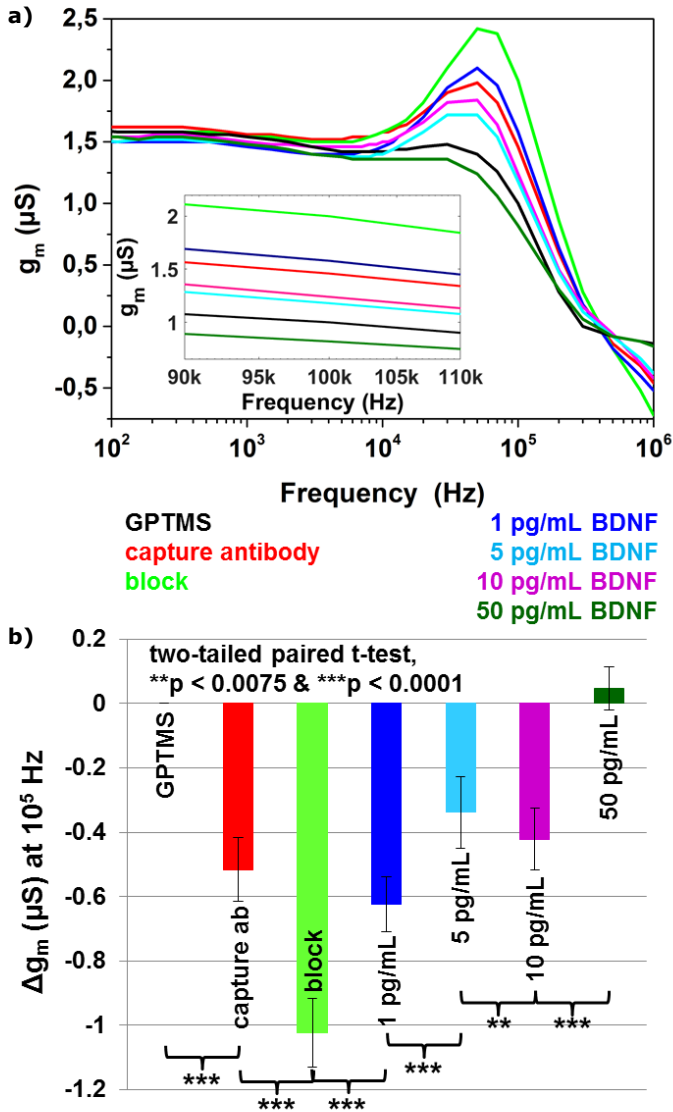
Figure 58: BDNF assay on a SiNW FET – AC evaluation.

In (a), an exemplary TTF evaluation of one channel is shown. It can be seen that the curves shift after each experimental step (immobilization, blocking, 1 pg/mL BNDF, 5 pg/mL BDNF, 10 pg/mL BDNF and 50 pg/mL BDNF). In (b), the statistical evaluation for eleven channels of one chip is displayed.

A second chip, in another independent experiment, showed the same tendency. In this trial, the experimental procedure was the same as for the chip, shown in this thesis. The parameters, such as the position of the reference electrode and

the composition of the buffer, were also identical and kept stable. The only differences were the dimensions of the nanowires on the chips and the obtained signal strengths. Therefore, both chips were not considered in the statistics represented here. Nevertheless, these observations show the advantage of the AC readout for biomedical assays, in which the detection of low concentrations is needed. However, to verify these examinations more experiments with further chips need to be performed. As for the DC readout, the results for the AC detection were compared with those of the ELISA. The corresponding evaluation can be seen in *Figure 59*.
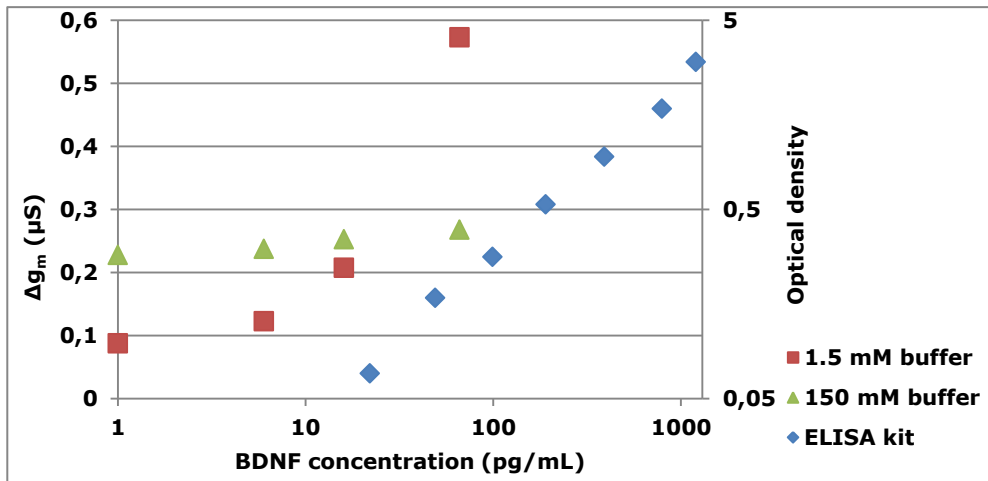
Figure 59: BDNF assay - Commercial ELISA kit versus SiNW FET AC recording.
The shift in transconductance measured in 1.5 mM and 150 mM phosphate buffer on SiNW device was evaluated against the optical density result of a BDNF ELISA kit. Like shown for the DC detection, the AC readout of nanowire FETs seem to be more sensitive than a standard ELISA kit. This could be of great interest for the early-stage detection of diseases.

For this purpose, a comparison of the Δg_m-values measured in 1.5 mM and 150 mM buffer solution was plotted versus the optical density of the commercial ELISA kit. Similar to the observation with the DC method, the measurement of the TTF by performing the AC method seems to be 30× more sensitive than the optical assay. By comparing the DC with the AC readout, the results seem to be almost the same. To derive further conclusions about the sensitivity of both readout methods, the applied concentrations need to be further decreased. By doing so, it should be possible, to determine the ultimate limit-of-detection of

the nanowire platform. These data support the previously postulated assumption that the SiNW FETs can be applied as biomedical platform for the detection of low biomolecule concentrations. Due to a combination of the DC-and AC-method the results could become more significant and, therefore, more reliable. This would be an important step towards an application in the medical field, where reliable results avoiding false positive and – negative detections are crucial.

6.3.4 DC and AC readout of BDNF in balanced salt solution – Preliminary results

In the experiments previously reported in this thesis, the measurements were performed in phosphate buffer, which only consisted of two components, *i.e.* Na_2HPO_4 and NaH_2PO_4. In a first trial, the BDNF readout was done in Hank's balanced salt solution (HBSS). This solution possesses a physiological pH and the salt concentration is isotonic. It is most commonly used in cell cultures as buffer system to ensure cell growth. In contrast to phosphate buffer, it consists of more than two ingredients which could unspecifically bind on insufficiently blocked sensor areas. HBSS contains following components: NaCl, KCl, $CaCl_2$, KH_2PO_4, $MgSO_4 \times 7H_2O$, $MgCl_2 \times 6H_2O$, $Na_2HPO_4 \times 2H_2O$, glucose and $NaHCO_3$. Therefore, this experiment represents a first step towards measuring in synthetic serum and, finally, in human serum or whole blood.

To examine whether it is still possible to detect BDNF in a measuring solution consisting of various components, the same experimental procedure was used as described in Chapter 3.6.2. The applied concentrations and analytes were the same as well, only the phosphate buffer was exchanged against HBSS. The exemplary DC and AC results of one channel are represented in *Figure 60 a and b*, respectively. The TC measurements showed the same tendency as those, which were done in the two components buffer. After each step, the curves are shifted to more negative values, which is in agreement with the positive charge of the used biomolecules. In contrast to the V_{TH} results, the change in the g_m value was different compared to the measurements performed in phosphate buffer reported in Chapter 6.3.3. As shown for the measurements in phosphate buffer, the g_m value of the TTF is increased after immobilization of the capture molecule. Opposite to the blocking results in phosphate buffer, the AC curve is lowered after blocking.

135
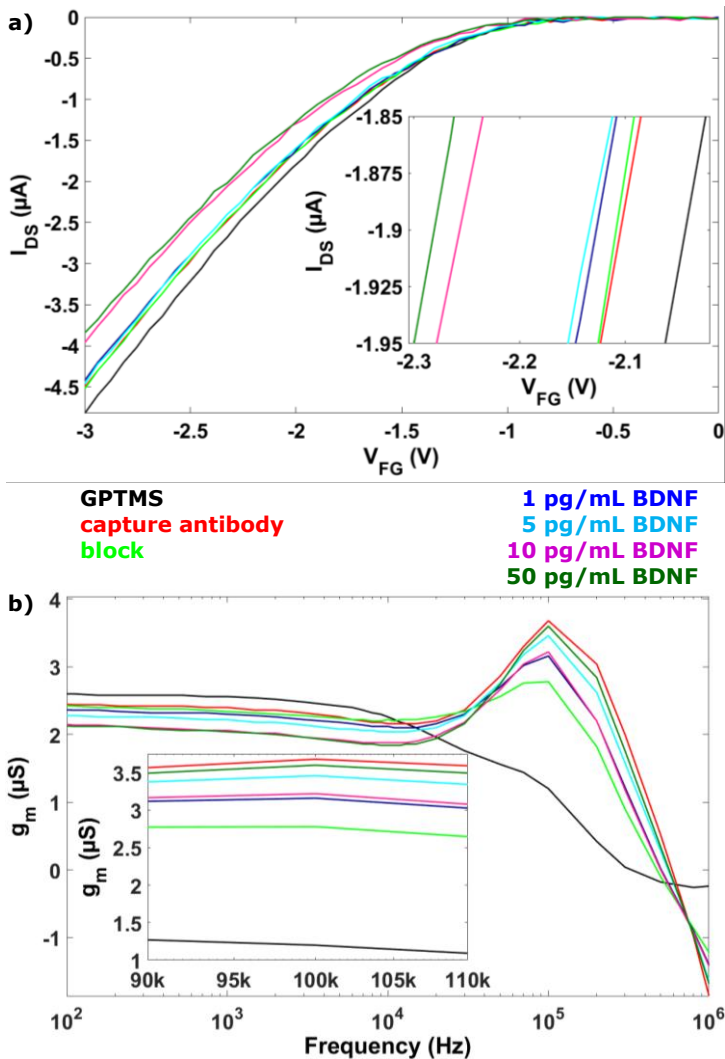
Figure 60: Exemplary DC & AC readout results of BDNF in physiological HBSS.

In (a), the TC results for one BDNF experiment made on a SiNW FET are displayed, whereas the corresponding TTF results can be seen in (b).

The subsequent binding of 1 pg/mL and 5 pg/mL BDNF in HBSS lead to a rise of the g_m value to higher values, respectively, whereas the same concentrations decreased the g_m value in phosphate buffer. The attachment of 10 pg/mL BDNF in HBSS decreased the TTF and 50 pg/mL BDNF increased the TTF. The reason for these observations can be the difference in conductance and components of the HBSS buffer, in which the BDNF binding was done. The evaluation indicates

that, besides the BDNF binding to the specific capture antibody, some ingredients of the applied buffer bound unspecifically to not completely blocked areas on the nanowire surface. The evaluated results give another hint that the AC readout is more sensitive than the DC mode and the evaluated data indicate that the sensors can be used in physiological buffer solutions. As already mentioned before, this could be a first step towards measuring in complex matrix such as blood, tears, saliva or liquor.

6.4 Advanced BDNF data analysis

In the last subchapter of this thesis, the focus is set on a multivariant data analysis and a classification of the previously presented BDNF results. The rational is to combine the AC and the DC data in a combined analysis to increase the reliability of the assay.

Besides evaluating ΔV_{TH} and Δg_m, more variables can be extracted from the measured raw data so that a multivariant data analysis is created. The idea of a multivariant data extraction is to cancel out influences of side parameters within a measurement and to gain further information about the target. The multivariant data analysis should help to eliminate sensor variations by considering the different variables of the measurements and, hence, to increase the reliability. Furthermore, statistical deviations should be reduced to a minimum. It should be feasible to determine different concentrations of one type of molecules in the measurement solution. The ultimate goal would be to identify an unknown molecule or substance in an arbitrary solution including its concentration. Moreover, a classification of the BDNF data was done with help of machine learning. In doing so, various classification trees had to be created to distinguish between the experimental steps and the applied concentrations. Finally, the accuracy of this classification model was determined by using the K-fold cross validation method.

6.4.1 Multivariant data analysis

For all calculations, the results measured after silanization were set to zero and served as baseline. In the framework of this thesis, the following DC variants were extracted and calculated with a custom-made Matlab program:

1. V_{TH}: The threshold voltage, V_{TH}, was described in more detail in Chapter 3.7.1. In short, it is the parallel shift between two TC curves. For the determination of this shift, the steepest slope of the baseline curve was evaluated (*Figure 61 a)* [16,20][152]. Unit = mV

2. $\dfrac{\Delta I_{DS}}{\Delta V_{GS}}$: This variant is derived from the first derivation of the TC curve.

   The steepest point of the TC of the baseline corresponds to the maximum derivative. Furthermore, the I_{DS} value at that steepest slope is needed to determine $\dfrac{\Delta I_{DS}}{\Delta V_{GS}}$ of the TC curve of the experimental step.

   Then $\Delta\left(\dfrac{\Delta I_{DS}}{\Delta V_{GS}}\right)$ can be calculated by subtracting $\dfrac{\Delta I_{DS}}{\Delta V_{GS}}$ of the baseline

   from $\dfrac{\Delta I_{DS}}{\Delta V_{GS}}$ of the experimental step (*Figure 61 a* and *b*) [265–267].

   Unit = nanoSiemens (nS)

3. $\left(\dfrac{\Delta I_{DS}}{\Delta V_{GS}}\right)_{max}$: The first derivation of the TC of the baseline and the TC of

   the experimental step is calculated. Then, the highest point of both derivatives is set and subtracted from each other (*Figure 61 c*) [265–267]. Unit = nS

To aid for a better overview of the individual parameters, a schematic was prepared as an example (*Figure 61*).
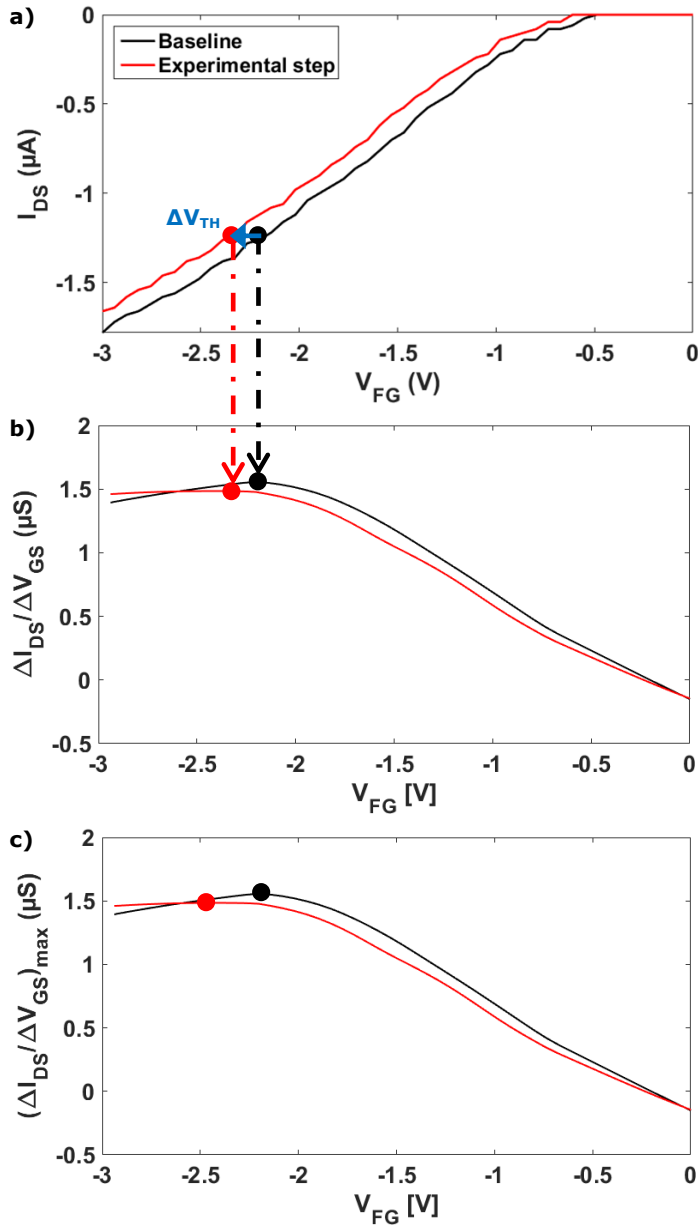
Figure 61: Overview of the DC variants of the multivariant data analysis.

In this schematic, the variants of the DC mode for the multivariant data analysis are displayed. The black curve (=baseline) was measured after silanization and the red curve (=experimental step) after the incubation with 10 pg/mL BDNF on SiNW FETs.

Besides these three DC parameters, four AC variables were evaluated. For a better

understanding, all the variants of the AC readout are represented in a schematic in *Figure 62*.
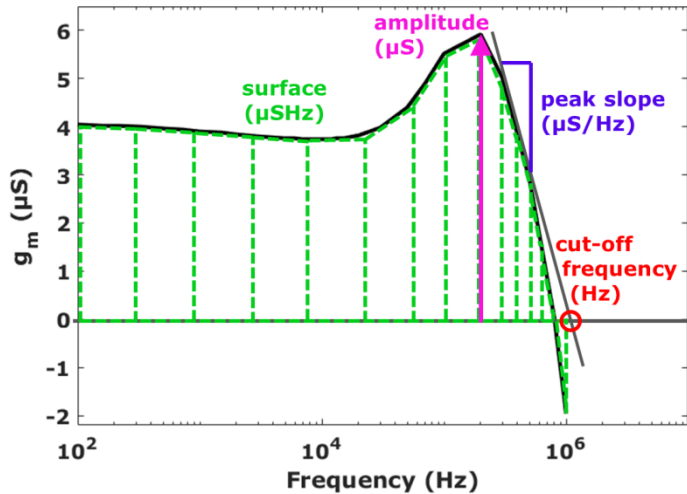
Figure 62: Overview of the four AC variants of the multivariant data analysis.

In this figure, a schematic explanation of amplitude, peak slope, surface and cut-off frequency, which were evaluated for the multivariant data analysis are shown.

The variables can be described as follows:

1. Amplitude Δg_m: The transconductance, g_m, was already described in chapter 3.7.2. To calculate the amplitude, the g_m–value at the highest point of the TTF curve was determined and subtracted from the zero line [156,211,215,216]. Unit = µS

2. Surface: For evaluating the surface, the trapezoid rule was used, which is only an approximation of the complete surface [268]. In doing so, the surface of a trapezoid was calculated by

$$surface = (b-a)\left(\frac{f(a)+f(b)}{2}\right) \tag{6.1}$$

Since the whole TTF curve consists of 41 measuring points, the surface of 40 trapezoids was determined and summed. Unit = µS·Hz

3. Peak slope: To extract the peak slope, a first degree polynomial fit, also known as linear fit, was done between two measuring points of the TTF [211]. The peak slope corresponds to the slope of this fit and was calculated as

140

$$slope = \frac{\Delta g_m}{\Delta frequency} \tag{6.2}$$

Unit = µS/Hz

4. Cut-off frequency τ_2: Similar to the peak slope determination, a linear fit between two measuring points of the TTF curve was done after the resonance peak started. The frequency at which the fit met the zero line was evaluated to be the cut-off frequency τ_2 [156,211,269]. Unit = Hz

For calculating the Δ-values, all variants were subtracted from the baseline. Afterwards, radar plots were created, which are a typical tool in multivariant data analysis [270–273]. In one radar plot, the previously mentioned variants of the AC and DC readout were gathered so that a seven-axle radar plot was resulting (*Figure 63*).
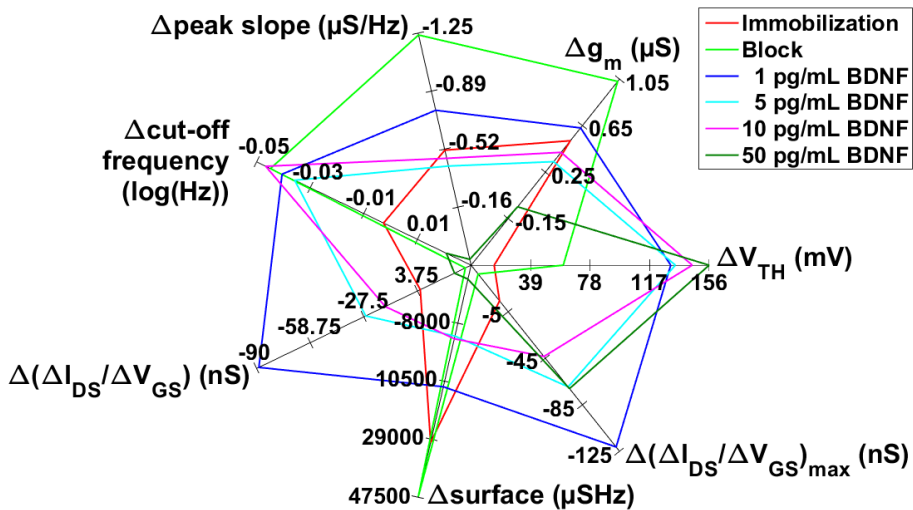
Figure 63: Multivariant data analysis of BDNF detection – seven-axle radar plot.
The evaluation of all seven variants from DC and AC recording are plotted against each other. For the multivariant analysis, the BDNF data was used. The different steps of the assay were compared whereby the GPTMS results served as baseline and were set to zero. Except amplitude and transconductance, the unit of each parameter is different and, hence, the scale is varying form variant to variant.

The mean values of all experimental steps and the respective variant are displayed in *Table 7*.

DC variants	Immo-bili-zation	Block	1 pg/mL BDNF	5 pg/mL BDNF	10 pg/mL BDNF	50 pg/mL BDNF
ΔV_{TH} (mV)	15	60	130	133	144	155
$\Delta\left(\dfrac{\Delta I_{DS}}{\Delta V_{GS}}\right)$ (nS)	5.4	31.7	- 88.7	-26.4	-15.0	25.3
$\Delta\left(\dfrac{\Delta I_{DS}}{\Delta V_{GS}}\right)_{max}$ (nS)	4.3	27.4	-121.3	-69.6	-43.5	-71.1
AC variants						
Δg_m (µS)	0.52	1.03	0.63	0.34	0.42	- 0.048
Δpeak slope (µS/Hz)	-0.52	-1.24	-0.77	-0.42	-0.47	0.16
Δcut-off frequency (log(Hz))	-0.006	-0.045	-0.41	-0.037	-0.047	-0.016
Δsurface (µSHz)	30046	47307	12259	-3901	-3032	-22054

Table 7: Mean values of all variants of the multivariant data analysis.

In this table, an overview of the mean values of each variant is represented for every experimental step of the BDNF data set. As mentioned above, the GPTMS data served as baseline and, hence, was set to zero.

In *Figure 64 a,* the parameters derived from the DC readout are plotted in a triaxial plot and in *Figure 64 b,* the four variants evaluated from the AC results are represented in a four-axle plot. This is done to receive a better overview of

the two different readout methods. To be able to compare the individual variables of the DC and AC modes, the seven-axel plot is preferred.
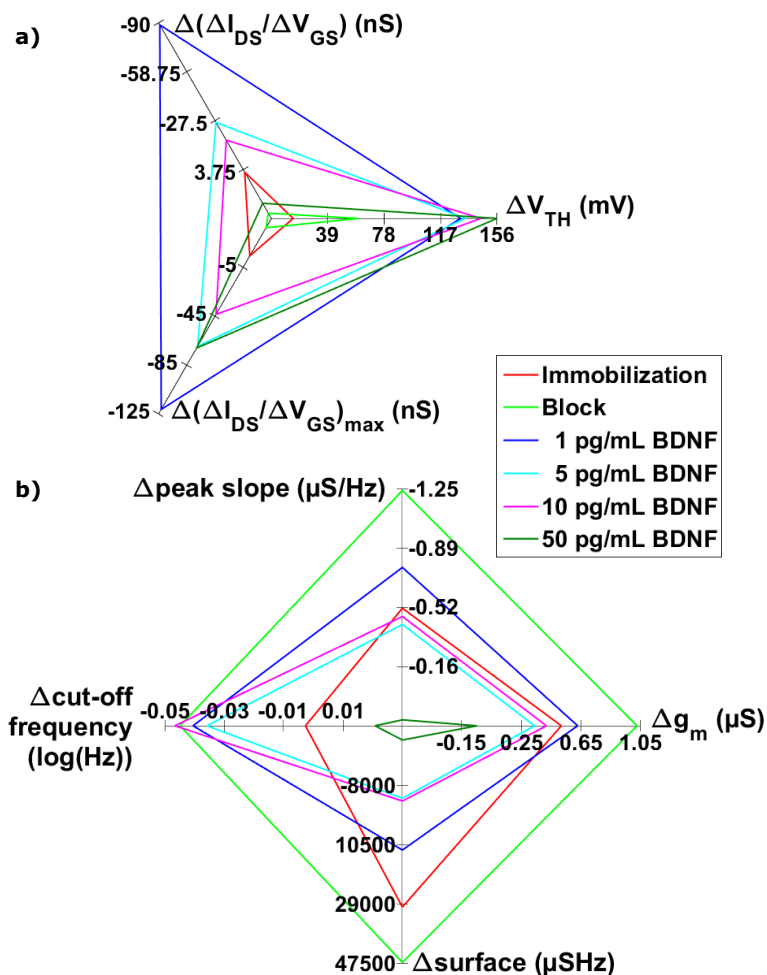
Figure 64: Multivariant data analysis – triaxial TC and four-axle TTF radar plot.
To obtain a better overview of the seven parameters of the multivariant data analysis, the seven-axle plot was separated into two radar plots. The triaxial plot is composed of the variants of the DC readout (a), whereas the four parameters of the TC evaluation are shown in the four-axle plot (b).

The change in threshold voltage, ΔV_{TH}, was already described in Chapter 6.3.2. Therefore, it is only briefly summarized in this section. By evaluating ΔV_{TH}, it was possible to detect the binding of the BDNF-specific capture antibody to the epoxy siloxane and the blocking of the unmodified sensor surface. Moreover,

1 pg/mL of the target protein BDNF was measured with the nanowire platform and evaluated to be significant.

Regarding the mean values for $\Delta\left(\dfrac{\Delta I_{DS}}{\Delta V_{GS}}\right)$, it can be seen that the immobilization caused an increase of the parameter as well as the blocking step, which further rose the value. After the binding of the first BDNF concentration $\Delta\left(\dfrac{\Delta I_{DS}}{\Delta V_{GS}}\right)$ dropped to lower number and then increased again with increasing BDNF concentration. This is in good agreement with the previously reported ΔV_{TH} results, since both parameters are directly correlated with each other.

Almost the same tendency was observed for $\Delta\left(\dfrac{\Delta I_{DS}}{\Delta V_{GS}}\right)_{max}$. After immobilization and blocking, the variant rose to higher values, whereas it dropped after the binding of 1 pg/mL BNDF. The incubation with 5 pg/mL and 10 pg/mL BDNF lead to an increase, but the attachment of 50 pg/mL BDNF decreased the parameter back to more negative values. This outlier can be explained by noise. Due to a high noise level at the highest point of the first derivative of the TC baseline, this highest point is set to a false value which is resulting in a wrong $\Delta\left(\dfrac{\Delta I_{DS}}{\Delta V_{GS}}\right)_{max}$.

The change in transconductance, Δg_m, was discussed more detailed in 6.3.3 and, hence, the results of this parameter are just shortly reviewed here. By performing the AC readout, it was possible to significantly detect the immobilization, blocking and the binding of four different BDNF concentrations. This implicated that reading-out Δg_m might be more promising than calculating ΔV_{TH} since it seemed to be more sensitive to changes on the sensor surface.

The results evaluated for Δpeak slope and for the Δcut-off frequency showed that both variants dropped after immobilization of the capture molecule and even decreased further after blocking the remaining free space on the sensor surface. Then, the values rose back to higher values after binding of 1 pg/mL and 5 pg/mL target protein. The parameters slightly decreased back to more negative values after 10 pg/mL BNDF and significantly increased to positive values after the attachment of 50 pg/mL molecule.

In case of Δsurface, the value is increasing after immobilization and the subsequent plotting, respectively, whereas it is decreasing after the binding of 1 pg/mL and 5 pg/mL BDNF. The attachment of 10 pg/mL target molecule raised the parameter back to higher values and the last concentration caused a decrease again.

For all AC variants, the evaluated values indicate that the binding of 10 pg/mL BDNF seems to be an outlier. The reason can be a slight error during the AC recording, which influenced the results false-positively.

6.4.2 Classification and accuracy

To classify the results and to differentiate between the different experimental steps, further statistical evaluation was done. In doing so, supervised machine learning was implemented to be able to predict, which data is read into the program [274]. For this purpose, the program is fed with known data and known results to identify specific patterns in data with the help of adaptive algorithms. The more input data is given to the program the better is its prediction ability [275]. According to the definition of MathWorks, supervised learning is separated into classification and regression. Classification is *e.g.* used for spam filtering to differentiate a class from various other classes to an observation. In the case of this thesis, this means that with the classification, the different experimental steps can be differentiated. In comparison to that, regression is applied to make predictions about continuous measurements for an observation [275]. When taking a concentration-dependent measurement into account, this means with regression a precise declaration of the concentration can be done (*e.g.* 15 pg/mL target molecule), whereas with classification the value is only predicted within a specific frame (*e.g.* 10 pg/mL to 49 pg/mL target molecules). However, to be able to implement a regression model, much more input data would be needed than for the classification algorithm.

In the framework of this thesis, a first classification was performed to demonstrate the proof-of-concept. The chosen statistical model is based on classification trees consisting of about 30 different trees (*Figure 65*). The trained program runs through the different classification trees, with which it is possible to predict which experimental data is imported into the program. Therefore, the program starts from the root (= start point), runs through the different

classification trees and ends at a leaf node that tells which experimental step was imported (= response). For this purpose, different parameters need to be answered with 'true' or 'false' so that a decision is made.
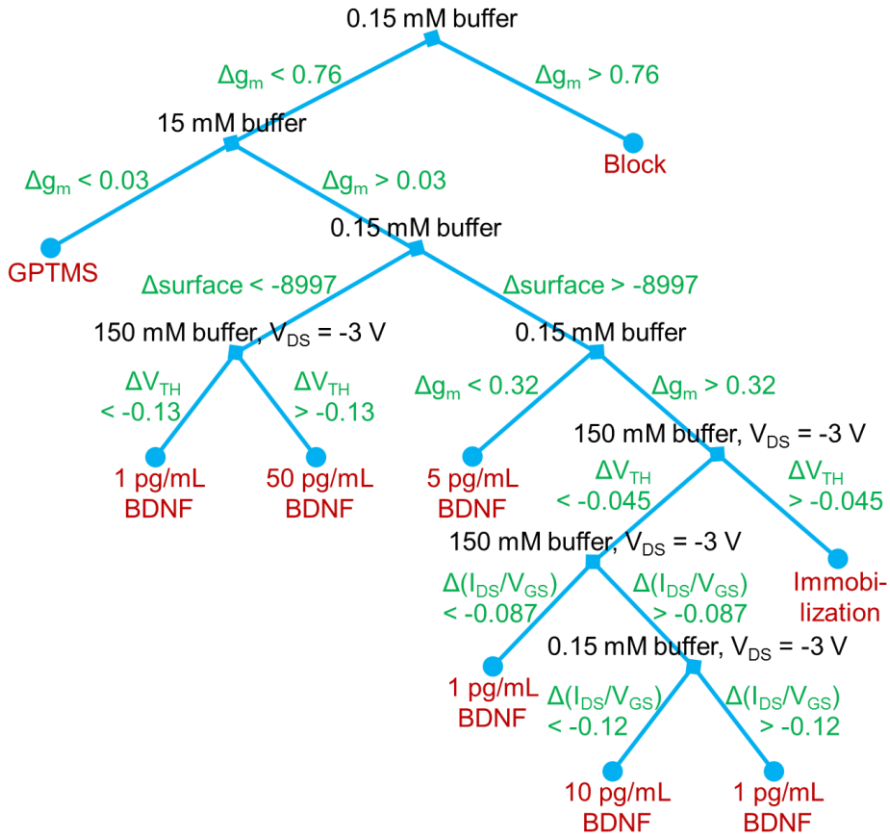
Figure 65: Classification tree to differentiate the BDNF data.

30 classification trees are used to determine the individual experimental steps of the BDNF results and to distinguish between the applied BDNF concentrations.

Depending on these decisions, the classification tree is followed until the final leaf node is reached [276,277]. The classification is done by majority votes, which means that the parameter with the highest concordance and the most matches is chosen and evaluated to be the predicted class. Therefore, the trees are also called 'bagged trees'. To derive conclusion about the reliability and stability of the applied model, *i. e.* the classification tree, the accuracy of this method was determined. By evaluating the accuracy, it is possible to estimate if a model can deliver a mean result close to the true value [278]. If the resulting

mean value is in approximation to the true value, an assay is accurate. For this purpose, the method k-fold cross validation was applied [279,280]. K stands for the number of subsets, in which the complete data set is separated. Usually, k amounts 5 or 10, but also other numbers are possible [280]. This technique differentiates between training and cross-validation set. The training set is used to train the program with a data set in order to implement a prediction algorithm. The reliability of this prediction algorithm is evaluated by cross-validation. Therefore, the cross-validation set consisting of experimental data is needed. It estimates how precise the program responses to unknown (untrained) data predicted by the algorithm [280]. The advantage of the k-fold validation is that the complete experimental data can be utilized to train the program. This is beneficial since no possibly important data characteristics or patterns are lost [280]. The BDNF results were composed of 70 data sets which were divided into 5 subsets (k = 5). This means that 14 data sets are within one subset. One of the five subsets was applied as validation set to validate the model and the remaining four subsets were taken as training set to train the model. This validation and training procedure was done five times so that the validation was done once for every subset [281]. The obtained accuracy results are shown in *Figure 66*. The statistic is composed of a y-axis, which represents the actual true classes, and an x-axis, where the predicted classes are displayed. The true positive rate (TPR, upper value) and the false negative rate (FNR, lower value) for each step is represented on the right side in *Figure 66*. Both rates are given in %-values. However, the performed statistics with the BDNF data set from this thesis is only a first step towards the classification of the given experimental steps. In a next step, regression models would need to be created. Within these regression models, only the concentration-dependent steps would be considered, and it would be performed to derive more exact conclusions about the unknown concentration. In doing so, more data than produced in the framework of this thesis would be necessary to create a reliable model. In the end, the final goal would be to import a data set of an unknown target analyte with an unknown concentration and use the classification and regression models to identify the analyte and its concentration. In future, this type of data analysis will be applied for the combined DC and AC readout of our sensor.

Figure 66: Accuracy of the classification model.

In this figure, the statistical evaluation of the accuracy of the whole model is shown. Besides the accuracy of the model for each single step, the overall accuracy and the overall error can be evaluated with the applied k-fold cross-validation method.

With this thesis, the large influence of the side parameters temperature, pH and ionic strength was cancelled out. By eliminating these side parameters, the multivariant data analysis offers a more robust and reliable readout, which is crucial for the application in the biomedical field, where clear and trustworthy results are essential.

Chapter 7 – Conclusions and outlook

7.1 Conclusions

Before establishing the bioassays onto the silicon nanowire field-effect transistors, three different kinds of proof-of-principle experiments were performed. In this initial research, the working principles of the DC and AC readout mode for SiNW FET sensors were studied in depth:

First, the changes of flatband and threshold voltages upon variation of the pH were investigated. These experiments were only performed with the nanowire device platform. The achieved results showed that, as expected for p–type transistors, the flatband voltage was shifted to higher values with increasing pH. This effect was caused by the deprotonation of the hydroxyl groups on the sensor surface due to high pH values. The pH induced and dependent formation of charges on the surface were leading to a change in the surface potential and, therefore, to a shift in the flatband voltage and the transfer characteristic. In a previous work, a sensitivity of 41 mV/pH with an α value of 0.69 was reported [54]. In this thesis, a sensitivity of only 34 mV/pH and an α value of 0.57 were obtained. Usually, both values are a slightly higher for SiO_2-based surfaces [166]. The reason could be that the sensors, used for the pH measurements, were already applied in various biomolecular experiments before. Furthermore, impurities on the sensor surface affected the results as well. However, the typical p-type sensor behavior upon changing the pH value of a buffer solution was also observed in the experiments in this thesis work.

In a second set of proof-of-principle experiments, conductivity measurements were done to study the influence of the ionic strength of a buffer solution on the transistor transfer function. This set of tests was performed on the micro- and nanoscaled FETs. With increasing buffer concentration, the TTF was shifted to higher frequencies, caused by a decrease in resistance. This was in a good agreement with previous publications [23,54,202].

A third kind of proof-of-principle experiment was the assembly of polyelectrolyte multilayers by means of the well-known layer-to-layer deposition. Comparisons of the transfer characteristics were done after adsorption of each polyelectrolyte

layer since this readout is charge sensitive. It was verified that the flatband voltage is shifted to lower values after binding of positively charged polymer molecules, whereas the adsorption of negatively charged polyelectrolytes shifted the flatband voltage to more positive values. This was in good agreement with previous publications [53] and proved that the applied SiNW FETs are charge sensitive. Furthermore, it was observed that the obtained signal strength was depending on the number of polyelectrolyte layers and, hence, on the distance to the sensor surface [17]. Besides the DC readout, the AC results were evaluated in this thesis was well. From the extracted data, it seems that both, the conductivity as well as the charge of the molecules influences the TTF measurements. However, it was also shown that the results for ISFETs and SiNW FETs are slightly different. It is possible that different effects are affecting both platforms, most likely the difference in parasitic parameters including contact lines and on-chip capacitance.

By measuring different pH values, different conductivities and the assembly of polyelectrolyte multilayers, it was shown that the used micro- and nanoscale devices were working reliably and stable and, hence, could be used for the detection of different biomolecules.

The immobilization and hybridization of artificial DNA was performed on ISFETs. Since DNA is negatively charged at a pH of 7.2, the TC curve shifted to more positive values. This observation was also reported before in [24,202,203,205]. Furthermore, denaturation was done after hybridization. After denaturation, the TC curve was almost shifted back to the values after immobilization, which indicated that the separation of the DNA double strand into two single-strands was successful and that the immobilization of the capture sequence was stable. Finally, the density of immobilized capture molecules was calculated to be 10^{13} DNA molecules per cm^2. Since epoxy silane was used instead of the amino silane APTES, this high yield can be explained. The AC readout showed the typical decrease in transconductance with each biomolecule layer, which was reported before [156].

To summarize the DNA experiments performed with the top-down processed SiNW FETs, the typical effects of a charge-based detection and a dependence of the signals on the buffer concentration used for recordings were observed. As reported in previous studies, the signal strength is enhanced in lower buffer

concentrations due to a weaker Debye screening effect. Upon binding of biomolecules, the transfer characteristic of the devices is shifting because of the change in surface potential, which was previously described for ISFET devices. As expected, the negatively charged DNA strands shifted the V_{TH} to more positive values. Therefore, we can be sure that the observed effects in these experiments were caused by the DNA molecules attached to the sensor surfaces. Furthermore, a second effect of the nanowire devices in the potentiometric readout was observed in DNA detection experiments. A change in the steepness of the transfer characteristic curves was obtained besides the shift in the threshold voltage upon biomolecular binding. This additional effect was clearly more pronounced in thinner than in wider nanowires. For the former ones, the shift and shape of the TC characteristics is steeper in comparison to the latter wires, where the shift between two TC curves is more parallel. By modeling, we concluded that this effect relies on an accumulation of charge carriers inside of the nanowires which is more affected in the thinner wires. This examination strongly points toward a charge injection effect from the highly doped source and drain contact sides. This could also be another explanation why nanowire-based FETs are more sensitive than the microscaled ISFETs. However, more investigations need to be performed to verify these observations.

The study shows that for experiments with SiNW FET sensors in linear operation regime, the selection and the stabilization of the working point is extremely important and directly influences the amplitude of the recordings, especially, if a time-dependent readout was used like done by many others in the field. For a final proof of our hypothesis, a systematic variation of the sizes of our top–down fabricated SiNW FETs in terms of width and length would be necessary. In an ideal case, this would reach down to the ultra-small size of the bottom-up grown devices in CVD processes (typically 10 nm in diameter) [46,231].

With the results, reported in this thesis, it was shown that the Debye screening also seems to influence the AC readout like it was previously published for the potentiometric measurements with nanowire FETs [163]. By calculating the signal change for two experimental steps measured in four different buffer concentrations, it was evaluated that the highest signal was obtained in the lowest buffer concentration, whereas the lowest signal was determined in the buffer with the highest ionic strength. It is assumed that variations of charges in

the biological membrane affect the interface impedance, too. However, this change is based on wide range of parameters. Furthermore, the evaluation of the obtained TTF spectra recordings showed that it is possible to distinguish between the different steps of a DNA hybridization assay. In doing so, the immobilization and the hybridization with two different target molecules concentration were successfully detected with the TTF method. The calculated differences in transconductance were evaluated to be statistically significant.

After having successfully detected the immobilization and hybridization of artificial DNA, first trials with HLA-B27 DNA sequences, provided by Euroimmun Medizinische Labordiagnostika AG, were implemented. Carriers of the HLA-B27 allele have a high risk for different auto immune diseases as Morbus Bechterew [108,109], Morbus Reiter [111], schizophrenia [117], various inflammatory diseases [105,112,113]. Both, the preliminary DC and AC results, indicate that the assay can be detected on the microscaled platform, which is an important step towards the application of the platform towards its usage as biomedical tool.

Besides performing DNA assays, the microscaled field-effect based devices were used for the detection of the protein BDNF. BDNF was found to be related to Parkinson's disease [68], Huntington's disease [78] and Alzheimer disease [83]. Since the limit of detection of the applied ELISA assay was reported to be 30 pg/mL, 1 pg/mL, 5 pg/mL, 10 pg/mL and 50 pg/mL BDNF were used to verify if the readout with the ISFETs was possible. However, the implemented trials showed that only the immobilization of the capture antibody was successful, whereas the protein binding itself could not be detected.

The top-down fabricated SiNW FETs were also used as immunosensors to detect low concentrations of the clinically relevant neurotrophic factor BDNF. It was possible to immobilize the mouse anti-human BDNF antibody to our epoxy silane modified transistor surface. The electronic detection of the BDNF antigen was firstly performed by measuring the potentiometric mode. Like reported for the microscaled ISFETs, the typical shift in threshold voltage upon binding of the biomolecules was measured. The binding of the target molecule led to a shift in the TC to more negative values. Since the isoelectric point of BDNF is reported to be around 9.99 [262], BDNF is positively charged when it is diluted in a buffer

solution with pH 7.0. Furthermore, it was possible to detect BDNF down to a concentration of 1 pg/ml BDNF (35.7 fM BDNF), which is lower than the concentration, which can be detected with a commercially available ELISA assay. It was also feasible to detect 1 pg/mL BDNF with the AC method. The statistical evaluation showed a significant change after the binding of the target analyte. This means that both readout methods were evaluated to be more sensitive than the used commercial BDNF ELISA kit, which had a limit-of-detection of 30 pg/mL BDNF, meaning that the applied nanowire platform is at least 30× more sensitive than the optical assay. To investigate the ultimate sensitivity of the device, the concentration of the target molecules would need to be decreased further. Furthermore, the evaluated results reveal that the nanowire devices are also more sensitive than the microscaled ISFETs, which is in good agreement with the beneficial properties of the nanosized sensors [231,282,283]. The addition of higher BDNF concentrations led to a change of the TC to more negative values as well. Besides that, it was possible to detect low concentrations of BDNF (50 pg/ml (~1.79 pM) BDNF) physiological buffer solutions. The ionic strength of the used solution was about 150 mM, which is in the range of the ionic strength of human blood [263]. This indicates that our silicon nanowire devices might be a potential tool for the detection of clinically relevant BNDF concentrations in high buffer strength. However, more experiments, in synthetic plasma and real human blood need to be performed to verify the results. Moreover, the reported observations indicate that our nanowire readout platform possesses the potential for a sensitive detection of biomolecules. The SiNW FETs might be a suitable as tool for biomedical purposes, *e.g.* as immunosensors, and they might serve as platform for the detection of ultra-low molecule concentrations.

In preliminary tests, the BDNF assay was also performed in HBSS as a first step towards measuring in synthetic serum. These results led to the conclusion that the detection of the BDNF binding could be successfully done with the AC and the DC mode. However, to verify the results, further experiments need to be performed.

The studies presented in this thesis work were continued in a biomedical startup. A patent was published, in which it was shown that measurements of C-reactive protein in 200 mM buffer were possible [284]. Even though the results are not

published, promising experiments with glucose, proteins and DNA were performed, in which the biomedically relevant analytes were successfully measured in synthetic and human serum.

In the last section of the thesis, a multivariant data analysis of the BDNF data was performed. The obtained parameters were plotted in one seven-axle radar plot composed of three DC variants and four AC variants. The change in V_{TH} and the change of the first derivation of the transfer function curve showed a concentrations-dependency of the assay. By evaluating the change of the derivate of the transfer function baseline at the steepest slope, it was visible that the addition of 50 pg/mL BDNF led to an outlier, which was reasoned by a high noise level of the first derivative. The four AC variants showed all the same tendency. For these values, a concentration-dependency was recognized as well. However, the addition of 10 pg/mL led to an outlier, which could most likely by explained by an error during the measurement. With help of a classification model, consisting of 30 classification trees, it was possible to distinguish between the individual experimental step and the applied buffer concentrations. The overall accuracy of the classification model was evaluated to amount 94.7 %. The obtained results and information can be used to increase the accuracy of the applied model in future trails and, hence, decrease the error, simultaneously. Moreover, by producing more experimental data, it could be verified if the shift of the different parameters and the respective experimental step behave linearly. This would be especially beneficial for concentration-dependent measurements.

As an overall conclusion, very low molecule concentrations down to the fM-regime were detected with the silicon nanowire platform in physiological test buffer solutions. Therefore, this platform might offer the possibility for the detection of ultralow analyte concentrations in complex matrix. The sensors represent a promising candidate for early-stage detection of biomarkers. It was possible to detect target biomolecules with DC- and AC-methods, simultaneously. It is suggested to combine both methods to achieve more meaningful and reliable results.

Furthermore, the results from biomedically relevant bioassays in this thesis showed that the analytes can also be measured in highly concentrated buffer solutions. These observations indicate that it might be feasible to directly

measure in human liquids after optimization of the surface modification and functionalization. With the help of the multivariant data analysis, outliers of the BDNF assay were determined, a classification model was created to distinguish between different experimental steps and applied concentrations and the accuracy of this model was calculated. Furthermore, several side parameters were cancelled out. With this novel procedure a more robust, stable and reliable biosensor could be developed in future. This thesis demonstrated that the SiNW FET platform is an innovative, prime candidate for the future application as readout tool in medical diagnostics.

7.2 Outlook

A more exact model for SOI sensors would be necessary in future experiment to be able to do a more precise description for the influence of the nanowire dimensions on the TC characteristics. In further trials, the sensors dimensions should be systematically varied in width and in length to validate the proposed hypothesis and to examine the effects in potentiometric readout more precisely. It might be feasible that this effect could be used to explain the higher sensitivities of nanowire devices compared to microscale ISFET devices, which were previously reported by other groups. Moreover, it would be possible to detect lower concentrations of the analyte by further scaling down the device dimensions and, hence, lower volumes of the probe would be needed for the detection. This would be of great benefit for biomedical purposes and would enable the usage of this top-down processed SiNW FET platform for diagnostic applications in biomolecular research.

Besides recording the TC characteristic, measuring the TTF spectra of a biomolecule assay on SiNW FETs is an auspicious readout principle. By controlling the influencing side parameters (*e.g.* pH and ionic strength of the buffer solution, biolayer dimension etc.), this method might be promising to achieve more reliable and stable results in combination with the potentiometric recording. Since it was possible to distinguish different experimental steps of a bioassay by performing AC measurements in physiological buffer concentration, this readout could be applicable for the detection of analytes in patient samples. However, further tests in physiological solutions and, finally, in human liquids

need to be performed. This will also include several optimization steps in terms of surface chemistry and system integration.

We assume that our nanowire devices are suitable for the detection of clinical relevant BNDF concentration in high buffer strength, such as available in blood. Nevertheless, more experiments, in synthetic plasma and real human blood would need to be performed to verify the results. It would also be necessary to investigate if the transistor's specificity is good enough to measure the biomolecule of interest out of a pool of different components.

Furthermore, the results obtained in the framework of this thesis reveal that SiNW FETs are applicable for the detection of ultralow biomolecule concentrations. The concentration of the applied target molecules would need to be decreased further to investigate the ultimate sensitivity of the device.

To verify the results of the multivariant data analysis, more measurements should be performed. To gain further information about the individual variants, simulation and modeling would need to be done. The final goal of the multivariant data analysis, the classification and the regression model is to be able to identify an unknown target molecule and its applied concentration. In doing so, the programming and development of a neuronal network would be feasible with which different structures could be recognized. In the end, a library of various parameters would be built up, which would allow gathering more information about the unknown target molecule, for example like surface activity, charge, size, layer thickness. This would also help to identify if an analyte of interest is present in its native or in a mutated form, which would be further beneficial in medical diagnostics and in the treatment of diseases.

References

[1]   I.G. Neizvestny, "Semiconductor Nanowire Sensors." *Russian Microelectronics*, 38 (4), 223–238 (2009).

[2]   J.-R. Gong, "Label-Free Attomolar Detection Of Proteins Using Integrated Nanoelectronic And Electrokinetic Devices." *Small*, 6 (8), 967–973 (2010).

[3]   S. Carrara, V. Bhalla, C. Stagni, L. Benini, A. Ferretti, F. Valle, A. Gallotta, B. Riccò, B. Samorì, "Label-Free Cancer Markers Detection By Capacitance Biochip." *Sensors and Actuators B: Chemical*, 136 (1), 163–172 (2008).

[4]   M. Chiesa, P.P. Cardenas, F. Otón, J. Martinez, M. Mas-Torrent, F. Garcia, J.C. Alonso, C. Rovira, R. Garcia, "Detection Of The Early Stage Of Recombinational DNA Repair By Silicon Nanowire Transistors." *Nano Letters*, 12 (3), 1275–1281 (2012).

[5]   Z. Liu, S. Tabakman, K. Welsher, H. Dai, "Carbon Nanotubes In Biology And Medicine: In Vitro And In Vivo Detection, Imaging And Drug Delivery." *Nano Research*, 2 (2), 85–120 (2009).

[6]   Y. Zhang, Y. Guo, Y. Xianyu, W. Chen, Y. Zhao, X. Jiang, "Nanomaterials For Ultrasensitive Protein Detection." *Advanced Materials*, 25 (28), 3802–3819 (2013).

[7]   J. Wang, "Electrochemical Biosensors: Towards Point-Of-Care Cancer Diagnostics." *Biosensors and Bioelectronics*, 21 (10), 1887–1892 (2006).

[8]   K. Kivirand, M. Kaga, T. Rinken, "Calibrating Biosensors In Flow-Through Set-Ups: Studies With Glucose Optrodes." *State of the Art in Biosensors - General Aspects*, InTech, London, 331–352 (2013).

[9]   G. Zhang, "Nanotechnology-Based Biosensors In Drug Delivery." *Nanotechnology in Drug Discovery*, Springer, New York, 163–192 (2009).

[10]   M. Curreli, R. Zhang, F.N. Ishikawa, H.-K. Chang, R.J. Cote, C. Zhou, M.E. Thompson, "Real-Time, Label-Free Detection Of Biological Entities Using Nanowire-Based FETs." *IEEE Transactions on Nanotechnology*, 7 (6), 651–667 (2008).

[11]   Z. Li, Y. Chen, X. Li, T.I. Kamins, K. Nauka, R.S. Williams, "Sequence-Specific Label-Free DNA Sensors Based On Silicon Nanowires." *Nano Letters*, 4 (2), 245–247 (2004).

[12]   J.-H. Ahn, M. Im, T.J. Park, S.Y. Lee, Y. Choi, "Label-Free And Real-Time Detection Of Avian Influenza Using Nanowire Field Effect Transistors." *Journal of Biomedical Nanotechnology*, 9 (3), 3–6 (2013).

[13]   D.A. Raorane, M.D. Lim, F.F. Chen, C.S. Craik, A. Majumdar, "Quantitative And Label-Free Technique For Measuring Protease Activity And Inhibition Using A Microfluidic Cantilever Array." *Nano Letters*, 8 (9), 2968–2974 (2008).

[14]   H.K. Hunt, A.M. Armani, "Label-Free Biological And Chemical Sensors." *Nanoscale*, 2 (9), 1544–1559 (2010).

[15]   E.T. Carlen, A. van den Berg, "Nanowire Electrochemical Sensors: Can We Live Without Labels?" *Lab on a Chip*, 7 (1), 19–23 (2007).

[16]   J. Fritz, E.B. Cooper, S. Gaudet, P.K. Sorger, S.R. Manalis, "Electronic Detection Of DNA By Its Intrinsic Molecular Charge." *Proceedings of the National Academy of Sciences*, 99 (22), 14142–14146 (2002).

[17]   F. Uslu, S. Ingebrandt, D. Mayer, S. Böcker-Meffert, M. Odenthal, A. Offenhäusser, "Labelfree Fully Electronic Nucleic Acid Detection System Based On A Field-Effect Transistor Device." *Biosensors and Bioelectronics*, 19 (12), 1723–1731 (2004).

[18]   P. Bergveld, "Development Of An Ion-Sensitive Solid-State Device For Neurophysiological Measurements." *IEEE Transactions on Biomedical Engineering*, 17 (1), 70–71 (1970).

[19]   P. Bergveld, "Development, Operation, And Application Of The Tool For Electrophysiology." *IEEE Transactions on Biomedical Engineering*, 19 (5), 342–351 (1972).

[20]   P. Bergveld, "The Development And Application Of FET-Based Biosensors." *Biosensors*, 2 (1), 15–33 (1986).

[21]   A. van den Berg, P. Bergveld, D.N. Reinhoudt, E.J. Sudhölter, "Sensitivity Control Of ISFETs By Chemical Surface Modification." *Sensors and Actuators B: Chemical*, 8 (2), 129–148 (1985).

[22]   U. Bockelmann, "Detecting DNA By Field Effect Transistor Arrays." *2006 IFIP International Conference on Very Large Scale Integration*, IEEE, 164–168 (2006).

[23]   Y. Han, D. Mayer, A. Offenhäusser, S. Ingebrandt, "Surface Activation Of Thin Silicon Oxides By Wet Cleaning And Silanization." *Thin Solid Films*, 510 (1–2), 175–180 (2006).

[24]   S. Ingebrandt, A. Offenhäusser, "Label-Free Detection Of DNA Using Field-Effect Transistors." *Physica Status Solidi (A): Applications and Materials Science*, 203 (14), 3399–3411 (2006).

[25]   E. Souteyrand, J.P. Cloarec, J.R. Martin, C. Wilson, I. Lawrence, S. Mikkelsen, M.F. Lawrence, "Direct Detection Of The Hybridization Of Synthetic Homo-Oligomer DNA Sequences By Field Effect." *Journal of Physical Chemistry B*, 101 (15), 2980–2985 (1997).

[26]   W.H. Baumann, M. Lehmann, A. Schwinde, R. Ehret, M. Brischwein, B. Wolf, "Microelectronic Sensor System For Microphysiological Application On Living Cells." *Sensors and Actuators B: Chemical*, 55 (1), 77–89 (1999).

[27]   S. Martinoia, N. Rosso, M. Grattarola, L. Lorenzelli, B. Margesin, M. Zen, "Development Of ISFET Array-Based Microsystems For Bioelectrochemical Measurements Of Cell Populations." *Biosensors and Bioelectronics*, 16 (9–12), 1043–1050 (2001).

[28]   A. Offenhäusser, C. Sprössler, M. Matsuzawa, W. Knoll, "Field-Effect Transistor Array For Monitoring Electrical Activity From Mammalian Neurons In Culture." *Biosensors and Bioelectronics*, 12 (8), 819–826 (1997).

[29]   S. Caras, J. Janata, "Field Effect Transistor Sensitive To Penicillin." *Analytical Chemistry*, 52 (8), 1935–1937 (1980).

[30]   X.-L. Luo, J.-J. Xu, W. Zhao, H.-Y. Chen, "Glucose Biosensor Based On ENFET Doped With SiO_2 Nanoparticles." *Sensors and Actuators B: Chemical*, 97 (2–3), 249–255 (2004).

[31]   M. Zayats, A.B. Kharitonov, E. Katz, A.F. Bückmann, I. Willner, "An Integrated NAD^+-Dependent Enzyme-Functionalized Field-Effect Transistor (ENFET) System: Development Of A Lactate Biosensor." *Biosensors and Bioelectronics*, 15 (11–12), 671–680 (2000).

[32]   A.B. Kharitonov, J. Wasserman, E. Katz, I. Willner, "The Use Of Impedance Spectroscopy For The Characterization Of Protein-Modified ISFET Devices: Application Of The Method For The Analysis Of Biorecognition Processes." *Journal of Physical Chemistry B*, 105 (19), 4205–4213 (2001).

[33]   J. Kruise, J.G. Rispens, P. Bergveld, F.J.B. Kremer, D. Starmans, J.R. Haak, J. Feijen, D.N. Reinhoudt, "Detection Of Charged Proteins By Means Of Impedance Measurements." *Sensors and Actuators B: Chemical*, 6 (1–3), 101–105 (1992).

[34]   N.F. Starodub, B.B. Dzantiev, V.M. Starodub, A.V. Zherdev, "Immunosensor For The Determination Of The Herbicide Simazine Based On An Ion-Selective Field-Effect Transistor." *Analytica Chimica Acta*, 424 (1), 37–43 (2000).

[35]   N. Elfström, R. Juhasz, I. Sychugov, T. Engfeldt, A. Eriksson Karlström, J. Linnros, "Surface Charge Sensitivity Of Silicon Nanowires: Size Dependence." *Nano Letters*, 7 (9), 2608–2612 (2007).

[36]   G.-J. Zhang, G. Zhang, J.H. Chua, R.-E. Chee, E.H. Wong, A. Agarwal, K.D. Buddharaju, N. Singh, Z. Gao, N. Balasubramanian, "DNA Sensing By Silicon Nanowire: Charge Layer Distance Dependence." *Nano Letters*, 8 (4), 1066–1070 (2008).

[37]   Z. Gao, A. Agarwal, A.D. Trigg, N. Singh, C. Fang, C.-H. Tung, Y. Fan, K.D. Buddharaju, J. Kong, "Silicon Nanowire Arrays For Label-Free Detection Of DNA." *Analytical Chemistry*, 79 (9), 3291–3297 (2007).

[38]   J. Hahm, C.M. Lieber, "Direct Ultrasensitive Electrical Detection Of DNA And DNA Sequence Variations Using Nanowire Nanosensors." *Nano Letters*, 4 (1), 51–54 (2004).

[39]   X.T. Vu, R. Stockmann, B. Wolfrum, A. Offenhäusser, S. Ingebrandt, "Fabrication And Application Of A Microfluidic-Embedded Silicon Nanowire Biosensor Chip." *Physica Status Solidi (A): Applications and Materials Science*, 207 (4), 850–857 (2010).

[40]   C.-C. Wu, F.-H. Ko, Y.-S. Yang, D.-L. Hsia, B.-S. Lee, T.-S. Su, "Label-Free Biosensing Of A Gene Mutation Using A Silicon Nanowire Field-Effect Transistor." *Biosensors and Bioelectronics*, 25 (4), 820–825 (2009).

[41] E. Stern, J.F. Klemic, D.A. Routenberg, P.N. Wyrembak, D.B. Turner-Evans, A.D. Hamilton, D.A. LaVan, T.M. Fahmy, M.A. Reed, "Label-Free Immunodetection With CMOS-Compatible Semiconducting Nanowires." *Nature*, 445 (7127), 519–522 (2007).

[42] J.F. Eschermann, R. Stockmann, M. Hueske, X.T. Vu, S. Ingebrandt, A. Offenhäusser, "Action Potentials Of HL-1 Cells Recorded With Silicon Nanowire Transistors." *Applied Physics Letters*, 95 (8), 83703-1-83703–3 (2009).

[43] C.M. Lieber, "Semiconductor Nanowires: A Platform For Nanoscience And Nanotechnology." *MRS Bulletin*, 36 (12), 1052–1063 (2011).

[44] T.-S. Pui, A. Agarwal, F. Ye, N. Balasubramanian, P. Chen, "CMOS-Compatible Nanowire Sensor Arrays For Detection Of Cellular Bioelectricity." *Small*, 5 (2), 208–212 (2009).

[45] A. Gao, N. Lu, Y. Wang, P. Dai, T. Li, X. Gao, Y. Wang, C. Fan, "Enhanced Sensing Of Nucleic Acids With Silicon Nanowire Field Effect Transistor Biosensors." *Nano Letters*, 12 (10), 5262–5268 (2012).

[46] F. Patolsky, G. Zheng, O. Hayden, M. Lakadamyali, X. Zhuang, C.M. Lieber, "Electrical Detection Of Single Viruses." *Proceedings of the National Academy of Sciences*, 101 (39), 14017–14022 (2004).

[47] F. Patolsky, G. Zheng, C.M. Lieber, "Nanowire-Based Biosensors." *Analytical Chemistry*, 78 (13), 4260–4269 (2006).

[48] F. Patolsky, B.P. Timko, G. Yu, Y. Fang, A.B. Greytak, G. Zheng, C.M. Lieber, "Detection, Stimulation, And Inhibition Of Neuronal Signals With High-Density Nanowire Transistor Arrays." *Science*, 313 (5790), 1100–1104 (2006).

[49] S. Baumgartner, M. Vasicek, A. Bulyha, C. Heitzinger, "Optimization Of Nanowire DNA Sensor Sensitivity Using Self-Consistent Simulation." *Nanotechnology*, 22 (42), 425503 (2011).

[50] Y. Cui, Z. Zhong, D. Wang, W.U. Wang, C.M. Lieber, "High Performance Silicon Nanowire Field Effect Transistors." *Nano Letters*, 3 (2), 149–152 (2003).

[51] Y. Paska, T. Stelzner, O. Assad, U. Tisch, S. Christiansen, H. Haick, "Molecular Gating Of Silicon Nanowire Field-Effect Transistors With Nonpolar Analytes." *ACS Nano*, 6 (1), 335–345 (2012).

[52] C.-C. Tsai, P.-L. Chiang, C.-J. Sun, T.-W. Lin, M.-H. Tsai, Y.-C. Chang, Y.-T. Chen, "Surface Potential Variations On A Silicon Nanowire Transistor In Biomolecular Modification And Detection." *Nanotechnology*, 22 (13), 135503 (2011).

[53] X.T. Vu, J.F. Eschermann, R. Stockmann, R. GhoshMoulick, A. Offenhäusser, S. Ingebrandt, "Top-Down Processed Silicon Nanowire Transistor Arrays For Biosensing." *Physica Status Solidi (A): Applications and Materials Science*, 206 (3), 426–434 (2009).

[54] X.T. Vu, "Silicon Nanowire Transistor Arrays For Biomolecular Detection.," *PhD Thesis*, *Fakultät für Mathematik, Informatik und Naturwissenschaften der Rheinisch-Westfälischen Technischen Hochschule Aachen* (2011).

[55]   C. O'Connor, J.U. Adams, "Essentials Of Cell Biology," *NPG Education*, Cambridge, Massachusetts (2010).

[56]   G. Walsh, "Proteins: Biochemistry And Biotechnology," *John Wiley & Sons Ltd.*, New Jersey (2002).

[57]   F. Horn, "Biochemie Des Menschen: Das Lehrbuch Für Das Medizinstudium," *Georg Thieme Verlag*, Stuttgart (2012).

[58]   J.M. Berg, J.L. Tymoczko, L. Stryer, "Biochemie," *Spektrum Akademischer Verlag*, Heidelberg (2007).

[59]   H. Will, "Molekularbiologie Kurz Und Bündig," *Springer-Verlag*, Berlin (2014).

[60]   A. McLennan, A. Bates, P. Turner, M. White, "Molekularbiologie Für Biologen, Biochemiker, Pharmazeuten Und Mediziner," *Wiley VCH Verlag GmbH & Co. KGaA*, Weinheim (2013).

[61]   S. Silbernagel, F. Lang, "Taschenatlas Pathophysiologie," *Georg Thieme Verlag KG*, Stuttgart (2012).

[62]   E.L. Logigian, R.F. Kaplan, A.C. Steere, "Chronic Neurologic Manifestations Of Lyme Disease." *The New England Journal of Medicine*, 323 (21), 1438–1444 (1990).

[63]   R.B. Nadelman, G.P. Wormser, "Lyme Borreliosis." *Lancet*, 352 (9127), 557–565 (1998).

[64]   M.E. Aguero-Rosenfeld, G. Wang, I. Schwartz, G.P. Wormser, "Diagnosis Of Lyme Borreliosis." *Clinical Microbiology Reviews*, 18 (3), 484–509 (2005).

[65]   J. Henry M. Feder, B.J.B. Johnson, S. O'Connell, E.D. Shapiro, A.C. Steere, G.P. Wormser, "A Critical Appraisal Of Chronic Lyme Disease." *The New England Journal of Medicine*, 357 (14), 1422–1430 (2007).

[66]   J.J. Nocton, F. Dressler, B.J. Rutledge, P.N. Rys, D.H. Persing, A.C. Steere, "Detection Of Borrelia Burgdoferi DNA By Polymerase Chain Reaction In Synovial Fluid From Patients With Lyme Arthritis." *The New England Journal of Medicine*, 330 (4), 229–234 (1994).

[67]   C. Laske, E. Stransky, T. Leyhe, G.W. Eschweiler, A. Wittorf, E. Richartz, M. Bartels, G. Buchkremer, K. Schott, "Stage-Dependent BDNF Serum Concentrations In Alzheimer's Disease." *Journal of Neural Transmission*, 113 (9), 1217–1224 (2006).

[68]   C. Hyman, M. Hofer, Y.-A. Barde, M. Juhasz, G.D. Yancopoulos, S.P. Squinto, R.M. Lindsay, "BDNF Is A Neurotrophic Factor Of Dopaminergic Neurons Of The Substantia Nigra." *Nature*, 350 (6315), 230–232 (1991).

[69]   A. Nowak, J.P. Szaflik, M. Gacek, K. Przybylowska-Sygut, A. Kamińska, J. Szaflik, I. Majsterek, "BDNF And HSP Gene Polymorphisms And Their Influence On The Progression Of Primary Open-Angle Glaucoma In A Polish Population." *Archives of Medical Science*, 10 (6), 1206–1213 (2014).

[70]   C. Alzheimer, "Molecular And Cellular Biology Of Neuroprotection In The CNS," *Kluwer Academic/Plenum Publisher and Landes Bioscience*, New York (2002).

[71] A.L. Mandel, H. Ozdener, V. Utermohlen, "Brain-Derived Neurotrophic Factor In Human Saliva: ELISA Optimization And Biological Correlates." *Journal of Immunoassay and Immunochemistry*, 32 (1), 18–30 (2011).

[72] C. Vrijen, H.M. Schenk, C.A. Hartman, A.J. Oldehinkel, "Measuring BDNF In Saliva Using Commercial ELISA: Results From A Small Pilot Study." *Psychiatry Research*, 254, 340–346 (2017).

[73] A. Mohammad, V.G. Amooeian, E. Rashidi, "Dysfunction In Brain-Derived Neurotrophic Factor Signaling Pathway And Susceptibility To Schizophrenia, Parkinson's And Alzheimer's Diseases." *Current Gene Therapy*, availabe online (2018).

[74] L. Minichiello, "TrkB Signalling Pathways In LTP And Learning." *Nature Reviews Neuroscience*, 10 (12), 850–860 (2009).

[75] J.B. Takahashi, M. Hoshimarub, H. Kikuchib, M. Hatanaka, "Developmental Expression Of TrkB And Low-Affinity NGF Receptor In The Rat Retina." *Neuroscience Letters*, 151 (2), 174–177 (1993).

[76] J. Jankovic, Eduardo Tolosa, "Parkinson's Disease And Movement Disorders," *Lippincott Williams & Wilkins*, Philadelphia (2007).

[77] R.F. Pfeiffer, Z.K. Wszolek, M. Ebadi, "Parkinson's Disease," *Taylor & Francis Group*, London (2012).

[78] B.K. Pedersen, M. Pedersen, K.S. Krabbe, H. Bruunsgaard, V.B. Matthews, M. a Febbraio, "Role Of Exercise-Induced Brain-Derived Neurotrophic Factor Production In The Regulation Of Energy Homeostasis In Mammals." *Experimental Physiology*, 94 (12), 1153–1160 (2009).

[79] C. Zuccato, A. Ciammola, D. Rigamonti, B.R. Leavitt, D. Goffredo, L. Conti, M.E. MacDonald, R.M. Friedlander, V. Silani, M.R. Hayden, T. Timmusk, S. Sipione, E. Cattaneo, "Loss Of Huntingtin-Mediated BDNF Gene Transcription In Huntington's Disease." *Science*, 293 (5529), 493–498 (2001).

[80] C. Zuccato, D. Liber, C. Ramos, A. Tarditi, D. Rigamonti, M. Tartari, M. Valenza, E. Cattaneo, "Progressive Loss Of BDNF In A Mouse Model Of Huntington's Disease And Rescue By BDNF Delivery." *Pharmacological Research*, 52 (2), 133–139 (2005).

[81] "Http://www.huntington-hilfe.de." *Deutsche Huntington-Hilfe e.V.* (2016).

[82] "Http://www.mayoclinic.org." *Mayo Clinic* (2017).

[83] H.S. Phillips, J.M. Hains, M. Armanini, G.R. Laramee, S.A. Johnson, J.W. Winslow, P.A. Gerontology, "BDNF MRNA Is Decreased In The Hippocampus Of Individuals With Alzheimer's Disease." *Neuron*, 7 (5), 695–702 (1991).

[84] X.-Y. Qi, C. Cao, N.X. Cawley, T.-T. Liu, J. Yuan, Y.P. Loh, Y. Cheng, "Decreased Peripheral Brain-Derived Neurotrophic Factor Levels In Alzheimer's Disease: A Meta-Analysis Study (N=7277)." *Molecular Psychiatry*, 22, 312–320 (2017).

[85] L. Tapia-Arancibia, E. Aliaga, M. Silhol, S. Arancibia, "New Insights Into Brain BDNF Function In Normal Aging And Alzheimer Disease." *Brain Research Reviews*, 59 (1), 201–220 (2008).

[86]   "Https://www.alzheimer-forschung.de." *Alzheimer-Forschung Initiative e.V.* (2017).

[87]   G. Richter, "Praktische Biochemie: Grundlagen Und Techniken," *Georg Thieme Verlag*, Stuttgart (2003).

[88]   C. Hamers-Casterman, T. Atarhouch, S. Muyldermans, G. Robinson, C. Hamers, E. Songa, N. Bendahman, R. Hamers, "Naturally Occurring Antibodies Devoid Of Light Chains." *Nature*, 363 (6428), 446–448 (1993).

[89]   M.F. Flajnik, N. Deschacht, S. Muyldermans, "A Case Of Convergence: Why Did A Simple Alternative To Canonical Antibodies Arise In Sharks And Camels?" *PLOS Biology*, 9 (8), 1–5 (2011).

[90]   J. Wesolowski, V. Alzogaray, J. Reyelt, M. Unger, K. Juarez, M. Urrutia, A. Cauerhff, W. Danquah, B. Rissiek, F. Scheuplein, N. Schwarz, S. Adriouch, O. Boyer, M. Seman, A. Licea, D.V. Serreze, F.A. Goldbaum, F. Haag, F. Koch-Nolte, "Single Domain Antibodies: Promising Experimental And Therapeutic Tools In Infection And Immunity." *Medical Microbiology and Immunology*, 198 (3), 157–174 (2009).

[91]   K.K. Jain, "The Handbook Of Nanomedicine," *Springer Nature*, New York (2017).

[92]   M.M. Harmsen, H.J. De Haard, "Properties, Production, And Applications Of Camelid Single-Domain Antibody Fragments." *Applied Microbiology and Biotechnology*, 77 (1), 13–22 (2007).

[93]   A. Liesz, C. Kleinschnitz, "Mechanisms Of Neuroinflammation And Inflammatory Neurodegeneration In Acute Brain Injury," *Frontiers Media SA*, Lausanne (2015).

[94]   L. Rink, A. Kruse, H. Haase, "Immunologie Für Einsteiger," *Spektrum Akademischer Verlag*, Heidelberg (2012).

[95]   H.R. Horton, L.A. Moran, K.G. Scrimgeour, M.D. Perry, J.D. Rawn, "Biochemie," *Pearson Education Inc.*, London (2008).

[96]   T.A. Brown, "Genome Und Gene: Lehrbuch Der Molekularen Genetik," *Spektrum Akademischer Verlag*, Heidelberg (2007).

[97]   D.P. Clark, N.J. Pazdernik, "Molecular Biology: Understanding The Genetic Revolution," *Academic Press Inc.*, Oxford (2012).

[98]   R.R. Sinden, "DNA Structure And Function," *Academic Press Inc.*, Oxford (1994).

[99]   J.U. Adams, "DNA Sequencing Technologies." *Nature Education*, 1 (1), (2008).

[100]   E.C. Friedberg, G.C. Walker, W. Siede, "DNA Repair And Mutagenesis," *American Society for Microbiology*, Washington (1995).

[101]   T.H. McConnell, "The Nature Of Disease: Pathology For The Health Professions," *Lippincott Williams & Wilkins*, Philadelphia (2007).

[102]   P.S. Frenette, G.F. Atweh, "Science In Medicine Sickle Cell Disease: Old Discoveries, New Concepts, And Future Promise." *The Journal of Clinical Investigation*, 117 (4), 850–858 (2007).

[103] D.C. Rees, T.N. Williams, M.T. Gladwin, "Sickle-Cell Disease." *Lancet*, 376 (9757), 2018–2031 (2010).

[104] "Sickle-Cell Anaemia," *World Health Organization* (2005).

[105] "Http://www.uniklinik-ulm.de/struktur/institute/klinische-chemie/home/praeanalytik/untersuchungen-leistungsverzeichnis/hij/hla-b27-mutation." *Universitätsklinikum Ulm* (2017).

[106] M.P. Martin, X. Gao, J.-H. Lee, G.W. Nelson, R. Detels, J.J. Goedert, S. Buchbinder, K. Hoots, D. Vlahov, J. Trowsdale, M. Wilson, S.J. O'Brien, M. Carrington, "Epistatic Interaction Between KIR3DS1 And HLA-B Delays The Progression To AIDS." *Nature Genetics*, 31 (4), 429–434 (2002).

[107] S.J. O'Brien, X. Gao, M. Carrington, "HLA And AIDS: A Cautionary Tale." *Trends in Molecular Medicine*, 7 (9), 379–381 (2001).

[108] "Http://www.bechterew.de." *Deutsche Vereinigung Morbus Bechterew e.V.* (2017).

[109] "Http://www.medizin.uni-halle.de." *Universitätsklinikum Halle (Saale)* (2017).

[110] R. Bartl, C. Bartl, "Bone Disorders," *Springer*, Switzerland (2017).

[111] E.-R. von Leitner, V. Kötter, R. Schröder, "Kardiale Spätmanifestationen Des Morbus Reiter." *Deutsche Medizinische Wochenschrift*, 106 (29–30), 939–941 (1981).

[112] J.M.H. Moll, V. Wright, "Psoriatic Arthritis." *Seminars in Arthritis and Rheumatism*, 3 (1), 55–78 (1973).

[113] L.J. McCann, L.R. Wedderburn, N. Hasson, "Juvenile Idiopathic Arthritis." *Archives of Disease in Childhood - Education and Practice*, 91 (2), 29–36 (2006).

[114] M. Di Paola, D. Cavalieri, D. Albanese, M. Sordo, M. Pindo, C. Donati, I. Pagnini, T. Giani, G. Simonini, A. Paladini, P. Lionetti, C. De Filippo, R. Cimaz, "Alteration Of Fecal Microbiota Profiles In Juvenile Idiopathic Arthritis. Associations With Hla-B27 Allele And Disease Status." *Frontiers in Microbiology*, 7, 1–13 (2016).

[115] H. Li, Q. Li, C. Ji, J. Gu, "Ankylosing Spondylitis Patients With HLA-B*2704 Have More Uveitis Than Patients With HLA-B*2705 In A North Chinese Population." *Ocular Immunology and Inflammation*, 26 (1), 65–69 (2018).

[116] E.M. D'Ambrosio, M. La Cava, P. Tortorella, M. Gharbiya, M. Campanella, L. Iannetti, "Clinical Features And Complications Of The HLA-B27-associated Acute Anterior Uveitis: A Metanalysis." *Seminars in Ophthalmology*, 32 (6), 689-701 (2017).

[117] W.F. Gattaz, S.K. Kasper, R. Ewald, H.B. Beckmann, "HLA, Schizophrenien Und Arthropathien." *Psychatria Clinica*, 14 (1), 49–55 (1971).

[118] C. Anasetti, D. Amos, P.G. Beatty, F.R. Appelbaum, W. Bensinger, C.D. Buckner, R. Clift, K. Doney, P.J. Martin, E. Mickelson, B. Nisperos, J. O'Quigley, R. Ramberg, J.E. Sanders, P. Stewart, R. Storb, K.M. Sullivan, R.P. Witherspoon, E.D. Thomas, J.A. Hansen, "Effect Of HLA Compatibility On Engraftment Of Bone Marrow Transplants In Patients With Leukemia Or Lymphoma." *The New England Journal of Medicine*, 320 (4), 197–204 (1989).

[119] S. Takemoto, F.K. Port, F.H.J. Claas, R.J. Duquesnoy, "HLA Matching For Kidney Transplantation." *Human Immunology*, 65 (12), 1489–1505 (2004).

[120] G. Opelz, T. Wujciak, B. Döhler, S. Scherer, J. Mytilineos, "HLA Compatibility And Organ Transplant Survival. Collaborative Transplant Study." *Reviews in Immunogenetics*, 1 (3), 334–342 (1999).

[121] Y. Morishima, T. Sasazuki, H. Inoko, T. Juji, T. Akaza, K. Yamamoto, Y. Ishikawa, S. Kato, H. Sao, H. Sakamaki, K. Kawa, N. Hamajima, S. Asano, Y. Kodera, "The Clinical Significance Of Human Leukocyte Antigen (HLA) Allele Compatibility In Patients Receiving A Marrow Transplant From Serologically HLA-A, HLA-B, And HLA-DR Matched Unrelated Donors." *Blood*, 99 (11), 4200–4206 (2002).

[122] G.U. Urban, "Micro- And Nanobiosensors: State Of The Art And Trends." *Measurement Science and Technology*, 20 (1–18), 12001 (2009).

[123] B. Lu, M.R. Smyth, R.O. Kennedy, "Oriented Immobilization Of Antibodies And Its Applications In Lmmunoassays And Immunosensors." *Analyst*, 121 (3), 29R–32R (1996).

[124] D. Wild, "The Immunoassay Handbook: Theory And Applications Of Ligand Binding, ELISA And Related Techniques," *Elsevier Ltd.*, Oxford (2005).

[125] A. Voller, D.E. Bidwell, A. Bartlett, "Enzyme Immunoassays In Diagnostic Medicine." *Bulletin of the World Health Organization*, 53 (1), 55–65 (1976).

[126] M.H. Gey, "Instrumentelle Analytik Und Bioanalytik: Biosubstanzen, Trennmethoden Strukturanalytik, Applikationen," *Springer Verlag*, Heidelberg (2008).

[127] J.R. Crowther, "ELISA: Theory And Practice," *Humana Press*, Totowa, New Jersey (1995).

[128] "Http://www.elisa-antibody.com." *Sino Biological Inc.* (2017).

[129] K.D. McClatchey, "Clinical Laboratory Medicine," *Lippincott Williams & Wilkins*, Philadelphia (2002).

[130] R.M. Sutherland, C. Dähne, J.F. Place, A.R. Ringrose, "Immunoassays At A Quartz-Liquid Interface: Theory, Instrumentation And Preliminary Application To The Fluorescent Immunoassay Of Human Immunoglobulin G." *Journal of Immunological Methods*, 74 (2), 253–265 (1984).

[131] X.-D. Yang, Y. Ci, W. Chang, "Time-Resolved Fluorescence Immunoassay With Measurement Of A Europium Chelate In Solution: Dissociation Conditions And Applications For Determination Of Cortisol." *Analytical Chemistry*, 66 (15), 2590–2594 (1994).

[132] A. Kar, "Pharmaceutical Drug Analysis," *New Age International Limited*, New Delhi (2005).

[133] A.L. Ghindilis, P. Atanasov, M. Wilkins, E. Wilkins, "Immunosensors: Electrochemical Sensing And Other Engineering Approaches." *Biosensors and Bioelectronics*, 13 (1), 113–131 (1998).

[134] C.L. Morgan, D.J. Newman, C.P. Price, "Immunosensors: Technology And Opportunities In Laboratory Medicine." *Clinical Chemistry*, 42 (2), 193–209 (1996).

[135] B. Hock, "Antibodies For Immunosensors A Review." *Analytica Chimica Acta*, 347 (1–2), 177–186 (1997).

[136] R. Bumgarner, "DNA Microarrays: Types, Applications And Their Future." *Current Protocols in Molecular Biology*, 6137 (206), 1–17 (2013).

[137] D. Shalon, S.J. Smith, P.O. Brown, "A DNA Microarray System For Analyzing Complex DNA Samples Using Two-Color Fluorescent Probe Hybridization." *Genome Research*, 6 (415), 639–645 (1996).

[138] J.M. Heather, B. Chain, "The Sequence Of Sequencers: The History Of Sequencing DNA." *Genomics*, 107 (1), 1–8 (2016).

[139] "Http://www.laborpraxis.vogel.de/bioanalytik-pharmaanalytik/articles/139687/." *Fuxius, S.M., Lisdat, F.* (2008).

[140] E.P. Diamandis, "Sequencing With Microarray Technology—A Powerful New Tool For Molecular Diagnostics." *Clinical Chemistry*, 46 (10), 1523–1525 (2000).

[141] "Http://en.wikipedia.org/wiki/DNA_microarray." *Wikimedia Foundation Inc.* (2017).

[142] A. Sassolas, B.D. Leca-Bouvier, L.J. Blum, "DNA Biosensors And Microarrays." *Chemical Reviews*, 108 (1), 109–139 (2008).

[143] H. Ju, H. Zhao, "Electrochemical Biosensors For DNA Analysis." *Frontiers in Bioscience*, 10, 37–46 (2005).

[144] T.G. Drummond, M.G. Hill, J.K. Barton, "Electrochemical DNA Sensors." *Nature Biotechnology*, 21 (10), 1192–1199 (2003).

[145] B. van Grinsven, N. Vanden Bon, L. Grieten, M. Murib, S.D. Janssens, K. Haenen, E. Schneider, S. Ingebrandt, M.J. Schöning, V. Vermeeren, M. Ameloot, L. Michiels, R. Thoelen, W. De Ceuninck, P. Wagner, "Rapid Assessment Of The Stability Of DNA Duplexes By Impedimetric Real-Time Monitoring Of Chemically Induced Denaturation." *Lab on a Chip*, 11 (9), 1656–1663 (2011).

[146] B. van Grinsven, N. Vanden Bon, H. Strauven, L. Grieten, M. Murib, S.D. Janssens, K. Haenen, M.J. Scho, K.L. Jime, V. Vermeeren, M. Ameloot, L. Michiels, R. Thoelen, W. De Ceuninck, P. Wagner, "Heat-Transfer Resistance At Solid-Liquid Interfaces: A Tool For The Detection Of Single-Nucleotide Polymorphisms In DNA." *ACS Nano*, 6 (3), 2712–2721 (2012).

[147] N. Vanden Bon, B. van Grinsven, M.S. Murib, W.S. Yeap, K. Haenen, W. De Ceuninck, P. Wagner, M. Ameloot, V. Vermeeren, L. Michiels, "Heat-Transfer-Based Detection Of SNPs In The PAH Gene Of PKU Patients." *International Journal of Nanomedicine*, 9 (1), 1629–1640 (2014).

[148] M.S. Murib, W.S. Yeap, Y. Eurlings, B. van Grinsven, H.G. Boyen, B. Conings, L. Michiels, M. Ameloot, R. Carleer, J. Warmer, P. Kaul, K. Haenen, M.J. Schöning, W. De Ceuninck, P. Wagner, "Heat-Transfer Based Characterization Of DNA On Synthetic Sapphire Chips." *Sensors and Actuators B: Chemical*, 230, 260–271 (2016).

[149] C. Kataoka-Hamai, Y. Miyahara, "Label-Free Detection Of DNA By Field-Effect Devices." *IEEE Sensors Journal*, 11 (12), 3153–3160 (2011).

[150] M.W. Shinwari, M.J. Deen, D. Landheer, "Study Of The Electrolyte-Insulator-Semiconductor Field-Effect Transistor (EISFET) With Applications In Biosensor Design." *Microelectronics Reliability*, 47 (12), 2025–2057 (2007).

[151] T. Kuriyama, J. Kimura, "Biosensor Principles And Applications," *Marcel Dekker Inc.*, New York (1991).

[152] C.-S. Lee, S.K. Kim, M. Kim, "Ion-Sensitive Field-Effect Transistor For Biological Sensing." *Sensors*, 9 (9), 7111–7131 (2009).

[153] M. Jansen, "Silizium Nanoribbon Feld-Effekt Transistoren Zur Kopplung An Elektroaktive Zellen," *PhD Thesis*, *Fakultät für Mathematik, Informatik und Naturwissenschaften der RWTH Aachen University* (2013).

[154] P. Bergveld, "Thirty Years Of ISFETOLOGY What Happened In The Past 30 Years And What May Happen In The Next 30 Years." *Sensors and Actuators B: Chemical*, 88 (1), 1–20 (2003).

[155] P. Bergveld, "ISFET, Theory And Practice." *IEEE Sensor Conference Toronto*, 1–26 (2003).

[156] S. Ingebrandt, Y. Han, F. Nakamura, A. Poghossian, M.J. Schöning, A. Offenhäusser, "Label-Free Detection Of Single Nucleotide Polymorphisms Utilizing The Differential Transfer Function Of Field-Effect Transistors." *Biosensors and Bioelectronics*, 22 (12), 2834–2840 (2007).

[157] X.T. Vu, R. GhoshMoulick, J.F. Eschermann, R. Stockmann, A. Offenhäusser, S. Ingebrandt, "Fabrication And Application Of Silicon Nanowire Transistor Arrays For Biomolecular Detection." *Sensors and Actuators B: Chemical*, 144 (2), 354–360 (2010).

[158] J.-Y. Kim, J.-H. Ahn, D.-I. Moon, S. Kim, T.J. Park, S.Y. Lee, Y.-K. Choi, "A Dual-Gate Field-Effect Transistor For Label-Free Electrical Detection Of Avian Influenza." *BioNanoScience*, 2 (1), 35–41 (2012).

[159] K.-I. Chen, B.-R. Li, Y.-T. Chen, "Silicon Nanowire Field-Effect Transistor-Based Biosensors For Biomedical Diagnosis And Cellular Recording Investigation." *Nano Today*, 6 (2), 131–154 (2011).

[160] Y. Cui, C.M. Lieber, "Functional Nanoscale Electronic Devices Assembled Using Silicon Nanowire Building Blocks." *Science*, 291 (5505), 851–853 (2001).

[161] O.H. Elibol, B. Reddy, R. Bashir, "Nanoscale Thickness Double-Gated Field Effect Silicon Sensors For Sensitive PH Detection In Fluid." *Applied Physics Letters*, 92 (19), 193904-1-193904–3 (2008).

[162] F. Patolsky, G. Zheng, C.M. Lieber, "Fabrication Of Silicon Nanowire Devices For Ultrasensitive, Label-Free, Real-Time Detection Of Biological And Chemical Species." *Nature Protocols*, 1 (4), 1711–1724 (2006).

[163] E. Stern, R. Wagner, F.J. Sigworth, R. Breaker, T.M. Fahmy, M.A. Reed, "Importance Of The Debye Screening Length On Nanowire Field Effect Transistor Sensors." *Nano Letters*, 7 (11), 3405–3409 (2007).

[164] Y.L. Bunimovich, Y.S. Shin, W.-S. Yeo, M. Amori, G. Kwong, J.R. Heath, "Quantitative Real-Time Measurements Of DNA Hybridization With Alkylated Nonoxidized Silicon Nanowires In Electrolyte Solution." *Journal of the American Chemical Society*, 128 (50), 16323–16331 (2006).

[165] S. Ingebrandt, X.T. Vu, J.F. Eschermann, R. Stockmann, A. Offenhäusser, "Top-Down Processed SOI Nanowire Devices For Biomedical Applications." *ECS Transactions*, 35 (7), 3–15 (2011).

[166] R.E.G. van Hal, J.C.T. Eijkel, P. Bergveld, "A General Model To Describe The Electrostatic Potential At Electrolyte Oxide Interfaces." *Advances in Colloid and Interface Science*, 69 (1–3), 31–62 (1996).

[167] D.E. Yates, S. Levine, T.W. Healy, "Site-Binding Model Of The Electrical Double Layer At The Oxide/Water Interface." *Journal of the Chemical Society, Faraday Transactions 1: Physical Chemistry in Condensed Phases*, 70 (0), 1807–1818 (1974).

[168] T. Hiemstra, J. De Wit, W. Van Riemsdijk, "Multisite Proton Adsorption Modeling At The Solid/solution Interface Of (Hydr)oxides: A New Approach." *Journal of Colloid and Interface Science*, 133 (1), 91–104 (1989).

[169] D.C. Grahame, "The Electrical Double Layer And The Theory Of Electrocapillarity." *Chemical Reviews*, 41 (3), 441–501 (1947).

[170] G. Quincke, "Über Die Fortführung Materieller Theilchen Durch Strömende Elektricität." *Annalen der Physik und Chemie*, 189 (8), 513–598 (1861).

[171] H.J. Butt, K. Graf, M. Kappl, "Physics And Chemistry Of Interfaces," *Wiley-VCH Verlag GmbH & Co. KGaA*, Weinheim (2003).

[172] P.W. Atkins, J. de Paula, "Physikalische Chemie," *Wiley-VCH Verlag GmbH & Co. KGaA*, Weinheim (2006).

[173] M. Gouy, "Sur La Constitution De La Charge Électrique À La Surface D'Un Électrolyte." *Journal des Physique Théorique et Appliquée*, 9 (1), 457–468 (1910).

[174] D.L. Chapman, "A Contribution To The Theory Of Electrocapillarity." *Philosophical Magazine*, 25 (148), 475–481 (1913).

[175] O. Stern, "Zur Theorie Der Elektrolytischen Doppelschicht." *Zeitschrift für Elektrochemie*, 30 (21–22), 508–516 (1924).

[176] L. Zhang, X. Zao, "Carbon-based Materials As Supercapacitor Electrodes." *Chemical Society Reviews*, 38 (9), 2520–2531 (2009).

[177] M. Reth, "Matching Cellular Dimensions With Molecular Sizes." *Nature Immunology*, 14 (8), 765–767 (2013).

[178] M. Krause, "Untersuchungen Zur Zell-Transistor Kopplung Mittels Der Voltage-Clamp Technik," *PhD Thesis*, *Fachbereich Chemie und Pharmazie der Johannes Gutenberg-Universität Mainz* (2000).

[179] Y. Han, "Label-Free Detection Of Biomolecules By A Field-Effect Transistor Microarray Biosensor With Bio-Functionalized Gate Surfaces," *PhD Thesis*, *Fakultät für Mathematik, Informatik und Naturwissenschaften der Rheinisch-Westfälischen Technischen Hochschule Aachen* (2005).

[180] L. Bousse, N.F. de Rooij, P. Bergveld, "Operation Of Chemically Sensitive Field-Effect Sensors As A Function Of The Insulator-Electrolyte Interface." *IEEE Transactions on Electron Devices*, 30 (10), 1263–1270 (1983).

[181] A.V. Dobrynin, M. Rubinstein, "Theory Of Polyelectrolytes In Solutions And At Surfaces." *Progress in Polymer Science*, 30 (11), 1049–1118 (2005).

[182] S. Lankalapalli, V.R.M. Kolapalli, "Polyelectrolyte Complexes: A Review Of Their Applicability In Drug Delivery Technology." *Indian Journal of Pharmaceutical Sciences*, 71 (5), 481–487 (2009).

[183] A. Poghossian, M. Weil, A.G. Cherstvy, M.J. Schöning, "Electrical Monitoring Of Polyelectrolyte Multilayer Formation By Means Of Capacitive Field-Effect Devices." *Analytical and Bioanalytical Chemistry*, 405 (20), 6425–6436 (2013).

[184] M.H. Abouzar, "Detection Of Molecular Interactions Using Field-Effect-Based Capacitive Devices," *PhD Thesis*, *Mathematisch-Naturwissenschaftlichen Fakultät I, Humboldt-Universität zu Berlin* (2011).

[185] R. GhoshMoulick, X.T. Vu, S. Gilles, D. Mayer, A. Offenhäusser, S. Ingebrandt, "Impedimetric Detection Of Covalently Attached Biomolecules On Field-Effect Transistors." *Physica Status Solidi (A): Applications and Materials Science*, 206 (3), 417–425 (2009).

[186] DataPhysics Instruments GmbH, "Operating Manual OCA 15 Plus," *DataPhysics Instruments GmbH*, Filderstadt (2002).

[187] D.C. Krüger, "Experimentelle Untersuchungen Zur Oberflächenveränderung Metallischer Implantatmaterialien Durch Plasmabehandlung," *PhD Thesis*, *Medizinische Fakultät der Ruhr-Universität Bochum* (2009).

[188] Y. Yuan, T.R. Lee, "Surface Science Techniques," *Springer-Verlag*, Berlin, Heidelberg (2013).

[189] S. Russell, "Contact Angle Measurement Technique For Rough Surfaces," *Master Thesis*, *Michigan Technological University* (2009).

[190] J. Sobek, C. Aquino, R. Schlapbach, "Analyzing Properties Of Fluorescent Dyes Used For Labeling DNA In Microarray Experiments." *BioFiles*, 2 (5), 5–8 (2007).

[191] "Http://www.genelink.com." *Gene Link* (2017).

[192] N. Panchuk-Voloshina, R.P. Haugland, J. Bishop-Stewart, M.K. Bhalgat, P.J. Millard, F. Mao, W.-Y. Leung, "Alexa Dyes, A Series Of New Fluorescent Dyes That Yield Exceptionally Bright, Photostable Conjugates." *Journal of Histochemistry and Cytochemistry*, 47 (9), 1179–1188 (1999).

[193] S. Schäfer, S. Eick, B. Hofmann, T. Dufaux, R. Stockmann, G. Wrobel, A. Offenhäusser, S. Ingebrandt, "Time-Dependent Observation Of Individual Cellular Binding Events To Field-Effect Transistors." *Biosensors and Bioelectronics*, 24 (5), 1201–1208 (2009).

[194] S. Ingebrandt, Y. Han, M.-R. Sakkari, R. Stockmann, O. Belinskyy, A. Offenhäusser, "Electronic Detection Of Nucleic Acid Molecules With A Field-Effect Transistor." *Semiconductor Materials For Sensing*, 828, 307–312 (2005).

[195] Y.-L. Chin, J.-C. Chou, T.-P. Sun, W.-Y. Chung, S.-K. Hsiung, "A Novel PH Sensitive ISFET With On Chip Temperature Sensing Using CMOS Standard Process." *Sensors and Actuators B: Chemical*, 76 (1–3), 582–593 (2001).

[196] A. Agarwal, K. Buddharaju, I.K. Lao, N. Singh, N. Balasubramanian, D.L. Kwong, "Silicon Nanowire Sensor Array Using Top-Down CMOS Technology." *Sensors and Actuators A: Physical*, 145–146, 207–213 (2008).

[197] Y. Cui, X. Duan, J. Hu, C.M. Lieber, "Doping And Electrical Transport In Silicon Nanowires." *Journal of Physical Chemistry B*, 104 (22), 5213–5216 (2000).

[198] H.H. Kampinga, "Thermotolerance In Mammalian Cells. Protein Denaturation And Aggregation, And Stress Proteins." *Journal of Cell Science*, 104 (1), 11–17 (1993).

[199] M. Peyrard, A.R. Bishop, "Statistical Mechanics Of A Nonlinear Model For DNA Denaturation." *Physical Review Letters*, 62 (23), 2755–2758 (1989).

[200] H.L. Casal, U. Köhler, H.H. Mantsch, "Structural And Conformational Changes Of B-Lactoglobulin B: An Infrared Spectroscopic Study Of The Effect Of PH And Temperature." *Biochimica et Biophysica Acta*, 957 (1), 11–20 (1988).

[201] A. Caflisch, M. Karplus, "Molecular Dynamics Simulation Of Protein Denaturation: Solvation Of The Hydrophobic Cores And Secondary Structure Of Barnase." *Proceedings of the National Academy of Sciences*, 91 (5), 1746–1750 (1994).

[202] Malla Reddy Sakkari, "Exploration Of ISFET Transfer-Function For Biochemical Applications," *Master Thesis*, *Department of Applied Physics, Aachen University of Applied Sciences, Campus Jülich* (2005).

[203] D. Landheer, W.R. McKinnon, G. Aers, W. Jiang, M.J. Deen, "Calculation Of The Response Of Field-Effect Transistors To Charged Biological Molecules." *IEEE Sensors Journal*, 7 (9), 1233–1242 (2007).

[204] D. Landheer, G. Aers, W.R. McKinnon, M.J. Deen, J.C. Ranuarez, "Model For The Field Effect From Layers Of Biological Macromolecules On The Gates Of Metal-Oxide-Semiconductor Transistors." *Journal of Applied Physics*, 98 (4), 44701 (2005).

[205] W.R. McKinnon, D. Landheer, G. Aers, "Sensitivity Of Field-Effect Biosensors To Charge, PH, And Ion Concentration In A Membrane Model." *Journal of Applied Physics*, 104 (12), 124701 (2009).

[206] G.-J. Zhang, J.H. Chua, R.-E. Chee, A. Agarwal, S.M. Wong, K.D. Buddharaju, N. Balasubramanian, "Highly Sensitive Measurements Of PNA-DNA Hybridization Using Oxide-Etched Silicon Nanowire Biosensors." *Biosensors and Bioelectronics*, 23 (11), 1701–1707 (2008).

[207] M. Schwartz, T.C. Nguyen, X.T. Vu, P. Wagner, R. Thoelen, S. Ingebrandt, "Impedimetric Sensing Of DNA With Silicon Nanowire Transistors As Alternative Transducer Principle." *Physica Status Solidi (A): Applications and Materials Science*, available online, 1700740 (2018).

[208] A. Susloparova, D. Koppenhöfer, J.K.-Y. Law, X.T. Vu, S. Ingebrandt, "Electrical Cell-Substrate Impedance Sensing With Field Effect Transistors Is Able To Unravel Cellular Adhesion And Detachment Processes On A Single Cell Level." *Lab on a Chip*, 15 (3), 668–679 (2012).

[209] D. Koppenhöfer, A. Susloparova, D. Docter, R.H. Stauber, S. Ingebrandt, "Monitoring Nanoparticle Induced Cell Death In H441 Cells Using Field-Effect Transistors." *Biosensors and Bioelectronics*, 40 (1), 89–95 (2012).

[210] R.B.M. Schasfoort, G.J. Streekstra, P. Bergveld, R.P.H. Kooyman, J. Greve, "Influence Of An Immunological Precipitate On D.C. And A.C. Behaviour Of An ISFET." *Sensors and Actuators*, 18 (2), 119–129 (1989).

[211] M.M. Antonisse, B.H. Snellink-Ruël, R.J. Lugtenberg, J.F. Engbersen, A. van den Berg, D.N. Reinhoudt, "Membrane Characterization Of Anion-Selective CHEMFETs By Impedance Spectroscopy." *Analytical Chemistry*, 72 (2), 343–348 (2000).

[212] E. Katz, I. Willner, "Probing Biomolecular Interactions At Conductive And Semiconductive Surfaces By Impedance Spectroscopy: Routes To Impedimetric Immunosensors, DNA-Sensors, And Enzyme Biosensors." *Electroanalysis*, 15 (11), 913–947 (2003).

[213] R.J.W. Lugtenberg, R.J.M. Egberink, A. van den Berg, J.F.J. Engbersen, D.N. Reinhoudt, "The Effects Of Covalent Binding Of The Electroactive Components In Durable CHEMFET Membranes-Impedance Spectroscopy And Ion Sensitivity Studies." *Journal of Electroanalytical Chemistry*, 452 (1), 69–86 (1998).

[214] A.B. Kharitonov, M. Zayats, A. Lichtenstein, E. Katz, I. Willner, "Enzyme Monolayer-Functionalized Field-Effect Transistors For Biosensor Applications." *Sensors and Actuators B*, 70 (1–3), 222–231 (2000).

[215] P. Bergveld, A. van den Berg, P.D. van der Wal, M. Skowronska-Ptasinska, E.J.R. Sudhölter, D.N. Reinhoudt, "How Electrical And Chemical Requirements For REFETs May Coincide." *Sensors and Actuators*, 18 (3–4), 309–327 (1989).

[216] A. Susloparova, D. Koppenhöfer, X.T. Vu, M. Weil, S. Ingebrandt, "Impedance Spectroscopy With Field-Effect Transistor Arrays For The Analysis Of Anti-Cancer Drug Action On Individual Cells." *Biosensors and Bioelectronics*, 40 (1), 50–56 (2013).

[217] T.C. Nguyen, X.T. Vu, M. Freyler, S. Ingebrandt, "PSPICE Model For Silicon Nanowire Field-Effect Transistor Biosensors In Impedimetric Measurement Mode." *Physica Status Solidi (A): Applications and Materials Science*, 210 (5), 870–876 (2013).

[218] A. Susloparova, X.T. Vu, D. Koppenhöfer, J.K.-Y. Law, S. Ingebrandt, "Investigation Of ISFET Device Parameters To Optimize For Impedimetric Sensing Of Cellular Adhesion." *Physica Status Solidi (A): Applications and Materials Science*, 211 (6), 1395–1403 (2014).

[219] A. Susloparova, D. Koppenhöfer, J.K.-Y. Law, X.T. Vu, S. Ingebrandt, "Electrical Cell-Substrate Impedance Sensing With Field-Effect Transistors Is Able To Unravel Cellular Adhesion And Detachment Processes On A Single Cell Level." *Lab on a Chip*, 15 (3), 668–679 (2015).

[220] M.L. Pourciel-Gouzy, W. Sant, I. Humenyuk, L. Malaquin, X. Dollat, P. Temple-Boyer, "Development Of PH-ISFET Sensors For The Detection Of Bacterial Activity." *Sensors and Actuators B: Chemical*, 103 (1–2), 247–251 (2004).

[221] W. Bunjongpru, O. Trithaveesak, K. Sowsuwan, W. Jeamsaksiri, C. Hruanun, A. Poyai, "CMOS Compatible Ion Sensitive Field Effect Transistor With Silicon Nitride Membrane For PH Measurement System." *4th International Conference on Electrical Engineering/Electronics, Computer, Telecommunications and Information Technology*, 29–31 (2007).

[222] P. Georgiou, C. Toumazou, "ISFET Characteristics In CMOS And Their Application To Weak-Inversion Operation." *Sensors and Actuators B: Chemical*, 143 (1), 211–217 (2009).

[223] S. Jamasb, S. Collins, R.L. Smith, "A Physical Model For Drift In PH ISFETs." *Sensors and Actuators B: Chemical*, 49 (1–2), 146–155 (1998).

[224] M.H. Abouzar, A. Poghossian, A.M. Pedraza, D. Gandhi, S. Ingebrandt, W. Moritz, M.J. Schöning, "An Array Of Field-Effect Nanoplate SOI Capacitors For (Bio-)Chemical Sensing." *Biosensors and Bioelectronics*, 26 (6), 3023–3028 (2011).

[225] Y. Chen, X. Wang, S. Erramilli, P. Mohanty, A. Kalinowski, "Silicon-Based Nanoelectronic Field-Effect PH Sensor With Local Gate Control." *Applied Physics Letters*, 89 (22), 223512 (2006).

[226] W.M. Siu, R.S.C. Cobbold, "Basic Properties Of The Electrolyte-SiO_2-Si System: Physical And Theoretical Aspects." *IEEE Transactions on Electron Devices*, 26 (11), 1805–1815 (1979).

[227] L. Bousse, P. Bergveld, "The Role Of Buried OH Sites In The Response Mechanism Of Inorganic-Gate PH-Sensitive ISFETs." *Sensors and Actuators*, 6 (1), 65–87 (1984).

[228] N.F. de Rooij, P. Bergveld, "The Influence Of The PH On The Electrolyte-SiO_2-Si System Studied By Ion-Sensitive Fet Measurements And Quasi-Static C-V Measurements." *Thin Solid Films*, 71 (2), 327–331 (1980).

[229] L. Bousse, "Single Electrode Potentials Related To Flat-Band Voltage Measurements On EOS And MOS Structures." *The Journal of Chemical Physics*, 76 (10), 5128–5133 (1982).

[230] T.C. Nguyen, M. Schwartz, X.T. Vu, J. Blinn, S. Ingebrandt, "Handheld Readout System For Field-Effect Transistor Biosensor Arrays For Label-Free Detection Of Biomolecules." *Physica Status Solidi (A): Applications and Materials Science*, 212 (6), 1313–1319 (2015).

[231] Y. Cui, Q. Wei, H. Park, C.M. Lieber, "Nanowire Nanosensors For Highly Sensitive And Selective Detection Of Biological And Chemical Species." *Science*, 293 (5533), 1289–1292 (2001).

[232] R. Tian, S. Regonda, J. Gao, Y. Liuc, W. Hu, "Ultrasensitive Protein Detection Using Lithographically Defined Si Multinanowire Field Effect Transistors." *Lab on a Chip*, 11 (11), 1952–1961 (2011).

[233] L.C.P.M. de Smet, D. Ullien, M. Mescher, E.J.R. Sudhölter, "Organic Surface Modification Of Silicon Nanowire-Based Sensor Devices.," *INTECH Open Access Publisher*, Rijeka (2011).

[234] R.N. Smith, M. McCormick, C.J. Barrett, L. Reven, H.W. Spiess, "NMR Studies Of PAH/PSS Polyelectrolyte Multilayers Adsorbed Onto Silica." *Macromolecules*, 37 (13), 4830–4838 (2004).

[235] M.H. Abouzar, A. Poghossian, A. Razavi, O.A. Williams, N. Bijnens, P. Wagner, M.J. Schöning, "Characterisation Of Capacitive Field-Effect Sensors With A Nanocrystalline-Diamond Film As Transducer Material For Multi-Parameter Sensing." *Biosensors and Bioelectronics*, 24 (5), 1298–1304 (2009).

[236] G. Decher, J. Schmitt, "Fine-Tuning Of The Film Thickness Of Ultrathin Multilayer Films Composed Of Consecutively Alternating Layers Of Anionic And Cationic Polyelectrolytes." *Progress in Colloid and Polymer Science*, 89, 160–164 (1992).

[237] S.S. Shiratori, M.F. Rubner, "PH-Dependent Thickness Behavior Of Sequentially Adsorbed Layers Of Weak Polyelectrolytes." *Macromolecules*, 33 (11), 4213–4219 (2000).

[238] A. Poghossian, M.J. Schöning, "Label-Free Sensing Of Biomolecules With Field-Effect Devices For Clinical Applications." *Electroanalysis*, 26 (6), 1197–1213 (2014).

[239] "Https://www.sciencetechblog.com." *A. Burgess* (2011).

[240] R.A. McCloy, S. Rogers, C.E. Aldon, T. Lorca, A. Castro, A. Burgess, "Partial Inhibition Of Cdk1 In G2 Phase Overrides The SAC And Decouples Mitotic Events." *Cell Cycle*, 13 (9), 1400–1412 (2014).

[241] A. Burgess, S. Vigneron, E. Brioudes, J.-C. Labbé, T. Lorca, A. Castro, "Loss Of Human Greatwall Results In G2 Arrest And Multiple Mitotic Defects Due To Deregulation Of The Cyclin B-Cdc2/PP2A Balance." *Proceedings of the National Academy of Sciences*, 107 (28), 12564–12569 (2010).

[242] I.D. Johnson, "Molecular Probes Handbook: A Guide To Fluorescent Probes And Labeling Technologies," *Life Technologies Corporation*, Carlsbad, California (2010).

[243] J.N. Israelachvili, "Intermolecular And Surface Forces," *Academic Press, Inc.*, Amsterdam (2011).

[244] Y. Dong, S. V. Pappu, Z. Xu, "Detection Of Local Density Distribution Of Isolated Silanol Groups On Planar Silica Surfaces Using Nonlinear Optical Molecular Probes." *Analytical Chemistry*, 70 (22), 4730–4735 (1998).

[245] L.A. Chrisey, G.U. Lee, C.E. O'Ferrall, "Covalent Attachment Of Synthetic DNA To Self-Assembled Monolayer Films." *Nucleic Acids Research*, 24 (15), 3031–3039 (1996).

[246] J.P. Cloarec, J.R. Martina, C. Polychronakosc, I. Lawrenceb, M.F. Lawrenceb, E. Souteyranda, "Functionalization Of Si/SiO$_2$ Substrates With Homooligonucleotides For A DNA Biosensor." *Sensors and Actuators B: Chemical*, 58 (1–3), 394–398 (1999).

[247] T. Sakata, M. Kamahori, Y. Miyahara, "Immobilization Of Oligonucleotide Probes On Si$_3$N$_4$ Surface And Its Application To Genetic Field Effect Transistor." *Materials Science and Engineering: C*, 24 (6–8), 827–832 (2004).

[248] M. Schwartz, T.C. Nguyen, X.T. Vu, M. Weil, J. Wilhelm, P. Wagner, R. Thoelen, S. Ingebrandt, "DNA Detection With Top-Down Fabricated Silicon Nanowire Transistor Arrays In The Linear Operation Regime." *Physica Status Solidi (A): Applications and Materials Science*, 213 (6), 1510–1519 (2016).

[249] A. Kim, C.S. Ah, C.W. Park, J.-H. Yang, T. Kim, C.-G. Ahn, S.H. Park, G.Y. Sung, "Direct Label-Free Electrical Immunodetection In Human Serum Using A Flow-Through-Apparatus Approach With Integrated Field-Effect Transistors." *Biosensors and Bioelectronics*, 25 (7), 1767–1773 (2010).

[250] A. Poghossian, A. Cherstvy, S. Ingebrandt, A. Offenhäusser, M.J. Schöning, "Possibilities And Limitations Of Label-Free Detection Of DNA Hybridization With Field-Effect-Based Devices." *Sensors and Actuators B: Chemical*, 111–112 470–480 (2005).

[251] P. Xie, Q. Xiong, Y. Fang, Q. Qing, C.M. Lieber, "Local Electrical Potential Detection Of DNA By Nanowire-nanopore Sensors." *Nature Nanotechnology*, 7 (2), 119–125 (2012).

[252] "Http://www.graphpad.com/." *GraphPad Software Inc.* (2017).

[253] "Http://www.statstutor.ac.uk/." *Sheer, R.* (2004).

[254] "Https://stats.idre.ucla.edu/." *UCLA: Statistical Consulting Group* (2017).

[255] T.C. Nguyen, "Readout Concepts For Label-Free Biomolecule Detection With Advanced ISFET And Silicon Nanowire Biosensors," *PhD Thesis, Department of Electrical and Computer Engineering, University of Kaiserslautern* (2017).

[256] Y. Liu, R.W. Dutton, "Effects Of Charge Screening And Surface Properties On Signal Transduction In Field Effect Nanowire Biosensors." *Journal of Applied Physics*, 106 (1), 14701–14708 (2009).

[257] R.B.M. Schasfoort, P. Bergveld, R.P.H. Kooyman, J. Greve, "Possibilities And Limitations Of Direct Detection Of Protein Charges By Means Of An Immunological Field-Effect Transistor." *Analytica Chimica Acta*, 238 323–329 (1990).

[258] L. De Vico, L. Iversen, M.H. Sorensen, M. Brandbyge, J.Nygard, K.L. Martinez, J.H. Jensen, "Predicting And Rationalizing The Effect Of Surface Charge Distribution And Orientation On Nano-Wire Based FET Bio-Sensors." *Nanoscale*, 3 (9), 3635–3640 (2011).

[259] M.W. Shinwari, M.J. Deen, "Impedance Modelling Of FET-Based Biosensors." *Journal of the Electrochemical Society*, 158 (6), J189–J194 (2011).

[260] S. Das, "Explicit Interrelationship Between Donnan And Surface Potentials And Explicit Quantification Of Capacitance Of Charged Soft Interfaces With PH-Dependent Charge Density." *Colloids and Surfaces A: Physicochemical and Engineering Aspects*, 462, 69–74 (2014).

[261] K. Heileman, J. Daoud, M. Tabrizian, "Dielectric Spectroscopy As A Viable Biosensing Tool For Cell And Tissue Characterization And Analysis." *Biosensors and Bioelectronics*, 49, 348–359 (2013).

[262] S.L. Patterson, T. Abel, T.A.S. Deuel, K.C. Martin, J.C. Rose, E.R. Kandel, "Recombinant BDNF Rescues Deficits In Basal Synaptic Transmission And Hippocampal LTP In BDNF Knockout Mice." *Neuron*, 16 (6), 1137–1145 (1996).

[263] I. Bertini, H.B. Gray, S.J. Lippard, J.S. Valentine, "Bioinorganic Chemistry," *University Science Book*, Mill Valley, California (1994).

[264] U.E. Lang, R. Hellweg, J. Gallinat, "BDNF Serum Concentrations In Healthy Volunteers Are Associated With Depression-Related Personality Traits." *Neuropsychopharmacology*, 29 (4), 795–798 (2004).

[265] K.M. Chang, C.T. Chang, K.M. Chan, "Development Of An Ion Sensitive Field Effect Transistor Based Urea Biosensor With Solid State Reference Systems." *Sensors*, 10 (6), 6115–6127 (2010).

[266] K.-M. Chang, C.-T. Chang, K.-Y. Chao, J.-L. Chen, "Development Of FET-Type Reference Electrodes For PH-ISFET Applications." *Journal of the Electrochemical Society*, 157 (5), J143–J148 (2010).

[267] D. Borstlap, "High-k Dielectrics As Bioelectronic Interface For Field-Effect Transistors," *PhD Thesis, Mathematik, Informatik und Naturwissenschaften, Rheinisch-Westfälische Technische Hochschule Aachen* (2006).

[268] "Http://www.mathwords.com/a/area_under_a_curve.htm." *Simmons, B.* (2017).

[269] M. Crescentini, M. Rossi, P. Ashburn, M. Lombardini, E. Sangiorgi, H. Morgan, M. Tartagni, "AC And Phase Sensing Of Nanowires For Biosensing." *Biosensors*, 6 (2), 1–14 (2016).

[270] P. Verboon, "Graphical Tools In Multivariate Analysis." *Report, Department of Human and Computer Studies, University of Leiden* (1988).

[271] J.H.S. Dayal, M.J. Sales, W.E. Corver, C.A. Purdie, L.B. Jordan, P.R. Quinlan, L. Baker, N.T. Haar, "Multiparameter DNA Content Analysis Identifies Distinct Groups In Primary Breast Cancer." *British Journal of Cancer*, 108 (4), 873–880 (2013).

[272] A. Lichtenstein, E. Havivi, R. Shacham, E. Hahamy, R. Leibovich, A. Pevzner, V. Krivitsky, G. Davivi, I. Presman, R. Elnathan, Y. Engel, E. Flaxer, F. Patolsky, "Supersensitive Finngerprinting Of Explosives By Chemically Modified Nanosensors Arrays." *Nature Communications*, 5 (4195), 1–12 (2014).

[273] M.J. Saary, "Radar Plots: A Useful Way For Presenting Multivariate Health Care Data." *Journal of Clinical Epidemiology*, 60 (4), 311–317 (2008).

[274] Rory Adams, "Machine Learning For Predicitve Modelling." *Matlab Expo 2015*, United Kingdom (2015).

[275] "Http://de.mathworks.com/help/stats/supervised-learning-machine-learning-workflow-and-algorithms.html." *The MathWorks Inc.* (2016).

[276] "Http://de.mathworks.com/help/stats/classification-trees-and-regression-trees.html." *The MathWorks Inc.* (2016).

[277] "Http://de.mathworks.com/help/stats/train-decision-trees-in-classification-learner-app.html." *The MathWorks Inc.* (2016).

[278] N. Bhalla, P. Jolly, N. Formisano, P. Estrela, "Introduction To Biosensors." *Essays in Biochemistry*, 60, 1–8 (2016).

[279] "Https://www.talend.com/blog/2017/05/15/testing-machine-learning-algorithms-with-k-fold-cross-validation/." *Krupa, Norbert* (2017).

[280] "Https://towardsdatascience.com/cross-validation-in-machine-learning-72924a69872f." *Gupta, Prashant* (2017).

[281] "Https://de.mathworks.com/discovery/cross-validation.html." *The MathWorks Inc.* (2018).

[282] G.-J. Zhang, A. Agarwal, K.D. Buddharaju, S. Navab, Z. Gao, "Highly Sensitive Sensors For Alkali Metal Ions Based On Complementarymetal-Oxide-Semiconductor-Compatible Silicon Nanowires." *Applied Physics Letters*, 90 (23), 233903 (2007).

[283] N.N. Mishra, W.C. Maki, E. Cameron, R. Nelson, P. Winterrowd, S.K. Rastogi, B. Filanoski, G.K. Maki, "Ultra-Sensitive Detection Of Bacterial Toxin With Silicon Nanowire Transistor." *Lab on a Chip*, 8 (6), 868–871 (2008).

[284] A. Ram, A. Lichtenstein, X.-T. Vu, J.K.-Y. Law, M. Schwartz, J. Wilhelm, T.C. Nguyen, "Nanoelectronic Sensor Pixel.," *Patent* (2016).

List of Figures

List of Tables

List of Abbreviations

Aa	
AC	Alternating current
APTES	(3-aminopropyl)triethoxysilane
a.u.	Arbitrary unit
Bb	
BDNF	Brain derived neurotrophic factor
BG	Back gate
BOX	Buried oxide
BSA	Bovine serum albumin
Cc	
cDNA	Complementary deoxyribonucleic acid
Chan	Channel
CFTR	Cystic fibrosis transmembrane conductance regulator
CMOS	Complementary metal-oxide semiconductor
CTF	Corrected total fluorescence
Cy3	Cyanine 3
Dd	
D	Drain
DC	Direct current
DNA	Deoxyribonucleic acid
Ee	
EBL	Electron beam lithography
ELISA	Enzyme-linked immunosorbent assay
Ff	
Fab	Antigen binding fragment
FET	Field-effect transistor
FG	Front gate
FPR	False positive rate
Gg	
GPTMS	3-(glycidoxypropyl)trimethoxysilane

Hh	
HBSS	Hank's balanced salt solution
HIV	Human immunodeficiency virus
HLA	Human leukocyte antigen
Ii	
Ig	Immunoglobulin
IHP	Inner Helmholtz plane
IntDen	Integrated density
IP	Isoelectric point
ISFET	Ion-sensitive field-effect transistor
Ll	
LPCVD	Low-pressure chemical vapor deposition
LNGFR	Low affinity nerve growth factor receptor
Mm	
MOSEFT	Metal-oxide semiconductor field-effect transistor
MUSIC	Multisite complexation
Nn	
NGF	Nerve Growth Factor
NIL	Nanoimprint lithography
NW	Nanowire
Oo	
OHP	Outer Helmholtz plane
ONO	Oxide-nitride-oxide
OP	Operation point
Pp	
PAH	Poly(allylamine hydrochloride)
PBS	Phosphate buffer saline
PCR	Polymerase chain reaction
PE	Polyelectrolyte
PECVD	Plasma enhanced chemical vapor deposition
PMMA	Poly(methyl methacrylate)
PNA	Peptide nucleic acid
PSS	Poly(sodium4-styrensulfonate)

PZC	Point of zero charge
Qq	
QCM	Quartz crystal microbalance
Rr	
RE	Reference electrode
RIE	Reactive ion etching
RNA	Ribonucleic acid
Ss	
S	Source
SEM	Scanning electron microscopy
Si	Silicon
SiNW	Silicon nanowire
SSC	Saline-sodium citrate
ssDNA	Single-stranded deoxyribonucleic acid
SOI	Silicon-on-insulator
Tt	
TC	Transfer characteristic
TMAH	Tetramethylammonium hydroxide
TPR	True positive rate
TrkB	Tropomyosin related kinase B
TTF	Transistor transfer function
Vv	
V	Voltage

List of Symbols

Latin alphabet

Cc	
C_{Bio}	Capacitance of the biomolecular layer
C_{CLCS}	Capacitances of the source contact lines
C_{CLD}	Capacitances of the drain contact lines
C_{DL}	Capacitance of the double layer
C_{Ox}	Capacitance of the insulting oxide layer

Ee	
e	Elementary charge
E_{ref}	Potential of the reference electrode
Gg	
G	Gate
g_m	Transconductance
Hh	
$H(j\omega)$	Theoretical transfer function
Ii	
I	Ionic strength
i_{DS}	Small-signal drain-source current
I_{DS}	Drain-source current
Kk	
k	Boltzmann constant
K_a/K_b	Dissociation constant acid/base
Ll	
L	Length
Nn	
N_A	Avogadro constant
nS	nanoSiemens
N_S	Density of the available sites on the surface
n_0	Concentration of each individual ion in the bulk solution
Pp	
P	Laplace pressure
pH_S	pH value at the surface
pH_B	pH value in the electrolyte bulk
Qq	
q	Elementary charge
Q_B	Depletion charge in silicon
Q_{Ox}	Fixed oxide charge
Q_{SS}	Surface state density at silicon surface
Rr	
R	Radius

R_{Bio}	Resistance of the biomolecule
R_{RE}	Resistance of the reference solution
R_{Sol}	Resistance of the electrolyte solution
Tt	
T	Temperature
T_m	Melting temperature
Vv	
V_{BG}	Back-gate voltage
V_D	Drain voltage
V_{FG}	Front-gate voltage
V_G	Gate voltage
v_{GS}	Small-signal gate-source voltage
V_{GS}	Gate-source voltage
V_{stit}	Input signal
v_{out}	Small-signal output signal
V_{out}	Output signal
V_0	Constant voltage
V_S	Source voltage
V_{TH}	Threshold voltage
Ww	
W	Width
Xx	
x	Distance of the center of the charge from the surface
Zz	
z	Charge of the ions
Greek alphabet	
A α	
α	Sensitivity parameter
Bß	
ß	Intrinsic buffer capacity
Γγ	
γ	Interfacial energy
γ_{LG}	Liquid-gas interfacial energy

γ_{SG}	Solid-gas interfacial energy
γ_{SL}	Solid-liquid interfacial energy
Εε	
ε	Dielectric constant of the bulk solution
ε_0	Dielectric constant in vacuum
ε_{Bio}	Dielectric constant of the biomolecular layer
ε_{Ox}	Dielectric constant of the oxide
ε_S	Dielectric constant of the solution
ε_W	Dielectric constant of the measuring solution
Ζζ	
ζ	Zeta potential
Θθ	
θ_{CA}	Contact angle
Λλ	
λ_D	Debye length
Μμ	
μ	Carrier mobility
Σσ	
σ_0	Surface charge density
σ_{DNA}	Surface charge density of DNA
Ττ	
τ_1/τ_2	Time constant
Φφ	
Φ_F	Potential difference between Fermi level in silicon between source and drain and Fermi level of intrinsic silicon
Χχ	
χ_{sol}	Surface dipole potential of the solution at the gate oxide-electrolyte interface
Ψψ	
ψ_S	Surface potential
ψ_{Si}	Silicon work function
Ωω	
ω	Angular frequency

List of Biomolecules and Chemicals

DNA sequences

Name	Sequence	5'-modifier	3'-modifier	Company
ssDNA	5'AC6-ATGAACACTGCATGTAGTCA-3'	Amino-C6	-----------	Eurofins Genomics
Cy3 ssDNA	5'Cy3-ATGAACACTGCATGTAGTCA-3'-AC6	Cy3	Amino-C6	Eurofins Genomics
FMM DNA	5'AC6-TACTTGTGATGTACATCAGT-3'	Amino-C6	-----------	Eurofins Genomics
Capture HLA-B27		Amino-C6	-----------	Euroimmun AG
cDNA	5'-TGACTACATGCAGTGTTCAT-3'	-----------	-----------	Eurofins Genomics
Cy3 cDNA	5'Cy3-TGACTACATGCAGTGTTCAT-3'	Cy3	-----------	Eurofins Genomics
HLA-B27		-----------	------------	Euroimmun AG

Antibodies and Cytokine

Goat anti-mouse Alexa Fluor® dye 488 (GAM 488) secondary antibody, Molecular Probes™, ThermoFisher Scientific, Germany

Biotinylated mouse anti-human BDNF detection antibody, R&D Systems, Inc., USA

Brain-Derived Neurotrophic Factor (BDNF), R&D Systems, Inc., USA

Mouse anti-human BDNF antibody, R&D Systems, Inc., USA

Streptavidin-ALEXA 488 conjugate, Molecular Probes™, ThermoFisher Scientific, Germany

Chemicals

Bovine serum albumin (BSA), Sigma-Aldrich, Germany

Epoxy glue, 377 1LB kit, Epoxy Technology, Inc., USA

3-(glycidoxypropyl)trimethoxysilane (GPTMS) Sigma-Aldrich, Germany

Hydrogen peroxide (H_2O_2), Sigma-Aldrich, Germany

Phosphate buffered saline (PBS), Sigma-Aldrich, Germany

Poly(sodium 4-styrenesulfonate) (PSS; $(C_8H_7NaO_3S)_n$), Sigma-Aldrich, Germany

Poly(allylamine hydrochloride) (PAH; C_3H_8ClN), Sigma-Aldrich, Germany

Saline sodium citrate buffer (SSC), Sigma-Aldrich, Germany

Silicone elastomer, Sylgard® 184 silicone elastomer kit, Dow Corning, Germany

Silicone adhesive, 96-083 silicon adhesive kit, Dow Corning, Germany

Skimmed milk, Sigma-Aldrich, Germany

Sodium chloride (NaCl), Sigma-Aldrich, Germany

Sodium phosphate monobasic monohydrate ($NaH_2PO_4 \cdot H_2O$), Sigma-Aldrich, Germany

Sodium phosphate dibasic, anhydrous (Na_2HPO_4), Sigma-Aldrich, Germany

Sulfuric acid (H_2SO_4), Sigma-Aldrich, Germany

Acknowledgements

I would like to express my deepest gratitude to my advisors, collaborators, colleagues, friends and family, who always supported.

First, I want to thank Prof. Sven Ingebrandt for giving me the possibility to do my PhD thesis in his group, for his guidance, motivation and support: Lieber Sven, vielen Dank, dass du mir die Chance gegeben hast, in deiner Gruppe meine Doktorarbeit zu machen. Es war schön mit anzusehen, wie aus einer relativ kleinen Arbeitsgruppe ein großes, internationales Team wurde. Ich möchte mich herzlich bei dir bedanken, dass du es mir stets ermöglicht hast, an vielen Konferenzen teilzunehmen. Danke, für die hilfreichen und motivierenden Gespräche. Motivieren ist etwas, dass du hervorragend kannst. Danke, für das Korrigieren meiner Paper, der etlichen Poster und meiner Dissertation. Was lange währt, wird (hoffentlich) endlich gut ;).

I am grateful to Prof. Dr. Patrick Wagner who made it possible to graduate at the university Hasselt by taking over the supervision of my PhD thesis as promoter and for being in my committee: Vielen Dank für das Korrekturlesen meiner Arbeit und die vielen wertvollen Ratschläge. Darüber hinaus möchte ich mich herzlich für die Hilfe beim bürokratischen Prozedere und beim Zusammenstellen meines Prüfungskomitees bedanken.

I would like to express my thanks to Prof. Dr. Ronald Thoelen for being my co-promoter and a member of the committee as well as for the help with the administrative process. Furthermore, I am grateful for the valuable comments on this thesis.

I would like to appreciate Prof. Dr. Patricia Losada-Pérez, Prof. Dr. Luc Michiels and Prof. Dr. Jef Hooyberghs for being in my committee and for the helpful comments on this thesis.

My sincerest thanks to Euroimmun AG, especially to the founder and chairman Prof. Dr. Winfried Stöcker, for supporting my project by providing the HLA-B27 assay reagents. Thanks to Daniel Flindt, who always helped me answering various question concerning their HLA-B27 assay.

شكرا على الحديث الممتبادل عن كل المواضيع وعلى الكلمات المشجعة. أنت واحد من القليلين الذين أتكلم معهم بهذه الإنفتاحية والجدية. إبقاكما أنت عليه.

Moreover, I thank Nina Stock for helping me with the regular cleaning and maintaining of the microspotter as well as for the preparation of different solutions: Liebe Nina, vielen Dank, dass du die dir aufgetragenen Aufgaben immer gewissenvoll und zuverlässig durchgeführt hast. Ich wusste es stets zu schätzen, dass ich mich immer auf dich verlassen konnte.

I am thankful to Dr. Maryam Weil, who was guiding me in the beginning of my PhD time: مريم، شما از من تشكر كه نمیشه شما كه یشه هواگوش بر رای من تدید داشت. روزهای در خصوص به من، از حمایت بر رای شما از تشكر با.بر ودید دخوبی الگوی و الهام من بر رای شما هؤی نه یك طراحی در ارزشمند راهنمایی و ارشد كارشناسی دوره داد شجوی یك عنوان به من اول یه هله تان كمك بر رای شما از تشكر با.)دیدار امید به ه.آزمایش به شده اضافه و جذاب كذ فرادس

I would also like to say 'Thank you' to all (former) members of the biomedical signalling group. It was a great pleasure and inspiration to work with you guys. Thank you, Danke, Dank je wel, спасибо, gracias, 谢谢, 多謝, Cảm ơn, Merci, شكر.

Thanks to my family and friends who supported me all the way through my PhD: Einen herzlichen Dank an euch alle. Es ist so schön, wie sehr euch meine Arbeit und das, was ich tue, interessiert. Danke für euer offenes Ohr, eure Motivation und die vielen lieben Worte.

Most of all, I would like to thank my parents, who always believed in me: Liebe Mama, lieber Papa, ich bin so dankbar, dass ihr immer für mich da seid und mich bei allem unterstützt. Tausend Dank für die Zeit, die ihr euch immer genommen habt und für eure Hilfe, die des Öfteren vonnöten waren. Danke, dass ihr auf unsere kleine Maus Elly aufgepasst habt, während ich an meiner Doktorarbeit gearbeitet habe. Vielen Dank aus ganzem Herzen.

Finally, I would like to thank my husband, who accompanied me through all ups and downs: Lieber David, vielen Dank, dass du mich bei jeder meiner Entscheidungen unterstützt und immer hinter mir stehst. Vielen Dank, dass du die Arbeit durchgelesen hast, obwohl diese eigentlich ein spanisches Dorf für dich ist ;). Vielen Dank, dass du mein ruhiger Pol bist und es (fast) immer

geschafft hast, dass ich nicht zu nervös vor anstehenden Prüfungen und Vorträgen war. Vielen Dank, dass du stets an mich geglaubt und mich fortwährend motiviert hast.

Publications

Publications in peer-reviewed journals

1. Nguyen, T. C., Vu, X. T., **Freyler, M.**, Ingebrandt, S., "PSPICE model for silicon nanowire field-effect transistor biosensors in impedimetric measurement mode", Physica Status Solidi A, 210 (5), 870–876 (2013).

2. Nguyen, T. C.*, **Schwartz, M.***, Vu, X. T., Blinn, J., Ingebrandt, S., "Handheld readout system for field-effect transistor biosensor arrays for label-free detection of biomolecules", Physica Status Solidi A, 210 (5), 870–876 (2015).

3. **Schwartz, M.***, Nguyen, T. C.*, Vu, X. T., Weil, M., Wilhelm, J., Wagner, P., Thoelen, R., Ingebrandt, S., "DNA detection with top–down fabricated silicon nanowire transistor arrays in linear operation regime", Physica Status Solidi A, 213 (6), 1510-1519 (2016).

4. **Schwartz, M.**, Nguyen, T. C., Vu, X. T., Wagner, P., Thoelen, R., Ingebrandt, S., "Impedimetric sensing of DNA with silicon nanowire transistors as alternative transducer principle", Physica Status Solidi A, available online, 1700740 (2018).

5. Lanche, R., Pachauri, V., Munief, W.-M., Mueller, A., **Schwartz, M.**, Wagner, P., Thoelen, R., Ingebrandt, S., "Graphite oxide electrical sensors are able to distinguish single nucleotide polymorphisms in physiological buffers", Chemistry of Flat Materials, 7, 1-9 (2018).

* Both authors contributed equally

Oral Presentations

1. **Freyler, M.**, Nguyen, T. C., Weil, M., Vu, X. T., Ingebrandt, S., "Silicon nanowire arrays as label-free platform for point-of-care applications", Engineering of Functional Interfaces (EnFI), University of Applied Sciences, Campus Zweibrücken, Germany, July 16 – 17, 2012.

2. **Schwartz, M.**, Vu, X. T., Nguyen, T. C., Wagner, P., Ingebrandt, S., "Detection of biomolecules based on transfer function measurements on SiNW transistor arrays", Engineering of Functional Interfaces (EnFI), Hasselt University, Belgium, July 8 – 9, 2013.

3. **Schwartz, M.**, Vu, X. T., Nguyen, T. C., Wagner, P., Ingebrandt, S., "Detection of biomolecules based on transfer function measurements on SiNW transistor arrays", International Conference in Advanced Manufacturing for Multifunctional Miniaturised Devices (M6), University of Applied Sciences, Campus Zweibrücken, Germany, July 15 – 16, 2013.

4. **Schwartz, M.**, Nguyen, T. C., Vu, X. T., Wagner, P., Ingebrandt, S., "Immunosensing based on impedimetric readout using micro- and nanoscale transistors", Engineering of Functional Interfaces (EnFI), Aachen University of Applied Sciences, July 14 - 15, 2014.

5. **Schwartz, M.**, Vu, X. T., Nguyen, T. C., Wagner, P., Ingebrandt, S., "Micro- and Nanoscale Field-Effect Transistors for the detection of DNA and PCR Products", Third International Conference in Advanced Manufacturing for Multifunctional Miniaturised Devices (ICAM3D-2014), Tsukuba International Congress Center, Tsukuba, Ibaraki, Japan, August 27-28, 2014.

6. **Schwartz, M.**, Nguyen, T. C., Vu, X. T., Wagner, P., Ingebrandt, S., "Detection of PCR Products by Micro- and Nanoscale Field-Effect Transistors", International Conference on Solid State Devices and Materials (SSDM), Tsukuba International Congress Center, Tsukuba, Ibaraki, Japan, September 8 - 11, 2014.

Posters

1. **Freyler, M.**, Nguyen, T. C., Vu, X. T., Weil, M., Ingebrandt, S., "Evaluation of the Point-of-Care Usability of Silicon Nanowire Arrays in Biomedical Diagnostics", 2nd NanoSensEU Symposium on Biosensor Development "Trends and Technology", Hasselt University, Belgium, April 25, 2012.

2. **Freyler, M.**, Nguyen, T. C., Weil, M., Vu, X. T., Ingebrandt, S., "Silicon nanowire arrays as label-free platform for point-of-care applications", Engineering of Functional Interfaces (EnFI), University of Applied Sciences, Campus Zweibrücken, Germany, June 16 – 17, 2012.

3. **Freyler, M.**, Nguyen, T. C., Weil, M., Vu, X. T., Ingebrandt, S., "Label-free detection of DNA out of PCR products on silicon nanowires for biomedical diagnostics", Label-Free Technologies 2012, Amsterdam, The Netherlands, November 1 – 3, 2012.

4. **Freyler, M.**, Nguyen, T. C., Vu, X. T., Ingebrandt, S., "Detection of PCR products by Silicon Nanowire Field-Effect Transistor Arrays", Deutsches BioSensor Symposium, Technical University of Applied Sciences Wildau, Germany, March 10 – 13, 2013.

5. **Schwartz, M.**, Vu, X. T., Nguyen, T. C., Wagner, P., Ingebrandt, S., "Detection of biomolecules based on transfer function measurements on SiNW transistor arrays", Engineering of Functional Interfaces (EnFI), Hasselt University, Belgium, July 8 – 9, 2013.

6. **Schwartz, M.**, Vu, X. T., Nguyen, T. C., Wagner, P., Ingebrandt, S., "Detection of biomolecules based on transfer function measurements on SiNW transistor arrays", International Conference in Advanced Manufacturing for Multifunctional Miniaturised Devices (M6), University of Applied Sciences, Campus Zweibrücken, Germany, July 15 – 16, 2013.

7. **Schwartz, M.**, Vu, X. T., Nguyen, T. C., Weil, M., Wagner, P., Ingebrandt, S., "Detection of human diseases using impedance spectroscopy with micro- and nanoscale field-effect sensor arrays", Biosensors 2014, 23rd Anniversary World Congress on Biosensors, Melbourne, Australia, May 27 - 30, 2014.

8. **Schwartz, M.**, Nguyen, T. C., Vu, X. T., Wagner, P., Ingebrandt, S., "Immunosensing based on impedimetric readout using micro- and nanoscale transistors", Engineering of Functional Interfaces (EnFI), Aachen University of Applied Sciences, July 14 - 15, 2014.

9. **Schwartz, M.**, Nguyen, T. C., Vu, X. T., Wagner, P., Ingebrandt, S., "Detection of PCR Products by Micro- and Nanoscale Field-Effect Transistors", International Conference on Solid State Devices and Materials (SSDM), Tsukuba International Congress Center, Tsukuba, Ibaraki, Japan, September 8 - 11, 2014.

Poster prices

1. **Freyler, M.**, Nguyen, T. C., Weil, M., Vu, X. T., Ingebrandt, S., "Label-free detection of DNA out of PCR products on silicon nanowires for biomedical diagnostics", Label-Free Technologies 2012, Amsterdam, The Netherlands, November 1 – 3, 2012.

2. **Schwartz, M.**, Vu, X. T., Nguyen, T. C., Wagner, P., Ingebrandt, S., "Detection of biomolecules based on transfer function measurements on SiNW transistor arrays", International Conference in Advanced Manufacturing for Multifunctional Miniaturised Devices (M6), University of Applied Sciences, Campus Zweibrücken, Germany, July 15 – 16, 2013.